ANALYSIS OF BINARY FLUID HEAT AND MASS TRANSFER IN AMMONIA-WATER ABSORPTION

A Dissertation
Presented to
The Academic Faculty

by

Lalit Kumar Bohra

In Partial Fulfillment
of the Requirements for the Degree
Doctor of Philosophy in Mechanical Engineering

Georgia Institute of Technology

December 2007

ANALYSIS OF BINARY FLUID HEAT AND MASS TRANSFER IN AMMONIA-WATER ABSORPTION

Approved by:

Dr. Srinivas Garimella, Advisor
George W. Woodruff School of
Mechanical Engineering
Georgia Institute of Technology

Dr. Samuel Graham
George W. Woodruff School of
Mechanical Engineering
Georgia Institute of Technology

Dr. William Wepfer
George W. Woodruff School of
Mechanical Engineering
Georgia Institute of Technology

Dr. Michael Bergin
School of Civil & Environmental
Engineering
Georgia Institute of Technology

Dr. James Frederick
School of Chemical and Bio-Medical
Engineering
Georgia Institute of Technology

Date Approved: July 13, 2007

To my parents Mohan Lal Bohra and Kanta Devi Bohra and to my siblings who have

always shown unfaltering faith in me

ACKNOWLEDGEMENTS

First and the foremost, I would like to express my deep sense of gratitude towards my major advisor Dr Srinivas Garimella for his expert guidance and constant support throughout the course of my graduate studies. I am sure that whatever I have learned while working with him, will be very useful in my future endeavors. He has been a great mentor.

I sincerely thank all the current and the past members of the Sustainable Thermal Systems Laboratory (STSL) for their support. I specially thank Sangsoo Lee for being a great help in conducting this research. It was very interesting and fun to work with him. I thank Jesse Killion, Matthew Determan and Tim Ernst for their help during fabrication of the test facility and for the interesting discussions regarding experimentation and analysis. They have been good friends outside the laboratory as well. I thank Biswajit Mitra, Akhil Agarwal and Ulf Andresen for discussions of concerns regarding our studies, and Chris Goodman, Brian Fronk and other STSL members who have been good friends.

I cannot leave out my friends Abhinav Saxena, Vipul Kumar and Apurva Mohan who were a great support in difficult times during the course of my studies in Atlanta.

Finally, I thank my committee members for their cooperation on various deadlines, and for the patient perusal of my dissertation and the valuable comments.

TABLE OF CONTENTS

LIST OF TABLES

LIST OF FIGURES

NOMENCLATURE

A	Area (m^2)
C_T	Total molar concentration ($kMol/m^3$)
Cp	Specific heat capacity (kJ/kg-K)
C_V	Flow coefficient
D	Binary diffusion coefficient (m^2/s)
d	Diameter (mm)
$d\dot{m}$	Differential mass flow rate (kg/s)
g	Acceleration due to gravity (m^2/s)
GAX	Generator-Absorber-Exchange
Ga	Galileo number
Gr	Grashof number
h	Enthalpy (kJ/kg)
ID	Inner diameter (mm, m)
H_2O	Water
Ja	Jakob number
k	Conductivity (W/m-K)
L	Length (mm, m)
LiBr	Lithium Bromide
LMTD	Log Mean Temperature Difference (^{o}C)
m	Mass (kg)

$\dot{m}$	Mass flow rate (kg/s)
M	Molecular weight (kg/kMol)
N	Number
$\dot{n}$	Molar flux (kMol/m^2-s)
NH_3	Ammonia
Nu	Nusselt number
O.D.	Outer diameter (mm, m)
P	Absolute pressure (kPa)
Pr	Prandtl number
ppm	Parts per million
q	Quality
Q	Heat duty (kW)
R	Thermal resistance (K/W or m^2-K/W)
Ra	Rayleigh number
Re	Reynolds number
Sc	Schmidt number
Sh	Sherwood number
t	Time (s)
T	Temperature (^{o}C)
U	Overall heat transfer coefficient (W/m^2-K)
V	Velocity (m/s)
x	Mass concentration
$\tilde{x}$	Molar concentration

y	Coordinate normal to tube surface
z	Mass concentration of condensing flux
z̃	Molar concentration of condensing flux

Greek Symbols

α	Heat transfer coefficient (W/m^2-K)
β	Mass transfer coefficient (m/s)
Δ	Differential
δ	Film thickness (m)
Γ	Solution mass flux (kg/m-s)
λ	Droplet site spacing (mm)
μ	Dynamic viscosity (kg/m-s)
Ω	Angular coordinate along film flow on tube
ν	Kinematic viscosity (m^2/s)
ρ	Density (kg/m^3)
σ	Surface tension (kg/s^2)

Subscripts

Abs/abs	Absorber
Ave/ave	Average
amb	Ambient
air	Air
bulk	Bulk values
C	Coolant

char	Characteristic
cap	Capillary
Con	Condenser
Concentrated	Concentrated solution
conv	Convection
cr	Cross-sectional
Des	Desorber
Dilute	Dilute solution
DT	Drip tray
dp	Droplet
Evap	Evaporator
FF	Falling-film
Film	Solution film
fg	Latent (phase change)
form	Forming droplet
free	Free-falling droplet
ID	Inner diameter (mm, m)
in	Inlet
ins	Insulation
int	Interface
l	Liquid
Measured	Measured value
MT	Mass transfer

min	Minimum
OD	Outer diameter (mm, m)
or	Original
out	Outlet
pool	Solution pool
pr	Primary
rad	Radiation
Rec	Rectifier
Ref	Refrigerant
Reflux	Reflux
Sep	Separator
seg	Segment
shell	Absorber shell
sol	Solution
surf	Surface
t	Total/Tube
V	Vapor
W	Wall

SUMMARY

An investigation of binary fluid heat and mass transfer in a horizontal tube falling-film ammonia-water absorber was conducted. A tube bank consisting of four columns of six 9.5 mm (3/8") nominal OD, 0.292 m (11.5") long tubes was installed in an absorber shell that allowed heat and mass transfer measurements and optical access. A test facility consisting of all the components of a functional absorption chiller was fabricated. Thus, a steam-heated desorber was used to generate ammonia-water vapor over a wide range of conditions. The ammonia-water vapor was rectified and condensed, followed by recuperative heat exchange before being expanded to the evaporator pressure. The cooling load was supplied to the evaporator by a combination of resistance heating and closed loop fluid heating. The evaporated refrigerant was preheated recuperatively by the fluid exiting the condenser and then flowed to the absorber to be absorbed in the test section. A solution heat exchanger between the absorber and desorber (and in some tests, a solution pre-conditioner upstream of the absorber) completed the ammonia-water loop.

Measurements were recorded at both system and local levels within the absorber for a wide range of operating conditions (nominally, desorber solution outlet concentrations of 5 - 40% for three nominal absorber pressures of 150, 345 and 500 kPa, for solution flow rates of 0.019 - 0.034 kg/s.). Local measurements were supplemented by high-speed, high-resolution visualization of the flow over the tube banks. Using the measurements and observations from videos, heat and mass transfer rates, heat and mass

transfer coefficients for each test condition were determined at the component and local levels. Care was also taken throughout the study to not only establish the desired conditions, but also to maintain the solution-side thermal resistance as the governing resistance so that absorption heat and mass transfer phenomena could be measured accurately. For the range of experiments conducted, at the component level, the solution heat transfer coefficient varied from 923 to 2857 W/m^2-K, while the vapor mass transfer coefficient varied from 0.0026 to 0.25 m/s, and the liquid mass transfer coefficient varied from 5.51×10^{-6} to 3.31×10^{-5} m/s, depending on the test condition. The local measurements allowed dividing the absorber into segments that were analyzed to obtain the variations in heat and mass transfer rates along the solution flow path. Videos revealed several interesting features of falling-film and droplet flow modes. Local measurements and insights from the video frames were used to obtain the contributions of falling-film and droplet modes to the total absorption rates. Local heat and mass transfer rates were then obtained for several segments. The local heat transfer coefficients varied from 78 to 6116 W/m^2-K, while the local vapor mass transfer coefficients varied from -0.04 (indicating local desorption in some cases) to 2.8 m/s and the local liquid mass transfer coefficients varied from -3.59×10^{-5} (indicating local desorption in some cases) to 8.96×10^{-5} m/s. The solution heat transfer coefficient increased with increasing solution flow rate, both at the component and the segmental levels; however, the mass transfer coefficient seems to remain unaffected by variations in solution flow rate and was found to be primarily determined by the vapor and solution properties.

Pertinent dimensionless parameters were also computed from the measured solution heat and vapor mass transfer coefficients. The experimental heat and mass transfer coefficients were compared with the relevant studies from the literature. Based on the observed trends in the experimental data and from comparisons with the other studies, heat and mass transfer correlations were developed to predict heat and mass transfer coefficients for the range of experimental conditions tested. These correlations can be used to design horizontal-tube falling-film absorbers for ammonia-water absorption systems.

CHAPTER 1 INTRODUCTION

Electrically driven compression systems for space-conditioning contribute to high peak loads at utilities. In addition, older versions of these systems use working fluids (chloro fluoro carbons (CFCs) and derivatives) that have been proven harmful to the environment and are responsible in part for ozone depletion in the stratosphere and global climate change. Replacement fluids such as HFCs are also slated for phaseout in the near future. These considerations, along with the availability of waste heat at many industrial process locations, have generated interest in thermally activated space-conditioning systems such as absorption heat pumps. These systems use environmentally friendly working fluids such as ammonia-water and water-lithium bromide fluid pairs. They can use a variety of heat sources including waste heat and solar energy (Kurem and Horuz 2001). However, absorption systems use more components because desorption, rectification (for NH_3-H_2O), absorption, and solution pumping replace the role of the compressor.

1.1 Absorption Heat Pump

A basic single-stage absorption heat pump is shown schematically in Figure 1.1 (Herold *et al.* 1996). It consists of an absorber, desorber, condenser, expansion valve, evaporator, and a pressure reduction valve. Usually, a solution heat exchanger and a pre-cooler are also used as internal heat recuperators. The working fluid is a binary mixture of an absorbent and a refrigerant. Among the two main refrigerant-absorbent pairs (ammonia-water and water-LiBr), water-LiBr systems are more common but their

application is limited to air-conditioning purposes, since water is the refrigerant (0°C freezing point). In the case of the ammonia-water fluid pair, ammonia is the refrigerant and water is the absorbent, which therefore allows operation at temperatures lower than 0°C, which is necessary for cold ambient heat pumping applications. An ammonia-water absorption heat pump also requires a rectifier, placed between the desorber and the condenser, to reduce the water content from the refrigerant vapor entering the condenser.

Figure 1.1 Schematic of Single-stage Vapor Absorption System

1.1.1 Cycle Description

The system operates at two different nominal pressure levels: high pressure at the condenser, rectifier and desorber, and low pressure at the absorber and evaporator. Concentrated solution (with a higher concentration of the refrigerant) is pumped from the low pressure at the absorber to the desorber at high pressure. Before entering the desorber, the solution flows through a solution heat exchanger, which recuperatively heats the concentrated solution toward the desorber inlet conditions. At the desorber, the necessary heat input is supplied to generate ammonia vapor and dilute solution from the concentrated solution. The vapor flows to the rectifier (ammonia-water fluid pair), while dilute solution (with a lesser concentration of the refrigerant) flows through the solution heat exchanger. Downstream of the solution heat exchanger, the pressure of the dilute solution is reduced by an expansion device before it flows into the absorber to complete the solution circuit. The ammonia vapor is purified at the rectifier and sent to the condenser, while the reflux at the rectifier produced during rectification is usually sent back to the desorber. The ammonia vapor is condensed in the condenser and flows to the pre-cooler. The ammonia solution exiting the pre-cooler is expanded to the evaporator pressure using an expansion device and flows through the evaporator, where it receives the cooling load. Ammonia exiting the evaporator flows through a pre-cooler, where it serves as the coolant for the condenser outlet stream. The pre-cooler reduces the enthalpy of the refrigerant exiting the condenser, thereby increasing the cooling capacity of the evaporator. After exiting the pre-cooler, the ammonia vapor is introduced to the absorber, where it is absorbed in the dilute solution while rejecting heat to a coolant stream, thus completing the refrigerant circuit.

1.2 Absorber

The absorption process that takes place in the absorber has been referred to as the "bottleneck" of the entire absorption system (Bogart 1982). Several different absorber configurations are in use. Most commonly used are the falling-film and bubble-type absorbers. In the falling-film absorbers, the dilute solution flows on the outside of horizontal tubes (horizontal-tube falling-film absorber) or on the inside or outside of vertical tubes while the vapor may flow either parallel or counter-current to the solution. In the bubble absorber, both the solution and the vapor flow together as a two-phase mixture usually in forced convective flow through a tube. Some researchers have used other geometries as well such as the plate-type vertical absorbers (Garrabrant and Christensen 1997; Kang *et al.* 2000; Lee *et al.* 2002). This study focuses on a horizontal-tube falling-film type of absorber used in an ammonia-water absorption heat pump.

1.3 Research Issues in Ammonia-Water Absorption

Despite the use of absorption systems for a long time (first used in the 1850s), there appears to be a lack of understanding of the inherently complex, coupled heat and mass transfer processes occurring in the absorber. This has led to poor designs of the absorbers, often leading to the use of expensive and oversized heat and mass exchangers. The ammonia-water fluid pair has a volatile absorbent that results in heat and mass transfer resistances in the vapor as well as the liquid phase. This makes analysis and experimental validation of the respective resistances very challenging. Among the main issues in ammonia-water absorption are the quantification of the various resistances in the different phases and the underlying fluid flow characteristics over horizontal tubes in the

absorber. Most of the models available in the literature use many simplifying assumptions that are unrealistic, such as smooth laminar flow over tubes, and often these models do not come to similar conclusions about the dominant resistances (Killion and Garimella 2001). Also, most of the experimental studies in the literature are overall component level studies rather than detailed heat and mass transfer investigations. In addition, the operating conditions in these studies can differ significantly from those in real systems. In these studies, heat and mass transfer models have often been validated only using overall component measurements, without adequate corroboration at the local level.

1.3.1 Scope of the Present Research

This research aims to improve the understanding of the absorption process in a horizontal-tube falling-film type absorber used in ammonia-water absorption systems by addressing some of the issues mentioned above. In an actual heat pump, the absorber operating conditions are affected by several other components. To account for the influences of these components, it is necessary to conduct experiments on a system that replicates a complete absorption heat pump. A complete ammonia-water absorption system is designed and fabricated that enables experiments over wide ranges of operating conditions, e.g., dilute solution concentrations of 5 – 40%, absorber pressures of 150 – 500 kPa, and multiple solution flow rates. These operating conditions simulate several heat pump modes, i.e., cold-ambient heat pump and refrigeration mode (150 kPa), normal-ambient heat pump and cooling mode (345 kPa), and warm-ambient heat pump mode (500 kPa). Absorption heat and mass transfer strongly depends on the local solution conditions such as the solution concentration and temperature, which vary along

the solution flow path. However, little attention has been given in past experimental studies to the variation of transport rates within the absorber. This study aims to understand local phenomena within the absorber and obtain the corresponding local heat and mass transfer rates. This understanding is supplemented with visualization of the local mechanism of solution flow over the horizontal tube bank. The effect of these flow mechanisms on heat and mass transfer characteristics is investigated. Based on the insights gained from these analyses, models for absorption heat and mass transfer are developed that can help in the design of horizontal falling-film absorbers operating under realistic conditions.

1.4 Dissertation Organization

This dissertation is organized in several chapters as follows:

- Chapter 2 provides background information available in literature on experimental, numerical/analytical and flow visualization studies of ammonia-water absorption and discusses the need for further research in this area.

- Chapter 3 describes the ammonia-water absorption test facility and procedures developed for conducting the experiments.

- Chapter 4 describes the data reduction methodology used to obtain heat and mass transfer rates in the absorber. It also presents representative results at the overall component level.

- Chapter 5 discusses the solution flow patterns over horizontal tube banks in the flow visualization studies.

- Chapter 6 presents analyses of the transfer processes within the absorber at the local level, aided by the flow visualization studies, and the development of

empirical heat and mass transfer correlations. This chapter also discusses the relative contributions of the different flow modes to the overall absorption rates.

- Chapter 7 summarizes the important conclusions of this study and provides recommendations for future work in the area.

CHAPTER 2 LITERATURE REVIEW

Absorption systems have been in use for a very long time and have seen peaks of popularity. There are numerous studies in the literature that address various working fluids, absorber configurations and applications. The present study focuses on ammonia-water absorption systems employing horizontal tube falling-film type absorbers. Therefore, a major portion of the literature presented here is for ammonia-water systems; however, other pertinent studies related to other absorber configurations and working fluids are also summarized. Experimental, numerical and analytical studies have been conducted on the absorption process. There are also a few studies available addressing fluid flow over horizontal and vertical tubes; and on other geometries such as flat plates (encountered in the plate-fin type of absorbers). This chapter summarizes these studies and emphasizes the need for further investigation of horizontal-tube falling-film absorption in ammonia-water systems. The available studies are categorized into Experimental, Numerical/Analytical, and Flow Regime Studies. At the end of the chapter, a summary of the reviewed literature is presented in tabular form.

2.1 Experimental Studies

Experiments have been reported on both falling-film and bubble-type absorbers with the ammonia-water fluid pair as the working fluid. Haselden and Malaty (1959) reported experiments on the absorption of anhydrous ammonia at atmospheric pressure into water and into weak ammonia solution flowing as a film down the outside of a vertical tube of 12.7 mm OD with an absorption length of 12.7 mm to 1.22 m. They

conducted experiments at atmospheric pressure because they found it difficult to achieve a steady and non-pulsating flow of the absorbent at other pressures. They relied on varying the mass-transfer driving force by changing the inlet feed concentration. To address the incomplete wetting of the tube, the absorber tube was "blued" (heating the tube to redness, and then quenching in water), which helped burn away organic contaminants and produced an oxide layer that increased the affinity for water. They deduced from their experiments that the effect of the absorber inlet temperature on the absorption process will be minimal, while the solution concentration and the coolant temperature are the main controlling parameters. The mass transfer coefficient was found to be relatively insensitive to the solution Reynolds number but was found to increase significantly as the dilute solution concentration increased. They compared their experimental results with Higbie's Penetration Theory (1935), and found the experimental values of mass transfer coefficient to be 2-5 times larger than those predicted by this theory. This was attributed to the mixing produced by the ripples in the liquid layer. They also conducted experiments in the absence of absorption and found that the nature of ripples produced was different than that observed with absorption (where ripples were more violent and extended nearer to the top of the tube). Although their experiments covered a wide range of solution concentrations, they were not sufficient to trace the variation of absorption rate along the length of the absorber, and did not include the effects of the dilute solution temperature and the absorber pressure. Furthermore, the vapor conditions were constant for the range of their experiments and their influence was not examined.

Among the more recent studies on ammonia-water absorption experiments, Hoffmann and Ziegler (1996) fabricated an experimental set-up that allowed absorption experiments over a range of dilute solution concentrations and flow rates. Their set-up consists of an absorber, a desorber and a dephlegmator, all housed in a cylindrical shell. The absorber is a horizontal tube falling-film type absorber consisting of 24 tubes of 18 mm OD arranged in a staggered fashion of 8 rows × 3 columns with a total of four coolant passes. The set-up also had provisions for local temperature measurement. They outlined the data reduction procedures in terms of the log mean temperature/concentration differences for counter- and parallel-flow, respectively. However, no data were reported in this study; therefore, the actual influence of solution properties and operating conditions on absorption heat and mass transfer could not be determined.

Jeong *et al.* (1998) studied a coiled-tube absorber in which the dilute solution flowed on the outside of the tubes with the ammonia vapor flowing upward in the shell and coolant flowing within the tube. The helical coil of 82.6 mm diameter is made of a 12.7 mm OD tube. The total absorber length was 0.6 m. The absorption experiments were conducted over a dilute solution concentration (x_{dil}) range of $0.012 - 0.022$ and a vapor concentration (x_V) range of $0.63 - 0.77$ for solution flow rates in the range of $0.049 - 0.019$ kg/s. They did not report the absorber pressure range. They also conducted experiments without absorption and found that the film heat transfer coefficients were lower for experiments with absorption than for those without absorption, perhaps due to insufficient wetting caused by vapor shear. They also noted that for coolant flow rates smaller than a certain value (1.3×10^{-2} kg/s), the total heat duty did not increase even if

10

the solution flow rate was increased significantly. They concluded that the coolant-side heat transfer resistance was dominant at those small coolant flow rates. For the cases with absorption, a significant scatter was observed in the film heat transfer coefficient which was attributed to a thick film and insufficient wetting caused by shear force at the vapor-liquid interface; however, the effect of local variation of the solution properties was not examined. Also, their experiments covered only small ranges of the dilute solution concentration and the absorber pressure. They provided the following correlations based on their data:

$$Nu_{No,absortion} = 0.00035 \, \mathrm{Re}_l; \quad 20 < \mathrm{Re}_l = 4\Gamma/\mu_l < 500 \tag{2.1}$$

$$Nu_{absorption} = 0.00022 \, \mathrm{Re}_l; \quad 50 < \mathrm{Re}_l = 4\Gamma/\mu_l < 300 \tag{2.2}$$

where $\Gamma = \dot{m}/(2\pi d_{coil})$ in the above equations.

Kang *et al.* (1999) developed correlations for heat and mass transfer by correlating the data obtained using a plate heat exchanger with offset strip fins (OSF) for surface enhancement. The overall absorber dimensions were $130 \times 110 \times 34$ mm. Both the dilute solution and vapor entered at the top of the plate heat exchanger and flowed down together along the vertical plate surface. The tests were conducted at an absorber pressure of 101.3 kPa (atmospheric) for three dilute solution concentrations of 0.05, 0.1 and 0.15 over a solution flow rate range of $0.004 - 0.0102$ kg/s. The overall film heat transfer coefficient and mass transfer coefficient were obtained using a log mean temperature/concentration difference, respectively. They noted that a lower inlet solution temperature and a higher vapor temperature improved heat and mass transfer performance; however, the inlet sub-cooling was found to have a more pronounced effect on the heat transfer. They also noted that as the inlet concentration difference $(x_{v,in} - x_{l,in})$

11

increased, the heat transfer coefficient decreased, while the mass transfer coefficient increased for a given solution flow rate and an inlet sub-cooling. The increase in the mass transfer coefficient (Sh_l) was attributed to an increase in the driving potential ($x_{dil,in}^{eq}(T_{V,in}) - x_{dil,in}$) while the decrease in Nu_l was attributed to smaller rectification at the top (smaller $x_{V,int}$ as the $x_{dil,in}$ decreases). In their experiments, the sensible liquid and vapor heat transfer ranged 5.4 – 23% and 1.5 – 38% of the total heat transferred to the coolant, respectively. They inferred from the sensible heat transfer values that these can affect the total heat transfer. They also reported rectification at the top due to inlet sub-cooling and water desorption near the exit (bottom of the heat exchanger). The following heat and mass transfer correlations were developed as the functions of solution and vapor Re, inlet sub-cooling, and the concentration difference between the vapor and inlet dilute solution concentrations.

$$Nu_{abs} = 0.8530 \times 10^{-3} \, \text{Re}_l^{1.5180} \, \text{Re}_V^{0.1759} \left(\frac{\Delta T_{sub,inlet}}{T_{dil,inlet}} \right)^{1.879} \left(\frac{x_{V,in} - x_{dil,in}}{x_{dil,in}} \right)^{-0.5756} \qquad (2.3)$$

$$Sh_l = 0.6996 \times 10^{-7} \, \text{Re}_l^{0.8874} \, \text{Re}_V^{1.265} \left(\frac{\Delta T_{sub,inlet}}{T_{dil,inlet}} \right)^{0.8844} \left(\frac{x_{V,in} - x_{dil,in}}{x_{dil,in}} \right)^{0.5304} \qquad (2.4)$$

where $\text{Re}_l = 4\Gamma/\mu_l$ and $\Gamma = \dot{m}/Perimeter$. They recommended that the vapor flow rate should be maximized to increase heat and mass transfer performance in the ammonia-water absorption process. Their experiments were, however, conducted on a component test facility and did not investigate the effect of absorber pressure.

Lee *et al.* (2002) studied the effect of solution and vapor flow rates on a plate-type counter-current bubble absorber. The plate dimensions were 0.112 × 0.264 × 0.003 m. To examine the effect of solution flow rate, the solution flow rate was varied between

0.002 – 0.015 kg/s for three different vapor flow rates of 1.67×10^{-5}, 8.3×10^{-5} and 1.5×10^{-4} m^3/s. To study the effect of the vapor flow rate, the solution flow rate was fixed at 0.3 kg/min and the vapor flow rate was varied between $0.2 – 1.45 \times 10^{-4}$ m^3/s for two dilute solution concentrations of 0.2 and 0.3. They found that the solution flow rate affects only the heat transfer performance; however, increasing the vapor flow rate increases the mass transfer for a given inlet solution concentration. In the calculations of the mass transfer coefficient, they neglected mass transfer in the vapor-phase. They probably meant that the mass transfer resistance is negligible in the vapor-phase. The effect of solution flow rate on the mass transfer coefficient was negligible in their study. Interestingly, the amount of heat generated showed a very small dependence on the dilute solution concentration. They also found that in bubble absorption, the liquid-side heat transfer resistance is dominant; however, at higher vapor flow rates, better heat transfer performance was observed that was attributed to changes in the thermal boundary layer. They concluded from the temperature profile within the absorber that most of the ammonia vapor was absorbed in the lower part (near the vapor entrance at the bottom) of the absorber. This was confirmed by visual observations through a transparent window, but they did not provide details of the criteria used to arrive at this conclusion.

In a follow-up study, Kwon and Jeong (2004) studied the effect of vapor flow direction on heat and mass transfer in a helical coil falling-film type absorber. The absorber used was the same as that used by Jeong *et al.* (1998). The conducted experiments at three dilute solution concentrations of 0.03, 0.14 and 0.3 over a solution flow rate range of 0.0043 – 0.09 kg/s. The absorber pressure varied over a range of 17 – 193 kPa; however, the pressure seems to have been determined by saturation conditions

(corresponding to the solution temperature and concentration) rather than being independently controlled. They found that the total heat transfer rate increases with the solution flow rate and the solution temperature irrespective of the vapor flow direction; however, heat and mass transfer performance deteriorates in counter-current flow if the specific volume of the vapor is large. The specific volume of the vapor that is in equilibrium with the solution (at 50°C temperature) increases almost 10 times from 0.679 to 6.797 m^3/kg when the solution concentration changes from 0.3 to 0.031. A large specific volume results in higher vapor velocities, which in turn causes unfavorable distribution of the falling-film. The variation of the specific volume of the vapor changes the interfacial shear stress and the authors recommended that its effect should be accounted for when the liquid and vapor flow in a counter-current manner. The effect of vapor flow direction decreases as the ammonia solution concentration is increased (smaller vapor specific volume results in smaller vapor velocity, therefore smaller shear at the interface). They also noted that despite the solution film being in the laminar regime, heat transfer coefficient increases with the solution flow rate. This was attributed to intensified mixing and wetting. They developed heat transfer correlations in terms of the solution Re and the interfacial shear stress for both co- and counter-current absorption modes.

$$Nu_{Co-current} = 1.975 \times 10^{-3} \, Re_l^{0.6895} \, \tau_v^{-0.0249} \tag{2.5}$$

$$Nu_{Counter-current} = 1.683 \times 10^{-4} \, Re_l^{0.8672} \, \tau_v^{-0.3018} \tag{2.6}$$

where $Re_l = 4\Gamma/\mu_l$ and $\Gamma = \dot{m}/Perimeter$. In their study, however, the solution and vapor inlet conditions are saturated and do not include the influence of the other components of a complete absorption system. Furthermore, since the absorber pressures

are very small in their study (< 200 kPa), their results may not be extrapolated to higher absorber pressures that correspond to warm ambient heat pump modes (e.g., 500 kPa).

Merrill *et al.* (1994; 1995) used numerous passive enhancement techniques on vertical-tube bubble absorbers for the GAX cycle such as repeated roughness elements, internal spacers, and increased thermal conductivity metal to improve heat transfer, while mass transfer improvement was achieved through the use of static mixers, variable cross-section flow areas, and numerous vapor injector designs. They initiated experiments based on a design goal of 3.52 kW heat pumping capacity and a GAX absorber load of 2.6 kW. The absorber was an inverted concentric U-tube with the dilute solution and vapor flowing inside the inner tube (12.7 mm OD) and the coolant flowing in the annulus formed by the outer tube (23.8 mm OD). The system pressure was maintained at 503 kPa. This absorber, however, did not meet the design specifications and it was inferred that both the solution and the coolant sides need significant heat and mass transfer improvements. Therefore, they used spacers on the coolant-side and repeated roughness elements on the solution-side. To reduce the wall heat transfer resistance, they used a low carbon steel tube with a three times larger thermal conductivity than that of the stainless steel tube. During the experiments, they also observed a falling-film type flow rather than a two-phase (bubbly) flow from the sight-glass in the descending leg of the inverted U-tube. To ensure a two-phase flow, they used a smaller diameter descending leg in the next generation of the bubble absorber. Although these improvements increased the GAX load, they also increased the approach temperature difference. They found that the coolant-side heat transfer resistance was dominant. They also concluded

that it is necessary to increase the absorber overall heat transfer area and the vapor distribution method.

More recently, a miniaturization technology for ammonia-water absorbers (Garimella 1999; 2000; 2004) that uses short lengths (0.127 m) of very small diameter (1.587 mm OD) tubes placed in a square array, with several such arrays being stacked vertically, has been reported. Successive tube arrays are oriented in a transverse orientation perpendicular to the tubes in adjacent levels. Liquid solution flows in the falling-film mode counter-current to the coolant through the tube rows. Vapor flows upward through the lattice formed by the tube banks, counter-current to the falling solution. The effective vapor-solution contact minimizes heat and mass transfer resistances, the solution and vapor streams are self-distributing, and wetting problems are minimized. Coolant-side heat transfer coefficients are extremely high without any passive or active surface treatment or enhancement, due to the small tube diameter. A preliminary model using the Price and Bell (1973) approach demonstrated that a 19 kW absorber, which corresponds to a 3-ton cooling system, can be built in a very small 0.127 m $\times$ 0.127 m $\times$ 0.476 m envelope with a surface area of 1.9 m^2. In this design, the microchannel tubes were arranged in 5 passes, where each pass consists of 15 tube rows. Each of the tube rows had 40 tubes in it. Extensions of the compact, modular concept to other components in an absorption system were also noted.   Meacham and Garimella (2002a) demonstrated a prototype of this concept and achieved absorption duties of up to 16 kW with a surface area of 1.5 m^2. The absorber geometry consists of short lengths (0.14 m) of microchannel tubes (1.575 OD) arranged in a square array. These tubes were arranged in 5 passes, where each pass consists of 16 tube rows. Each of the tube rows

had 27 tubes in it. Their solution mass flux varied in the range 0.011 – 0.036 kg/s and the vapor generation fraction varied in the range 5 – 50%. The average absorber heat duties transferred were between 4.86 and 16.23 kW with solution heat transfer coefficients in the range 145 – 510 W/m^2-K. The overall heat transfer coefficient varied from 133 to 403 W/m^2-K. In a subsequent study, Meacham and Garimella (2003) developed an experimentally validated absorption heat and mass transfer model to predict the detailed temperature, concentration and mass flow rate profiles through the absorber. A surface area effectiveness ratio was defined to account for potential solution distribution and surface wetting problems, which resulted in excellent agreement between the predictions of the model and the measured data both for the overall absorber as well as the local level. Improved absorption rates were then achieved, guided by high speed visualization of the flow patterns and a revised distribution device, which substantially improved the solution distribution and wetting of the tubes (Meacham and Garimella 2004). In this absorber, a total of 660 tubes were arranged in 10 passes, where each pass consists of 2 tube rows. Each of the tube rows had 33 tubes in it. This geometry provided a total surface area of 0.456 m^2. Their solution mass flux varied in the range 0.015 – 0.027 kg/s and the vapor generation fraction varied in the range 15 – 30%. The average absorber heat duties transferred were between 4.5 and 15.1 kW with solution heat transfer coefficients of 638 - 1648 W/m^2-K. The overall heat transfer coefficient varied from 545 to 940 W/m^2-K. In related research (Meacham and Garimella 2002b), a shell-and-tube heat exchanger with small diameter tubes was also demonstrated as an absorber for residential heat pumps. With a high surface/volume ratio, it was demonstrated that an extremely compact absorber (76.2 mm outside diameter, 0.508 m long) with vapor and solution flowing co-

current through 253 tubes of 2.54 mm ID can transfer the absorption duty of a 10.55 kW cooling load absorption heat pump. Experiments over wide ranges of solution flow rate (0.018 – 0.032 kg/s), coolant flow rates (2.52, 3.79 and 5.05×10^{-4} m^3/s) and vapor fractions (15 – 30%) were used to deduce overall (330 – 825 W/m^2-K) and tube-side absorption heat transfer coefficients (370 – 900 W/m^2-K). The high performance was achieved without any surface enhancement, and with very low solution and coolant pressure drops. It was noted that improvement in the distribution of the vapor-liquid mixture would further reduce potential mal-distribution at the entrance, resulting in even larger transfer rates.

2.1.1 Summary of Experimental Studies

Table 2.1 shows a summary of the literature presented above on ammonia-water absorption investigated experimentally by various researchers. The absorption experiments in these studies have been conducted on component test facilities (that include an absorber, a desorber and solution pump); therefore, influences of the other components (the rectifier, condenser and the evaporator) are not addressed. In such facilities, the dilute solution and vapor are typically generated in a desorber and directly routed to the test absorber at the same pressure and concentration. In an actual absorption system, however, the refrigerant undergoes rectification and expansion to a lower pressure, thus arriving at the absorber at a different concentration and pressure. These conditions are, in turn, influenced by condenser (heat rejection) and evaporation (cooling load) conditions that are determined by ambient and conditioned space conditions. Similarly, the dilute solution undergoes cooling in a recuperative heat exchanger, which leads to a subcooled solution condition at the absorber inlet. These realistic effects are

not replicated in the type of experiments reported in the studies cited above. It is also seen that the available studies cover only a limited range of the operating conditions ($x_{dil} \leq 0.3$; $P_{abs} \leq 200$ kPa); while all of them cover a range of solution flow rates, most of them cover only either a range of solution concentrations or temperatures or absorber pressures. None of the available studies provides data over wide ranges of the solution flow rates and concentrations, vapor concentrations, and absorber pressures simultaneously.

2.2 Numerical/Analytical Studies

In the analytical/numerical treatment of ammonia-water absorption, there are some general assumptions found in most studies. These common assumptions are listed here and not mentioned while discussing each study separately:

- Steady-state absorption

- Constant system pressure

- Thermodynamic equilibrium at the liquid-vapor interface

- No flooding in the case of counter-current flow between the solution and the vapor

- Mass transfer only due to the concentration gradient (effects of the temperature and pressure gradients are negligible)

- Heat and mass diffusion in the solution flow direction are negligible

- No non-condensable gases

There are some other assumptions such as negligible liquid- or vapor-phase mass transfer resistance and complete wetting of the absorption surface. These assumptions will be cited wherever applicable (specific to a particular study).

Most of the analytical models are based on the methodology originally developed by Colburn and Drew (1937) and later adapted by Price and Bell (1973) for the design of binary vapor condensers. The absorption process is similar to condensation, except that in absorption, the liquid layer exists from the beginning of the process. The Colburn-Drew methodology is best suited to analyze binary vapor condensation when the condensation rate is high or the temperature difference between the vapor and the coolant is large. In either of these situations, the condensation process will be vapor-side dominated and the primary assumption of complete mixing in the liquid phase (in their method) is justifiable. Assuming the interface liquid concentration to be same as the bulk liquid concentration enables calculation of the interface temperature, and therefore, the vapor interface concentration needed to compute the condensation rate. The Colburn-Drew heat and mass transfer equations are applicable to the local condensation process. The local analysis is necessary because the non-uniformity of composition in both the liquid and vapor phase means that there is mass transfer resistance in each phase. In their method, however, complete mixing in the liquid-phase is assumed. In general, the bulk concentration will also change through the condenser (or absorber). Price and Bell (1973) developed a computational framework to implement the Colburn-Drew method that could be used to design binary vapor condensers. In their framework, the local transport rates are integrated over the entire condensation process to get the condenser size. They also pointed out that although the vapor sensible heat load is generally small, it may be critical in determining the size due to poor vapor-side heat transfer rates.

Killion and Garimella (2001) presented a critical review of various models developed to study coupled heat and mass transfer in absorption systems. They pointed

out that a majority of the models available for ammonia-water absorption neglect either liquid-side or vapor-side mass transfer resistance. The models that account for mass transfer resistance in both the phases often disagree on the dominant resistance. Furthermore, many of these models make use of empirical correlations for the heat and mass transfer coefficients. They concluded that although the recent models are removing some of the standard simplifications, there is still a significant lack of models that addresses deviations from idealized flow behavior, such as droplets, wavy films, and films flowing over horizontal tubes.

Ruhemann (1947) presented a simple 1-D heat and mass transfer model for the absorption of ammonia vapor in a coiled-tube absorber (coil tube dimensions were not reported). The solution flow was approximated as a falling-film on a vertical wall. He assumed a zero concentration gradient in the vapor-phase as the ammonia vapor was anhydrous (or pure). In the other words, the mass-transfer resistance in the vapor phase was neglected. By formulating the heat balance, and the heat and mass transfer equations in the terms of an overall heat transfer coefficient and a mass transfer coefficient, he suggested that both the heat and mass transfer resistances in the liquid phase need to be considered for an accurate analysis. He also concluded that the mass transfer resistance in the liquid phase is the dominant resistance, despite the high solubility of the ammonia, provided that the heat transfer performance is reasonable. In the examples presented in his study, dilute solution at a concentration of 0.095 and anhydrous ammonia entered at the top of the absorber. The absorber pressure was maintained at 38 kPa. In an actual absorption system, however, the vapor concentration will be determined by the operating conditions.

For laminar, steady flow at low Reynolds numbers with uniform wetting, Perez-Blanco (1988) presented a simple 1-D model for absorption in a horizontal-tube, falling-film absorber, while accounting for water transport both into and out of the solution film. To avoid unrealistic excessively high mass transfer rates at the interface, he used a two-film model to decouple the interface concentrations of ammonia in the liquid and vapor. The interface temperature was calculated by accounting for the heat transfer coefficients and the bulk temperatures in both the liquid and vapor phases. The film heat transfer coefficient was found using simple penetration theory (Higbie 1935; Ruckenstein and Berkente 1968). The penetration theory is applicable to laminar falling-films for short exposure times. The heat and mass transfer coefficients are predicted to be proportional to the square root of the thermal diffusivity and of the molecular diffusivity, respectively, while both the coefficients are proportional to square root of the exposure time. The solution flow rate and liquid-phase mass transfer coefficient influenced absorber performance significantly, with the sensitivity to other parameters being small, although the relative importance of the coolant heat transfer coefficient increased as the solution approached saturation conditions. He presented limited experimental verification of the model and emphasized that data over a wide range of operating conditions are necessary for further validation. He used a coiled tube (coil diameter: 82.6 mm; 6 turns) absorber made of a 12.7 mm OD tube. Dilute solution with a concentration of 0.033 entered the absorber at the top while pure ammonia (x_V:1) entered at the bottom of the absorber. The experimental mass transfer coefficient was 2 to 2.5 times higher than the predictions of laminar film theory and was fairly insensitive to the solution flow rate. By comparing two different modes of an absorption heat pump, e.g. low concentration and high

22

temperature (typical GAX (Generator-Absorber-Exchanger) mode), and high concentration and low temperature (typical cooling mode), he pointed out the possibility of water evaporation due to low volatility ratio of ammonia to water in the case of low concentration and high temperature conditions (GAX conditions).

Takuma *et al.* (1993) analyzed condensation of ammonia-water mixtures on horizontal tube bundles using a heat and mass transfer analogy and confirmed their predictions using measurements on a full-scale, shell-and-tube condenser as well as on a test apparatus using the Coherent Anti-Stokes Raman Spectroscopy (CARS) technique for ammonia concentration measurement. They concluded that the accumulation of ammonia at the interface presents an important resistance to condensation. The analytical model was first applied to the miniaturized test apparatus (used to measure the concentration). The apparatus was a shell-and-tube heat exchanger consisting of 30 mm long tubes of 10 mm OD. Good agreement (±10%) between the predicted and experimental heat transfer coefficients was observed; however, at the lower tube, the predictions degraded somewhat due to disturbances in the vapor flow caused by the upper tube. The measured heat transfer rates during binary condensation experiments on a condenser that was part of a Rankine cycle test plant differed on average ±20% from the predicted values. The shell-and-tube condenser consisted of 1 m long tubes of 11.24 mm ID and 15.88 mm OD arranged in a total of 38 tube rows with 17 tubes in each of the row (the shell diameter is not reported). In their study, however, the condenser pressure (196 kPa), and the vapor inlet temperature (146.8^{o}C) and concentration (0.55) were maintained constant.

Potnis *et al.* (1997) developed a computer program that simulated the GAX process with liquid-film absorption over a coiled fluted tube with countercurrent vapor flow, and convective desorption inside the 39 m long fluted tube. The Colburn and Drew (1937) approach was used to model absorption as the condensation of a binary mixture. They found that the mass transfer resistance was primarily in the vapor phase, although the liquid-phase mass transfer resistance was not negligible and can be as high as 25% of the total resistance. The higher liquid-side mass transfer resistance could be due to the higher absorber pressure (1551 kPa) and solution concentrations (0.31 – 0.52) in their study. Similarly, by comparing the heat transfer coefficients in the liquid and vapor phases, they found that the heat transfer resistance also lies in the vapor phase. The significant reduction in the vapor-phase heat transfer coefficient near the top (vapor exit) was attributed to the reduced vapor velocities (because most of the vapor is already absorbed by the solution). They recommended targeting the vapor-phase mass transfer boundary layer to promote absorption rates as this layer was found to be thicker than the heat transfer boundary layer. The flow-boiling-side heat transfer coefficients were an order of magnitude higher than those on the absorption-side, so they primarily focused on the absorption-side.

Panchal *et al.* (1997) developed a model of condensation of ammonia-water mixtures flowing on the outside of vertical tubes using the Colburn-Drew approach, and compared the results of their model with tests on similar geometries. However, their work focused not on absorption into an incoming liquid solution stream, but rather on condensation of a vapor stream of varying ammonia-water concentrations. The vertical tube length was 1.22 m with a nominal OD of 25.4 mm. Using different assumptions for

liquid-phase mass transfer including complete mixing and no mixing, they predicted that the assumption of complete mixing in the liquid phase approximated the data better than the other limiting cases. By comparing condensation of the pure ammonia and ammonia-water mixtures, they found that the heat transfer coefficient in the case of pure ammonia was much higher than for the ammonia-water mixture; however, the heat transfer coefficient decreased as the heat flux increased in the case of pure ammonia while it increased in the other case. The increase in the case of ammonia-water mixture was attributed to a higher mass transfer coefficient (due to higher vapor flow rates at higher heat fluxes). They also concluded that vapor-phase diffusion presented a significant resistance to the binary-fluid condensation process. The model validation, however, was carried out over a narrow range of absorber pressures. The absorber pressure varied between 904 – 965 kPa, the vapor concentration varied between 0.89 – 1 and the vapor temperature varied between 104.6 – 113.7°C.

Erickson *et al.* (1998) rearranged the Colburn-Drew equations to obtain a form that combines the mass transfer contributions of diffusion and bulk flow in one coefficient. A two-film Colburn-Drew analysis was used to illustrate the relative values of the liquid- and vapor-phase mass transfer resistance at a specific operating condition (P_{abs}: 560 kPa, $x_{l,bulk}$: 0.0969, $x_{V,bulk}$: 0.8251). It was found that both the mass transfer resistances were comparable based either on an overall liquid-side or vapor-side mass transfer resistance.

Attempts at obtaining compact ammonia-water absorber geometries include counter-current fluted-tube absorbers (Kang and Christensen 1994; 1995; Palmer and Christensen 1996). Kang and Christensen (1994) developed a model based on the

Colburn-Drew method for their vertical fluted GAX absorber. The fluted tube length was 1.75 m and a total of 7 tubes were used in the absorber. For a representative case, the dilute solution entered the GAX absorber (at the top) at a concentration of 0.052 and exited the hydronically cooled absorber at a solution concentration of 0.489 while pure vapor ($x_V = 1$) entered at the bottom flowing counter-current to the solution. Higher absorption rates were predicted near the solution inlet with some water evaporation near the solution outlet (towards the bottom). The interface temperature was much higher than the bulk vapor temperature but was relatively closer to the wall temperature. The bulk solution temperature was not reported, so it is not clear how it compared to the interface temperature. It appears from the formulation of equations that the liquid-phase mass transfer was not accounted for (similar to the Colburn-Drew method). The absorber pressure was not reported; therefore, it could not be determined if the solution/vapor were saturated. They concluded that as the interface and the bulk vapor temperature difference increases, higher absorption rates are achieved. They also proposed that the liquid-side film heat-transfer resistance is small compared to the coolant-side; however, no values were provided. Generally, the coolant-side flow rates (and temperature) are maintained such that the heat transfer process is solution-side limited. They also recommended that the vapor velocities should be increased to maximize the absorption rates. Palmer and Christensen (1996) developed a model for predicting the performance of three different fluid distribution inserts in a vertical fluted-tube absorber for the GAX cycle. They used a wetted area in their model that was varied until both the dilute solution inlet conditions and the length of the absorber matched the experimental values. The model was validated with experiments conducted on all the three inserts. They found the wetting

fraction to increase with the concentrated solution concentration (the concentrated solution flow rate was held constant); the increased wetting was attributed to the reduction in surface tension at higher concentrations. For the representative case, the dilute and concentrated solution concentrations were 0.16 and 0.33, respectively.

Garrabrant and Christensen (1997) tested and analyzed an absorber consisting of corrugated and perforated finned surfaces placed between rectangular coolant channels that was patented by Christensen *et al.* (1998). The perforations were pentagons in the shape of an inverted house. They presented α- and β- versions of the prototype. The heat exchanger was constructed using a 0.432 m × 0.127 m section of 0.25 mm thick, carbon steel perforated fin, with 6 or 7 alternating perforations per row. The solution and vapor flow in a counter-current manner. The concentrated solution concentrations varied between 0.13 – 0.41 and flow rate between 0.0042 – 0.0118 kg/s in the experiments on the α-prototype. The concentrated solution exited the absorber at saturated conditions. The offset perforations were expected to induce a horizontal vapor flow over the wetted fin surface enhancing mass transfer to the solution and the solution-to-fin heat transfer. They modeled the absorber using the Colburn-Drew methodology by neglecting both the temperature and concentration gradients in the solution film (i.e. the bulk solution concentration and temperature are the same as those at the interface). The vapor-phase heat transfer coefficient was obtained by treating the vapor flow as a single phase flow over a flat plate; however, it is not clear how the vapor Reynolds number was calculated.

A generalized design tool capable of modeling several components within an absorption system was presented by Kang *et al.* (1997). They presented a condensing flux composition (z) map for these components. They concluded that the value of z will

vary as follows: condenser (all the vapor condensed, $x_l < z < x_{V,bulk}$); evaporator (all the liquid evaporated, $x_l < z < x_{V,int}$); rectifier ($z < x_l$); absorber (absorption/desorption, $z > x_{V,bulk}$); and desorber (desorption/absorption, $z > x_{V,int}$). They also noted that the vapor-phase heat transfer coefficient has a larger effect on the size of the desorber and the rectifier while the liquid-phase heat transfer coefficient has a larger effect on the size of the absorber and condenser. However, they concluded that to obtain a smaller heat exchanger, the best method is to increase the coolant-side heat transfer coefficient. Kang *et al.* (2000) compared falling-film and bubble-mode absorption analytically and found that the bubble mode can have significantly higher mass transfer performance due to the larger mass transfer area. The absorber geometry was a plate-fin heat exchanger with offset strip fins (OSF). The solution and vapor flowed inside the channel of 6.22 mm width with a wall thickness of 0.71 mm. In the case of the bubble mode, a total of 8 orifices of 2.54 mm diameter were used for vapor distribution. They presented numerical results for the absorption of ammonia vapor (x_V: 0.987) in a dilute solution of concentration 0.279 at an absorber pressure of 557 kPa. They also concluded that in falling-film absorption, the mass transfer resistance is dominant in the liquid phase while both heat and mass transfer resistances are significant in the vapor phase. In the case of bubble absorption, they concluded that the mass transfer resistance is dominant in the liquid phase while the heat transfer resistance is dominant in the vapor phase. Therefore, the heat transfer coefficients were found to be more important in the falling-film mode and the mass transfer coefficients in the bubble mode.

Chen and Christensen (2000) developed a mathematical model for simultaneous heat and mass transfer by treating the overall absorption as two basic processes: due to

the sub-cooling of the liquid solution, and due to the cooling from the wall. These two processes can be superimposed directly. The absorption process took place in a solution film falling over a vertical flat plate. With the assumption of a laminar, smooth film and negligible rate of absorption (compared to total solution flow rate for a small length interval), they decoupled the momentum equations for the solution flow from the vapor flow. They then solved coupled heat and mass transfer equations numerically with the appropriate boundary conditions. While formulating the mass transfer boundary condition at the interface, diffusion effects in the vapor were neglected. They found that in the case of a sub-cooled inlet condition (in the absence of external cooling), the mass absorption rate decreases along the liquid flow direction due to the increase in liquid temperature caused by absorption, while with the continuous cooling from the wall, the mass absorption rate increases asymptotically along the liquid flow direction. However, inlet sub-cooling was found to affect the heat and mass transfer coefficient adversely. The solution film heat and mass transfer coefficients decreased as the inlet sub-cooling increased. They also compared their simulation results with that of Pigford (1941) for an isothermal wall and found their results to be significantly higher (due to simultaneous heat and mass transfer that includes mass transfer both by diffusion and bulk flow).

Fernandez-Seara *et al.* (2005) presented an analysis of the heat and mass transfer processes taking place in a co-current vertical bubble absorber. A shell-and-tube heat exchanger was used as the absorber where both the solution and vapor flowed inside tubes of 22 mm ID (entering from the bottom of the absorber) and water as the coolant (counter-current to the solution and vapor) on the shell-side. They developed a finite difference model based on the Colburn-Drew methodology while accounting for the mass

transfer resistance in both the solution and vapor phases. Their model accounts for churn, slug and bubbly flow patterns inside vertical tubes. The numerical results were presented for a dilute solution concentration of 0.225, a vapor concentration of 0.999 and an absorber pressure of 200 kPa. The interface temperature was found to be equal to the bulk solution temperature and hence, they concluded that the heat transfer resistance is mainly located in the vapor phase. For a significant length of their absorber, the value of the condensing flux concentration (z) was less than the bulk vapor concentration ($x_{V,bulk}$). This is contradictory to the condensing flux concentration map provided by Kang *et al.* (1997) where they concluded that $z > x_{V,bulk}$ in the absorber. The mass transfer area was same as the heat transfer area in their study, but Kang *et al.* (2000) mentioned that in the case of bubble absorption, the mass transfer area is usually different from the heat transfer area. From a parametric evaluation, Fernandez-Seara *et al.* (2005) found the existence of an optimal tube diameter to achieve the shortest length of the absorber needed for complete absorption. The required tube length decreased with the number of tubes; however, the decrease was progressively smaller with each additional tube. Both the dilute solution concentration and the coolant temperature influenced the absorber length, which increased with an increase in both the parameters.

Goel and Goswami (2005a; 2005b) analytically investigated heat and mass transfer in a lamella plate based absorber (an array of several plates). The solution and vapor flowed in a channel of 10 mm width formed by lamella plates of 0.15 m width and 1.3 mm thickness. The required length of the absorber was calculated based on the desired operating conditions. Their analysis of vertical falling-film absorption was based on the Colburn-Drew method. By accounting for the mass transfer resistance in both the

vapor and liquid phases and using a finite difference numerical scheme, they concluded that the liquid-phase mass transfer resistance controls the overall absorption process. Sub-cooling the solution was found to improve the performance slightly, but the coolant inlet temperature was found to have a significant effect on the absorption rate. By comparing temperature profiles of the interface, the bulk solution and vapor temperatures, they concluded that the liquid-phase heat transfer resistance is negligible compared to other constituents of the heat transfer resistance. The interface temperature was always found to be higher than the bulk solution temperature but the difference between them was very small. The simulation results were obtained at an absorber pressure of 200 kPa with a dilute solution concentration of 0.25 and a vapor concentration of 0.997.

All of the studies discussed above use empirical heat and mass transfer coefficients to model the absorption phenomena at the absorber. Although numerical studies have generally focused on LiBr-H_2O absorption, there have been some attempts to develop similar models for ammonia-water absorption that do not use any empirical correlations. These models are solutions of the momentum, energy and the diffusion equations with appropriate boundary conditions for the geometry and flow under consideration. Kim (1998) analyzed the ammonia-water absorption process using an integral formulation of continuity, momentum, energy and diffusion equations in a vertical tube (OD: 25 mm, L: 1 m) falling-film absorber. Dilute solution flow was on the inside surface of the tube with the vapor flowing in the core region. Velocity, temperature and concentration profiles were assumed to be parabolic in the radial direction (across the film). The simulation results were presented at an absorber pressure of 450 kPa. The dilute solution concentration varied between 0.05 - 0.25 and the vapor

concentration varied between 0.85 - 0.99. The absorption characteristics were found to be governed by the relative significance of the mass transfer resistances in the solution film and the vapor mixture; however, he concluded that the absorption process is controlled by the heat transfer resistance. He also recommended that reducing the mass transfer resistance in the liquid-phase will be more helpful to enhance the absorption rates. The coolant conditions were assumed to be either isothermal or adiabatic and the solution film to be smooth.

Gommed *et al.* (2001), extending their prior work (Gommed *et al.* 1999), numerically studied heat and mass transfer during absorption of ammonia-water vapor into a laminar falling-film inside a vertical tube where the vapor flows parallel to the solution. They solved momentum, heat and mass transfer equations in both the axial and radial directions. They transformed the non-uniform calculation domain to a uniform domain using a coordinate transformation based on stream function normalization. The numerical solution based on Finite Volume Method was obtained for laminar film flow conditions and does not account for potential enhancements due to waviness. They obtained velocity, temperature and concentration profiles in the liquid and the vapor phases, and also the heat and mass fluxes. For a reference case (similar to that of a hydronically cooled absorber (Kang and Christensen 1994)), a tube radius of 0.015 m and a length of 1 m were used in the simulations. The dilute solution and the vapor entered at concentrations of 0.35 and 0.999, respectively, at an absorber pressure of 600 kPa. The temperature varied almost linearly in the solution film while the temperature profile was relatively sharper near the interface in the vapor. There was not much variation in the temperature along the interface. This small variation was attributed to small changes in

the pressure and liquid interface mass fractions along the tube. While the inlet conditions of the liquid and vapor were found to affect the absorption significantly, inter-diffusion effects were found to have a negligible effect on absorption. They also found that the bulk solution inlet temperature affects the absorption considerably more than the wall temperature near the solution entrance; therefore, they recommended that it is worth considering short adiabatic absorbers fed by sub-cooled solution. The diffusion coefficient and thermal conductivity in the liquid-phase were also found to affect absorption significantly, although the effect of thermal conductivity was more pronounced. By comparing the effects of both the diffusivity and the thermal conductivity in the liquid and vapor phases, they concluded that the absorption process is solution-side dominated.

Lee *et al.* (2005) developed a combined empirical and numerical method to estimate the actual film thickness during horizontal tube falling-film absorption in a shell-and-tube type absorber. The absorber consisted of 91 tubes of 10 mm diameter and 1 m length housed in a 1.5 m long shell of 0.3 m diameter. The numerical model approximated the half circumference of the tube as a vertical wall. The model also neglected heat and mass transfer in the vapor-phase to keep the numerical model simple. The mass, momentum and energy balance equations were solved numerically using a Finite Volume Method. They noted that the absorption rate decreases as the inlet temperatures of the solution and coolant increase with the effect of coolant temperature being more pronounced. The absorption rate was also found to decrease with the increasing dilute solution concentration. The effects of absorber pressure were not studied as all the experiments were conducted at an absorber pressure of 162 kPa.

2.2.1 Summary of Numerical/ Analytical Studies

The various analytical/numerical models from the literature presented above can be categorized into two broad categories. The first category of models use the Colburn-Drew methodology originally developed for condensation of binary vapors and requires the use of empirical correlations for heat and mass transfer coefficients, while the second category of models solves mass, energy and diffusion equations numerically and do not require empirical correlations. A majority of the studies based on the Colburn-Drew methodology have neglected either the vapor-phase or the liquid-phase mass transfer resistance. Some of the more recent studies have included the mass transfer resistance in both phases, but often disagree on the dominant resistance (that controls the overall absorption process). Some of the studies concluded that liquid-phase mass transfer resistance is dominant (Goel and Goswami 2005a; b; Kim 1998; Perez-Blanco 1988), while others concluded that it is the vapor-phase mass transfer resistance (Potnis *et al.* 1997) that dominates. The numerical models have been developed for smooth and laminar falling films and do not account for various flow regimes as well as the wavy nature of the falling film. Furthermore, a very few studies (Lee *et al.* 2005; Perez-Blanco 1988) have investigated horizontal tube falling-film absorption in ammonia-water systems. Lee *et al.* (2005) approximated the half circumference of the tube to a vertical wall and solved the governing equations for a flat vertical wall. The experimental verification of these models is very limited.

2.3 Flow Regime Studies

Much of the literature on horizontal, falling-film type absorbers has treated the flow of the solution on tubes as a smooth laminar film. However, in reality, this is rarely

the case (Killion and Garimella 2003). Researchers have conducted studies characterizing the fluid flow behavior on horizontal tubes with different working fluids. In general, the flow pattern on horizontal tubes depends on the solution flow rate, the physical properties of the solution and the tube spacing (Mitrovic 2005). Some researchers have stated that the presence of vapor in the vicinity of the solution film can significantly affect the flow pattern. The main flow modes (regimes) in horizontal falling-film flow, as shown in Figure 2.1, are: droplet, column (jet), and sheet flow. In this figure, λ is the droplet/column site spacing, d is the tube diameter and s is the tube vertical spacing. Some researchers also define intermediate flow regimes such as droplet-column and column-sheet modes, where two flow regimes co-exist. The main parameters used to develop flow regime transition criteria are the solution Reynolds number (Re_l) and the Kapitza number (Ka_l) (Mitrovic 2005).

(a) Droplet   (b) Colum (Jet)   (c) Falling-Film
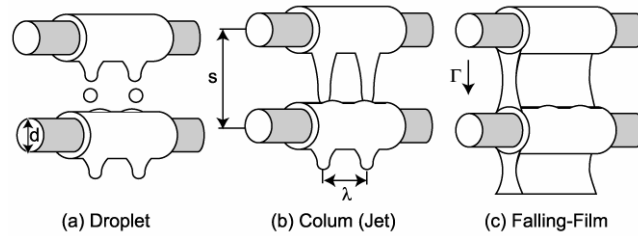
Figure 2.1 Primary Flow Modes in Horizontal-Tube Flow

Generally, the solution Re_l and Ka_l are defined as follows:

$$Re_l = \frac{4\Gamma}{\mu_l} \tag{2.7}$$

35

$$\mathrm{Ka}_l = \frac{\sigma_l^3 \rho_l}{\mu_l^4 g} \tag{2.8}$$

Here, $\Gamma = \left(\dfrac{\dot{m}}{2 \times L_t} \right)$ is the solution mass flow rate per length per side of the tube (as the solution flows symmetrically on the two sides of a horizontal tube); μ_l is the viscosity, ρ_l is the density, and σ_l is the surface tension of the solution; and g is the acceleration due to gravity. The generic form of the transition criteria proposed by various researchers is the following:

$$\mathrm{Re}_l = a \mathrm{Ka}_l^b \tag{2.9}$$

It should be kept in mind that the definition of Re_l varies among different studies as some studies use the solution mass flux per tube length per side, and some use the total mass flux, to define the Re_l. Therefore, care should be exercised when comparing these studies. Interestingly, the Re_l that dictates the transition from one mode to the other seems to depend only on the solution properties (Ka_l).

Honda *et al.* (1987) studied flow characteristics during condensation of stationary vapors of Propanol, R-113 and Methanol over a column of low-finned horizontal tubes. They defined a dimensionless parameter, $K = \left(\Gamma \cdot (g/\rho)^{1/4} \right) \big/ \sigma^{3/4}$, that dictates the mode transitions. They defined four distinct flow modes: droplet, column, column-sheet and sheet. They neglected the effect of tube spacing as the tube spacing in their study was less than the most unstable Taylor wavelength (associated with the flow regime transition).

$$\lambda_{Taylor} = 2\pi \sqrt{2\sigma_l / \rho_l g} \tag{2.10}$$

They also found that the wetted surface area increased with an increase in K, reaching a constant value for the sheet mode depending on the fluid. From the results reported in the paper, the maximum wetting ratio was about 0.5. The number of dripping sites also increased with the flow rate. They conducted the experiments at atmospheric pressure with stagnant vapor. The effect of vapor flow became evident, in a later study by Honda *et al.* (1991), where they found that when the vapor in the vicinity was stagnant, transition occurred from jet (column) to sheet mode for Reynolds number greater than 400, while sheet mode was not observed even at Reynolds numbers larger than 1800 when a vapor velocity (flowing vertically downward) of 3.4 m/s was present.

Hu and Jacobi (1996a) presented a flow regime map to predict various flow modes over horizontal tubes and investigated the effects of fluid properties. The experiments were conducted using water, ethylene glycol, water/glycol, oil, and alcohol as liquid streams, and in the absence as well as in the presence of air as the gas stream. They defined several flow modes in their study: droplet, droplet-jet (column), jet, jet-sheet and sheet. They presented the flow regime transition criteria in the following form:

$$\text{Re}_l = a Ga_{\text{mod},l}^{b} \tag{2.11}$$

Here, $Ga_{mod,l}$ is the modified Galileo number, defined as $\dfrac{\sigma_l^3 \rho_l}{\mu_l^4 g}$; and the values of the coefficients a and b depend on the flow mode. It should be noted that the definition of Ga_l is the same as the definition of the Kapitza number (Ka_l). They found that at low flow rates, all the droplet sites were not active simultaneously and droplets fell alternately from neighboring sites. As the flow rate increased, many sites became active. In the Jet mode, depending on the flow rate and the liquid, in-line (impinging and departure sites

are same), staggered and mixed type of jets were observed. Based on their criteria, they concluded that inertia driven flows (at higher Re_l) will predominantly be in the sheet mode while gravity driven (at higher Ga_l values, e.g., $(Ga_l)^{0.25} > 300$, Ga_l includes the influence of both surface tension and gravitation forces) flows will predominantly be in the droplet mode unless the influence of Re_l takes over that of Ga_l. They studied flow mode transition by increasing and decreasing the solution flow rate to find the presence of hysteresis in the flow mode transition, i.e., droplet to jet vs. jet to droplet. Although they found transition hysteresis in all the flow modes, its effect on the transitional Re was negligible. The experiments were conducted on adiabatic tubes. They also conducted limited experiments with a co-current air flow. They, however, didn't find a significant effect of the air flow on the flow modes for a majority of the operating conditions. This finding is in contrast to that of Honda *et al.* (1991) as discussed above. Since the tubes were adiabatic and there was no gas absorption in their experiments, the solution properties remained constant in the solution flow direction.

Nosoko *et al.* (2002) conducted an experimental study to characterize falling films on a completely wetted horizontal tube using water as the solution with the absorption of oxygen. Their geometries consisted of single-columns of 2-, 4-, 6-, and 8-tubes with 16 mm OD and 284 mm wetted length copper tubes. The tube spacings tested were 2, 5, 10, 15 mm. They conducted experiments at atmospheric pressure (103.2 kPa) for a Reynolds number range of $10 < Re_l = \dfrac{\Gamma}{\nu_l} < 150$. Here, Γ (m^2/s) is defined as the half volumetric flow rate per unit length of the tubes, and ν_l is the kinematic viscosity of the solution. Their experiments were conducted over a narrow range of solution temperatures (18 – 23°C); therefore, the effects of the change in solution properties were not discussed.

They observed smooth sheet flow at a tube spacing of 2 mm for $Re_l < 30$ with waves appearing at higher Reynolds numbers. For tube spacings of 5 mm or larger, only discontinuous droplet flow was observed. Although at higher tube spacings and larger Reynolds numbers, the column mode seems to appear, they termed it a discontinuous behavior where the bottom surface of the columns was periodically touching the surface of the film on the lower tube at high frequency. Therefore, this flow mode was also considered as droplet mode. They observed the droplet spacing to increase at the lower tubes due to the merging of neighboring sites on the upper tubes. Both the dripping sites and the time intervals were found to be more random at higher Reynolds numbers. They also noted that at reasonably high Re_l, many droplets jump off the tubes. At smaller Re_l (< 20), gas absorption was higher at the smaller tube spacing, probably due to the droplet type of solution distribution. They provided a correlation for mass transfer coefficient in terms of the Sherwood number (Sh_l) as a function of Reynolds number and Schmidt number (Sc_l). The Sh_l was proportional to $Re_l^{0.86}$ for tube spacings of $5 - 15$ mm as shown in the correlation below:

$$Sh_l = 0.0377 \, Re_l^{0.86} \, Sc_l^{0.5} \tag{2.12}$$

Here, $Sc_l = \nu_l / D_l$ and D_l is the diffusivity of the solution. The Sh_l was found to increase as $Re_l^{1.15}$ for $Re_l < 30$ and $Re_l^{0.96}$ for $Re_l > 30$ for the tube spacing of 2 mm. They observed higher values of Sh_l for discontinuous droplet mode compared to those for the sheet mode. It can be seen that the flow modes significantly affect the absorption characteristics (different dependence of Sh_l on Re_l).

Roques *et al.* (2002) conducted flow visualization experiments to study falling-film mode transition on plain, low-finned (26 fins per inch, fpi), enhanced boiling, and

enhanced condensation tubes using water, glycol, and a water-glycol mixture (50% by volume) as the working fluids under adiabatic conditions. The ODs of the plain, low-finned, and the enhanced tubes were 19.05 mm, and the OD of the enhanced condensation tube was 12.7 mm. They used a total of three tubes with an effective visualization length of 200 mm in a vertical array where the flow patterns were observed between first two tubes, and the third tube was used to provide continuation to the flow. Videos were recorded for 1.3 seconds at 30 frames per second (fps). They also defined five different flow modes similar to Hu and Jacobi (1996a): droplet, droplet-column, column, column-sheet, and sheet. The transitional Re_l was presented as a function of Ga_l as shown in equation (2.11). They presented two sets of the transition criteria, one without accounting for the tube spacing, and the other with the tube spacing included. They found that accounting for tube spacing improves the prediction capabilities especially at lower tube-spacing/diameter ratios. Their results agreed reasonably well with the results of Hu and Jacobi (1996a) and Honda *et al.* (1987). They recommended that the sheet mode should be preferred for evaporation applications while the column mode should be preferred for condensation applications. In a later study, Roques and Thome (2003) extended the investigation to include two more low-finned tubes (19 and 40 fpi). They found the high density (40 fpi) finned-tube showed similar transition behavior compared to plain tubes.

Killion and Garimella (2003; 2004a) used high-speed, high-resolution videos of water and LiBr-H_2O flow to demonstrate that the assumption of a smooth laminar film over horizontal tubes is rarely true. Their experimental set-up consisted of a single column of six horizontal brass tubes of 12.7 OD and 300 mm length (Killion and

Garimella 2003). The experiments were conducted using water for $Re_l = \dfrac{4\Gamma}{\mu_l} < 100$.

Here, Γ is the mass flow rate per unit length per side of the tube and μ_l is the dynamic viscosity. They discussed droplet formation, detachment and fall as well as the film waviness due to droplet impact. At higher Reynolds numbers, neighboring sites were found to interact with each other and affect the film waviness. The experimental set-up (Killion and Garimella 2004a) consisted of a single column of nine horizontal copper tubes of 15.9 mm OD and 500 mm length. In this study, experiments were conducted using surfactant-free LiBr solution (53.4% by weight). Using a semi-automated edge-detection process, a mathematical description of the droplet interface was generated. In these studies, they pointed out that merely extending the existing models to account for waviness is not adequate to account for the effects of complex flow patterns in the absorber. For example, the impact of a droplet was seen to propel a significant portion of the liquid down to the bottom of tube very quickly, thus not conforming to the assumption of uniform flow of film around the tube. Interaction between impacting and forming droplets led to axial shifts in droplet formation sites, early detachment, significant undulation and shape oscillations of the forming drop and twisting, bulging and turning of the liquid bridges. They further pointed out that not only do the flow characteristics influence absorption, but also the absorption can affect the flow characteristics due to variation in properties. Therefore, to address the two-way coupling it is necessary to investigate the flow mechanism, in detail. In a follow-up study, Killion and Garimella (2004b) simulated droplets of aqueous LiBr on the horizontal tubes by solving equations of motion on a fixed three-dimensional (3-D) grid. The volume of fluid (VoF) technique was used to handle the interface condition. They concluded that a

3-D model is required capture important characteristics of the droplet formation, detachment, and impact better than a simple 1-D model.

The studies presented above have focused primarily on characterizing the falling film behavior on horizontal tubes. There are also a few studies that attempt to quantify heat and mass transfer in different modes as well as investigated the effects of surface waves on the absorption rate. In one such study, Patnaik and Perez-Blanco (1996a; 1996b) investigated the effect of waviness in the falling film in a vertical tubular water-LiBr absorber. They focused on inertial waves, also known as roll waves, which were observed for $200 < \mathrm{Re}_l = \dfrac{4\Gamma}{\mu_l} < 1000$. The roll waves are governed by the relative influence of inertia and gravity, with surface tension effects being negligible. They recorded videos of the falling film during flow of water over a 19 mm OD tube and of aqueous LiBr (60% by weight) over 9.5 and 12.7 mm OD tubes at $23.3^{\circ}\mathrm{C}$. An approximate velocity field was developed using image-processing and frequency analysis. Using the developed velocity field, they solved transient, two-dimensional (2-D) governing equations for simultaneous heat and mass transfer. They compared the mass transfer performance in the presence of roll waves against smooth laminar films. They found good agreement with the penetration theory (Higbie 1935) in the case of smooth film, but much higher transport rates were obtained with the roll waves. They found Sherwood numbers on the order of 300 with the roll waves, whereas smooth film values varied from 30 to 80 for the same flow regime. Furthermore, they observed a maximum mass transfer coefficient for $\mathrm{Re}_l \cong 300$. The decrease in the mass transfer coefficient at higher Reynolds number was attributed to a reduced frequency of the roll waves. The solution Nusselt number, however, peaked at $\mathrm{Re}_l \cong 200$, although the effect of the roll

waves on the heat transfer was not as pronounced as on the mass transfer. They assumed constant thermo-physical properties of the solution and stagnant vapor in their numerical solution.

Kirby and Perez-Blanco (1994) developed a 2-dimensional numerical model to quantify the relative contributions of various flow modes during absorption of the water vapor flowing co-current to the absorbent aqueous LiBr. The solution flow on horizontal tubes was divided into three distinct regimes, a falling-film regime on the tube surface, a droplet-formation regime on the underside of each tube, and droplet free-fall from one tube to the next. For each of the flow regimes, they used different heat and mass transfer correlations. Transient heat and mass transfer equations were solved using a fourth order Runge-Kutta scheme. Their absorber consisted of copper tubes of 19 mm OD and 280 mm length. They presented results for two different LiBr mass fractions of 60% and 62% entering the absorber at saturation conditions corresponding to absorber pressures in the range $0.77 - 0.93$ kPa for solution flow rates in the range $0.006 - 0.04$ kg/s. The simulations were conducted with the assumption of complete wetting of the tubes and in the absence of any additives for heat and mass transfer enhancement. They found most of the absorption taking place in the droplet-formation regime that accounted for a majority of the mass transfer while the falling film on the tube surface accounted for a majority of the heat transfer. The contribution of the droplet-fall regime was very small, primarily due to the increased temperature during the droplet-formation regime (because the absorption process is mainly adiabatic during droplet formation) and smaller residence time between tubes. They also found that the solution film thickness plays an important role in determining heat and mass transfer characteristics as the heat transfer

43

occurs at the solution-tube interface while the mass transfer occurs at the solution-vapor interface. For thicker films, therefore, cooling of the film may not have as significant an effect on the solution-vapor interface as in thinner films. They concluded that better absorber performance can be achieved by increasing the absorber vapor pressure, and increasing the solution and coolant flow rates.

Jeong and Garimella (2002) developed a flow-regime based model that estimates the relative contributions of different flow modes during absorption of water vapor by LiBr solution in a horizontal tube falling-film absorber. Their model was similar to that of Kirby and Perez-Blanco (1994), but they provided a very detailed description of the model and accounted for incomplete wetting of the tubes. They reported simulation results for solution mass flux in the range 0.006 – 0.106 kg/m-s at a refrigerant temperature of 12°C. They found that vapor is primary absorbed in the falling-film and droplet-formation modes while heat and mass transfer are negligible in the free-fall mode. At a lower flow rate of 0.006 kg/m-s, the falling-film mode accounted for a majority of the absorption, ranging from 86% of the total at the first tube to 80% of the total at the last tube. The smaller contribution of the droplet-formation mode to the mass transfer is due to the lower frequency of droplet formation at smaller mass fluxes. The droplet-formation mode becomes increasingly significant with the increasing solution flow rate. At a solution mass flux of 0.024 kg/m-s, the droplet-formation mode accounted for about half of the total vapor absorbed. In the absence of reliable models for wetting ratio, they used it as a parameter and found that both heat transfer and vapor absorption into the falling-film reduces significantly as the ratio decreases; however, the droplet-formation regime does not show any appreciable effect because the droplet-formation sites are

essentially independent of the wetting ratio. They also found that the vapor absorption rate in the droplet-formation regime increases with increased wetting. This is due to the fact that better heat transfer performance is achieved with increased wetting resulting in larger sub-cooling of the solution, which in turn, increases the driving potential for mass transfer.

2.3.1 Summary of Flow Regime Studies

It can be seen from the above discussion that the solution flow over horizontal tubes is rarely in the smooth falling-film regime (Killion and Garimella 2003). In fact, the droplet-mode is the preferred mode for absorption applications due to the advantage of mixing during impact and formation of the droplets that enhances the transport processes (Jeong and Garimella 2002; 2005; Kirby and Perez-Blanco 1994; Nosoko *et al.* 2002). While the deviation from idealized flow behavior is a well-acknowledged fact, a majority of the studies usually model the heat and mass transfer processes by treating the solution flow as a smooth, laminar falling-film. Jeong and Garimella (2002) demonstrated that the droplet-formation mode could account for more than 50% of the total absorption rate (depending upon the flow rate). It is, therefore, necessary to consider various flow modes to accurately model the absorption process. These studies, however, have focused on working fluids other than the ammonia-water fluid pair. As was discussed above, the solution conditions remained relatively constant in these studies. In an actual ammonia-water absorption process, the solution properties are a strong function of operating conditions (i.e. concentration, temperature and pressure); therefore, extension of these studies to ammonia-water absorption is difficult. Furthermore, a majority of the studies either did not involve any vapor absorption or involved stagnant

vapor. Honda *et al.* (1991) found significantly different results when the vapor was moving in the vicinity of the solution compared to a stationary vapor condition in a prior study (Honda *et al.* 1987). Clearly, a better understanding of the fluid flow behavior and its implications on the transport process under realistic operating conditions is required.

2.4 Research Needs

It is clear from the review of the literature presented above that there are numerous studies that have investigated absorption phenomena experimentally, numerically and analytically. The studies discussed are primarily those that use ammonia-water as the working fluid and employ a horizontal-tube falling-film type of configuration. In each category of the available studies, there are some deficiencies. In a vast majority of experimental studies, the absorption experiments are conducted on a component test facility (that includes only the absorber, solution heat exchanger, and desorber). The results of these studies do not consider influences of several other components that will be present in an actual heat pump or chiller. Furthermore, the experiments were conducted over a limited range of operating conditions in these studies. Many of these test conditions do not represent a range wide enough to cover the operating conditions of the heating and cooling modes in higher efficiency cycles. The operating pressures for these studies were limited to a narrow range of 17 - 193 kPa (Kwon and Jeong 2004) or were conducted in test facilities where absorption and desorption occurred at the same absorber operating pressure and did not include the rectification, condensation, expansion, and evaporation steps (Garimella 1999; 2000; Goel and Goswami 2005a; b; Gommed *et al.* 2001; Meacham and Garimella 2002a; 2004; Perez-Blanco 1988). Many of these studies were conducted at absorber operating

pressures in the range 20 - 40 kPa (Jeong *et al.* 1998) and at atmospheric pressures (Haselden and Malaty 1959), whereas the absorber pressure in actual NH_3/H_2O absorption systems for even the refrigeration mode is greater than 150 kPa. Yet other studies were conducted with extremely low vapor concentrations such as $64.7 - 79.7\%$ (Kang *et al.* 1999) compared to the almost pure ammonia concentration in actual NH_3/H_2O absorption systems. Other studies used very low solution concentrations such as $1.2 - 2.2\%$ (Jeong *et al.* 1998) at very low pressures $(20 - 40$ kPa$)$, whereas such low concentrations are rarely seen in absorption systems except at GAX conditions that must exhibit simultaneously high pressures. Absorber pressures in actual NH_3/H_2O absorption systems are typically between $150 - 500$ kPa for refrigerating, cooling, and heating mode operation.

The studies that investigate absorption phenomena analytically or numerically have seldom agreed upon the dominant heat and mass transfer resistances. The liquid-phase mass transfer resistance is considered dominant in some studies (Fernandez-Seara *et al.* 2005; Goel and Goswami 2005a; Gommed *et al.* 2001; Perez-Blanco 1988), while the others concluded that the vapor-phase mass transfer resistance was dominant (Panchal *et al.* 1997; Potnis *et al.* 1997).

Heat and mass transfer characteristics of an absorber can strongly be affected by fluid flow mechanisms. In studies on falling-film type absorbers, heat transfer correlations were developed for falling films with (Dorokhov and Bochagov 1983) or without (Wilke 1962) absorption. However, these studies were conducted with fluids pairs other than ammonia-water, e.g., LiBr/Water (Dorokhov and Bochagov 1983), and Water/Glycol mixture (Wilke 1962). In the case of a horizontal-tube falling-film

absorber, the droplet mode is a preferred and dominant flow mode. However, most of the numerical/analytical models usually consider the flow as being uniform laminar falling film flow. Recent experimental and theoretical studies (Hu and Jacobi 1996b; Nosoko *et al.* 2002) have addressed flow modes (sheet, jet, and droplet) in such absorbers. These studies were also conducted with fluid pairs other than ammonia-water, e.g., Water/Glycol mixture (Hu and Jacobi 1996a; b), and Water/Oxygen (Nosoko *et al.* 2002).

In addition to all the above deficiencies, only a few of these study local variation of absorption rates.

The present study aims at addressing some of these deficiencies. The main objectives of this study are:

- Design and fabricate a test facility replicating an actual absorption system

- Conduct experiments over a wide range of operating conditions for multiple combinations of solution concentration and absorber pressure for several solution flow rates

- Record measurements at the local level in the absorber to analyze the progression of the absorption process along the solution flow path

- Visually document and analyze the flow characteristics in the absorber

- Develop theory based models for absorption heat and mass transfer using the data for validation

Table 2.1 Summary of Experimental Studies Reviewed

Study	Absorber Type and Fluid Pair	Absorber Geometry	Operating Conditions	Specific Details	Key Findings
Haselden and Malaty (1959)	Vertical Tube NH_3-H_2O	<u>Tube:</u> OD^1: 12.7 mm L: 2.75 m $L_{exposed}$: 12. 7 mm to 1.22 m <u>Enclosure:</u> Pyrex tube, L: 1.52 m	P: 101.32 kPa $\dot{m}_{dil}$: 0.015 – 0.105 kg/min x_{dil}: 0 – 0.214 x_{conc}: 0.055 – 0.32 $T_{abs,in}$: 18.9 – 23.2^{o}C $T_{abs,out}$: 20.1 – 50.7^{o}C % Air in NH_3: 0 – 13%	- NH_3 vapor from a supply tank - Constant heat of solution for each experiment - x_V :100%. - Interface conditions same as bulk solution conditions	- ΔT and Δx across the film were negligible - Effect of $T_{abs,in}$ is minimal - x_{dil} and T_C are the main controlling parameters - β is relatively insensitive to Re_l : $4\Gamma / \mu_l$ - Absorption of vapor causes ripples that increase the mixing, and therefore β
Hoffmann and Ziegler (1996)	Horizontal Tube NH_3-H_2O	Tube OD: 18 mm t: 1 mm N_t: 24 (8×3) Staggered Fashion Area: 0.8 m^2	$P \le 2500$ kPa (Sytem limit) $T \le 90^o$C (System limit) x_{dil}: 0.2 – 0.5 (planned) Heat load: 20 kW/m^2 $\dot{m}_{dil}$:50-500 l/m-h	- Tubes were sandblasted to increase wetting - Absorber, desorber and dephlegmator are enclosed in a single cylindrical shell	- Experimental set-up was built but no data are reported
Jeong *et al.* (1998)	Coiled Tube NH_3-H_2O	Tube ID: 10.7 mm Tube OD: 12.7 mm Coil Dia: 82.6 mm L_{total}: 0.6 m	<u>Without Absorption</u> $\dot{m}_{dil}$: 1.5–29 g/s; $T_{abs,in}$: 60- 8°C; $T_{abs,out}$: 37-47°C; $\dot{m}_c$: 13–35 g/s $T_{C,in}$: 36 - 46°C; $T_{C,out}$: 43 - 59°C <u>With Absorption</u> $\dot{m}_{dil}$: 4.9 – 19.7 g/s $T_{abs,in}$: 66-69°C; $T_{abs,out}$: 45-54°C x_{dil}: 0.012–0.022 x_{conc}: 0.018 – 0.037 $\dot{m}_V$: 0.09–0.42 g/s; $\dot{m}_c$: 27 g/s $T_{V,in}$: 66–69°C, x_V: 0.63–0.77 $T_{C,in}$: 41 - 46°C; $T_{C,out}$: 45 - 54°C	- Assumed a constant specific heat of solution (CP_S) since $\Delta(x_{out}$-$x_{in})$ was small - $T_{abs,in}$ close to saturation; $T_{abs,out}$ slightly sub-cooled - No dripping distance (Coil Pitch = 0)	- α_{film} is smaller with absorption than without absorption; most probably due to insufficient wetting caused by the vapor shear - Heat transfer rate increased with the solution flow rate - For the coiled tube absorber, for a fixed heat transfer area, heat transfer rates could be increased by reducing the radius of curvature of the coil tube (thereby increasing number of turns)

---

[1] L: Length, N: Number, OD: Outer Diameter, P= Pressure, T: Temperature, t = Thickness, x: concentration; Subscripts: t = tube, dil: dilute, conc: concentrated; Δ: differential; $\Gamma = \dot{m} / Perimeter$

Table 2.1 Continued...

Study	Absorber Type and Fluid Pair	Absorber Geometry	Operating Conditions	Specific Details	Key Findings
Kang *et al.* (1999)	Vertical Falling-Film (Plate Heat Exchanger with OSF) NH₃-H₂O	H^2: 130 mm L: 110 mm W: 34 mm <u>Off Strip Fin (mm)</u> H: 4.88; t: 0.2; L: 3.18; Pitch: 1.95 Separation: 1.75 <u>Plain Fin (mm)</u> H: 3.0; t$_{fin}$: 0.2; L$_{fin}$: 95; Pitch: 2.97 Separation: 3.18	$\dot{m}_{dil}$: 4.0 – 10.15 g/s $\dot{m}_{v}$: 0.62 – 0.9 g/s x$_{dil}$: 0.05, 0.1, 0.15 x$_{V}$: 0.647 – 0.797 P: 101.32 kPa T$_{abs,in}$: 17 – 37.2°C T$_{V,in}$: 54.5 – 66.5°C $\dot{m}_{c}$: 98.83 – 121.25 g/s	- Co-current arrangement for liquid and vapor flow - Inlet vapor is saturated - Effect of vapor shear was neglected - Heat losses to ambient were neglected	- Rectification near the top (solution/vapor inlet) due to sub-cooled inlet - Water desorption towards bottom - Higher Nu and Sh are obtained for lower solution inlet and higher inlet vapor temperature - $\dot{m}_{v}$ should be maximized to increase the heat and mass transfer performance
Merrill *et al.* (1994)	Vertical tube Bubble Absorber NH₃-H₂O	Concentric U-tube (in mm) Inner tube OD: 12.7 Outer tube OD: 23.8 H: 508	P: 503 kPa x$_{gen}$: 0.08 Feed flow rate: 5.75 g/s x$_{V}$: 0.99 $\dot{m}_{v}$: 1.07 g/s	- For a GAX cycle	- Coolant-side resistance dominant - Higher absorber overall heat transfer area required for better performance
Lee *et al.* (2002)	Bubble Absorber (Plate-type) NH₃-H₂O	Plate dimensions: 0.112×0.264×0.003 m^3	<u>To study effect of $\dot{m}_{dil}$</u> $\dot{m}_{dil}$: 1 – 9 l/min $\dot{m}_{v}$:1.67, 8.3×10^{-5},1.5×10^{-4} m^3/s <u>To study effect of $\dot{m}_{v}$:</u> x$_{dil}$: 0 – 0.3; T$_{abs,in}$: 20°C $\dot{m}_{dil}$: 0.3 kg/min $\dot{m}_{v}$: 0.2 – 1.45×10^{-4} m^3/s	- Sand paper treated plates retained laminar flow and showed good wetting - Solution concentration was determined from conductivity - Three plate types: Smooth; Hairline treated by laser; treated by sand paper plates	- $\dot{m}_{dil}$ increase does not affect mass transfer but increases heat transfer - Liquid-side heat transfer resistance dominant

---

[2] H: Height, L: Length, W: Width, N: Number, P= Pressure, T: Temperature, t = Thickness, x: concentration; Subscripts: t = tube, r = row, p = pass, Trans: Transverse

Table 2.1 Continued...

Study	Absorber Type and Fluid Pair	Absorber Geometry	Operating Conditions	Specific Details	Key Findings
Kwon and Jeong (2004)	Helical Coil NH_3-H_2O	Tube ID[3]: 10.7 mm Tube OD: 12.7 mm Coil Dia: 82.6 mm Shell Dia.: 114.3 mm Total Length: 0.6 m No of turns:30	$\dot{m}_{dil}$: 4.43 - 90.0 g/s-m x_{dil}: 0.03, 0.14, 0.30 $T_{abs,in}$: 45, 55, 60°C $T_{C,in}$: 30°C P: 17 - 193 kPa	- Solution temperatures close to saturation - Vapor in equilibrium with the inlet solution - Both co- and counter-current arrangement tested	- Effect of $\dot{m}_{dil}$ and $T_{abs,in}$ is similar irrespective of the vapor flow direction - In counter-current flow heat transfer performance can deteriorate if the specific volume of vapor becomes large - Effect of vapor flow decreases as the dilute solution concentration increases
Garimella (2000)	Micro-channel Horizontal Tube NH_3-H_2O	Tube (in mm) OD: 1.587; ID: 1.079 L: 127; N_{tr}: 40 N_r: 75; N_{rp}: 15 Trans Pitch: 3.175 Row width: 0.127 m Vertical Pitch: 6.35 Absorber: H: 0.476 m Area: 1.9 m^2	Used in the simulation: $\dot{m}_{conc}$: 0.0284 kg/s; x_{conc}: 0.47 $\dot{m}_v$: 0.0095 kg/s; x_V: 0.995 $T_{V,in}$: 38°C; $\dot{m}_c$: 0.5 kg/s $T_{C,in}$: 42°C	- Design of a novel micro-channel absorber was presented - No experimental data reported in this study	- Micro-channel tube based absorber can be used for small absorption systems - Same design can be used for many components of an absorption system - Can make the absorption system modular
Meacham and Garimella (2002a)	Micro-channel Horizontal Tube NH_3-H_2O	Tube (in mm) OD: 1.575; ID: 1.067 L: 140; N_{tr}: 27 N_r: 80; N_{rp}: 16 Trans Pitch: 4.76 Vertical Pitch: 4.76 Absorber: H: 0.508 m Area: 1.5 m^2	$\dot{m}_{conc}$: 0.010 - 0.040 kg/s Vapor Fraction: 10 - 50% x_{dil}: 0.16 – 0.32 x_{conc}: 0.3 – 0.56 x_V: 0.76 - 95 $\dot{m}_c$: 0.23 – 0.38 kg/s	- No surface treatment - Micro-channel tubes arranged in a square array	- $\dot{m}_{conc}$ has largest impact - Vapor fraction has small effect - Increase in α_{film} due to higher $\dot{m}_v$ - Solution distribution (wetting) is a key to performance - Q_{abs}: up to 16 kW - α_{film}: 145 – 510 W/m^2-K
Meacham and Garimella (2002b)	Shell-and-tube Absorber NH_3-H_2O	Tube ID: 2.54 mm N_t: 253 Shell OD: 76.2 mm L_{shell}: 0.508 m A: 1.026 m^2	$\dot{m}_{conc}$: 0.018 - 0.032 kg/s x_{dil}: 0.15, 0.20, 0.25, 0.30 $\dot{m}_c$: (2.52 – 5.05) × 10^{-4} m^3/s	- Solution and vapor on the tube-side and coolant on the shell-side - Dilute solution and vapor stream are combined before entering the absorber	- α_{film} increases with $\dot{m}_v$ and vapor fraction - Smaller α_{film} due to flow mal-distribution - Q_{abs}: up to 10.5 kW - α_{film}: 330 – 825 W/m^2-K

[3] H: Height, ID: Inner Diameter, L: Length, W: Width, N: Number, P= Pressure, T: Temperature, t = Thickness, x: concentration; Subscripts: t = tube, r = row, p = pass, Trans: Transverse

Table 2.1 Continued...

Study	Absorber Type and Fluid Pair	Absorber Geometry	Operating Conditions	Specific Details	Key Findings
Meacham and Garimella (2004)	Micro-channel Horizontal Tube NH_3-H_2O	<u>Tube (in mm)</u> OD[4]: 1.575; ID: 1.067 L: 140; N_{tr}: 33 N_r: 20; N_{rp}: 2 Trans Pitch: 4.76 Vertical Pitch: 7.94 <u>Absorber:</u> H: 0.15 m Area: 0.456 m^2	$\dot{m}_{conc}$: 0.015 - 0.027 kg/s Vapor Fraction: 15, 20, 25, 30% x_{dil}: 0.27 – 0.36 x_{conc}: 0.44 – 0.53 x_V: 0.93 - 0.98 $\dot{m}_c$: 0.09 – 0.15 kg/s	- To allow visual access, the adjacent tube arrays were oriented in same direction as opposed to perpendicular transverse orientation in the previous design - Vertical pitch was increased due to U-bend in the tubes rather than use of headers	- Absorber heat duty of 15.1 kW was achieved with 30% of the original surface area (1.5 m^2) - Q_{abs}: 4.5 - 15.1 kW - α_{film}: 638 – 1648 W/m^2-K

---

[4] H: Height, ID: Inner Diameter, L: Length, OD: Outer Diameter, W: Width, N: Number, P= Pressure, T: Temperature, t = Thickness, x: concentration; Subscripts: t = tube, r = row, p = pass, Trans: Transverse

Table 2.2 Summary of Numerical/Analytical Studies Reviewed[5]

Study	Absorber Type	Fluid Pair/ Conditions	Specific Details	Key Assumptions	Key Conclusions
Colburn and Drew (1937)	Film condensation inside a vertical tube	In the example: (molar): Methanol: 70% Water: 30%	- Condensation of binary vapor, not absorption	- Liquid states of the two components are miscible in all proportions - Isobaric film condensation - Assumed transfer coefficients - $x_{l,bulk} = x_{l,int}$; no concentration gradient in the solution	- Composition of condensing flux (dynamic dew), z, is different than $x_{V,int}$ and $x_{V,bulk}$ - z approaches $x_{v,bulk}$ as the $\Delta(T_V - T_C)$ increase - For large rate of condensation, assuming $x_{l,bulk} = x_{l,int}$ will result small error in overall results - MTR in the vapor-phase exists even at the beginning of condensation - Vapor-phase MTR dominant - At higher T_C, accurate interface evaluation is critical
Ruhemann (1947)	Coiled tube falling-film	NH_3-H_2O In the example: P: 38 kPa $T_{abs,in}$: 30°C x_{dil}: 0.095; x_V: 1 x_{conc}: 0.19	- Absorber is modeled as vertical film falling along a wall - Counter-current	- Vapor is pure ammonia; vapor-phase MTR negligible - No wall thermal resistance	- Both heat and mass transfer should be considered - Liquid-phase MTR dominant - H & MTC may have different significance near the top of the absorber but always balance each other along the solution flow path
Perez-Blanco (1988)	Horizontal tube falling-film Coil tube OD: 12.7 mm Coil Dia: 82.6 mm N_{turns}: 6	NH_3-H_2O x_V: 1 $\dot{m}_{dil}$: 0.0063 kg/s x_{dil}: 0.033	- A simple model due to limited computer memory, and availability of property data	- Smooth laminar falling-film - Uniformly wetted tube surface - 1-Dimensional flow	- Mass transfer in falling-film controls the absorption - At low x_l and high T_l, water may evaporate reducing the tube load - Coolant HTC $\geq$ 2000 W/m²-K does not affect transfer process significantly except when solution is saturated - Higher vapor velocities improve absorption rates - Chemical additives may reduce the interface resistance
Takuma et al. (1993)	Shell-and-tube condenser OD: 15.88 mm ID: 11.24 mm L: 1 m N_{tube} = 17×38	NH_3-H_2O P: 196 kPa $T_{V,in}$: 146.8°C x_V: 0.55 $T_{C,in}$: 27.5°C	- x_V distribution was measured by Coherent Anti-Stokes Raman Spectroscopy	- Saturated vapor	- Accumulation of ammonia vapor at the interface presents a significant resistance to heat transfer - H&MT analogy can be used to simplify the condensation analysis

---

[5] MTR/C: Mass Transfer Resistance/Coefficient; HTR/C: Heat Transfer Resistance/Coefficient; C-D: Colburn-Drew; x: Concentration; T: Temperature; D: Diameter; L: length; N: Number; Subscripts: C: coolant; in,: inlet; int: interface; l: liquid; V: vapor; dil: dilute; conc: concentrated

53

Table 2.2 Continued...

Study	Absorber Type	Fluid Pair/ Conditions	Specific Details	Key Assumptions	Key Conclusions
Potnis *et al.* (1997)	Fluted coil sandwiched between two shrouds	NH_3-H_2O P^6: 1551 kPa x: 0.31 – 0.52	- Simultaneous heat and mass transfer analysis of coexisting absorption and flow boiling in GAX component	- C-D method with inclusion of liquid-side H&MT - Flow-boiling-side heat and mass transfer assumed bulk vapor-liquid equilibrium - Flow-boiling-side MTR negligible compared to absorption-side	- Both HTR and MTR lie in the vapor phase - During water desorption, the diffusional mass flow is the major contributor to the total mass flux - Vapor-phase MT boundary layer thicker than HT boundary layers
Erickson *et al.* (1998)	Vertical falling-film	NH_3-H_2O P: 0.56 MPa $x_{l,bulk}$: 0.0969 $x_{V,bulk}$: 0.8251	- C-D equations were re-arranged	- Similar assumptions as in C-D method - both the liquid- and vapor-phase MTR were calculated	- None of the liquid or vapor-phase MTR was found to be dominating in the numerical example
Panchal *et al.* (1997)	Vertical Tube OD: 25.4 mm L: 1.22 m	NH_3-H_2O x_V: 0.89 - 1 P: 904 – 965 kPa	- Condensation, not absorption - Saturated vapor	- No liquid-phase MTR - LMTD based on T_{sat}	- Complete mixing in the liquid-phase (no MTR) approximates the data better than no mixing
Kang and Christensen (1994)	Vertical Fluted Tube L: 1.075×7 m	NH_3-H_2O $x_{l,int}$: 0.32 – 0.49 $x_{v,int}$: 0.952 – 1 x_V: 0.997 - 1	- GAX absorber - Counter-current	- Complete wetting	- Coolant HTR is much higher than liquid film - Vapor-phase MTR dominant - Vapor velocity to be maximized for compact size
Palmer and Christensen (1996)	Vertical Fluted Tube with Inserts	NH_3-H_2O x_{dil}: 0.16 x_{conc}: 0.33	- Inserts geometry proprietary	- Solution leaving the generator and entering the absorber is at its bubble point (in data reduction) - Final vapor absorbed is in equilibrium with dilute solution entering the absorber (data reduction) - Complete mixing in the solution	- Wetting area increases with the solution concentration - Small experimental errors in the solution conditions measurement (flow rate, x) can cause large errors in vapor conditions (flow rate, x) at generator
Garrabrant and Christensen (1997)	Perforate Plate-Fin (falling-film) 0.432 m × 0.127 m × 0.25 mm	NH_3-H_2O x_{conc}: 0.13 – 0.41 $\dot{m}_{dil}$: 0.004-0.012	- Counter-current - Concentrated solution saturated	- No MTR in the liquid film; concentration and temperature of liquid are same as interface	- x_l (though its effect on surface tension and wetting) and solution/vapor Re affects the absorption - Shear forces due to counter-flow vapor can enhance the falling-film HTC

---

[6] MTR/C: Mass Transfer Resistance/Coefficient; HTR/C: Heat Transfer Resistance/Coefficient; C-D: Colburn-Drew; x: Concentration; T: Temperature; D: Diameter; L: length; N: Number; Subscripts: C: coolant; in,: inlet; int: interface; l: liquid; V: vapor; dil: dilute; conc: concentrated

Table 2.2 Continued...

Study	Absorber Type	Fluid Pair/ Conditions	Specific Details	Key Assumptions	Key Conclusions
Kang *et al.* (1997)	Falling-film	NH_3-H_2O	- GAX conditions - Counter-current absorber and desorber	- Similar to Colburn-Drew method i.e. complete mixing in the solution	- Mass transfer of ammonia and water is in the same direction for rectifier, evaporator and condenser; but can be in opposite directions for absorber and desorber - Minimize the ΔT[7] between the solution and bulk vapor - Higher coolant-side HTC, smaller heat exchanger
Kang *et al.* (2000)	Plate heat exchanger with Offset Strip Fins (OSF) Falling-film and Bubble Channel Width: 6.22 mm	NH_3-H_2O $\dot{m}_{dil}$: 3.91 kmol/h $\dot{m}_v$: 2.42 kmol/h x_{dil}: 0.2795 x_{conc}: 0.4558 x_V: 0.9873 P: 557.2 kPa	- Same heat exchanger for falling-film and bubble modes	Falling-film mode: - Complete wetting - Liquid film thin and well mixed Bubble mode: - Bubble sizes and velocities are same at each location - No direct heat transfer between vapor and coolant - Bubble coalescence and breakup negligible	- In falling-film mode liquid-phase MTR dominant, while both H&MTR in vapor-phase - In bubble mode, liquid-phase MTR dominant, while HTR in vapor-phase - HTC more important in falling-film and MTC in bubble mode
Chen and Christensen (2000)	Falling-film over flat wall	NH_3-H_2O	- Counter-current - Solved H&MT equations for small intervals	- T and x are uniform across the solution film - Absorption is small within any interval than flow rate (uniform thickness) - Laminar smooth film - Negligible sensible heat transfer from vapor to interface	- Absorption process can be decomposed into two processes: due to sub-cooling; and due to wall cooling - Sub-cooling decreases H&MTC - Exothermal mass transfer (such as in absorption due both to diffusion and convection) is greater than isothermal (simple diffusion without any heat transfer)
Kim (1998)	Vertical Tube Falling-film D: 0.025 m L: 1 m	NH_3-H_2O P: 450 kPa x_{dil}: 0.05 – 0.25 $\dot{m}_{dil}$: 0.004 kg/s x_V: 0.85 – 0.99	- Solution at the inlet is saturated - Does not use empirical correlations	- Smooth, laminar solution film - Fully developed velocity and temperature profiles - Vapor mixture has a uniform-plug profile for velocity, temperature and concentration	- HTR dominates absorption process - MTR in both liquid and vapor phases should be considered, although liquid-phase is dominant

---

[7] MTR/C: Mass Transfer Resistance/Coefficient; HTR/C: Heat Transfer Resistance/Coefficient; C-D: Colburn-Drew; x: Concentration; T: Temperature; D: Diameter; L: length; N: Number; Subscripts: C: coolant; in,: inlet; int: interface; l: liquid; V: vapor; dil: dilute; conc: concentrated

Table 2.2 Continued...

Study	Absorber Type	Fluid Pair/ Conditions	Specific Details	Key Assumptions	Key Conclusions
Gommed *et al.* (2001)	Vertical Tube Falling-film $D^{\mathbf{8}}$: 0.03 m L: 1 m	NH_3-H_2O x_{dil}: 0.35 x_V: 0.999	- Co-current - Governing equations are solved in both radial and axial directions	- Axi-symmetric geometry - Smooth, laminar solution film - Negligible natural convection	- Solution inlet temperature affects the absorption more than wall temperature - Thermal conductivity significantly affects the absorption performance - Absorption process is solution-side dominated
Fernandez-Seara *et al.* (2005)	Vertical Shell-and-tube (Bubble) L: 0.9 mm Inner tube Dia: 22 mm N_t: 40	NH_3-H_2O $\dot{m}_{dil}$: 100 kg/h x_{dil}: 0.225 x_V: 0.999 $\dot{m}_V$: 15 kg/h P: 200 kPa	- Co-current - Churn, plug and bubbly flow patterns	- Same heat and mass transfer areas between liquid and vapor phases - No direct heat transfer between vapor and coolant - Bubble coalescence and breakup negligible	- Interface temperature was found to be equal to solution bulk temperature - Vapor-phase HTR is dominant - Required absorber length decreases as the inner tube diameter and number of tubes increases - Required absorber length increases with increase in coolant temperature and dilute solution concentration
Goel and Goswami (2005a)	Lamella plate based Absorber Falling-film Width: 0.15 m Spacing: 10 mm Thickness: 1.3 mm	NH_3-H_2O P: 200 kPa $\dot{m}_{dil}$: 0.02 kg/s $\dot{m}_V$: 0.004 kg/s x_{dil}: 0.25 x_V:0.997	- Counter-current	- Complete wetting - Mass transfer only due to concentration gradients	- Liquid-phase HTR is negligible - Liquid-side MTR is dominant - T_C and coolant HTC significantly affect the absorption performance
Lee *et al.* (2005)	Shell-and-tube Horizontal falling-film Shell OD: 0.3 m Shell L: 1.5 m Tube OD: 10 mm Tube L: 1 m N_t: 91	NH_3-H_2O $\dot{m}_{dil}$: 8 – 9 kg/min $\dot{m}_V$: 2 -3 kg/min P: 162 kPa	- Half circumference of the tube was approximated as a vertical wall	- 1-Dimensional laminar falling film - Film thickness change due to absorption is negligible	- Absorption performance increases with decreasing dilute x_l, $T_{abs,in}$, $T_{C,in}$

---

[8] MTR/C: Mass Transfer Resistance/Coefficient; HTR/C: Heat Transfer Resistance/Coefficient; C-D: Colburn-Drew; x: Concentration; T: Temperature; D: Diameter; L: length; N: Number; Subscripts: C: coolant; in,: inlet; int: interface; l: liquid; V: vapor; dil: dilute; conc: concentrated

Table 2.3 Summary of Flow Regime Studies Reviewed

Study	Geometry	Fluids/Operating Condition	Gas Absorption	Key Conclusions
Honda *et al.* (1987)	Low finned-tube Vertical Column N_t: 2 or 3 OD: 15.8 mm L_t: 160 mm s/d: 1.4, 2.8	Propanol: $\dot{m}$: $3.25 \times 10^{-3} - 7.15 \times 10^{-2}$ kg/m-s R-113: $\dot{m}$: $5.41 \times 10^{-3} - 1.09 \times 10^{-1}$ kg/m-s Methanol P: 101.3 kPa Photos using 35 mm camera	- Vapor condensation - Stationary vapor	- Flow mode transition is governed by a parameter $$K = \left(\Gamma \cdot (g/\rho)^{1/4}\right)\Big/\sigma^{3/4}$$ - Number of falling sites increases with $\dot{m}$
Hu and Jacobi (1996a)	Smooth tube N_t: 2 OD: 9.5, 12.7, 15.9, 19.0, 22.2 mm s: 5 -50 mm s/d: 0.25 – 5.2	Water; Ethylene Glycol; Water/Glycol; Oil; and Alcohol $\dot{m}$: ≤ 0.22 kg/m-s V_{air}: ≤ 15 m/s $$Re_l = \frac{2\Gamma}{\mu_l} \leq 580$$	- Co-current air flow but no absorption	- Flow mode transition is governed by modified Galileo number, $\dfrac{\sigma_l^3 \rho_l}{\mu_l^4 g}$, and the criteria can be presented as $Re_l = aGa_l^b$ - Air flow does not have significant effect on mode transition - Effect of hysteresis on transitional Re is negligible
Roques *et al.* (2002)	Plain (P); Low-finned (LF); Enhanced boiling (EB) /condensation (EC) OD(P,LF,EB):19 mm OD(EC): 12.7 mm L_t: 200 mm; N_t: 3 s: 3.2, 4.8, 6.4, 9.5, 19.4, 24.9 mm	Water; Glycol; Water-Glycol mixture (50% by volume) Fluids properties used at T: 20°C	- No absorption	- Transition criteria presented as $Re_l = aGa_l^b$ - Inclusion of tube spacing improves the predictive capabilities of the criteria, especially at low s/d ratios - Sheet mode preferable for evaporation and column mode for condensation
Nosoko *et al.* (2002)	Vertical column of Horizontal tubes OD: 16 mm; L: 284 mm Nt: 2, 4, 6, 8 s: 2, 5, 10, 15 mm	Water and Oxygen P: 103.2 kPa $10 < Re_l = \dfrac{\Gamma}{v_l} < 150$; Γ: half volumetric flow rate per length T: 18 – 23°C	- Oxygen absorption by water	- Sheet at lower tube spacing while discontinuous droplet and column flow at larger tube spacing - Droplet site and time interval becomes more random at higher Re - Gas absorption is higher in discontinuous droplet mode

Table 2.3 Continued...

Study	Geometry	Fluids/Operating Condition	Gas Absorption	Key Conclusions
Killion and Garimella (2003; 2004a; 2004b)	Vertical column of horizontal tubes OD: 12.7 mm L: 300 mm N_t: 6 s: 38.1 mm	Water $Re_l = \dfrac{4\Gamma}{\mu_l} < 100$	- No absorption	- Assumption of smooth, laminar film is rarely true - Documented wavy film, droplet formation, elongation, breakup, satellite droplet formation and impact in detail - Flow behavior and absorption characteristics can influence each other - Interaction between forming and impacting droplets can lead to axial shift
Kirby and Perez-Blanco (1994)	Horizontal tube Falling-film OD: 19 mm L: 280 mm	H_2O - LiBr P: 0.77 – 0.93 kPa x_{in}: 0.6, 0.62 (by weight) $13 < Re_l = \dfrac{4\Gamma}{\mu_l} < 98$	- Yes (water vapor) - Co-current	- Droplet formation accounts for a majority of the absorption - Solution-film thickness influences heat and mass transfer processes
Patnaik and Perez-Blanco (1996a; 1996b)	Vertical tube OD: 19.05 mm (water) OD: 9.5 and 12.7 mm (aqueous LiBr)	Water; aqueous LiBr (60%) T: 23.3°C	- Yes	- Roll waves enhance the transport process through convection - Sh values of up to 300 are possible in the presence of roll waves as compared to 30 – 80 in the similar flow regime without waves - Developed closed form models for velocity and heat and mass transfer
Jeong and Garimella (2002)	Horizontal tube falling-film	H_2O - LiBr	- Yes	- Quantified absorption in film and droplet formation modes in detail - At small solution flow rate, falling-film mode accounts for majority of the mass transfer - Significance of the droplet-formation regime becomes important at higher solution flow rates - Heat and mass transfer in droplet-fall regime are negligible

CHAPTER 3 EXPERIMENTAL SET-UP AND PROCEDURES

A single-stage absorption system was designed and fabricated to conduct ammonia-water absorption experiments over a wide range of operating conditions. The test facility consists of several primary and secondary heat exchangers, pumps and flow meters. The main components are the absorber, desorber, separator, rectifier, condenser, evaporator, refrigerant pre-cooler and the solution heat exchanger. In this chapter, the details of the absorber are presented first and a description of the other components is presented in the following section while describing the complete system. Finally, a description of the test procedures is presented.

It should be noted that this study was conducted in collaboration with another researcher (Lee 2007). The test facility was designed and fabricated by the present author and Lee. In view of larger number of experimental parameters to be controlled and monitored simultaneously on the large test facility, tests were conducted together by both researchers. This also ensured that safety practices were followed in handling this potentially toxic working fluid. Lee (2007) focuses on analysis of the overall system level quantities, and describes the experimental set-up and procedures in greater detail. The present research focuses on heat and mass transfer phenomena at local level within the absorber, and studies the effects of the fluid flow regimes on absorption characteristics.

3.1 Horizontal-tube Falling-Film Absorber

The absorber is the main component for this study, in which ammonia vapor flowing from the evaporator is absorbed by the dilute solution from the desorber, rejecting its heat to a coolant loop. The assembly consists of two main parts: an outer shell and a tube array. In this falling-film absorber, the solution flows by gravity from the top to the bottom of the tube array. The heat of absorption is transferred to the absorber coolant flowing through the tubes. The absorber as installed in the loop is shown in Figure 3.1.
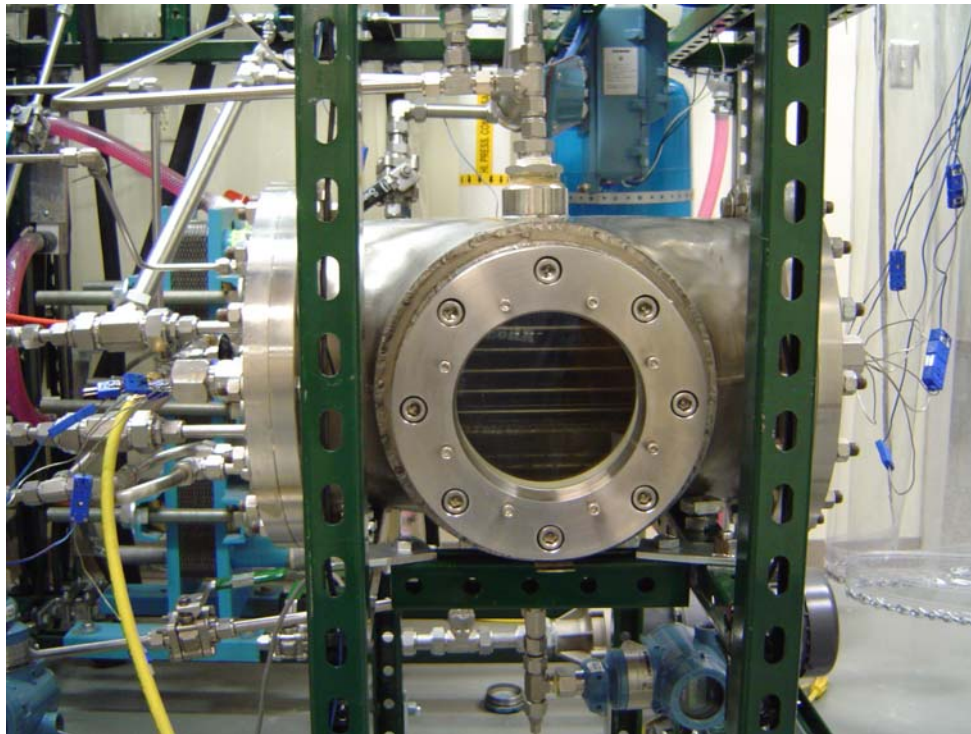
Figure 3.1 Absorber as Installed in the Test Facility

3.1.1 Outer Shell

The absorber tube array is housed in a 0.5 m long × 0.30 m diameter (19.5" long × 12" diameter) outer shell with a large 0.27 m (10") port, and three additional 64 mm (2.5") sight ports for illumination and viewing at other angles. Figure 3.2 shows a drawing of the outer shell.
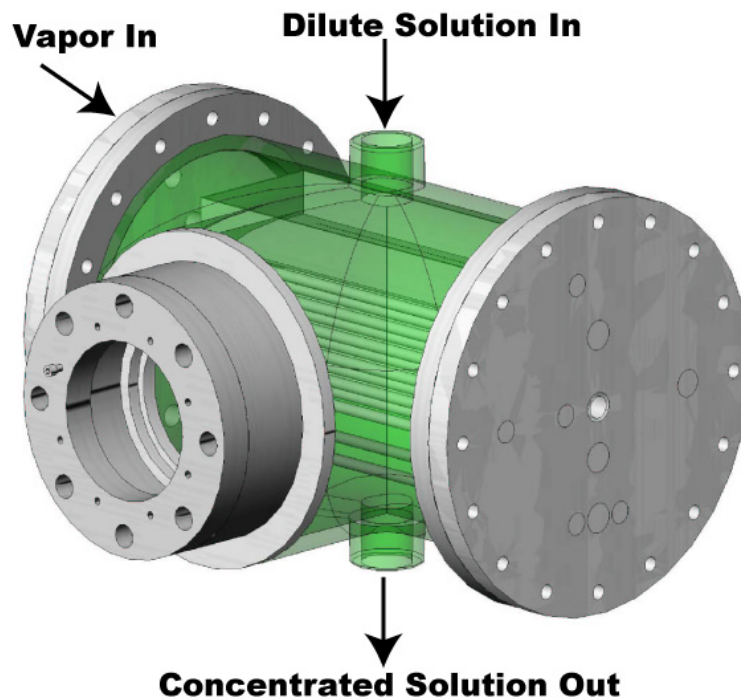
Figure 3.2 Drawing of the Absorber Outer Shell

The large port of the outer shell is located at the front and equipped with a sight glass that facilitates visualization. This front port is equipped with a B-weld sight glass manufactured by Pressure Products Company, Inc. It consists of a stainless steel body,

cap, cap screws, compression ring, lens, lens packing, compression adjustment screws and two cushion gaskets. The body dimensions are 0.32 m (12.5") OD and 89 mm (3.5") height (or thickness). The view port diameter is 0.15 m (6"). The 0.15 m OD (6 3/16"), 51 mm (2") thick tempered borosilicate lens can withstand a maximum pressure of 2068 kPa (300 psi). Two of the smaller ports are located at the top and bottom and one is located at the back, aligned with the large front port, and therefore used to illuminate the inside of the shell. A Bull's Eye NPT 38 mm (1½") sight glass from Pressure Products Company, Inc. rated for 4137 kPa (600 psi), 232.2°C (450°F) service is installed at the back port. Teflon gaskets, compression rings, and O-rings are used for the sight glasses for compatibility with ammonia. The two other ports at the top and bottom are used as a solution inlet and outlet, respectively.

3.1.2 Tube Array

The tube array inside the shell consists of four columns of 9.5 mm (3/8") nominal OD, 0.7 mm (0.028") wall thickness, 0.29 m (11.5") long tubes, each column containing 6 tubes for a total of 24 tubes in the bundle. Figure 3.3 shows a drawing and a photograph of the tube array. The two absorber coolant headers at either side of the tube array are 0.13 m (5.12") long, 0.12 m (4.72") wide, and 25 mm (1") in depth. The drip tray that distributes the dilute solution from above the tube array is 0.343 m (13.5") long × 0.12 m (4.72") wide × 38 mm (1.5") in height. These dimensions are shown in Figure 3.4.

The tube array is connected to one of the flanges and inserted from one end of the shell. Ammonia vapor is introduced into the chamber through the same flange. The

tubes are arranged in a serpentine configuration with a horizontal pitch of 30 mm (1.2"), a vertical pitch of 20 mm (0.79"), and a surface area of 0.210 m^2 (2.26 ft^2).

(a)

(b)
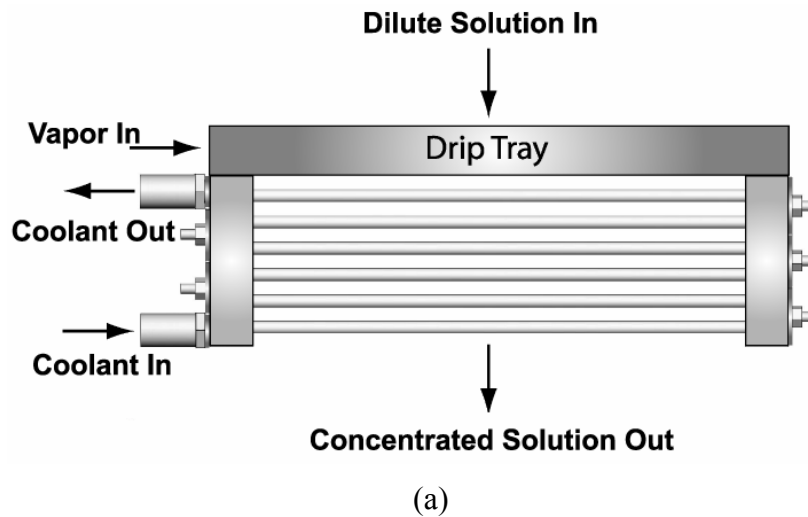
Figure 3.3 Absorber Tube Array

Figure 3.4 shows these pitch values. The tube array was initially designed for one header and U-bends at the other header to achieve the serpentine flow arrangement; however,

fabricating the U-bends with such a small bend radius using stainless steel was not feasible, which necessitated the two headers. The two headers have six coolant passes from the bottom to the top of the assembly with a total of seven ports for temperature measurements at each level. Thermocouples are placed at each level of the absorber to allow determination of row-wise heat duties, which, in turn, assist in the estimation of variation of heat and mass transfer coefficients within the absorber.
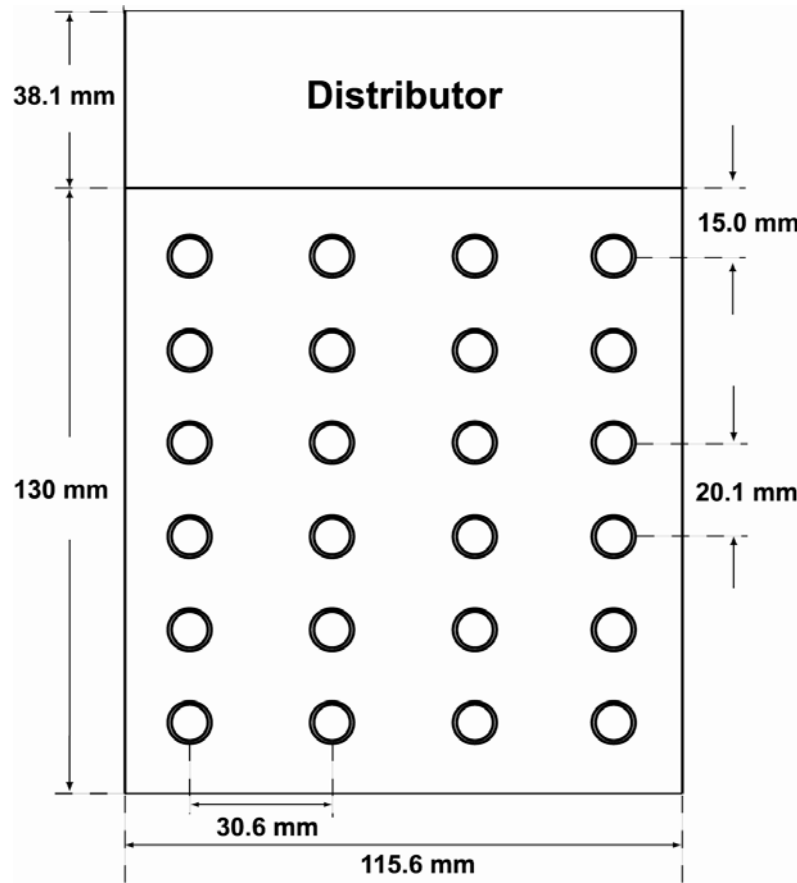
Figure 3.4 Tube Array Dimensions

The drip tray (Figure 3.5) is placed above the tube bundles, supported by the headers and designed to distribute dilute solution on the tubes. The tray has 4 rows of 75 holes (on a 30 mm × 3.8 mm or 1.2" × 0.15" pitch) for the insertion of 1.5 mm (0.06") capillary tubes (a total of 300), which distribute the dilute solution on the first row of the tube bundle. The distributor is located 15.0 mm above the centerline of the first row of tubes. The headers and the drip tray are welded from 1.5 mm (0.06") thick 316 stainless steel plate. Details of the absorber are summarized in Table 3.1.

Absolute pressures and temperatures at the solution inlet, outlet and vapor inlet are measured using absolute pressure transducers (Rosemount Model 2088). Measurements of pressures and temperatures at three different locations enable independent estimates of thermodynamic states at these locations.

Figure 3.5 Photograph of the Drip Tray

Table 3.1 Details of the Horizontal-Tube Falling-Film Absorber

Tube Assembly	
Tube O. D.	9.5 mm (3/8")
Tube Wall Thickness	0.7 mm (0.028")
Tube Length	0.292 m (11.5")
Number of Rows	6
Number of Columns	4
Horizontal Pitch	30.5 mm (1.2")
Vertical Pitch	20.1 mm (0.79")
Total Surface Area	0.210 m^2 (2.258 ft^2)
Drip Tray	
Length	0.343 m (13.5")
Width	0.120 m (4.72")
Height	38.1 mm (1.5")
Capillary Tube O. D.	1.5 mm (0.06")
Number of Rows	4
Number of capillary tubes per rows	75
Pitch (longitudinal)	3.8 mm (0.15")
Pitch (Transverse)	30.5 mm (1.2")
Coolant Headers	
Length	0.130 m (5.12")
Width	0.120 m (4.72")
Depth	25.4 mm (1")

3.1.3 Absorber Coolant Loop

A closed coolant loop with distilled water as the coolant is used to remove the heat of absorption from the absorber, which is eventually transferred to the lab chilled water-glycol coolant (cooled by a 50 RT Carrier AquaSnap Chiller) in a plate heat exchanger (Superchanger Model UX-016-UJ-21 by Tranter with a total heat transfer area of 1.65 m^2 or 17.8 ft^2). Most of the plumbing for the closed coolant lines is fabricated using 25.4 mm (1") nominal O.D. tubes to minimize frictional pressure drop except at the inlet and outlet of the absorber. To measure the coolant pressure drop in the absorber, a differential pressure transducer from Rosemount is used. The coolant is circulated using a centrifugal pump (Little Giant Model TE-7-MD-HC) with a ¾ hp motor. An expansion tank is used upstream of the pump inlet to compensate for thermal expansion of water and to provide additional positive head for the pump. The coolant flow rate is measured using a magnetic flow meter (Rosemount Model 8711). Temperatures of the absorber coolant and the chilled water are measured at the inlets and outlets of the plate heat exchanger. Chilled water-glycol flow rate is measured using a rotameter (VFC-143 by Dwyer Instrumentation). An energy balance at the plate heat exchanger provides an additional means of verifying the accuracy of the results over and above the energy balance between the ammonia and primary coolant in the absorber.

3.2 Test Facility

The test facility replicates a steam-fired absorption chiller system, and includes the absorber, desorber, condenser, evaporator, rectifier, solution heat exchanger and refrigerant pre-cooler, together with coupling loops and heat exchangers for the major externally coupled components. The system operates at two different nominal pressure

levels: high pressure at the condenser, rectifier and desorber, and low pressure at the absorber and evaporator. The different solution concentrations at different absorber pressures are obtained by controlling heat duties and temperatures of the desorber, condenser, rectifier and absorber cooling loops. A schematic of the test facility is shown in Figure 3.6 while a photograph is shown in Figure 3.7. In Figure 3.6, dotted lines show vapor flow while solid lines show solution flow. Concentrated solution from the absorber is pumped to the desorber using a solution pump (magnetic gear pump by Tuthill). The solution pump can provide a maximum flow rate of 1.44×10^{-4} m^3/s at zero pressure difference and can be used in continuous operation at up to 1034 kPa (150 psi) differential pressure. The operating temperature is between -46°C and 176°C, and the maximum operational viscosity is 2 kg/m-s (2000 cps). A variable frequency drive is used to operate the solution pump. The desorber is a coiled tube-in-tube heat exchanger (Model #00528 by Exergy, Inc.) and uses steam up to a pressure of 690 kPa (100 psi) as the heat source. A two-phase solution consisting of relatively impure vapor and dilute solution exits the desorber outlet and is separated into liquid and vapor streams in the separator. A level indicator is used to monitor the level in the separator. The dilute solution exiting the separator flows back to the absorber, exchanging heat with the concentrated solution from the absorber in the solution heat exchanger (a shell and tube heat exchanger by Exergy Inc, Model 00256-3). Because the vapor pressure of water (the absorbent) is not negligible as compared to that of ammonia (the refrigerant), water also vaporizes with ammonia in the desorber. Therefore, rectification of the vapor is necessary to avoid performance deterioration in the evaporator due to a rise in refrigerant temperature as the evaporation proceeds.
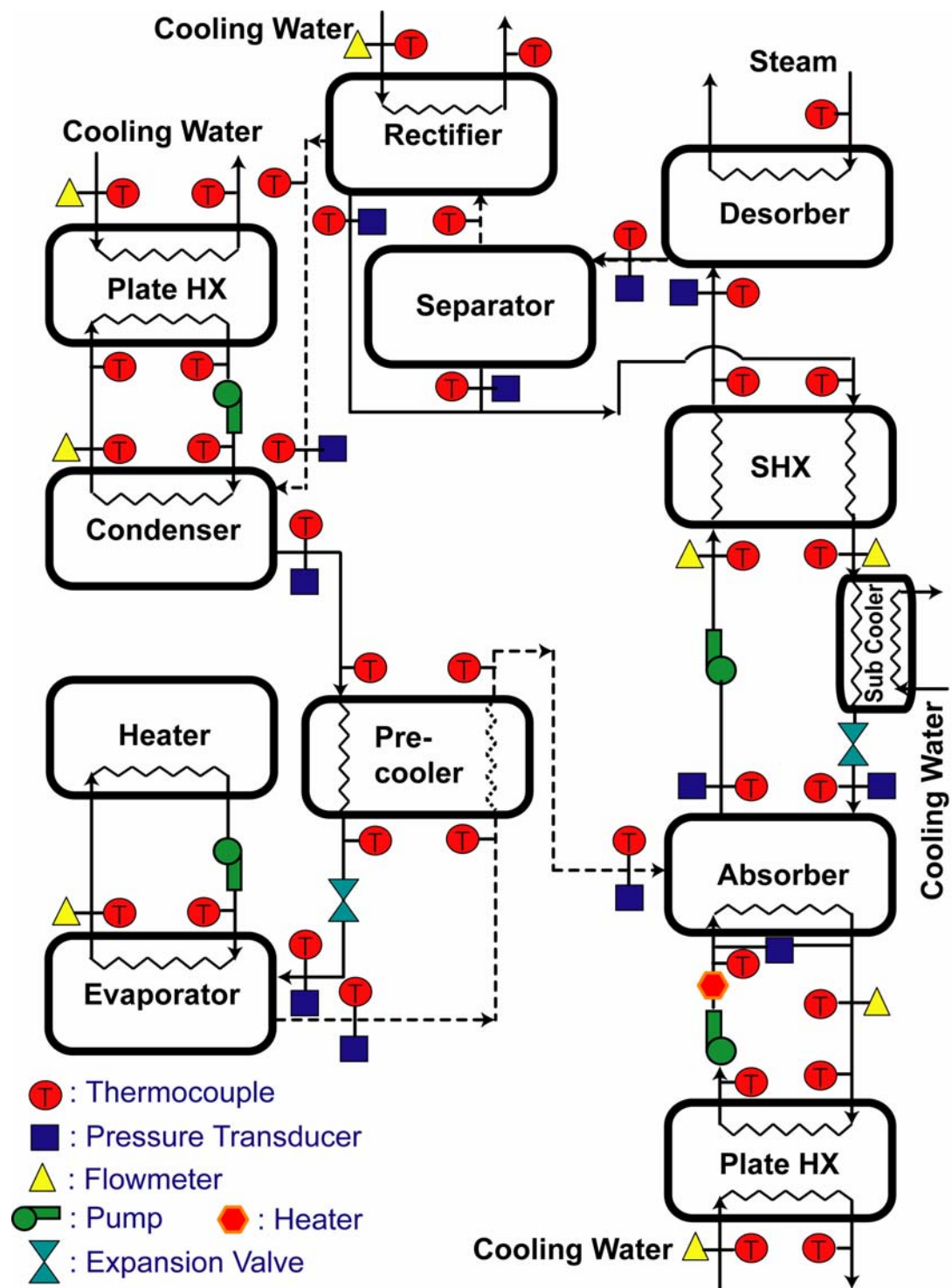
Figure 3.6 Test Facility Schematic
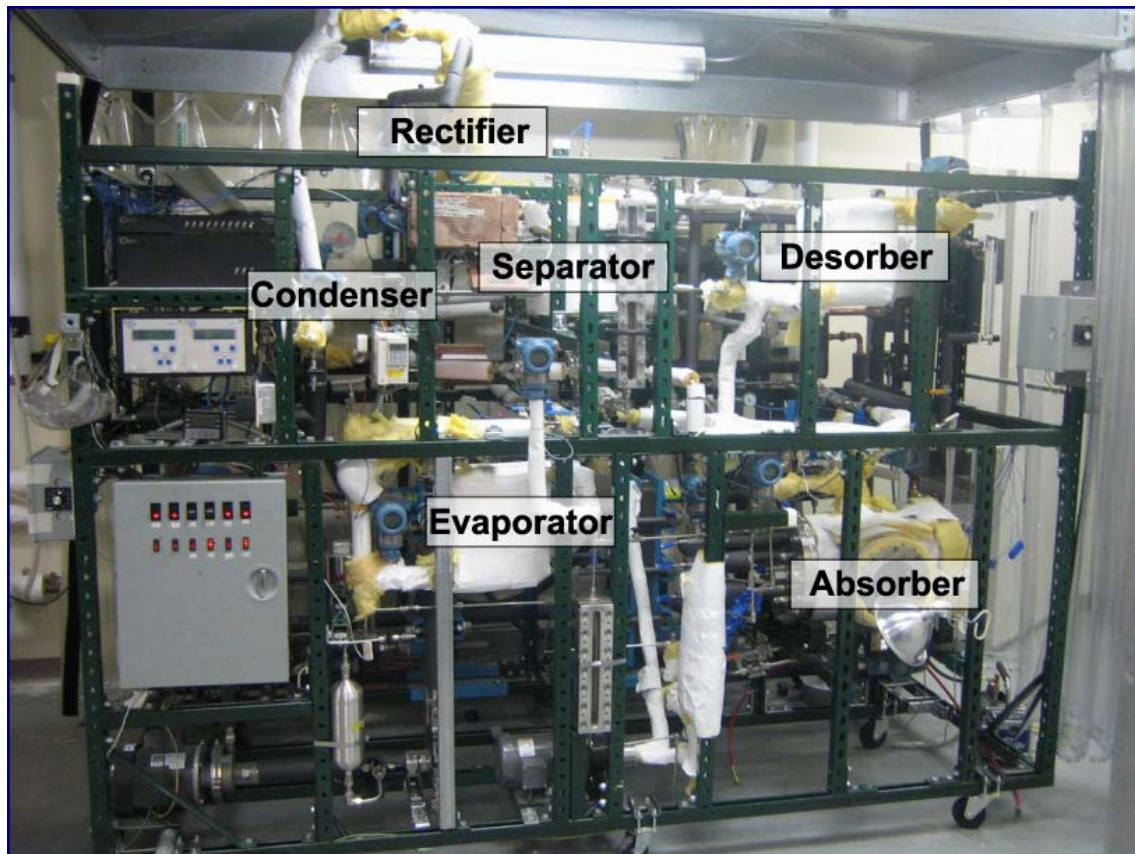
Figure 3.7 Photograph of Test Facility

The vapor from the separator is passed through an externally cooled rectifier to partially condense the water content and increase the ammonia concentration. The rectifier from Rocky Research consists of a 0.483 m (19") long and 0.114 m (4.5") diameter shell that encloses a helical coil of about 12.7 mm (0.5") tube diameter, with appropriate fill material in the space between the coil and the shell. The ammonia-rich (refrigerant) vapor exits the rectifier at the top and flows to the condenser while reflux (condensate) leaves the rectifier at the bottom and mixes with the dilute solution returning from the separator and flows to the absorber. The rectifier is located at the highest point in the system, thereby providing the necessary pressure difference for the flow of reflux from

the rectifier outlet to the separator outlet. A sight glass at the reflux outlet is used to ensure that only liquid reflux leaves the separator from the bottom. The refrigerant vapor is condensed in the condenser, which is a shell and tube heat exchanger (Model 00677-3 by Exergy, Inc.). Water/glycol solution (approximately 50% by volume) is used as the coolant in the condenser, which in turn exchanges heat with the lab chilled water/glycol solution in the plate heat exchanger (identical to one used in the absorber coolant loop). A sight glass at the condenser outlet ensures the liquid state of the condensate. The condensed refrigerant is expanded to the evaporator pressure through an expansion device. The refrigerant exiting the condenser first flows through a refrigerant pre-cooler, which recuperatively reduces its enthalpy before expansion to the lower pressure. A flow metering needle valve (Model #SS-4MG-MH by Swagelok, maximum C_V of 0.03) is used as the expansion device. Glycol/water solution (50% by volume) is used as the closed loop heating fluid in the evaporator. A 5 kW electric resistance heater provides the required heating duty to evaporate the refrigerant. Vapor from the evaporator returns to the absorber while exchanging heat with the condensed refrigerant from the condenser in the pre-cooler (a shell-and-tube heat exchanger, model#00256-2 by Exergy Inc.). The vapor leaving the pre-cooler is absorbed by the dilute solution in the absorber and the cycle is repeated. A pressure reduction valve is used upstream of the absorber inlet to reduce the high pressure of the dilute solution from the solution heat exchanger. For some of the extreme conditions, e.g., low pressure and high dilute solution concentration, this system alone is unable to maintain low absorber pressures of 150 kPa (21.8 psi) and 345 kPa (50 psi). To address this issue, an externally cooled sub-cooler is used between the solution heat exchanger and the absorber. This helps reduce the temperature of the

dilute solution entering the absorber, therefore reducing the absorber pressure. At the other extreme, e.g., low concentration and high pressure, it is necessary to keep the coolant flow rate very small to maintain a higher absorber pressure. However, this results in unrealistically large coolant temperature differences. To keep the coolant temperature differences reasonable and still maintain the higher absorber pressure, it is necessary to circulate the coolant at higher temperatures. Therefore, a 5 kW electric heater is used in the closed coolant loop to independently control the coolant temperatures. Wherever a pump is used in the system (e.g., absorber solution and coolant loops, condenser and evaporator coolant loops), an expansion tank is provided upstream of the pump suction port to eliminate the possibility of starving the pump. The dimensions of the several heat exchangers used in the test facility are summarized in Table 3.2.

Table 3.2 Summary of Heat Exchangers in the Test Facility

Component	Manufacturer (Model)	Dimensions/ Specifications	Operating Limits
Condenser	Exergy, Inc. (Model 00677–3)	Stainless steel Type: Shell–and–tube Length: 0.5 m Shell O.D.: 76.2 mm Number of Tubes: 253 Tube O.D.: 3.2 mm Tube Wall Thickness: 0.32 mm Heat Transfer Area: 1.24 m^2	Pressure (MPa): Tube–side: 5.171 Shell–side: 3.447 Working Fluid Temperatures: 427°C
Desorber/ Evaporator	Exergy, Inc. (Model 00528)	Type: Tube–in–Tube Material: Stainless Steel Length: 5.9 m Inner Tube O.D.: 12.7 mm Outer Tube O.D.: 25.4 mm Wall Thickness: 1.7 mm Heat Transfer Area: 0.23 m^2	Pressure (MPa): Tube–side: 31.026 Annulus–side: 13.790 Working Fluid Temperature: 427°C
Rectifier	Provided by Rocky Research	Type: Shell–Coiled Tube Material: Steel Shell Length: 0.48 m Shell O.D.: 0.11 m Coil O.D.: 12.7 mm	
Separator	In–House	Material: Stainless Steel Shell Length: 0.3 m Shell O.D.: 0.15 m Tube O.D.: 12.7 mm Tube Length: 0.15 m Number of Holes: 32 (1.6 mm) Pipe Nipples O.D.: 50 mm Pipe Nipples Length: 0.15 m Number of Holes: 56 (3.2 mm)	
Solution Sub–cooler	In–House	Type: Tube-in-Tube Material: Stainless steel Length: 0.61 m Inner Tube O.D.: 12.7 mm Outer Tube O.D.: 25.4 mm Wall Thickness: 1.7 mm Heat Transfer Area: 0.024 m^2	

Table 3.2 Continued...

Component	Manufacturer (Model)	Dimensions/ Specifications	Operating Limits
Solution Heat Exchanger	Exergy Inc. (Model 00256–3)	Type: Shell–and–tube Material: Stainless steel Length: 0.38 m Shell O.D.: 38.1 mm Number of Tube: 55 Tube O.D.: 3.2 mm Tube Wall Thickness: 0.3 mm Heat Transfer Area: 0.20 m^2	Pressure (MPa): Tube–side: 8.274 Shell–side: 5.516 Working Fluid Temperatures: 427$^{\text{o}}$C
Pre–cooler	Exergy Inc. (Model 00256–2)	Type: Shell–and–tube Material: Stainless Steel Length: 0.25 m Shell O.D.: 38.1 mm Number of Tube: 55 Tube O.D.: 3.2 mm Tube Wall Thickness: 0.3 mm Heat Transfer Area: 0.13 m^2	Pressure (MPa): Tube–side: 8.274 Shell–side: 5.516 Working Fluid Temperatures: 427$^{\text{o}}$C
Absorber/ Condenser Coolant Heat Exchanger	Tranter Inc. (Superchanger, Model UX–016–UJ–21)	Type: Plate Height: 0.774 m Length: 0.3 m Depth: 63 – 67.3 mm Heat Transfer Area: 1.65 m^2 Weight: 95.7 kg	Pressure (MPa): 1.034 Working Fluid Temperatures: 93.3$^{\text{o}}$C

3.3 Instrumentation and Data Acquisition

3.3.1 Instrumentation

Most of the temperatures in this study are measured using T-type thermocouples with an accuracy of ±0.5$^{\text{o}}$C, while some are measured using Pr-13 RTDs with an accuracy of ±(0.5 - 0.8)$^{\text{o}}$C. Solution-side temperatures at the inlet and the outlet of the condenser, desorber and solution heat exchanger, as well as at the inlet of the pre-cooler

and evaporator, are measured using RTDs, while the rest are measured using thermocouples. Absolute solution pressures in the system are measured using Rosemount pressure transducers (models 2088 and 3051) with an accuracy of $\pm(0.25 - 0.75)$ % of the calibrated span. These pressure transducers can be used to measure pressures of up to 68.95 MPa (10000 psi); however, the span can be set to any desirable range within this limit. The pressure in the coolant loops is monitored using dial gages with a range of $0 - 689.5$ kPa ($0 - 100$ psi) and an accuracy of $\pm3\%$ of the span. Dilute and concentrated solution flow rates are measured using Coriolis flow meters (model CMF025 ELITE by Micromotion). The flow rates are displayed on Micromotion RFT 9739 rack-mounted displays. The flow meters can read up to 0.6048 kg/s (if configured to read mass flow rate) or up to 6.309×10^{-4} m^3/s (if configured to read volumetric flow rate) with an accuracy of $\pm0.10\%$ of the flow range. The operating temperature range is -240 to 204°C, with a maximum operating pressure of 10 MPa (1450 psi). These flow meters can also measure the density of the solution. The refrigerant mass flow rate is measured using a Coriolis flow meter (model D12 by Micromotion) located at the exit of the condenser. The sub-cooled state of the condensate allows measurement of the refrigerant flow rate. The refrigerant flow meter can measure flow rates up to 0.02268 kg/s with an accuracy of $\pm0.10\%$ of the flow rate. The absorber coolant flow rate is measured using a magnetic flow meter (model 8711 by Rosemount) coupled to a flow transmitter (model 8712C by Rosemount), with an accuracy of $\pm0.5\%$, and can be used over the range -29 to 149°C up to system pressures of 5102 kPa (740 psi). The condenser coolant flow rate is measured using a Coriolis flow meter (model CMF100 Elite by Micromotion). The flow meter can measure flow rates of $0 - 7.6$ kg/s (1000 lb$_m$/min) with an accuracy of $\pm0.10\%$. The flow

rate of the coolant in the evaporator loop is measured using a positive displacement flow meter (model JVM-60KL by AW company) coupled to a flow transmitter (FEM-03 by AW Company). It can be used to measure flow rates in the range 1.262×10^{-4}-1.262×10^{-3} m^3/s with ±0.5% accuracy up to a system pressure of 34474 kPa (5000 psi). Other coolant flow rates in the secondary heat exchangers are measured using various rotameters.

A summary of the specifications of each instrument used in this study is provided in Table 3.3.

3.3.2 Data Acquisition

A PC-based data acquisition system (supplied by IO Tech) is used to display and record data during the tests. The Tempscan/1000A with an expansion unit EXP/11A interfaced with the computer through the program TempView 4.1 allows real-time display and recording of temperatures, pressures, and flow rates. Together with an expansion chassis, the Temp Scan/1100 enables the capacity to add up to 10 modules that could monitor up to 992 input channels. Data acquisition rates and durations can be programmed at desired scan rates using TempView interface.

Pressure transducers are connected to the Tempscan unit using a voltage scanning module (TempV/32B) that converts 4-20 mA current input to 1-5 V with 250 ohm resistors, while thermocouples and RTDs are directly connected to Tempscan through thermocouple scanning modules (TempTC/32B) and RTD scanning modules (TempRTD/16B). The thermocouple scanning module (TempTC/32B) can read 32 differential input channels, which can be configured for thermocouple types J, K, T, E, R, S, B, and N for a 100 mV input.

76

Table 3.3 Instrument Specifications Summary

Parameter/ Instrument	Model	Manufacturer	Quantity	Range	Accuracy	Operating Limits
Flow Meters and Transmitters Specifications						
Dil/Conc Solution	CMF025 Elite	MicroMotion Inc.	2	0 - 0.6048 kg/s 0 - 6.309 $\times 10^{-4}$ m^3/s	±0.1% (Flow) ±0.5 kg/m^3 (Density)	T: -240 to 204°C P: 10 MPa (1450psi)
Dil/Conc (Trans)	RFT9739-Rack Mounting	MicroMotion Inc.	2	0-5000 kg/m^3 -240 to 450°C		T: 0 to 50°C (Ambient)
Refrigerant	C25	MicroMotion Inc.	1	0 - 0.02268 kg/s	±0.1%	
Abs Coolant	8711	Rosemount	1	0 - 1.262 $\times 10^{-3}$ m^3/s	±0.5%	T: -29 to 149°C P: 5.1MPa (740psi)
Abs Coolant (Trans)	8712C	Rosemount	1			T: -29 to 60°C (Ambient)
Evap Coolant	JVM-60KL	AW Company	1	1.262×10^{-4} - 1.262×10^{-3} m^3/s	±0.5% @ $v = 3 \times 10^{-5}$ m^2/s	P: 34.474 MPa
Evap Coolant (Trans)	FEM-03	AW Company	1			
Cond Coolant	CMF100 Elite	MicroMotion Inc.	1	0-7.56 kg/s	±0.1% (Flow) ±0.5 kg/m^3 (Density)	T: -240 to 204°C P: 10 MPa (1450psi)
Cond Coolant (Trans)	RFT9739-Field Mounting	MicroMotion Inc.	1	0-5000 kg/m^3 -240 to 450°C		T: 0 to 50°C (Ambient)
Pressure Transducers and Dial Gauges Specifications						
Absolute	2088	Rosemount	5	0-5.516 MPa	±0.25% of Calibrated Span	T: -40 to121^{o}C
Absolute	3051	Rosemount	2	0-27.579 MPa	±0.075% of Calibrated Span	T: -40 to121^{o}C
Absolute	3051	Rosemount	4	0-68.948 MPa	±0.075% of Calibrated Span	T: -40 to121˚C
Differential	3051C	Rosemount	1	0-13.790 MPa	±0.075% of Calibrated Span	T: -40 to 121˚C P: 31MPa (4500psig)
Dial Gauge	1005P (ABS-Black)	Ashcroft	2	0-689.5 kPa	±3% of Span	T: -40 to 65°C
Dial Gauge	1005P (ABS-Black)	Ashcroft	1	0-2.068 MPa	±3% of Span	T: -40 to 65°C
Thermocouples and RTDs Specifications						
Thermocouple	T-type	Omega Engineering	44	-270 to 240°C	±0.5^{o}C	
RTD	Pr-13	Omega Engineering	12	-60 to 240°C	±0.5-0.8^{o}C	
Rotameters Specifications (m^3/s)						
Absorber	VFC-143 series	Dwyer Instrumentation	1	1.262×10^{-4}- 1.262×10^{-3}	±2% of Full Scale	T: 49°C P:690kPa (100psi)
Condenser	7530 7C-08	King Instrument Company	1	6.309×10^{-5}- 6.309×10^{-4}	±2% of Full Scale	T: 54°C P:862kPa (125psi)
Rectifier	VFB -85-EC	Dwyer Instrumentation	1	1.262×10^{-4}- 1.262×10^{-3}	±3% of Full Scale	T: 65°C P:690kPa (100psi)
Rectifier	VFB -86-EC	Dwyer Instrumentation	1	3.155×10^{-5}- 3.155×10^{-4}	±3% of Full Scale	T: 65°C P:690kPa (100psi)
Sub-cooler	7530 7C-06	King Instrument Company	1	2.524×10^{-5}- 3.155×10^{-4}	±2% of Full Scale	T: 54°C P:862kPa (125psi)

Measurements can be designated in units of ^{o}C, ^{o}F, K, R, or volts. The RTD scanning module (TempRTD/16B) can read 16 channels of 3- or 4-wire RTDs in units of ^{o}C, ^{o}F, K, or R. The voltage scanning module (TempV/32B) can read 32 input channels with programmable ranges of 10 V, 5 V, 1 V, or 100 mV. A Windows-based TempView program provides a graphical user interface for easy configuration of hardware, acquisition, and display parameters. Real time data can be monitored by the TempView program in graphical or spread-sheet mode.

For the present tests, a total of 4 scanning modules, two (TempTC/32B) for T-type thermocouples, one (TempRTD/16B) for RTDs, and one (TempV/32B) for pressure transducers as well as for flow meters that have 4-20 mA output, are used. For these experiments, 44 thermocouples, 12 RTDs, 11 absolute and 1 differential pressure transducers, and 6 flow meters are connected to Tempscan using these 4 scanning modules. For each data point therefore, 56 temperatures, 12 pressures, 6 flow rates and 2 densities are recorded over a span of 5 minutes at 3 second intervals yielding 100 readings.

3.4 Experimental Challenges

Over the course of this study, the facility underwent many modifications in different stages to enable testing at vastly different test conditions. These modifications were necessary because no single test facility configuration can accomplish testing at all the conditions required in this study. The modifications included changes to the coolant loops for each component including new heat exchangers and plumbing orientations, changes to ammonia (e.g., reflux flow rate) and coupling fluid measurement techniques, changes to control devices such as refrigerant expansion valves, changes to the heat

source supply method, and numerous other minor modifications that provided the ability to progressively conduct tests and measurements over an extremely large range of high and low temperature, pressure and concentration, and flow rate conditions. The most significant of these changes are briefly described here.

3.4.1 Two Pressure Operation and Regulation

During the initial phase of experiments, steady operation while maintaining high and low side pressures and the desired desorber outlet conditions could not be obtained. It was determined that the thermostatic expansion valve did not provide the required external pressure equalization. An external pressure equalizer was installed and connected to the thermostatic expansion valve from a location downstream of the evaporator. In addition, a shut off valve was installed between the evaporator and the absorber to provide isolation between different segments of the loop and flexibility for maintenance operations. A 6.4 mm (1/4") liquid line was also installed between the evaporator inlet and the pump inlet, which, if necessary, allowed removal of water-rich liquid accumulated in the evaporator to be mixed with the solution from the absorber outlet. This expansion valve was eventually replaced with a manually controlled needle valve (Model #SS-4MG-MH by Swagelok, maximum C_V of 0.03) to obtain precise control over refrigerant flow rate.

Maintaining pressure levels (in the initial design) with the two outlet-set pressure regulators (in the reflux line and in the dilute solution return line to the absorber) proved to be challenging. The regulators operating between relatively similar pressures were interfering with each other, making stable operation difficult. Whenever the pressure at the absorber, which is downstream of the regulator in the solution line, was increased, the

79

regulator interrupted the flow. A manually controlled needle valve with a variable C_V (Model # SS-4L-MH-NE by Swagelok, maximum C_V of 0.15) was therefore used to replace the pressure reduction valve and provide much better control over the flow rates and pressures. The pressure reduction valve in the reflux line, which was causing unstable operation, was also removed and the reflux was directly introduced at the separator outlet. To enable this modification, the rectifier was further elevated to increase the static head available for drainage of the reflux.

3.4.2 Extreme Pressure and Concentration Conditions

It was also found that the 150 kPa (21.8 psi) absorber pressure cases for 25%, and the 345 (50.0 psi) and 150 kPa (21.8 psi) absorber pressure cases for 40% dilute solution concentration at the desorber could not be obtained using the initial test configuration. For example, despite using the absorber coolant and the chilled water-glycol supply at their full capacities, it was not possible to obtain the lower pressures at the higher dilute solution concentrations. Therefore, it was decided that pre-cooling this absorber inlet solution over and above what was achievable in the solution heat exchanger would decrease the heat load that must be handled by the absorber in some of these higher dilute solution concentration cases. Such a provision would offer independent control of the dilute solution temperature at the absorber inlet, and also lower the sensible cooling component of the absorber heat load, making the latent heat load dominant. High fractions of sensible heat loads in the absorber could unduly overestimate the absorption heat transfer coefficient. Based on these considerations, a 0.61 m (2 ft) long water-cooled, tube-in-tube dilute solution subcooler was designed, fabricated and installed between the solution heat exchanger and the absorber. This stainless steel heat exchanger

consists of a 12.7 mm (0.5") nominal O.D. inner tube and a 25.4 mm (1") nominal O.D. outer tube. Dilute solution flows through the inner tube, while chilled water-glycol solution flows through the annulus in a counter-flow orientation.

3.4.3 Absorber Coolant Temperature Difference

It was also found that for some of the data at the 345 and 500 kPa (50 and 72.5 psi) absorber pressure cases, there were large temperature differences from the inlet to the outlet of the absorber coolant due to the relatively small absorber coolant flow rates required to maintain these specific conditions in the first place. Since coolant flow rate measurement errors would be relatively large at such low required coolant flow rates, and also since large coolant ΔTs could affect absorption characteristics, it was decided to find an alternate means to reduce absorber coolant ΔTs, while maintaining reasonably large coolant flow rates. The heat sink for the closed coolant loop of the absorber is the large plate heat exchanger, which is coupled to the common glycol-water solution coolant from the chiller. This heat sink cools the closed-loop coolant to temperatures very close to the chiller temperature, restricting the amount of control available over the absorber coolant inlet temperature. In view of these considerations, it was decided to use a high flow rate closed loop coolant for these test cases, but raise the temperature at the absorber inlet by introducing a 5 kW resistance heater between the plate heat exchanger and the absorber inlet. This heater therefore enabled the use of reasonably large (and measurable) absorber coolant flow rates while reducing the coolant temperature rise within the absorber, and added considerable flexibility to the control of the absorber conditions.

3.5 Experimental Procedures

3.5.1 Safety Precautions

Safety issues constitute a significant priority when working with chemicals that are harmful to humans. Ammonia has toxic and corrosive characteristics and causes freeze burns from its cold temperatures, and may affect the immune system in the case of large acute exposures. Ammonia vapor is toxic, corrosive, depletes oxygen, and acts as a poison when ingested. Whenever eyes are exposed to ammonia, immediate first aid is necessary. To avoid any possible mishaps, many safety and precautionary measures were taken throughout this study. Some of these important test practices are described here. A full face mask fitted with an ammonia/methylamine cartridge and gloves are worn whenever there is a possibility of direct contact with ammonia, especially during charging and discharging of the loop with ammonia. The system is located under a fume hood enclosed with a plastic curtain on all sides. An exhaust fan in the fume hood is turned on to trap and discharge any ammonia that might be present during charging and operation, or during plumbing modifications, to the outside atmosphere. An ammonia monitor that is always functional is installed on the wall next to the test facility. This monitor (SAM–NH308N, Fixed Single Gas Monitor by Lumidor Safety Products) has a working range of 0-99 ppm and an accuracy of ±2 ppm, and is calibrated to provide a loud alarm at 25 ppm of ammonia in its vicinity. Operators also wear protective safety glasses while operating the system.

3.5.2 Leak Testing and Charging

Before charging the system, it must be ensured that there are no leaks in the system. Extensive leak tests are performed before charging the system. The system is first charged with air at up to 793 kPa (115 psi), and fittings, gaskets, welded parts and sight glasses are checked for leaks using soap detection. In several instances, in addition to soap detection, the system is charged with air and R-134a up to 1379 kPa (200 psi) and a refrigerant leak detector (CPS model L-709) is used to detect leaks. The system is then kept pressurized overnight. If there is no appreciable pressure drop, the evacuation process is started using a vacuum pump (model DV-85N by DV industries) and maintained until the pressure in the system decreases to 20 Pa or lower. A vacuum gage (model 14571 by Thermal Engineering) is used to monitor the vacuum level, and pressure transducers are also used to run a pressure trace. This evacuation process removes non condensable gases, and also provides enough pressure difference to enable charging with water and ammonia. Distilled water is charged before charging ammonia so that when ammonia is charged, it is absorbed into water and the pressure can be maintained in a controlled manner. The total required charge for the system is estimated using expected void fractions and concentrations in the various components and plumbing of the loop at nominal test conditions. Because test conditions vary over a wide range of concentrations, the amount of charge is determined based on the conditions to be tested in a given period. The mass fraction of ammonia in the loop is generally kept within 15% of the desired test concentration to keep the desorber heat duties within a reasonable range. More ammonia is added whenever higher concentration cases are to be tested.

3.5.3 Testing

In this study, concentration, solution flow rate and absorber pressure vary over wide ranges. Three absorber pressures of 150, 345 and 500 kPa (21.8, 50.0 and 72.5 psi), and four different concentrations of 5, 15, 25 and 40% for three different flow rates for each combination of concentration and pressure result in 36 data points. To obtain data over these wide ranges, the ultimate driving forces are the laboratory chiller that works as the heat sink, and the steam that provides the required heat duty at the desorber. The laboratory chiller and the steam are adjusted accordingly for each data point. The laboratory chiller has a cooling capacity of 50 tons (175.8 kW or 600,000 BTU/hr) and can provide coolant at temperatures as low as $-9.45^{o}C$. Water-glycol solution (approximately 50% by volume) is the coolant, and serves as the heat sink for the rectifier, condenser, and absorber. The laboratory steam lines can supply steam at up to 1379 kPa (200 psi). Two pressure regulators in the range 0 to 689 kPa (100 psi) and 0 to 2068 kPa (300 psi) are used to control the steam pressure. The steam line is directly connected to the desorber and determines desorber outlet temperature and the dilute solution concentration.

A set of well established test procedures was developed and used to ensure that data were obtained with acceptable accuracies. The tests were initiated after appropriate amounts of ammonia and distilled water were charged into the system. The data acquisition system and TempView software are started first so that the progress of the changing states in the system can be monitored continuously. Before starting a test, the system is checked for leaks, and valves that need to be in the open mode are opened. It is also ensured that there is enough liquid level at the pump inlet. The laboratory chiller is

turned on and is set to the appropriate temperature. Since the desired dilute solution concentration depends on the pressure and temperature at the desorber outlet, and the desorber pressure depends on the condenser temperature, the laboratory chiller temperature to obtain the desired condensing temperature is first estimated. This laboratory chiller provides chilled water-glycol solution to serve as the heat sink for the rectifier, condenser and absorber. Once the laboratory chiller is turned on, condenser, absorber, and evaporator coolant pumps are started. After all coolant pumps are turned on and it is determined that they are running at steady state, the variable speed solution pump is started at a low frequency to yield a low solution flow rate. Since there is no pressure differential across the pump at the beginning, the status of the pump is carefully monitored based on the solution level using the sight level indicator that is connected to the expansion tank upstream of the solution pump. After the solution pump is started, steam supply to the desorber is turned on. Addition of steam starts heating up the solution from the pump and raising the high side pressure. The heat duty is increased in gradual steps. Expansion valves for the dilute solution and refrigerant are kept wide open during the above procedure to reduce any flow restriction before some steady circulation is achieved. The solution level in the separator is also checked to ensure that there is no significant accumulation, which avoids the possibility of inadvertently starving the pump of solution supply. The solution pump speed is then gradually increased while the steam supply is also increased according to the solution flow rate. As steam supply is increased, the desorber outlet temperature and pressure increase; however, the solution flow rate decreases since the differential pressure is now higher. It takes some time before vapor actually starts flowing out of the rectifier and condenses in the condenser.

As the amount of vapor generated at the desorber and flowing to the condenser is increased, the temperature at the evaporator starts decreasing. The heater in the evaporator heating loop is turned on when the evaporator heating fluid temperature starts decreasing. The steam supply to the desorber and the solution flow rate are adjusted to get the desired concentrations at the desorber outlet, and solution flow and rectifier coolant flow are adjusted to get the desired refrigerant concentration. When the system is running in a quasi-steady state, the evaporator expansion valve is gradually closed to achieve a better pressure separation and therefore obtain a liquid phase at the condenser outlet. Sometimes, this increases the high-side pressure and decreases the low-side pressure, resulting in increased differential pressure and decreased solution flow rate. The decreased solution flow rate is compensated by increasing the pump speed accompanied by an adjustment of the steam supply. If the high side pressure becomes too high, the laboratory chiller flow rate for the condenser loop is first increased, and in addition, if necessary, the rectifier flow rate is increased. The differential pressure is monitored to keep it within 1034 kPa (150 psi), which is the maximum operational differential pressure for the pump. Throughout this process, the dilute solution flow rate is controlled using the solution expansion valve in the dilute solution line, and the difference between the concentrated and dilute solution flow rates is kept close to the refrigerant flow rate measured at the condenser outlet. The absorber pressure is continuously varying during this startup process, and is controlled by varying the absorber coolant flow rates and temperatures. Once the desired concentration at the desorber outlet, the concentrated solution flow rate, and the absorber pressure are obtained, the system is observed for some time without changing any of the parameters.

If the values remain fairly steady, a preliminary data point is recorded and energy balances and concentrations are checked at various positions. If any of the heat balances at the different components are unacceptable, the coolant-side flow rate or temperature or both are varied to improve the agreement between the ammonia-water and coolant-side duties. If the dilute concentration at the desorber outlet is different from the desired concentration, the steam duty is varied accordingly. These processes are repeated until the dilute solution concentration, solution flow rate, and the desired absorber pressure are achieved, combined with acceptable energy balances at the absorber, evaporator and condenser. After acceptable heat balances are obtained for each component, the system is observed until the various measured quantities do not change for a significant amount of time, and the data are recorded and checked again. A full data set consisting of 100 readings over a span of 5 min is then recorded.

3.6 Range of Experiments

Nominally, three solution flow rates, 0.019, 0.026, and 0.034 kg/s (2.5, 3.5, and 4.5 lb$_m$/min) designated as low, medium and high flow rate were tested at each of the nominal absorber pressures of 150, 345 and 500 kPa (21.8, 50.0 and 72.5 psi) representing a wide range of heat source/sink combinations. Nominal concentrations at the desorber outlet of 5, 15, 25, and 40% were tested for the above combinations of absorber pressures and concentrated solution flow rates. Table 3.4 provides the ranges of dilute solution concentrations, absorber pressures, and solution flow rates considered in this study. The absorber pressures of 150, 345 and 500 kPa correspond to cold ambient heat pump and refrigeration mode, moderate ambient heat pump mode, and nominal cooling and warm-ambient heat pump mode, respectively.

Table 3.4 Nominal Experimental Test Conditions

Pressure (kPa)		150			345			500		
Flow Rate (kg/s)		0.019	0.026	0.034	0.019	0.026	0.034	0.019	0.026	0.034
Concentration	**5%**	GAX Cycle Conditions								
	15%	Cold Ambient Heat Pump/ Refrigeration (-25 to -20°C)			Normal Ambient Heat Pump/ Cooling (-5 to 0°C)			Warm Ambient Heat Pump/ Refrigeration (3 to 8°C)		
	25%									
	40%									

CHAPTER 4 DATA REDUCTION AND OVERALL RESULTS

As explained in the previous chapter, pressure, temperature and flow rate values at various points of interest were recorded using the Data Acquisition System. This chapter describes the procedures followed to define the thermodynamic state of the ammonia-water solution at various locations and to obtain heat and mass transfer coefficients at the absorber. A detailed system level analysis (for all the components) is presented by Lee (2007). For each data point, 100 readings were recorded over a duration of 5 minutes, and the average value was used to represent the conditions for that data point. The steps to analyze the processes around the test loop are described using a representative data point with the following nominal values: dilute solution concentration at the desorber outlet of 25%, absorber inlet pressure of 345 kPa (50.0 psi), and a concentrated solution flow rate of 0.026 kg/s (3.5 lb_m/min). The uncertainties in the calculated parameters are estimated using an error propagation method (Taylor and Kuyatt 1993).

The thermodynamic properties of ammonia-water solution in the liquid and vapor phases are obtained from *Engineering Equation Solver* (EES) V7.697-3D software (Klein 2006). The transport properties (the viscosity, conductivity and surface tension) of ammonia-water mixture in the liquid-phase are based on the curve-fits obtained from the data provided by Herold *et al.* (1996). The liquid-phase binary diffusion coefficient is obtained using the correlation of Frank *et al.* (1996). The transport properties of the ammonia-water mixture in the vapor-phase are based on the *Chapman-Enskog Kinetic*

Theory outlined by Mills (1995). Appendix A provides additional details on the property calculations.

4.1 Chemical Activity in Ammonia-Water Absorption

In any absorption process, before proceeding with a detailed heat and mass transfer analysis, it is necessary to determine if the absorbate (solute) and the absorbent engage in any significant chemical reaction which can result into dissociation of the species. In ammonia-water absorption, water acts as the absorbent. When water and hydrocarbon oils are used as absorbents, usually no significant chemical reaction takes place between the absorbent and the absorbate (solute) and the process is considered as physical absorption (Seader and Henley 1998). Therefore, the absorption of ammonia vapor by dilute ammonia-water solution is a physical phenomenon. This is also substantiated by the reaction that occurs when ammonia mixes with water as follows (Herold *et al.* 1996):

$$NH_3 + H_2O \rightleftharpoons NH_4^+ + OH^- \tag{4.1}$$

This reaction has an equilibrium constant of 1.8×10^{-5} which implies that a majority of the ammonia remains intact when ammonia vapor mixes (is absorbed into) with dilute ammonia-water solution. Therefore, the possibility of dissociation of ammonia or water can safely be ignored.

4.2 Thermodynamic State

The working fluid, which is a binary mixture of ammonia and water, requires three independent parameters to define its state at any location in the system. As stated above, 11 absolute pressures, 1 differential pressure, and 56 temperatures are measured at

various locations and used as two of the required independent parameters for directly establishing the state. For these state points, the additional required parameter is typically either concentration or quality. In this study, the quality at any given state was chosen as the third independent parameter (wherever appropriate), because the uncertainties associated with obtaining samples of the vapor and liquid states of the solution at different locations around the test loop during operation are expected to be considerable. At such state points, measured temperatures and pressures, and the expected quality (e.g., saturated liquid or saturated vapor) are used to obtain the solution concentration. Other properties such as enthalpy and specific volume are typically obtained using these three known independent parameters. (In some instances, the enthalpy obtained from energy balances is used as an input to compute quality or concentration, depending on the specific state point under consideration.) Three different flow rates are also measured directly: dilute solution, concentrated solution, and refrigerant flow rate.

The ammonia-water solution exits as a two-phase mixture from the desorber, with the liquid and vapor phases in equilibrium with each other. Therefore, the liquid and vapor phase concentrations are computed (Figure 4.1) based on the measured temperature and pressure at the desorber outlet as follows, where q represents the quality of the particular stream:

$$x_{Dilute,Des} = f\left(T_{Des,out}, \ P_{Des,out}, \ q = 0\right) \tag{4.2}$$

$$x_{Dilute,Des} = f\left(122.4°C, \ 1110 \, kPa, \ 0\right) = 0.2386 \tag{4.3}$$

$$x_{V,Des} = f\left(T_{Des,out}, \ P_{Des,out}, \ q = 1\right) \tag{4.4}$$

$$x_{V,Des} = f\left(122.4°C,\ 1110\ \text{kPa},\ 1\right) = 0.8427 \qquad (4.5)$$
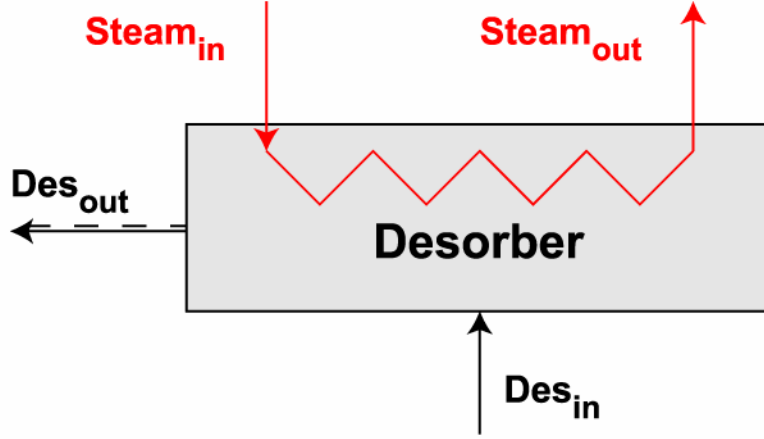
Figure 4.1 Schematic of the Desorber

The ammonia concentration flowing through the refrigerant circuit of the loop is obtained using an assumption of a saturated vapor condition at the measured rectifier outlet temperature and pressure (Figure 4.2). (The condenser inlet pressure is used as the rectifier outlet pressure, since there is no local pressure measurement at the rectifier vapor outlet.) The resulting refrigerant concentration applies for the condenser, evaporator, pre-cooler and absorber inlet. Thus,

$$x_V = f\left(T_{Rec,V,out},P_{Con,in},q=1\right) \qquad (4.6)$$

$$x_V = f\left(80.99°C,\ 1127\ \text{kPa},\ 1\right) = 0.9781 \qquad (4.7)$$

The reflux concentration is estimated by assuming a saturated liquid state leaving the rectifier at the measured temperature and pressure at reflux outlet location, as follows:
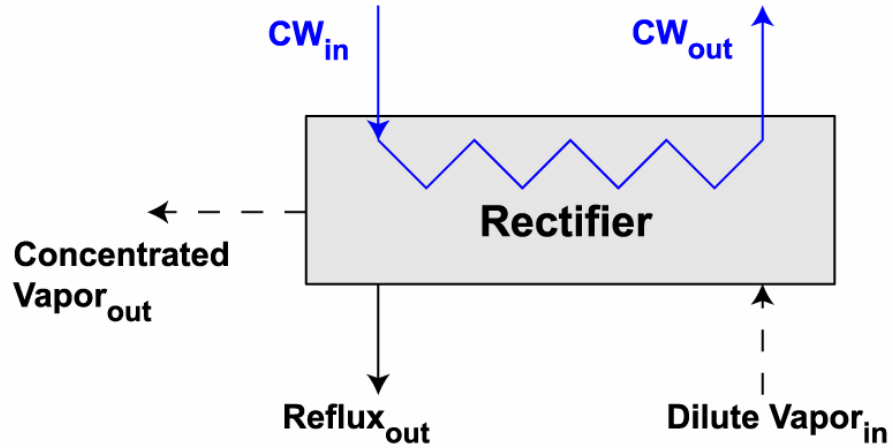
Figure 4.2 Schematic of the Rectifier

$$x_{Reflux} = f\left(T_{Reflux}, P_{Reflux}, q = 0\right) \tag{4.8}$$

$$x_{Reflux} = f\left(51.4°C,\ 1121\,kPa,\ 0\right) = 0.6182 \tag{4.9}$$

The vapor concentration at the rectifier inlet is the same as the concentration of the vapor leaving the separator (and therefore, also the desorber, because the separator simply accomplishes physical separation of the two phases exiting the desorber). The reflux flow rate and the rectifier inlet flow rate are calculated using mass and species balances at the rectifier using the refrigerant flow rate, and the concentrations at the rectifier inlet, rectifier vapor outlet and the reflux outlet as follows:

$$x_{V,des} = x_{Sep,V,out} = x_{Rec,in} = 0.8427 \tag{4.10}$$

$$\dot{m}_{Reflux} = \dot{m}_{Rec,in} - \dot{m}_{Ref,measured} \tag{4.11}$$

$$\dot{m}_{Reflux} = \dot{m}_{Rec,in} - 0.002826\,kg/s \tag{4.12}$$

$$\dot{m}_{Rec,in} \times x_{V,des} = \dot{m}_{Reflux} \times x_{Reflux} + \dot{m}_{Ref,measured} \times x_V \tag{4.13}$$

93

$$\dot{m}_{Rec,in} \times 0.8427 = \dot{m}_{Reflux} \times 0.6182 + 0.002826\,\mathrm{kg/s} \times 0.9781 \qquad (4.14)$$

$$\dot{m}_{Rec,in} = 0.004532\,\mathrm{kg/s} \qquad (4.15)$$

$$\dot{m}_{Reflux} = 0.001706\,\mathrm{kg/s} \qquad (4.16)$$

Mass and species balances at the separator outlet (Figure 4.3) are used to find the dilute solution concentration entering the absorber, and a species balance at the absorber is used to find the concentrated solution concentration, as follows:
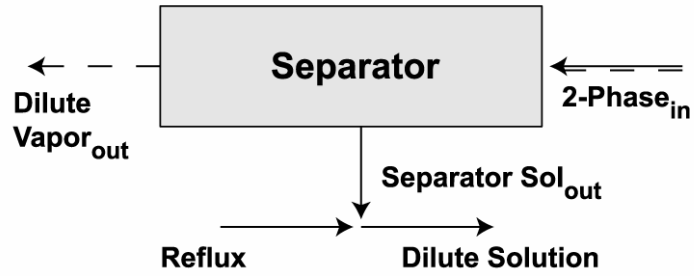
Figure 4.3 Schematic of the Separator

$$\dot{m}_{Sep,out} + \dot{m}_{Reflux} = \dot{m}_{Dilute} \qquad (4.17)$$

$$\begin{aligned} \dot{m}_{Sep,out} &= 0.02276\,\mathrm{kg/s} - 0.001706\,\mathrm{kg/s} \\ &= 0.02105\,\mathrm{kg/s} \end{aligned} \qquad (4.18)$$

$$x_{Dilute} \times \dot{m}_{Dilute} = \dot{m}_{Reflux} \times x_{Reflux} + \dot{m}_{Sep,out} \times x_{Dilute,Des} \qquad (4.19)$$

$$x_{Dilute} \times 0.02276\,\mathrm{kg/s} = 0.001706\,\mathrm{kg/s} \times 0.6182 + 0.02105 \times 0.2386 = 0.2671 \qquad (4.20)$$

$$x_{Concentrated} \times \dot{m}_{Concentrated} = \dot{m}_{Ref,measured} \times x_V + \dot{m}_{Dilute} \times x_{Dilute} \qquad (4.21)$$

$$x_{Concentrated} \times 0.02651\,\mathrm{kg/s} = 0.002826\,\mathrm{kg/s} \times 0.9781 + 0.02276\,\mathrm{kg/s} \times 0.2671 = 0.3336$$

$$(4.22)$$

It should be noted that the dilute solution concentration entering the absorber is different from the concentration at the desorber outlet, because the reflux mixes with the solution leaving the separator before it enters the absorber.

4.2.1 Concentration Range

Using the above methodology, concentrations of the various streams of interest (dilute solution, concentrated solution and vapor) are computed. Table 4.1 shows the ranges of these concentrations.

Table 4.1 Range of Concentrations

	Nominal Concentration			
	5%	15%	25%	40%
	P_{Abs}: 150 kPa			
$x_{Dilute,Des}$	9.3 - 10.9	13.5 - 15.6	24.0 - 25.9	38.3 - 40.2
x_{Dilute}	18.5 - 19.6	20.0 - 21.5	24.4 - 26.6	38.4 - 40.2
$x_{Concentrated}$	25.2 - 25.9	25.3 - 28.6	25.8 - 29.0	40.1 - 42.0
x_V	82.9 - 86.0	92.8 - 93.7	99.4 - 99.5	97.9 - 98.9
	P_{Abs}: 345 kPa			
$x_{Dilute,Des}$	9.1 - 10.3	14.5 - 15.5	23.9 - 25.2	36.2 - 40.8
x_{Dilute}	15.5 - 17.4	18.7 - 19.4	26.7 - 28.5	38.4 - 41.8
$x_{Concentrated}$	21.0 - 24.5	26.3 - 28.5	33.2 - 36.5	43.5 - 44.2
x_V	81.0 - 82.7	92.2 - 94.2	97.7 - 98.1	99.8 - 99.9
	P_{Abs}: 500 kPa			
$x_{Dilute,Des}$	9.9 - 11.5	14.6 - 15.6	24.9 - 26.8	34.2 - 38.7
x_{Dilute}	15.2 - 16.3	15.8 - 16.7	26.8 - 30.2	36.9 - 39.6
$x_{Concentrated}$	20.7 - 24.1	21.2 - 22.4	31.5 - 37.4	43.0 - 43.8
x_V	80.7 - 84.2	93.5 - 93.7	98.0 - 98.7	99.5 - 99.7

The nominal concentration is the desired concentration at the desorber outlet. As noted above, the absorber inlet concentration is different from the desorber outlet concentration because the reflux is mixed with the dilute solution stream before it enters the absorber. The difference in these two concentrations, therefore, depends on the reflux concentration and flow rate, which in turn change as the test conditions are varied. It can be seen that as the nominal solution concentration increases, the vapor concentration also increases. This is because lesser amount of heat is required at the desorber when the dilute solution exits at a higher concentration. At a similar pressure, but a lower temperature (due to less heat duty), the concentration of the vapor in equilibrium with the solution is higher. Therefore, a lesser amount of water evaporates in the desorber. For the same reason, the difference between the dilute solution concentration at the absorber inlet and the concentration at the desorber outlet decreases with the increasing solution concentration due to a reduced amount of the reflux in the rectifier.

Figures 4.4 - 4.6 show concentration ranges (change in concentration from the desorber outlet to the absorber solution inlet and then to the absorber solution outlet) for each data point obtained in the study. Thus, each data point is represented by three symbols, representing the solution concentration at the desorber outlet, the absorber inlet and the absorber outlet, with the symbols being plotted as a function of the concentrated solution flow rate. For the nominal 150 kPa (21.8 psi) case (Figure 4.4), for a given dilute solution concentration, the concentration range decreases slightly with increasing solution flow rate. As the dilute solution concentration increases, the concentration range decreases at any given flow rate. Concentration ranges are small for the 40% and 25% concentration cases, while the ranges are large for the 5% and 15% concentration cases.
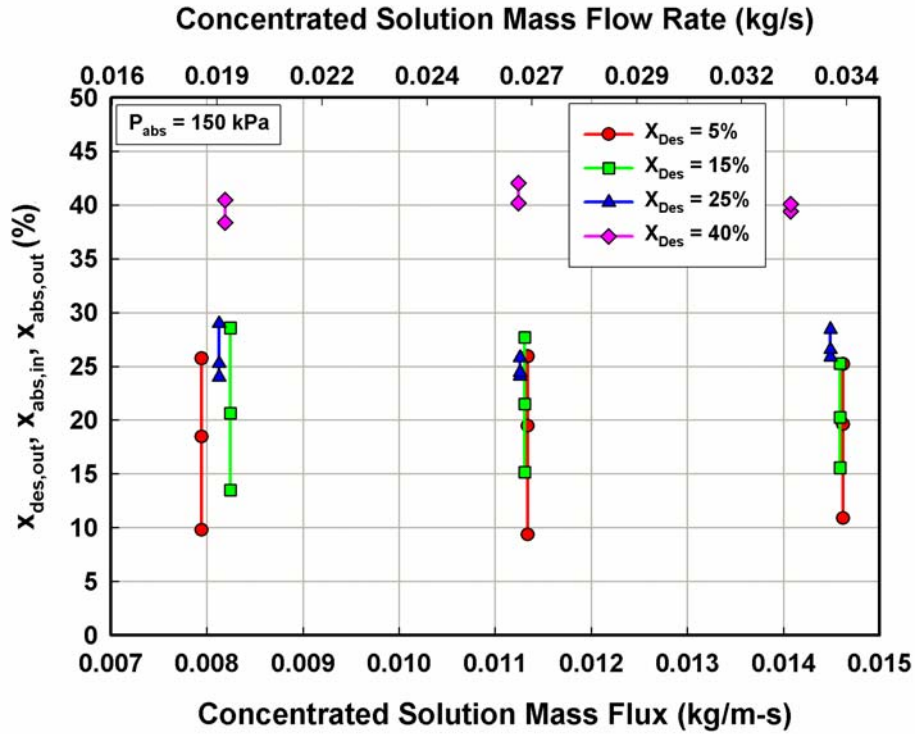
Figure 4.4 Concentration Ranges at Nominal Absorber Pressure of 150 kPa

The smaller concentration ranges at the higher dilute solution concentration cases are primarily due to the lower refrigerant flow rates in these cases. Figure 4.5 shows the variation of the concentration ranges for various dilute solution concentrations at the desorber outlet at a nominal absorber pressure of 345 kPa (50.0 psi). The concentration range shows similar trends as those for the 150 kPa (21.8 psi) cases. However, concentration ranges are larger at this pressure than for the 150 kPa (21.8 psi) nominal cases for 40% and 25% concentration, while the concentration ranges for the 5% and 15% concentration cases are similar to those of the 150 kPa (21.8 psi) nominal cases. Figure 4.6 shows the variation of concentration ranges for various dilute solution concentrations at the desorber outlet at a nominal absorber pressure of 500 kPa (72.5 psi).
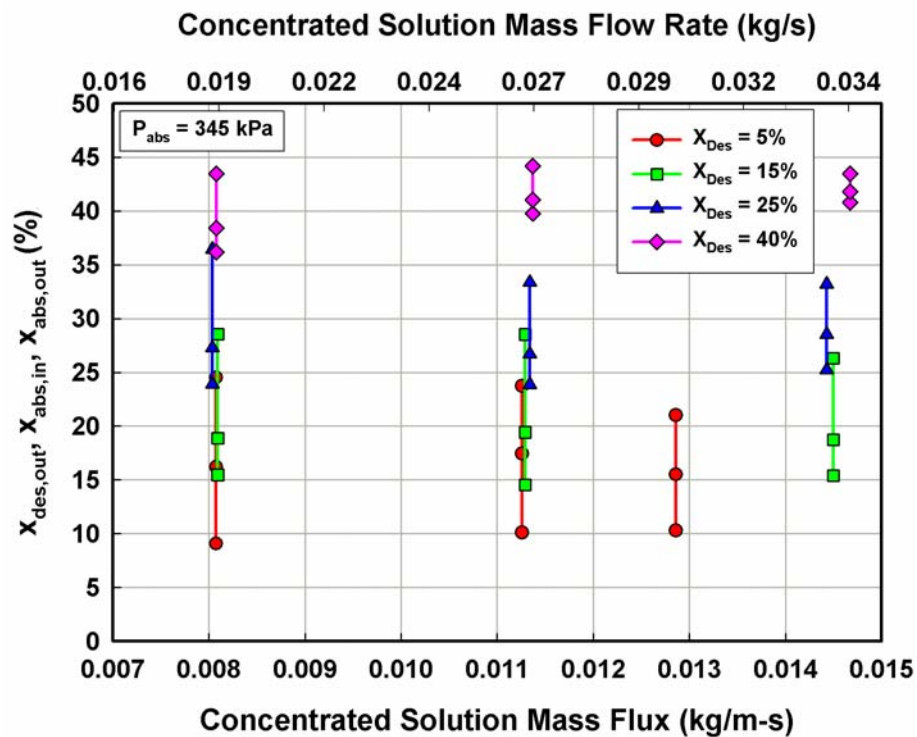
Figure 4.5 Concentration Ranges at Nominal Absorber Pressure of 345 kPa
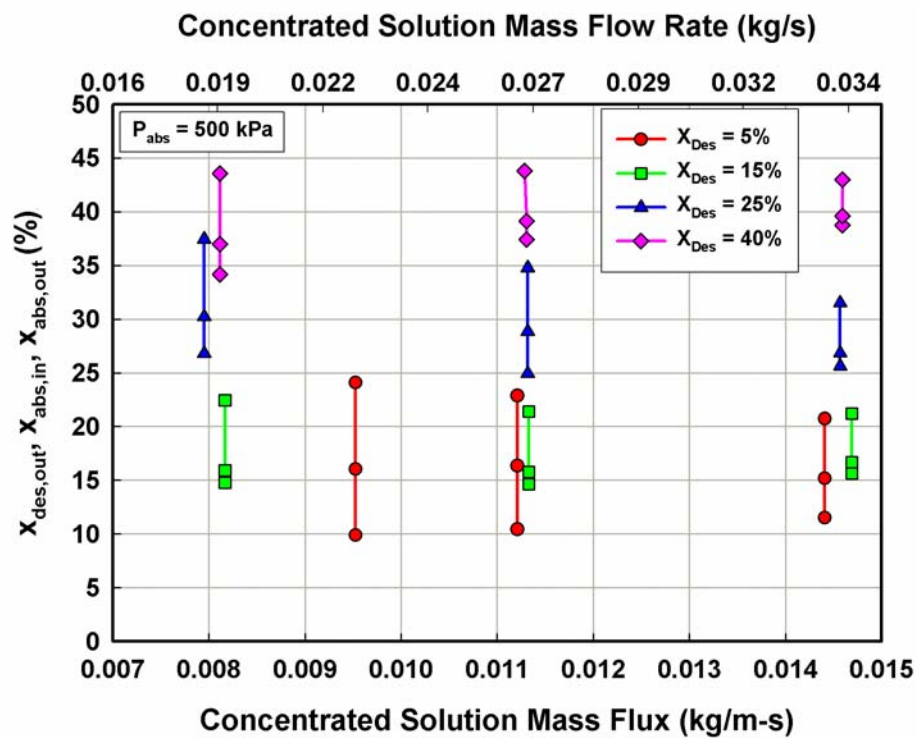
Figure 4.6 Concentration Ranges at Nominal Absorber Pressure of 500 kPa

As with the 150 kPa (21.8 psi) and 345 kPa (50 psi) cases, the concentration ranges decrease slightly as the solution flow rate increases. The concentration ranges for the various flow rates for 40% concentration are much larger than those at 150 and 345 kPa (21.8 and 50.0 psi), while for 5% and 15%, the concentration ranges are smaller than those at 150 and 345 kPa (21.8 and 50.0 psi). The various concentration ranges observed at these conditions can also be taken as an indicator of difficulties in establishing the particular test condition. In general, the more challenging test conditions result in smaller concentration ranges.

4.3 Heat Transfer Calculations

With the concentrations calculated as described above and measured temperatures and pressures at the various locations, the other properties at each location are obtained. The following sections describe the calculation of the heat duties and energy balances at absorber, and the calculation of the measured absorber heat transfer coefficient.

4.3.1 Absorber Heat Duty Calculations

There are three different working fluid streams entering and exiting the absorber: entering dilute solution, exiting concentrated solution and the entering refrigerant vapor (Figure 4.7). Pressures and temperatures are measured at these three locations. All three concentrations are calculated as explained in the previous section. Therefore, these states are fully established and the enthalpies at these three locations can be obtained as follows:

$$h_{Abs,in} = f\left(T_{Abs,in}, P_{Abs,in}, x_{Dilute}\right) \tag{4.23}$$
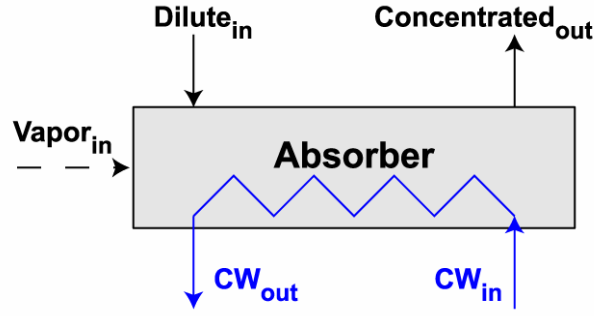
Figure 4.7 Schematic of the Absorber

$$h_{Abs,in} = f(70.42°C, 351.8\,kPa, 0.2671) = 128.9\,kJ/kg \qquad (4.24)$$

$$h_{Abs,out} = f\left(T_{Abs,out}, P_{Abs,out}, x_{Concentrated}\right) \qquad (4.25)$$

$$h_{Abs,out} = f(30.99°C, 350.6\,kPa, 0.3336) = -69.93\,kJ/kg \qquad (4.26)$$

$$h_{Abs,V,in} = f\left(T_{Abs,V,in}, P_{Abs,V,in}, x_V\right) \qquad (4.27)$$

$$h_{Abs,V,in} = f(-0.25°C, 362.8\,kPa, 0.9781) = 1086\,kJ/kg \qquad (4.28)$$

With the three enthalpies known, the solution side absorber heat duty is calculated as follows:

$$Q_{Abs} = \dot{m}_{Dilute} \times h_{Abs,in} + \dot{m}_{Ref,measured} \times h_{Abs,V,in} - \dot{m}_{Concentrated} \times h_{Abs,out} \qquad (4.29)$$

$$\begin{aligned}Q_{Abs} &= 0.02276\,kg/s \times 128.9\,kJ/kg + 0.002826\,kg/s \times 1086\,kJ/kg \\ &\quad - (-0.02651\,kg/s \times 69.93)\,kJ/kg = 7.854\,kW\end{aligned} \qquad (4.30)$$

The coolant-side heat duty is calculated using the absorber coolant flow rate and temperatures at the inlet and outlet:

$$Cp_{Abs,C} = f\left(T_{Abs,C,Ave}\right) \qquad (4.31)$$

$$Cp_{Abs,C} = f(15.61°C) = 4.183\,kJ/kg\text{-}°C \qquad (4.32)$$

$$Q_{Abs,C} = \dot{m}_{Abs,c} \times Cp_{Abs,C} \times (T_{Abs,C,out} - T_{Abs,C,in}) \qquad (4.33)$$

$$Q_{Abs,C} = 0.3028\,\text{kg/s} \times 4.183\,\text{kJ/kg-}°\text{C} \times (18.75°\text{C} - 12.47°\text{C}) = 7.954\,\text{kW} \qquad (4.34)$$

The coolant specific heat is calculated at the average absorber coolant temperature. The average absorber heat duty for the representative case is,

$$Q_{Abs,ave} = \left(\frac{7.854 + 7.954}{2}\right) = 7.904\,\text{kW} \qquad (4.35)$$

The error between two heat duties is,

$$\%\Delta Q_{Abs} = \left(\frac{Q_{Abs,C} - Q_{Abs}}{Q_{Abs,ave}}\right) \times 100 \qquad (4.36)$$

$$\%\Delta Q_{Abs} = \left(\frac{7.954 - 7.854}{7.904}\right) \times 100 = 1.26\% \qquad (4.37)$$

After the absorber heat duty is obtained, the overall heat transfer coefficient is obtained using the log mean temperature difference.

4.3.2 Selection of LMTD

As mentioned above, the solution and the coolant temperatures at the inlet and outlet of the absorber are known from measurements. To estimate an overall heat transfer coefficient in the absorber, a representative temperature difference is required between the solution and coolant streams. Initially, a log mean temperature difference (LMTD) was defined, along the lines of much of the literature, based on the solution saturation temperatures (corresponding to measured solution pressure, concentration and saturated liquid quality) and the measured coolant temperatures. The LMTD based on saturation temperatures represents the idealized driving temperature difference for heat transfer in the absorption process. This LMTD definition is preferable when the solution

101

temperature in the absorber is close to its saturation state. However, it is observed in the present study that the bulk solution is significantly sub-cooled (the degree of sub-cooling varied between -0.4 and 17°C at the absorber inlet, and between 15 and 33°C at the absorber outlet) throughout the absorber. Because the LMTD based on saturation temperatures is considerably higher than an LMTD based on actual temperatures, it may not correctly represent the heat transfer performance of the absorber. Thus, in the present study, the LMTD is defined based on the measured solution and coolant temperatures to calculate the overall heat transfer coefficient in the absorber.

$$LMTD_{Abs} = \frac{\left(T_{Abs,in} - T_{Abs,C,out}\right) - \left(T_{Abs,out} - T_{Abs,C,in}\right)}{\ln\left(\dfrac{T_{Abs,in} - T_{Abs,C,out}}{T_{Abs,out} - T_{Abs,C,in}}\right)} \qquad (4.38)$$

For this representative data point,

$$LMTD_{Abs} = \frac{\left(70.42^\circ C - 18.75^\circ C\right) - \left(30.99^\circ C - 12.47^\circ C\right)}{\ln\left(\dfrac{70.42^\circ C - 18.75^\circ C}{30.99^\circ C - 12.47^\circ C}\right)} = 30.87^\circ C \qquad (4.39)$$

4.3.3 Overall Heat Transfer Coefficient

The average of the solution- and coolant-side absorber heat duties is used as the representative absorber heat duty for the calculation of the overall heat transfer coefficient. The log mean temperature is calculated as discussed above.

$$U_{Abs} = \frac{Q_{Abs,ave}}{A_{Abs} \times LMTD_{Abs}} \qquad (4.40)$$

$$U_{Abs} = \frac{\left(7.854\ kW + 7.954\ kW\right)/2}{0.2098\ m^2 \times 30.87^\circ C} = 1221\ W/m^2\text{-K} \qquad (4.41)$$

102

4.3.4 Coolant Heat Transfer Coefficient

On the coolant side, the coolant flow rate, the inlet and outlet temperatures, and the pressure drop are measured. Also, coolant side geometrical details such as the tube length and the tube flow area are known. For the calculation of the coolant-side heat transfer coefficient, the coolant velocity and Reynolds number are first calculated:

$$V_{Abs,C} = \dot{V} / \left(Tube_{Cross,Area} \times N_{Column} \right) \tag{4.42}$$

$$V_{Abs,C} = \left(3.04 \times 10^{-4} \ m^3/s\right) / \left(5.156 \times 10^{-5} m^2 \times 4\right) = 1.472 \ m/s \tag{4.43}$$

$$Re_{Abs,C} = \frac{\rho_{Abs,C} \times V_{Abs,C} \times Tube_{ID}}{\mu_{Abs,C}} \tag{4.44}$$

$$Re_{Abs,C} = \frac{997.1 \ kg/m^3 \times 1.472 \ m/s \times 8.103 \times 10^{-3} m}{8.9808 \times 10^{-4} \ kg/m\text{-}s} = 13353 \tag{4.45}$$

Here, the absorber coolant density, viscosity, conductivity (0.595 W/m-K), and Prandtl number (6.265) are calculated at the average absorber coolant temperature (15.6°C). The tube-side friction factor and Nusselt number are calculated using Churchill's (1977a; 1977b) equations to yield f = 0.02867 and Nu = 104.3. The coolant-side heat transfer coefficient is obtained from the Nusselt number as follows:

$$\alpha_{Abs,C} = \frac{k_{Abs,C} \times Nu_{Abs,C}}{Tube_{ID}} \tag{4.46}$$

$$\alpha_{Abs,C} = \frac{0.595 \ W/m\text{-}K \times 104.3}{8.103 \times 10^{-3} m} = 7653 \ W/m^2 \text{-}K \tag{4.47}$$

4.3.5 Solution Heat Transfer Coefficient

A thermal resistance network (Figure 4.8) consisting of the coolant-side, tube-wall, and solution-side resistances is used to calculate the solution-side heat transfer

coefficient. The fouling resistance is neglected on both sides of the tube. The coolant-side heat transfer coefficient is calculated as discussed above.
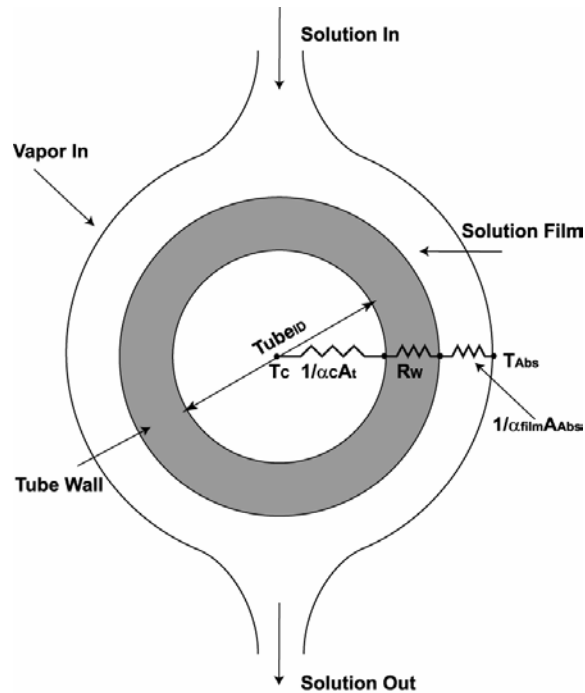
Figure 4.8 Thermal Resistance Network to Calculate $\alpha_{Abs,Film}$

The tube-wall thermal resistance is calculated as follows:

$$R_W = \frac{Tube_{OD}}{2 \times k_W} \ln\left(\frac{Tube_{OD}}{Tube_{ID}}\right) \tag{4.48}$$

$$R_W = \frac{9.525 \times 10^{-3} m}{2 \times 14.64 \, W/m\text{-}K} \ln\left(\frac{9.525 \times 10^{-3} m}{8.103 \times 10^{-3} m}\right) = 5.267 \times 10^{-5} \, m^2\text{-}K/W \tag{4.49}$$

With the coolant-side heat transfer coefficient and tube-wall resistance known, the solution-side heat transfer coefficient is calculated as follows:

104

$$\frac{1}{\alpha_{Abs,Film}} = \frac{1}{U_{Abs}} - \left(R_W + \frac{Tube_{OD}}{\alpha_{Abs,C} \times Tube_{ID}} \right) \qquad (4.50)$$

$$\frac{1}{\alpha_{Abs,Film}} = \frac{1}{1221\,W/m^2\text{-}K} - \left(5.267 \times 10^{-5}\,m^2\text{-}K/W + \frac{9.525 \times 10^{-3}m}{7653\,W/m^2\text{-}K \times 8.103 \times 10^{-3}m} \right)$$

$$\alpha_{Abs,Film} = 1632\,W/m^2\text{-}K$$

$$(4.51)$$

It should be noted that for all the test conditions, attempts were made to ensure that the solution-side heat transfer resistance dominates, which minimizes the errors in the estimation of the solution-side heat transfer coefficient from the measured overall heat transfer coefficient. The heat transfer resistances can be calculated as follows:

$$R_{Abs,film} = \left(\frac{1}{\alpha_{Abs,Film} \times A_{Abs}} \right) \qquad (4.52)$$

$$R_{Abs,C} = \left(\frac{1}{\alpha_{Abs,C} \times A_{Abs,C}} \right) \qquad (4.53)$$

Therefore, the resistance ratio is given by:

$$R_R = \left(\frac{1}{\alpha_{Abs,Film} \times A_{Abs}} \right) \Bigg/ \left(\frac{1}{\alpha_{Abs,C} \times A_{Abs,C}} \right) \qquad (4.54)$$

Or,

$$R_R = \frac{\alpha_{Abs,C} \times Tube_{ID}}{\alpha_{Abs,Film} \times Tube_{OD}} \qquad (4.55)$$

For the representative case,

$$R_R = \frac{7653(W/m^2\text{-}K) \times 8.103 \times 10^{-3}(m)}{1632(W/m^2\text{-}K) \times 9.525 \times 10^{-3}(m)} = 3.99 \qquad (4.56)$$

A resistance ratio of 4 means that the absorption heat transfer for the representative test condition is solution-side dominated, and errors due to the estimation of coolant-side heat

transfer coefficient are minimal. For the range of experiments conducted, the resistance ratio varied between 1.13 and 6.15. The ratio was less than 1.5 for only 6 test conditions (5 and 15% at 500 kPa). Table 4.2 shows the measured values and output parameters at some of the primary components for this representative test condition.

Table 4.2 Measured Parameters for the Representative Data Point (345 kPa, 25% and 0.026 kg/s)

Location	P (kPa)	T (°C)	$\dot{m}$ (kg/s)	Q	x	Output Parameters
Absorber Vapor inlet	363	-0.3	0.0028	0.865	0.978	$Q_{abs} = 7.8$ kW $U = 1221$ W/m^2-K
Absorber Solution inlet	352	70.4	0.0227	-0.001	0.267	$\alpha_{film} = 1632$ W/m^2-K
Absorber Solution Outlet	351	31.0	0.0265	-0.001	0.334	$\beta_V = 0.03$ m/s $\beta_l = 2.13 \times 10^{-5}$ m/s
Desorber inlet	1191	87.4	0.0265	-0.001	0.334	$Q_{des} = 10.5$ kW $x_{dil,des} = 0.239$
Desorber Outlet	1110	122.4	0.0265	0.152	0.330	$x_{V,des} = 0.843$
Separator Solution Outlet	1115	119	0.0211	-0.001	0.239	
Separator Vapor Outlet	1115	119.6	0.0045	0.972	0.843	
Rectifier Vapor Outlet	1127	81.0	0.0028	1	0.978	$Q_{Rec} = 3.3$ kW
Rectifier Reflux Outlet	1121	51.4	0.0017	0	0.618	
Condenser Inlet	1127	57.5	0.0028	0.958	0.978	$Q_{Con} = 3.5$ kW
Condenser Outlet	1133	20.9	0.0028	-0.001	0.978	
Evaporator Inlet	379	-3.8	0.0028	-0.001	0.978	$Q_{Evap} = 3.1$ kW
Evaporator Outlet	351	-1.9	0.0028	0.841	0.978	

4.4 Mass Transfer Calculations

It was mentioned above that the solution inlet and outlet as well as the vapor conditions are known at the absorber. Using an energy balance at the absorber, the overall and the solution heat transfer coefficients were obtained. Since the amount of refrigerant vapor is known along with all the thermodynamic conditions, it is possible to obtain a mass transfer coefficient. The ammonia-water absorption mass transfer analysis is, however, complicated by the fact that the vapor contains both refrigerant (ammonia) and absorbent (water). In addition, both the refrigerant and the absorbent are absorbed by the solution flowing over the tubes. This results in a different concentration of the mass absorbed at the vapor-liquid interface than of the bulk vapor, with no direct way to measure this concentration. Also, the liquid-vapor interface conditions could not be measured directly. Therefore, it is necessary to use some assumptions to determine these unknown conditions. In this section, the details of the calculations to estimate an overall mass transfer coefficient for the entire absorber are presented.

4.4.1 Vapor Condition Change

Refrigerant vapor is produced in the evaporator and flows through the pre-cooler before it enters the absorber. Once the vapor enters the absorber, it occupies the vapor space in the large absorber chamber. It is, therefore, not possible to define a preferred vapor flow direction and velocity. In addition, the solution pool at the absorber bottom provides a large solution surface at a relatively constant temperature. In absence of a vapor velocity and a large space, the vapor can be assumed stationary in the absorber except close to the solution film. Due to this motionlessness, it is assumed that the vapor achieves equilibrium with the solution pool where the solution is usually at the lowest

temperature within the absorber. Therefore, it is assumed that the bulk vapor achieves conditions corresponding to saturation at the minimum temperature in the absorber and the average absorber pressure upon entry into the chamber. It was mentioned in the previous chapter that solution temperatures inside the absorber are measured using thermocouples attached to one tube of each tube row. Using these measurements, a solution temperature profile is generated based on a 3rd order polynomial curve-fit. More details of the solution temperature profile will be discussed in a subsequent chapter on segmental analysis. The minimum temperature in the absorber is the minimum among the absorber outlet, the solution pool and the minimum solution temperature based on the curve fit of the solution-side thermocouple measurements. In a majority of the test cases, the temperature of either the solution pool or at the exit of the tube array is the minimum.

$$T_{min} = f\left(T_{Abs,out}, T_{sol,pool}, T_{min,profile}\right) \tag{4.57}$$

$$T_{min} = f\left(30.99, 29.84, 31.76\right) = 29.84^{\circ}C \tag{4.58}$$

The bulk vapor concentration during absorption is obtained from a vapor saturation state corresponding to the minimum solution temperature, and the average absorber pressure.

$$P_{Abs,ave} = \frac{P_{Abs,in} + P_{Abs,out}}{2} \tag{4.59}$$

$$P_{Abs,ave} = \frac{351.8 + 350.6}{2} = 351.2 \text{ kPa} \tag{4.60}$$

$$x_{V,bulk} = f\left(T_{min}, P_{Abs,ave}, q=1\right) \tag{4.61}$$

$$x_{V,bulk} = f\left(29.84^{\circ}C, 351.2 kPa, q = 1\right) = 0.9965 \tag{4.62}$$

Therefore, the bulk vapor state is fully defined at the minimum temperature, average pressure and the estimated concentration.

4.4.2 Interface Conditions and Heat Regions

The absorption process can be understood as the progression of the bulk vapor to the interface, and finally into the bulk solution. The steps in this progression, represented as heat regions, are discussed here. Figure 4.9 shows the various heat regions in the process of absorption.
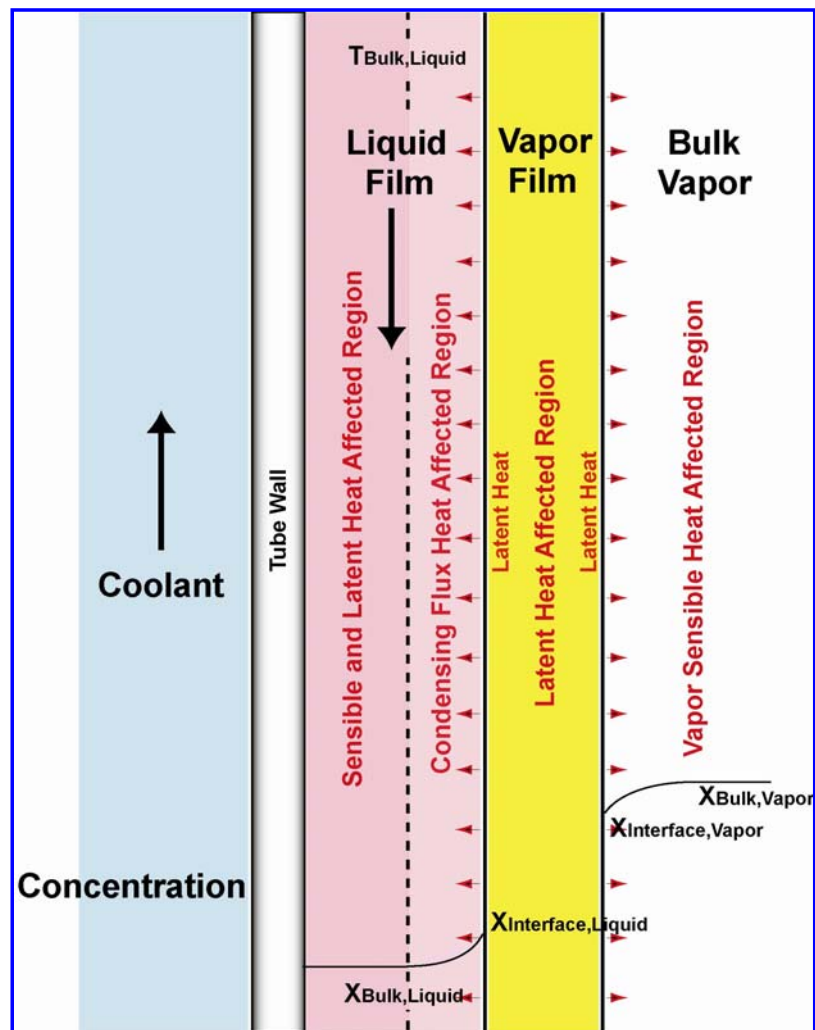
Figure 4.9 Absorption Regions

In this figure, the bulk solution and the bulk vapor conditions are specified from the preceding analysis. However, it is necessary to specify the vapor-liquid interface conditions. The interface during absorption is at different conditions than those of the bulk solution and vapor. The interface conditions have to be inferred from measurements and appropriate assumptions. Here, it is assumed that the interface temperature is the same as the solution bulk temperature. In much of the literature, the interface conditions are assumed to be those corresponding to saturated liquid at the solution bulk concentration. However, most of these studies involve saturated solution, therefore the interface temperature (estimated using the bulk concentration) does not differ significantly from the solution bulk temperature. But in the present experiments, the solution is observed to be considerably sub-cooled. The degree of sub-cooling varies between -0.4 and 17.2°C at the inlet and between 15.1 and 33.0°C at the outlet of the absorber. Assuming the interface liquid concentration to be the same as the solution bulk concentration results in unrealistically high interface temperatures. Therefore, it is more reasonable to assume the interface temperature to be equal to the solution bulk temperature. The average solution temperature and pressure at the inlet and outlet of the absorber are calculated as follows.

$$T_{int} = T_{sol,ave} = \frac{T_{Abs,in} + T_{Abs,out}}{2} \tag{4.63}$$

$$T_{int} = T_{sol,ave} = \frac{70.42 + 30.99}{2} = 50.71^{\circ}C \tag{4.64}$$

$$P_{int} = P_{Abs,ave} = \frac{351.8 + 350.6}{2} = 351.2 \text{ kPa} \tag{4.65}$$

110

Using the average solution temperature and absorber pressure along with saturated qualities, vapor and liquid concentrations at the interface can be estimated.

$$x_{sol,int} = f\left(T_{int}, P_{int}, q = 0\right) \tag{4.66}$$

$$x_{sol,int} = f\left(50.71°C, 351.2, q = 0\right) = 0.3716 \tag{4.67}$$

$$x_{V,int} = f\left(T_{int}, P_{int}, q = 1\right) \tag{4.68}$$

$$x_{V,int} = f\left(50.71°C, 351.2, q = 1\right) = 0.9814 \tag{4.69}$$

All the bulk and interface conditions for Figure 4.9 are now specified. Four distinct regions can be identified here. The region between the vapor bulk and the interface is the vapor sensible cooling or heating region (depending on the interface temperature). In addition, there is a latent heat region at the interface, a region from the interface to the solution bulk representing the condensed vapor sub-cooling region, and finally, the solution sub-cooling region. The heat duties for these various heat regions can be estimated once the various temperatures and concentrations are known. The heat duty for vapor sensible cooling or heating is calculated as follows. The heat duty is defined as positive when heat is transferred from the bulk vapor to the bulk solution.

$$Q_{V,sensible} = \dot{m}_{V,in} \times \left(h_{V,bulk}\left(T_{V,bulk}, P_{Abs,ave}, q = 1\right) - h_{V,int}\left(T_{int}, P_{int}, q = 1\right)\right) \tag{4.70}$$

$$Q_{V,sensible} = 0.002826 \text{kg/s} \times \left(1351 \text{kJ/kg} - 1416 \text{kJ/kg}\right) = -0.185 \text{kW} \tag{4.71}$$

The latent heat duty is calculated as follows:

$$Q_{V,latent} = \dot{m}_{V,in} \times \left(h_{V,int}\left(T_{int}, P_{int}, q = 1\right) - h_{sol,int}\left(T_{int}, P_{int}, q = 0\right)\right) \tag{4.72}$$

$$Q_{V,latent} = 0.002826 \text{kg/s} \times \left(1416 \text{kJ/kg} - 3.489 \text{kJ/kg}\right) = 3.992 \text{kW} \tag{4.73}$$

For the condensed vapor sub-cooling region, the heat duty is,

$$Q_{V,sensible,cond} = \dot{m}_{V,in} \times \left(h_{sol,int}(T_{int}, P_{int}, q=0) - h_{sol,}(T_{sol,bulk}, P_{int}, x = x_{Abs,ave}) \right) \quad (4.74)$$

$$Q_{V,sensible,cond} = 0.002826 \text{kg/s} \times (3.489 \text{ kJ/kg} - 28.73 \text{kJ/kg}) = -0.071 \text{kW} \quad (4.75)$$

Finally, for the solution sub-cooling region, the sub-cooling duty is:

$$Q_{sol,sensible} = Q_{Abs,C} - (Q_{V,sensible} + Q_{V,latent} + Q_{V,sensible,cond}) \quad (4.76)$$

$$Q_{sol,sensible} = 7.954 - (-0.185 + 3.992 - 0.071) = 4.218 \text{kW} \quad (4.77)$$

Here, $Q_{Abs,C}$ is calculated using the flow rate, and the inlet and outlet temperatures of the coolant in the absorber that are known from measurements. By computing the heat duties in the various heat regions, the relative contributions of the different processes to absorption can be estimated. It is found that the heat duties of the phase-change (absorption) at the interface and of the subsequent sub-cooling of the solution are the largest contributors to the overall absorption heat duty (that is removed by the coolant in the absorber). The latent heat duty is used for determining the condensing flux concentration as discussed in the next section.

4.4.3 Condensing Flux Concentration z

It was mentioned above that the concentration of the condensing mass flux is different from the vapor bulk concentration. This concentration is referred to as the concentration of the condensing flux. To calculate this concentration, an energy balance is performed at the interface. It is assumed that the latent heat generated at the interface is due to the phase change of the ammonia and water from the vapor to the liquid phase at the absorber pressure.

$$h_{fg,NH_3} = h_{NH_3}(P_{int}, q=1) - h_{NH_3}(P_{int}, q=0) \quad (4.78)$$

$$h_{fg,NH_3} = 1262 \text{ kJ/kg} - (-24.32 \text{ kJ/kg}) = 1287 \text{ kJ/kg} \tag{4.79}$$

$$h_{fg,H_2O} = h_{H_2O}\left(P_{int}, q = 1\right) - h_{H_2O}\left(P_{int}, q = 0\right) \tag{4.80}$$

$$h_{fg,H_2O} = 2732 \text{kJ/kg} - 585.3 \text{kJ/kg} = 2146 \text{kJ/kg} \tag{4.81}$$

The latent heat of absorption is calculated as follows:

$$\text{Heat}_{V,\text{latent}} = \left(h_{V,int}\left(T_{int}, P_{int}, q = 1\right) - h_{sol,int}\left(T_{int}, P_{int}, q = 0\right)\right) \tag{4.82}$$

$$\text{Heat}_{V,\text{latent}} = \left(1416 \text{ kJ/kg} - 3.489 \text{kJ/kg}\right) = 1412.5 \text{ kJ/kg} \tag{4.83}$$

Using an energy balance at the interface,

$$\text{Heat}_{V,\text{latent}} = z \times h_{fg,NH_3} + (1 - z) \times h_{fg,H_2O} \tag{4.84}$$

$$1412.5 \text{ kJ/kg} = z \times 1287 \text{ kJ/kg} + (1 - z) \times 2146 \text{ kJ/kg} \tag{4.85}$$

$$z = (1412.5 \text{ kJ/kg} - 2146 \text{ kJ/kg})/(1287 \text{ kJ/kg} - 2146 \text{ kJ/kg}) = 0.8534 \tag{4.86}$$

It can be seen from the above calculations that the concentration of the vapor mass absorbed at the interface is different from both the bulk vapor and the vapor concentration at the liquid-vapor interface. This is typical of binary vapors where both the components have the potential to condense (or to be absorbed). Note that water has a higher boiling point than that of ammonia, so as absorption occurs, water will first condense out of the vapor preferentially to ammonia. This is why z (e.g., 0.854 for the representative case) is generally lower than $x_{v,bulk}$ (e.g., 0.996 for the representative case), because the condensing flux is removing water from the vapor phase; hence it contains more water and therefore a lower ammonia concentration. The smaller value of z compared to the interface vapor concentration may also mean that there is accumulation of the vapor at the interface that provides resistance to absorption. This concentration of the condensing flux will be used to calculate the mass transfer coefficient.

4.4.4 Vapor-phase Mass Transfer Coefficient

All the information required to compute a mass transfer coefficient is now known. The Colburn-Drew (Colburn and Drew 1937) method for condensation of binary mixtures is used to calculate the mass transfer coefficient in the absorber where both the components are absorbed or condensed. To implement this method, all mass concentrations are first converted to molar concentrations using following equation.

$$\tilde{x} = \frac{x/M_{NH_3}}{x/M_{NH_3} + (1-x)/M_{H_2O}} \tag{4.87}$$

In this equation, x is a generic concentration. The substitution of bulk or interface concentration will yield the corresponding molar concentration (sample values are shown in Table 4.3).

Table 4.3 Representative Mass and Molar Concentrations

Mass Concentration	Molar Concentration
$z = 0.8534$	$\tilde{z} = 0.8603$
$x_{V,int} = 0.9814$	$\tilde{x}_{V,int} = 0.9824$
$x_{V,bulk} = 0.9965$	$\tilde{x}_{V,bulk} = 0.9967$

The molar flux is calculated next using the amount of vapor absorbed. (Here, a negative sign denotes absorption).

$$\dot{n}_t = \frac{-\dot{m}_V}{A_{MT} \times (\tilde{z} \times M_{NH_3} + (1 - \tilde{z}) \times M_{H_2O})} \tag{4.88}$$

$$\dot{n}_t = \frac{-0.002826\,kg/s}{0.3487\,m^2 \times (0.8603 \times 17.03\,kg/kMol + (1 - 0.8603) \times 18.02\,kg/kMol)} \tag{4.89}$$
$$= -4.721 \times 10^{-4}\,kMol/m^2\text{-s}$$

Where A_{MT} is the total mass transfer area (different from the heat transfer area) including the tube array (0.21 m²), drip tray (0.04 m²), drops at the capillary tubes (0.01 m²) and the solution pool (0.09 m²). The various segments of the absorber are discussed in the subsequent chapter on segmental analysis. It is also necessary to know the total molar concentration in the absorber. This is obtained using the ideal gas law for ammonia vapor at the average absorber pressure and temperature.

$$C_{T,V} = \frac{P_{Abs,ave}}{R \times (T_{min} + 273.15\,K)} \tag{4.90}$$

$$C_{T,V} = \frac{351200\,Pa}{8314\,J/kMol\text{-}K \times (29.84 + 273.15)\,K} = 0.1394\,kMol/m^2\text{-s} \tag{4.91}$$

Finally, the mass transfer coefficient is calculated as follows (It should be noted that the following definition of the mass transfer coefficient includes mass transfer due to molecular diffusion as well as due to bulk convection):

$$\beta_V = \frac{\dot{n}_t}{C_{T,V} \times \ln\left[\dfrac{\tilde{z} - \tilde{x}_{V,int}}{\tilde{z} - \tilde{x}_{V,bulk}}\right]} \tag{4.92}$$

$$\beta_V = \frac{-4.721 \times 10^{-4}\,kMol/m^2\text{-s}}{0.1394\,kMol/m^3 \times \ln\left[\dfrac{0.8603 - 0.9824}{0.8603 - 0.9967}\right]} = 0.030\,m/s \tag{4.93}$$

4.4.5 Liquid-phase Mass Transfer Coefficient

Mass transfer in the liquid-phase is treated primarily as convective mass transfer rather than as diffusive mass transfer as was the case for the vapor phase, since fluid motion in the liquid phase has a more important role. The convective mass transfer in the liquid phase occurs between the bulk liquid solution and the condensing flux that is condensed at the liquid-vapor interface. This convective mass transfer depends on the transport properties and dynamic characteristics of the flowing fluid. The convective mass transfer coefficient can be determined as follows:

$$\dot{n}_A = \beta_l \times \Delta C_A \tag{4.94}$$

where $\dot{n}_A$ is the measured molar mass of species A that is the absorbed into the falling-film, ΔC_A is the difference between the molar concentration at the boundary and the average molar concentration of the bulk fluid stream, and β_l is the convective mass transfer coefficient in the liquid-phase. The relationship between the molar- and mass-based equation is as follows:

$$\rho_A = C_A M_A \tag{4.95}$$

where ρ_A is the mass density of species, and M_A is the molar mass.

The molar-based convective mass transfer equation can be written on a mass basis as follows:

$$\dot{m}_A = \beta_l \times A_{MT} \times \Delta \rho_A \tag{4.96}$$

The mass concentration is defined as follows:

$$x_A = \frac{\rho_A}{\rho} \tag{4.97}$$

where ρ is the total mass density of the mixture.

Therefore, the convective mass transfer equation in the liquid phase, based on the mass concentration, is given as follows:

$$\dot{m}_A = \dot{m}_T \times x_{vap,in} = \beta_L \times A_{MT} \times \left(z_{A,sol,int} \times \rho_{sol,int} - x_{A,sol,bulk} \times \rho_{sol,bulk} \right) \qquad (4.98)$$

$$\beta_l = \frac{0.002826\,kg/s \times 0.9781}{0.3487\,m^2 \left(0.8534 \times 706.2\,kg/m^3 - 0.3 \times 865.8\,kg/m^3\right)} = 2.313 \times 10^{-5}\,m/s \qquad (4.99)$$

From the above equation, a convective mass transfer coefficient in the liquid phase can be obtained.

4.5 Overall Results

Using the approach outlined above, absorber heat duty, and overall and solution heat and mass transfer coefficients were calculated. This section discusses these overall results obtained from the experiments of the present study.

4.5.1 Component Energy Balances

Before accepting a data set, it was ensured that steady state conditions were established, and also that the coolant- and solution-side heat duties are within ±15% of each other at the absorber, condenser and the evaporator. Table 4.4 shows that a significant number of data points (34 out 36) have energy balances within 5% or 10%, with all the data having absorber energy balances within 15% (For 3 data points in the matrix, the condenser and/or evaporator balances are outside this limit.). The average difference between the heat duties on the two sides of the absorber for the whole text matrix is 4.8%.

Table 4.4 Energy Balances for Absorber, Condenser and Evaporator

Component	Number of Data within				Average Absolute Difference (%)
	±(0 - 5)%	±(5 - 10)%	±(10 - 15)%	±(15 - 18)%	
Absorber	20	14	2		4.77
Condenser	12	17	5	2	7.05
Evaporator	12	17	4	3	7.31

4.5.2 Heat Duty and Heat Transfer Coefficient

Table 4.5 shows the range of the absorber heat duty, overall and solution heat transfer coefficient along with the uncertainties in their calculation for the range of the experiments conducted. Appendix B provides additional details on the uncertainty calculations. Additional uncertainties in the vapor-phase properties due to the use of the Kinetic Theory are also explained in Appendix B.

Table 4.5 Observed Uncertainties in the Present Experimental Data

Parameter	Range	Uncertainty Range(Absolute)	Uncertainty Range (%)	Average Uncertainty (%)
Q_{Abs} (kW)	3.26 - 10.75	0.06 - 1.54	1.3 - 20.5	6.18
U_{Abs} (W/m^2-K)	753 - 1853	24.11 - 170.1	2.43 - 15.63	7.95
$\alpha_{Abs.Film}$ (W/m^2-K)	923 - 2857	68 - 431	4.17 - 20.04	11.21
β_V (m/s)	0.0025-0.2541	0.0001 - 0.0171	4.63 – 14.2	7.91
β_l (m/s)	$5.51 \times 10^{-6} - 3.31 \times 10^{-5}$	$7.34 \times 10^{-7} - 4.97 \times 10^{-8}$	0.47–2.92	1.06

In the presentation of the results that follows, the concentrated solution flow rates are shown in terms of the linear mass flux based on the tube length. Thus, the

concentrated solution flow rate is divided by the total length of the four tubes over which

the solution flows, and further divided by a factor of two to account for the fact that the

solution flows around two sides of a tube. This yields a concentrated solution mass flux

$\Gamma = \dot{m} / \left(2 \times L_{tube} \times N_{tube} \right)$. Therefore, a nominal flow rate of 0.019 kg/s (2.5 lb$_m$/min)

corresponds to 0.0081 kg/m-s, 0.026 kg/s (3.5 lb$_m$/min) corresponds to 0.0113 kg/m-s,

and 0.034 kg/s (4.5 lb$_m$/min) corresponds to 0.0146 kg/m-s.
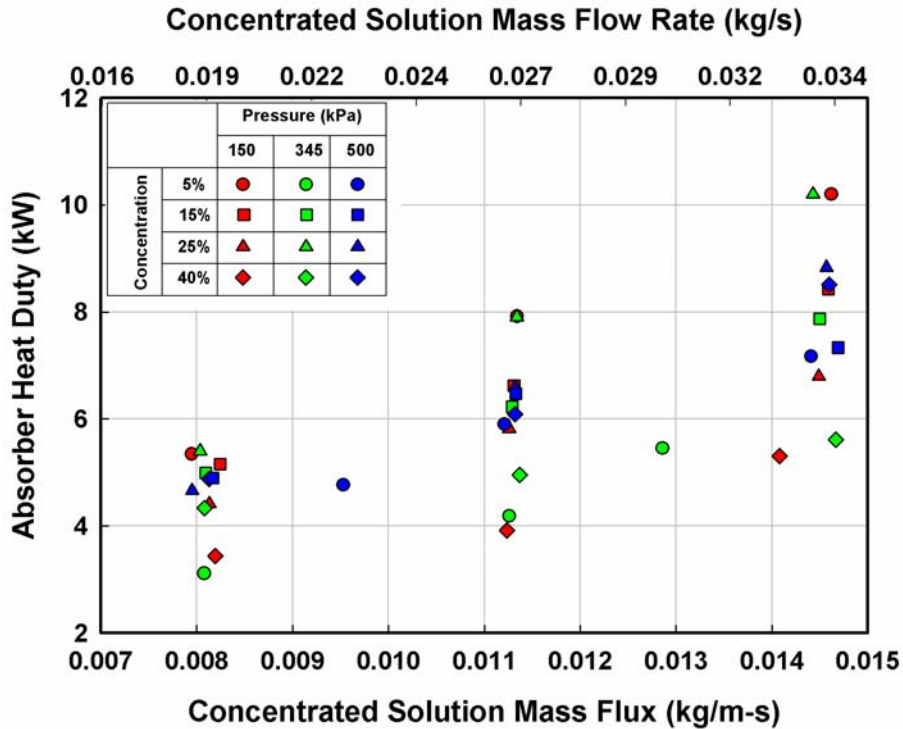
Figure 4.10 Variation of Q$_{Abs}$ with Solution Flow Rate

Figure 4.10 shows the absorber heat duties measured in this study as a function of

concentrated solution flow rate. At any pressure or solution concentration, the absorber

heat duty increases with increasing solution flow rate, ranging from 3.1 to 10.2 kW. No

other significant conclusions should be drawn about absorption heat and mass transfer from the heat duty variations at different operating conditions, because the duty also depends on the coolant flow rates and the log mean temperature difference provided. Figure 4.11 shows the overall heat transfer coefficient U as a function of the concentrated solution flow rate. The U varies from 753 to 1853 W/m^2-K over the entire test matrix depending on the test conditions, in general increasing as the concentrated solution flow rate is increased. The concentrated solution flow rate was found to have the largest impact on the heat duty and the overall heat transfer coefficient. The overall U is a function of tube-side and solution-side phenomena, and therefore, no significant conclusions should be drawn about absorption phenomena from these values also.
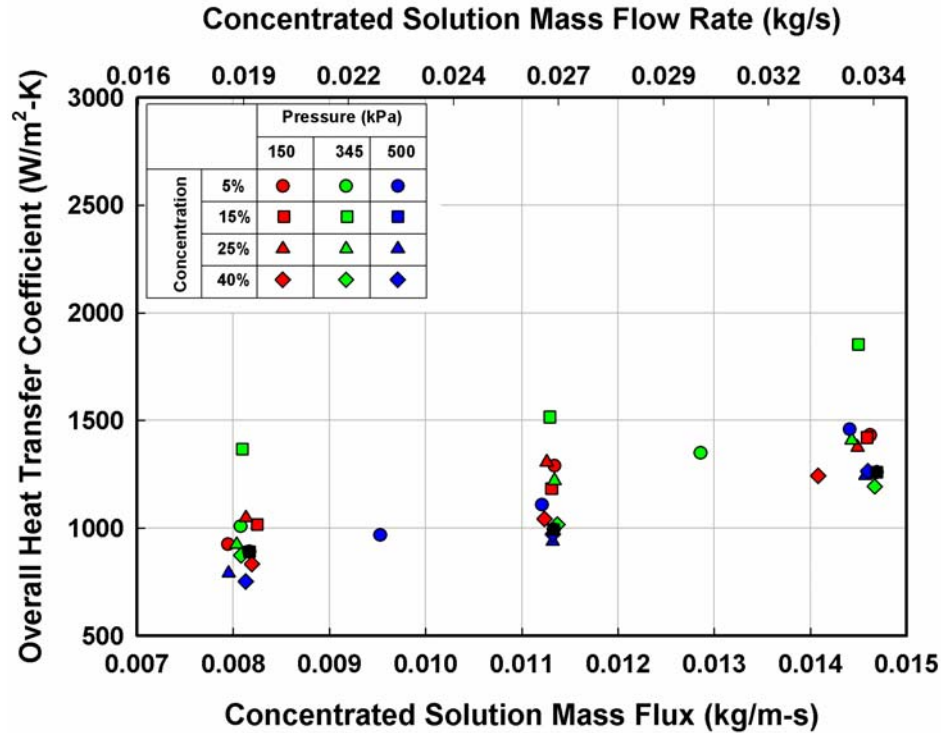
Figure 4.11 Variation of U$_{Abs}$ with Solution Flow Rate

Figure 4.12 shows the solution heat transfer coefficient for all the data points obtained in the present experiments. It should be noted that the solution heat transfer coefficients are based on the entire tube surface area (assuming complete wetting). The solution heat transfer coefficient ranges from 923 to 2857 W/m^2-K, depending on the test condition.
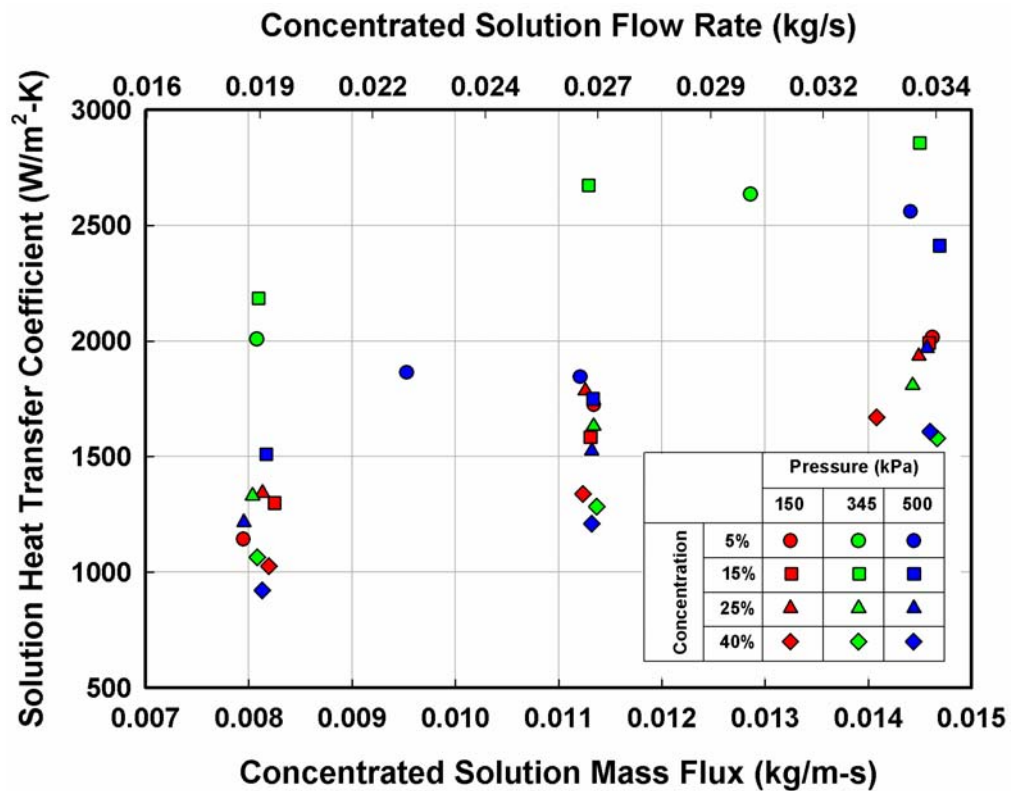
Figure 4.12 Variation of $\alpha_{Abs,Film}$ with Solution Flow Rate

An important aspect can be observed by comparing the graphs in Figures 4.11 and 4.12: the trend in the solution heat transfer coefficient is similar to the trend in the overall *U*. This is due to the large absorber coolant heat transfer coefficients for most of the test conditions. By keeping the coolant heat transfer coefficient high, the solution-

side resistance becomes dominant and the effect of the coolant-side heat transfer coefficient is minimized, which yields low uncertainties in the absorption heat transfer coefficients. For the range of experiments in the present study, the average resistance ratio ($R_R = R_{Abs,film}/R_{Abs,C}$) was 3.34 and it varied between 1.12 and 6.14. As expected, Figure 4.12 shows that the solution heat transfer coefficient increases with the solution flow rate. Although the absorber heat duty and the solution heat transfer coefficient graphs do not clearly indicate specific trends as a function of the absorber pressure and dilute solution concentration, in general, both the absorber heat duty and heat transfer coefficient decreased with an increase in P_{abs} and x_{Dilute} as summarized in Table 4.6.

Table 4.6 Effect of Operating Conditions on Absorber

Parameter	Change	$\alpha_{Abs,Film}$ and $Q_{Abs,ave}$
Concentrated Solution Flow Rate	↑	↑
P_{abs}	↑	↓
Dilute Solution Concentration	↑	↓

4.5.3 Vapor-phase Mass Transfer Coefficient

Figure 4.13 shows the variation of the overall vapor-phase mass transfer coefficient in the absorber with concentrated solution flow rate. For the range of experiments conducted, the mass transfer coefficient varies between 0.0025 m/s and 0.26 m/s. Uncertainties in the vapor-phase mass transfer coefficient varied between 4.6 and

14.2%, depending upon the operating condition (additional discussion of these uncertainties due to the uncertainties in property evaluation appears in Appendix B). The highest mass transfer coefficient is observed for 40% at 345 kPa (50 psi), while the smallest value is observed for 15% at 500 kPa. It is found that higher vapor-phase mass transfer coefficients at any pressure are obtained as the dilute solution concentration increases. In general, the vapor-phase mass transfer coefficient is found to decrease with the increasing pressure. However, except for the 40% concentration cases, the variation in vapor-phase mass transfer coefficient with pressure is very small. In addition, the variation of vapor-phase mass transfer coefficient with solution concentration also decreases as the absorber pressure increases.
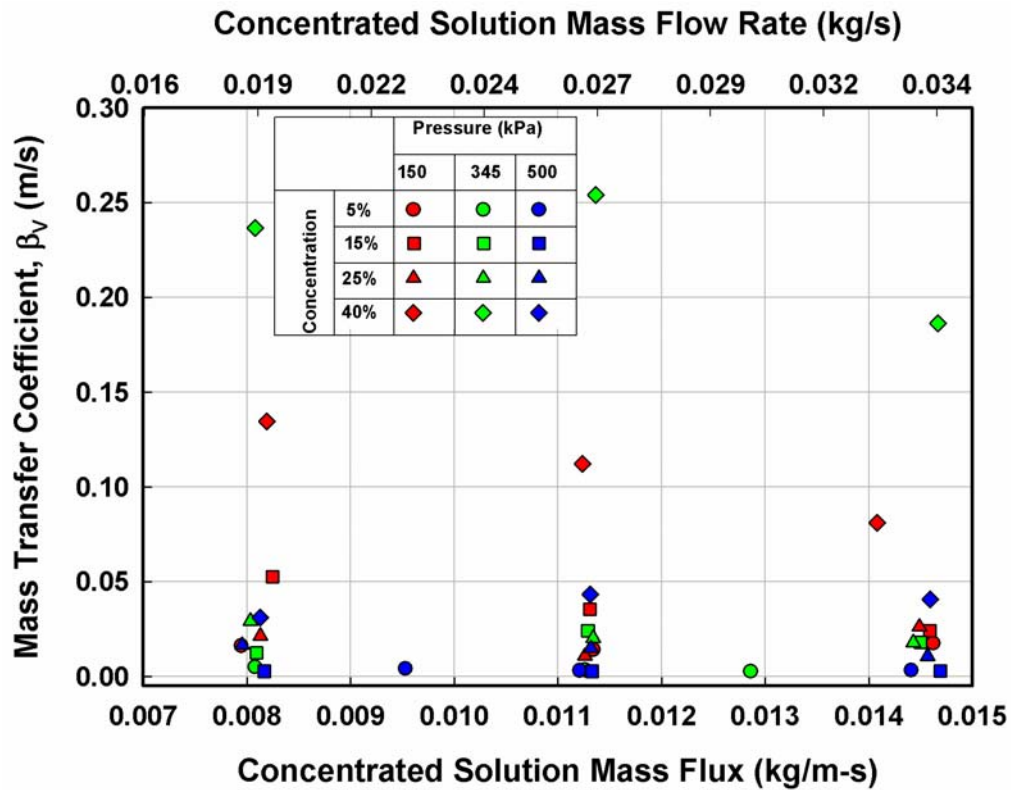
Figure 4.13 Variation of Overall β_V with Solution Flow Rate

It should be noted it was necessary to use different inlet conditions and driving potential differences to achieve these vastly different state points. Differences in coolant flow rates, coolant temperatures, degree of sub-cooling, and refrigerant mass flow rates all contribute simultaneously to these changes in mass transfer coefficient. It is also found that vapor-phase mass transfer coefficient is not very sensitive to the concentrated solution flow rate. This trend is different from that for the heat transfer coefficient, where the heat transfer coefficient increases monotonously with an increase in concentrated solution flow rate. The relative insensitivity of the vapor-phase mass transfer coefficient to the solution flow rate implies that the mass transfer process is governed by the vapor-phase mass transfer resistance. Since in the present study, the vapor phase is essentially a quiescent medium in the absorption chamber, this trend is as expected. The relatively large vapor-phase mass transfer resistance should not be influenced by the liquid-phase solution flow rate.

4.5.4 Liquid-phase Mass Transfer Coefficient

This section discusses the mass transfer coefficients in the liquid phase obtained from the present study. Figure 4.14 shows the variation of the overall mass transfer coefficient in the liquid phase. Effects of pressure and concentration can be seen in this figure; however, the concentrated solution flow rate does not appreciably affect the mass transfer coefficients in the liquid-phase except for the cases with a pressure of 500 kPa and a concentration of 40%. For the conditions investigated, the liquid-phase mass transfer coefficient varies between 5.51×10^{-6} m/s and 3.31×10^{-5} m/s. The highest mass transfer coefficient is observed for 40% at 500 kPa, while the smallest value is observed for 25% at 150 kPa. It is found that the liquid-phase mass transfer coefficient increases

with an increase in concentration at high pressures (e.g., 500 kPa). The lower liquid-phase mass transfer coefficients at the absorber pressure of 150 kPa and dilute solution concentrations of 25% and 40% could be due to the use of a sub-cooler to obtain these conditions. In addition, the 40% cases could only be tested at a pressure of 240 kPa, which is higher than the nominal pressure of 150 kPa.
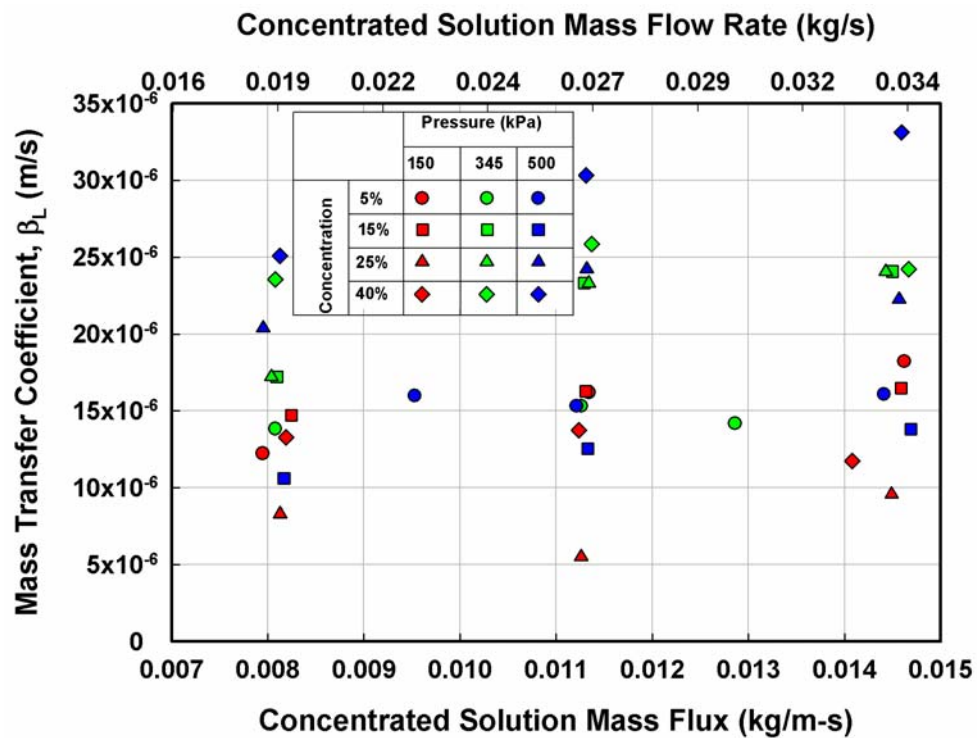
Figure 4.14 Variation of Overall β_l with Solution Flow Rate

Absorber pressure appears to be an important parameter in determining liquid-phase mass transfer coefficient at all concentrations except 5%. From these trends, it appears that the mass transfer process is governed by the transport properties in the liquid phase, since concentration and pressure affect the mass transfer coefficient in the liquid phase more

than the solution flow rate does. Changes in viscosity and binary diffusion coefficient were found to be more prominent than those in the other properties with the variation of concentration and absorber pressure. For example, at an absorber pressure of 345 kPa and a concentrated solution flow rate of 0.026 kg/s, with an increase in concentration from 5% to 40%, the viscosity increases from 3.8×10^{-4} to 9.65×10^{-4} kg/m-s, and the binary diffusion coefficient decreases from 7.34×10^{-9} to 3.54×10^{-9} m^2/s, while the mass transfer coefficient in the liquid phase increases from 1.53×10^{-5} to 2.58×10^{-5} m/s. At a constant dilute solution concentration of 15% and concentrated solution flow rate of 0.034 kg/s, with an increase in absorber pressure from 150 to 500 kPa, the viscosity decreases from 0.826×10^{-3} to 0.344×10^{-3} kg/m-s, while the binary diffusion coefficient increases from 3.98×10^{-9} to 7.86×10^{-9} m^2/s and the mass transfer coefficient in the liquid phase decreases from 1.65×10^{-5} to 1.38×10^{-5} m/s.

4.6 Summary

This chapter presented the methodology to deduce heat and mass transfer coefficients from the measured experimental data in terms of the temperature, pressure and flow rate of the solution and the vapor streams. Heat and mass transfer results at the component level are also presented in this chapter by considering the entire absorber as a single unit. It is found that the heat transfer coefficient increases with the solution flow rate. In general, the heat transfer coefficient is found to decrease with increasing solution concentration at any given pressure and solution flow rate, while the effect of the absorber pressure is not as pronounced as the effect of solution concentration.   In contrast, the mass transfer coefficient is found to be relatively insensitive to the solution flow rate and is found to increase with concentration. It should also be noted that the

varied trends in the transport coefficients are probably due to the different configurations of the test facility used to obtain a very diverse set of operating conditions.

The following chapters will attempt to obtain an understanding of these absorption phenomena on a local level with the aid of flow visualization studies simultaneously conducted at these same test conditions.

CHAPTER 5 FLOW VISUALIZATION

In horizontal-tube falling-film type absorbers, the solution flows on the outside of the tubes. During this flow, the solution may exhibit one of the several flow modes such as uniform sheet, column or droplet between consecutive tubes. As discussed in the literature review of flow regime studies, these modes are well-recognized and found to affect the heat and mass transfer characteristics. However, most of the heat and mass transfer models consider the flow over the tubes as a smooth, laminar sheet, while in reality this is rarely the case as demonstrated by Killion and Garimella (2003) (Figure 5.1). In fact, the droplet mode is the preferred flow mode for such absorbers since it enhances the mixing in the liquid-phase between the successive tube rows, thereby improving the mass transfer. However, it should be kept in mind that the solution always flows as a film on the tube surface. Therefore, the flow over horizontal tubes may consist of the following distinct combinations of modes: in the case of the uniform sheet mode between successive tubes, there will be a film on the tube surface and a sheet (or a film) between tubes; in the case of the column (jet) mode, there will be a film on the tube surface and a column of liquid between tubes; and, in the case of the droplet mode, there will be a solution film on the tube surface, a forming droplet underneath the tube and a free-falling droplet between tubes (although the existence of the free-falling droplet will depend on the tube spacing and the flow rate, as discussed later).

Droplet Formation	Droplet Fall and Impact
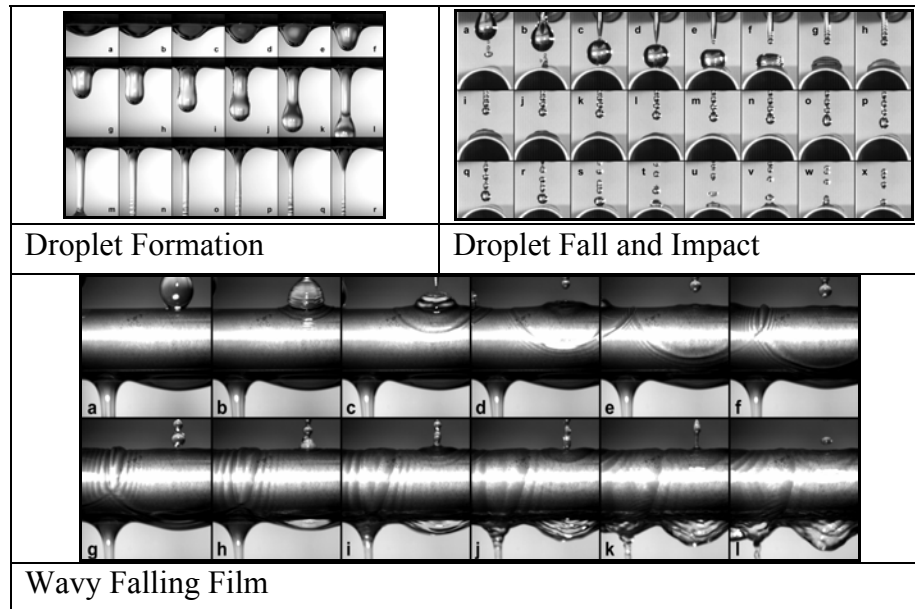
Wavy Falling Film

Figure 5.1 Representative Falling-Film and Droplet Absorption Modes (Killion and Garimella 2003)

The specific flow mode will depend on the solution flow rate, physical properties, geometry and surface properties, and other factors such as surface enhancement or the presence of heat and mass transfer additives. To study the flow characteristics and their effect on the heat and mass transfer in ammonia-water absorption, the flow around the tube bank under consideration was recorded using high-speed video equipment. This recording was conducted for each test condition during the heat and mass transfer tests. This chapter discusses the details of the visualization procedure, the dominant flow modes, and the effects of the operating conditions on the flow characteristics.

5.1 Visualization Set-Up

In the present absorber geometry, dilute solution flows on the outside of the horizontal tubes in an array of 4 columns and 6 rows in an in-line arrangement. This tube array is housed in an outer shell that has a large front port for visualization and a smaller

port aligned with this large port on the back-side for back-illumination. Multiple videos capture an overall view, and also views of specific locations within the absorber. The videos for the entire absorber assist in the understanding of variation in flow mechanisms and the wetting characteristics as the solution flows from the top to the bottom. Videos are also taken at many smaller sections of the visual area focusing on one or two tubes. This will help in understanding the formation, detachment and fall of the droplets as well as the characteristics of the film flow. These cross-sections are shown in Figure 5.2. It should be recalled here that the solution is distributed over the tube array using a drip tray (discussed in Chapter 3). Other measurement and instrumentation details were also discussed in Chapter 3.

Figure 5.3 shows the set-up for visually documenting the flow of the solution in the absorber. High speed and high resolution videos are taken using a digital video camera manufactured by Photron. The Fastcam Ultima 1024 utilizes a CMOS sensor with 1024×1024 pixel resolution that provides clear images, very good resistance to blooming (the glare of bright spots affecting adjacent regions of the image), and electronic shutter speeds of up to 1/128,000 sec, 7.8 microseconds. Images can be captured in full color at frame rates of 512 frames per second. Using zoom and fixed lenses, the desired magnification can be obtained. A full second of video is stored in internal RAM and can be downloaded directly to a PC via FireWire connection as an uncompressed AVI file. A 500 W tungsten/halogen bulb with an illumination temperature of 3200 K was used with a parabolic reflector to provide the high illumination power required for the high frame-rate and shutter speeds used.
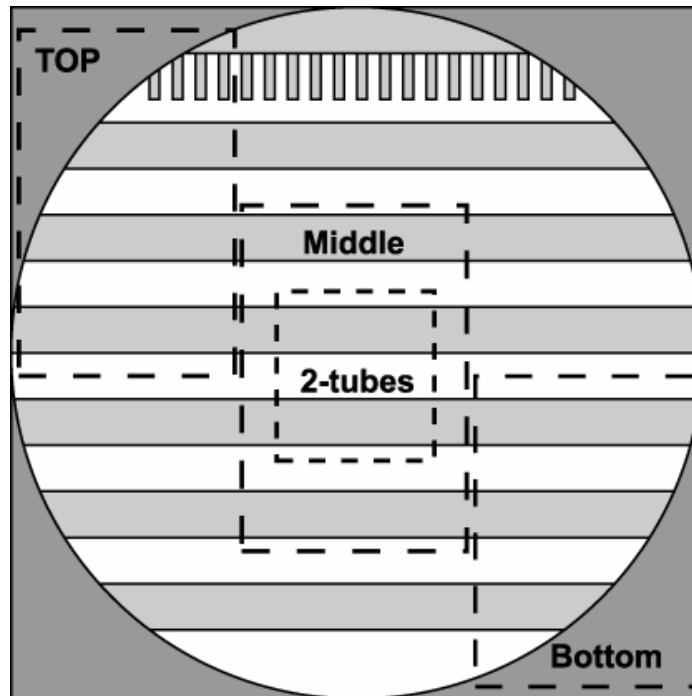
Figure 5.2 Visual Area
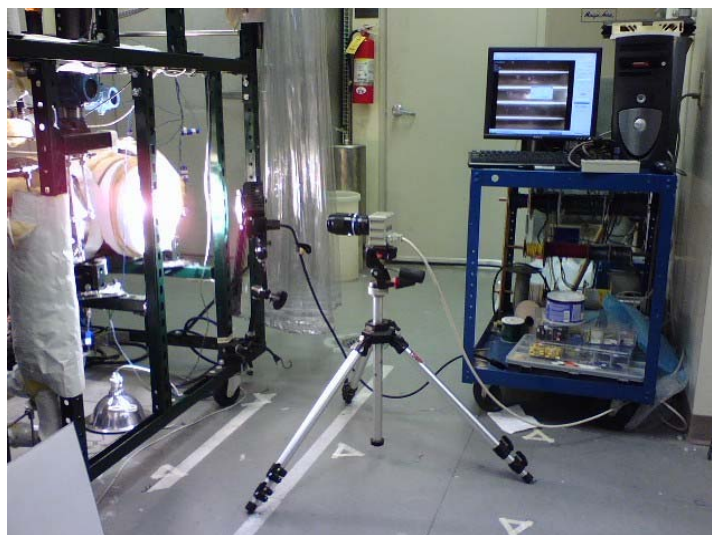
Figure 5.3 Visualization Set-Up

5.2 Visualization Results

Visualization videos are recorded for three different concentrated solution flow rates (0.019, 0.026 and 0.034 kg/s) for three different dilute solution concentrations (15%, 25% and 40%) and three different absorber pressures (150, 345 and 500 kPa). Table 5.1 summarizes the range of experiments conducted and the corresponding variations in the solution properties for these operating conditions. In the presentation of the results, two different flow mode transition criteria from the literature are compared with the observations. The droplet mode was found to be the dominant flow mode for the range of experiments conducted. Therefore, the next section discusses some of the salient features of the droplet flow mode. This is followed by a discussion of the effects of the operating conditions on the flow characteristics.

Table 5.1 Operating Conditions and Solution Properties

Parameter	Value
Operating Conditions	
P_{abs} (kPa)	$158 - 508$
x_{dil} (mass fraction)	$0.15 - 0.38$
$\dot{m}_{conc}$ (kg/s)	$0.019 - 0.034$
$Re = 4\dot{\Gamma}/\mu$	34 - 102
$Ka = \sigma^3 \rho / \mu^4 g$	$7.7 \times 10^9 - 2.23 \times 10^{11}$
Solution Properties	
ρ (kg/m^3)	$850 - 915$
μ (kg/m-s)	$4.1 - 9.1 \times 10^{-4}$
σ (kg/s^2)	$3.27 - 4.32 \times 10^{-2}$

5.2.1 Representative Flow Characteristics

Figure 5.4 shows an overview photograph of the flow around the tube bank for the entire visual area for a representative test condition at an absorber pressure of 345 kPa, dilute solution concentration of 40%, and concentrated solution flow rate of 0.026 kg/s. It can be seen that while the solution flows over tubes as a film, it primarily flows as droplets between successive tubes. At the middle of the figure a liquid-bridge supplying solution to the next tube is also seen. It is also evident from the figure that the entire length of the tubes is not wetted. In addition, progressively reduced wetting is observed along the solution flow path (from the top of the tube array to the bottom, highlighted using ovals in the figure). In the videos, in general, the tubes in the middle columns were seen to have larger solution flow than in the front column. However, it is difficult to observe this clearly in the figure shown here. The following sections discuss the details of these flow patterns at the local level within the absorber.

5.2.2 Dominant Flow Regime

As shown in Table 5.1, the solution Reynolds number (based on the average mass flow rate of the solution) varies between 34 and 102 in the present study. As will be seen in the following figures, the dominant flow mode between the tubes was observed to be the droplet mode. It is also confirmed by the transition criteria of Mitrovic (1986) and Hu and Jacobi (1996a) developed for plain tubes.

According to Mitrovic (1986), the droplet mode exists for

$$Re < 0.34 \times Ka^{1/4} \tag{5.1}$$

where,
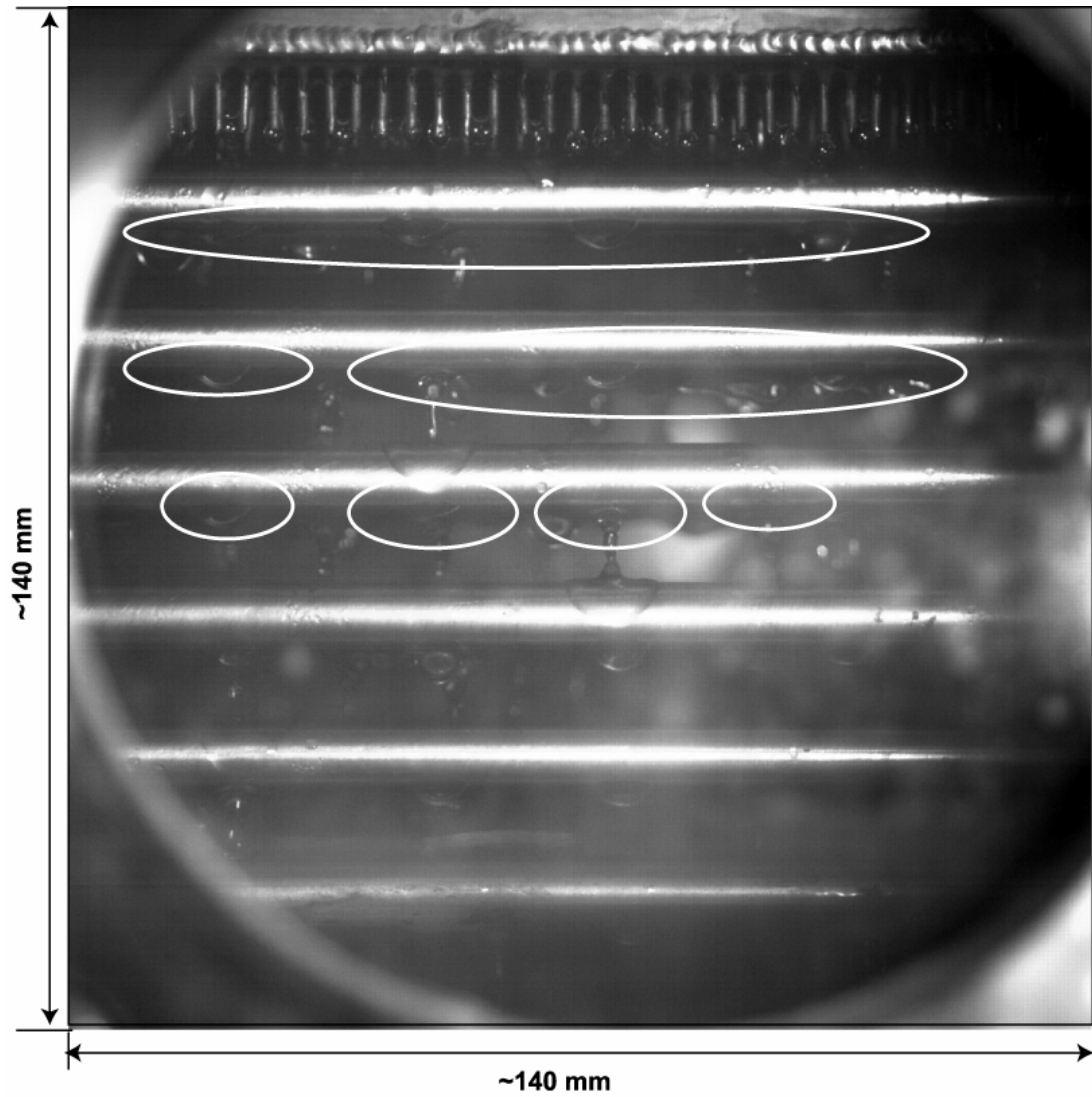
Figure 5.4 Representative Flow Over Horizontal Tube Array

$$Ka = \frac{\sigma^3 \rho}{\mu^4 g} \tag{5.2}$$

Here, all the symbols have their usual meanings. The Kapitza number is the most commonly used parameter to study flow modes during solution flow over horizontal tubes, since it combines the interaction of inertia, gravity and viscous forces.

It should be noted that the Re in the original equation by Mitrovic (1986) is half of the Re values obtained by the definition $Re = 4\dot{\Gamma}/\mu$; therefore, the coefficient 0.17 in his correlation has been replaced by 0.34. The transitional Reynolds number (from droplet to column mode) predicted by equation (5.1) varies from 99 to 234 while the values vary in this study vary between 34 and 102, depending on the specific operating condition. Similarly, Hu and Jacobi (1996a) predict the occurrence of the droplet mode (excluding the hysteresis effects) for

$$Re < 0.037 \times Ga_{mod}^{0.302} \tag{5.3}$$

Here, the definition of the modified Galileo number (Ga_{mod}) is identical to that of the Kapitza number (Ka). Thus, $Ga_{mod} = \sigma^3 \rho / \mu^4 g = Ka$. The original definition of the Galileo number (Ga_{or}) is given by Mitrovic (2005) as follows:

$$Ga_{or} = \frac{g \rho^2 l_{cap}^3}{\mu^2} \tag{5.4}$$

where l_{cap} is the capillary length defined as:

$$l_{cap} = \sqrt{\frac{\sigma}{g\rho}} \tag{5.5}$$

Combining these two equations,

$$Ga_{or} = \left(\frac{\sigma^3 \rho}{\mu^4 g} \right)^{1/2} = Ka^{1/2} \qquad (5.6)$$

While, as stated above, $Ga_{mod} = Ka$ was used by Hu and Jacobi (1996a). Equation (5.3) predicts transitional Reynolds numbers (from droplet to droplet/column mode) between 70 and 198 depending upon the operating conditions. Thus, according to both criteria, all the experiments in this study should yield the droplet mode. (The transitional Reynolds number predicted by Hu and Jacobi (1996a) is slightly smaller than that of Mitrovic (1986).)

While both criteria predict the droplet mode as the dominant mode in the present study, the primary droplet (Figure 5.5) never actually detached from the underside of the upper tube before impacting on the tube below. This is most likely due to smaller tube spacing (comparable to primary droplet diameter ~ 6 mm) used in the present study, which is about 10.6 mm (Figure 5.6). The tube spacing in the study of Killion and Garimella (2003) was 25.4 mm, and up to 50 mm in the study of Hu and Jacobi (1996a). However, the tube spacing was not found to have an appreciable effect on the flow modes for larger (> 15 mm) tube spacing by Hu and Jacobi (1996a), Mitrovic (2005), and Nosoko *et al.* (2002). The influence of smaller tube spacing in the present study is further substantiated by an estimate of the primary droplet diameter ($d_{pr,dp}$), estimated using equation (5.7) (Yung *et al.* 1980), which is found to vary between 5.9 to 6.6 mm for the conditions in the present study.
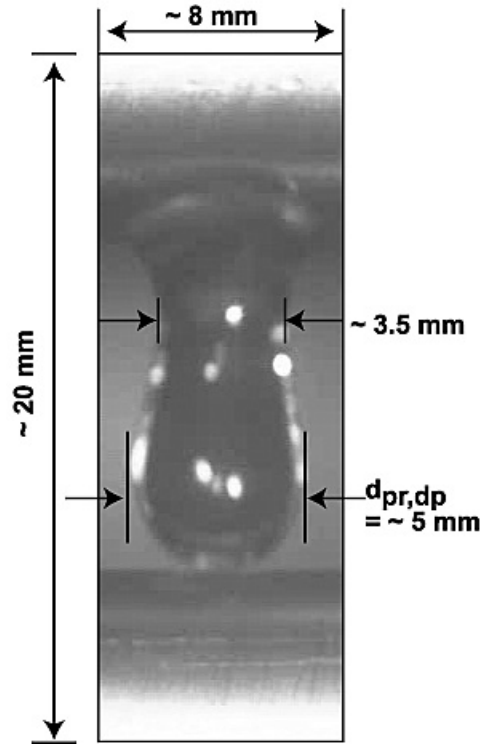
Figure 5.5 Primary Droplet Diameter
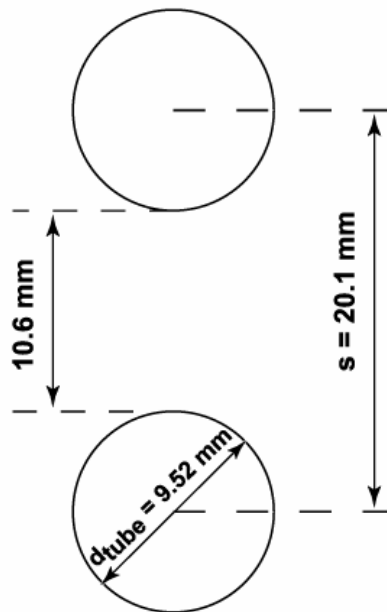
Figure 5.6 Tube Spacing in the Present Study

This is comparable on an order of magnitude basis to the distance between the tubes (10.6 mm).

$$d_{pr,dp} = 3 \times \left(\frac{\sigma}{\rho \times g} \right)^{1/2} \quad\quad\quad (5.7)$$

The estimation of the primary droplet diameter by the equation above is based on the capillary length, and is usually presented as:

$$d_{pr,dp} = C \times \left(\frac{\sigma}{\rho \times g} \right)^{1/2} \qu\ququad\quad (5.8)$$

Where C is a constant determined experimentally. The most common value used for C is 3, as determined by Yung *et al.* (1980). This is based on the fact that the mechanism by which the liquid breaks off from the film is the interplay of gravity and surface tension forces.

The primary droplet diameter varies in a very narrow range because both the surface tension and the density in the present study vary in similar manner as the operating conditions change. For example, as the dilute solution concentration changes from 15 to 40% at a given absorber pressure of 345 kPa, the solution density decreases from 896 to 857 kg/m^3, while the surface tension decreases from 4.17×10^{-2} to 3.32×10^{-2} kg/s^2, which implies that the droplet diameter would change only from 5.96 to 6.53 mm. Tables 5.3 and 5.4 present the variation of several solution properties as the dilute solution concentration and the absorber pressure change. The experimental value of the primary droplet diameter is found to be approximately 5 mm (Figure 5.5) which is in reasonable agreement with the value predicted by equation (5.7), which is 6.2 mm. Since

the primary droplet never detached from the solution bridge, an estimate is taken at the instant just before it touched the tube below.

The primary droplet diameter was estimated using the video frame and edge-detection techniques in Matlab (The Mathworks Inc. 2002). Since the tube spacing (10.6 mm) and tube center-to-center spacing (20.1 mm) are known, the pixel values corresponding to these values can be found from Matlab. The high-speed camera stores images at 1024×1024 pixel resolution and Matlab stores the video frame (a picture) as a square matrix; therefore, only one linear dimension is adequate to find the pixel/mm ratio. Once the pixel/mm ratio is known, other dimensions can be found by first measuring pixels between the points of interest. In Figure 5.5, the dimensions are shown as approximate values; this is due to errors associated with visual edge-detection used with Matlab. However, the uncertainties should not be large because it was possible to track the edge within 1 - 2 pixels, while the pixel/mm ratio was about 22.

Some other parameters that are associated with the droplet mode include the droplet site spacing, film thickness, residence time in the film (on tube surface), the droplet formation time and droplet free-fall time. Droplet formation phenomena are related to Rayleigh instabilities (Killion and Garimella 2003). The difference from classical instability problems, however, is that the liquid is not at rest initially or uniform in velocity in this study. Therefore, there can be several other influences such as initial velocity, disturbances due to vibrations, and impact of droplets on the upper tube surface, which can affect the actual droplet spacing and other parameters. The following equations taken from the literature (Armbruster and Mitrovic 1998; Jeong and Garimella 2002) should only be treated as estimates.

The falling-film thickness and velocity (Figure 5.7) can be obtained from the Nusselt equation (Bird *et al.* 2002). It should also be noted that the solution film thickness is based on the assumption of complete wetting of the tubes.
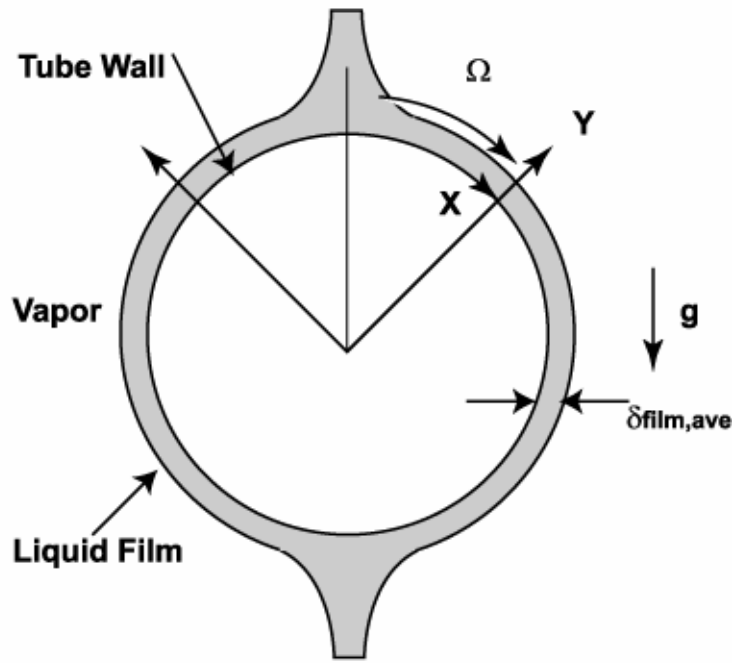
Figure 5.7 Flow around Tube

$$\delta_{film} = \left[\frac{3 \times \mu \times \dot{\Gamma}}{g \times \rho^2 \times \sin\Omega} \right]^{\frac{1}{3}} \tag{5.9}$$

$$\delta_{film,ave} = \left[\frac{3 \times \mu \times \dot{\Gamma}}{g \times \rho^2} \right]^{\frac{1}{3}} \times \frac{2}{\pi} \times \int_{0}^{\frac{\pi}{2}} \sin^{-\frac{1}{3}}\Omega \times d\Omega \tag{5.10}$$

$$u_{film} = \frac{\rho g}{\mu}\left(\delta_{film,ave}\, y - \frac{y^2}{2}\right)\sin\Omega \qquad (5.11)$$

where y is the coordinate along the film thickness from the tube surface. To calculate the residence time in the falling-film regime, the average velocity of the film is calculated first.

$$\overline{u}_{film} = \frac{\displaystyle\int_0^{\delta_{film,ave}} u\, dy}{\delta_{film,ave}} = \frac{\rho g \delta_{film,ave}^2}{3\mu} = \frac{\Gamma}{\delta_{film,ave}\rho} \qquad (5.12)$$

The residence time of the falling-film can be calculated as follows:

$$t_{film} = \int dt = \int_0^\pi \frac{d_{tube}/2}{\overline{u}}\, d\Omega = \left(\frac{\pi \times \delta_{film,ave} \times \rho \times d_{tube}}{2 \times \dot{\Gamma}}\right) \qquad (5.13)$$

The droplet formation time is calculated from continuity as follows:

$$t_{dp,form} = \left(\frac{m_{dp}}{2 \times \dot{\Gamma} \times \lambda_{dp}}\right) \qquad (5.14)$$

Here, $m_{dp} = 4\pi/3\left(d_{pd}/2\right)^3 \times \rho$ is the mass of the primary droplet and λ_{dp} is the droplet spacing (Armbruster and Mitrovic 1998).

$$\lambda_{dp} = 2\pi\sqrt{2}\left/\left(\frac{g\Delta\rho}{\sigma}\times\left(1 + \left(ReKa^{-1/4}\right)^{0.8}\right) + \frac{2}{d_{tube}^2}\right)^{1/2}\right. \qquad (5.15)$$

The droplet fall time is calculated using a simple free-fall equation,

$$t_{dp,fall} = \left(\frac{2 \times s}{g}\right) \qquad (5.16)$$

Here, s is the tube spacing and g is the acceleration due to gravity.

141

For the range of experiments conducted in this study, the falling-film thickness varies between 0.137 and 0.238 mm, resulting in a falling-film residence time of 0.16 to 0.33 s, the droplet formation time varies between 0.22 and 0.51 s, and the droplet spacing varies between 14.6 and 17.1 mm, as estimated using the equations discussed above at the average absorber conditions for each test. The droplet fall time remained constant at 0.064 s because the tube spacing is constant (10.6 mm) for all the tests. Some of these values will be compared with observed values from the videos in the following sections. Figure 5.8 shows these ranges of time spent in various flow regimes in the present study.
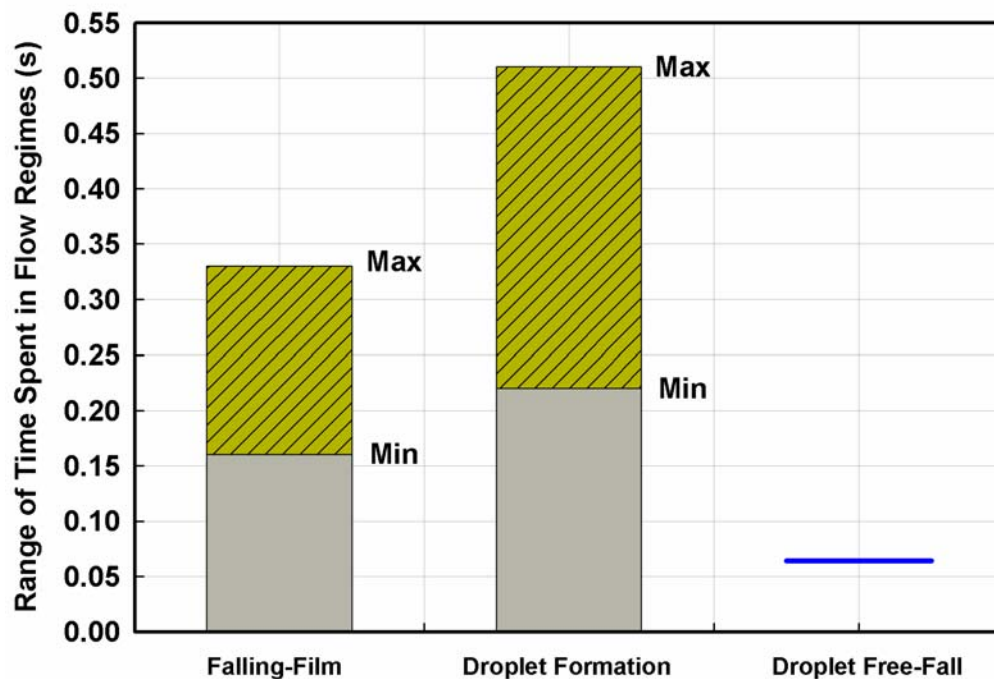
Note: Droplet Free-fall time was constant in the present study.

Figure 5.8 Time Spent in Various Flow Regimes

5.2.3 Falling-Film on Tube Surface

Figure 5.9 shows the sequence of solution flow over the tube surface for a representative case at an absorber pressure of 500 kPa, dilute solution concentration of 25% and concentrated solution flow rate of 0.026 kg/s. Several interesting features of flow over the tube surface can be observed in this figure. The video frames are shown at a constant interval of 10 ms. The following discussion refers to the flow over the bottom tube in each video frame. At 298 ms, the bottom tube starts receiving the solution from the tube above. A droplet is also seen hanging underneath this tube at this instant. As soon as the film starts spreading on the tube surface, a liquid-bridge of irregular shape can be seen (308 ms) between the top and bottom tubes. A moving liquid-bridge of an irregular shape will induce mixing in the film spreading on the tube surface, and also send a disturbance along the bridge length to the tube above. The tube at the bottom keeps receiving the solution while the liquid-bridge above is continuously thinning (318 ms). At this time step (318 ms), the liquid-bridge can be described as two cones attached at their tips and having bases on the two tubes. By 328 ms, the most of the solution has left the liquid-bridge and is on the tube surface. Throughout these time steps, the film flow on the tube surface can be described as a stretched triangle on the tube surface. Similar patterns are reported by Killion and Garimella (2003) for Lithium Bromide/Water flow over tube banks. In some of the frames (308, 318, 348 and 358 ms), the propagating wave on the solution film is outlined in the figure. It can be expected that the stretching film will induce mixing in the solution and will bring fresh surface to the surrounding vapor. The liquid-bridge is seen with a very thin neck just above the bottom tube and is about to break at 328 ms.
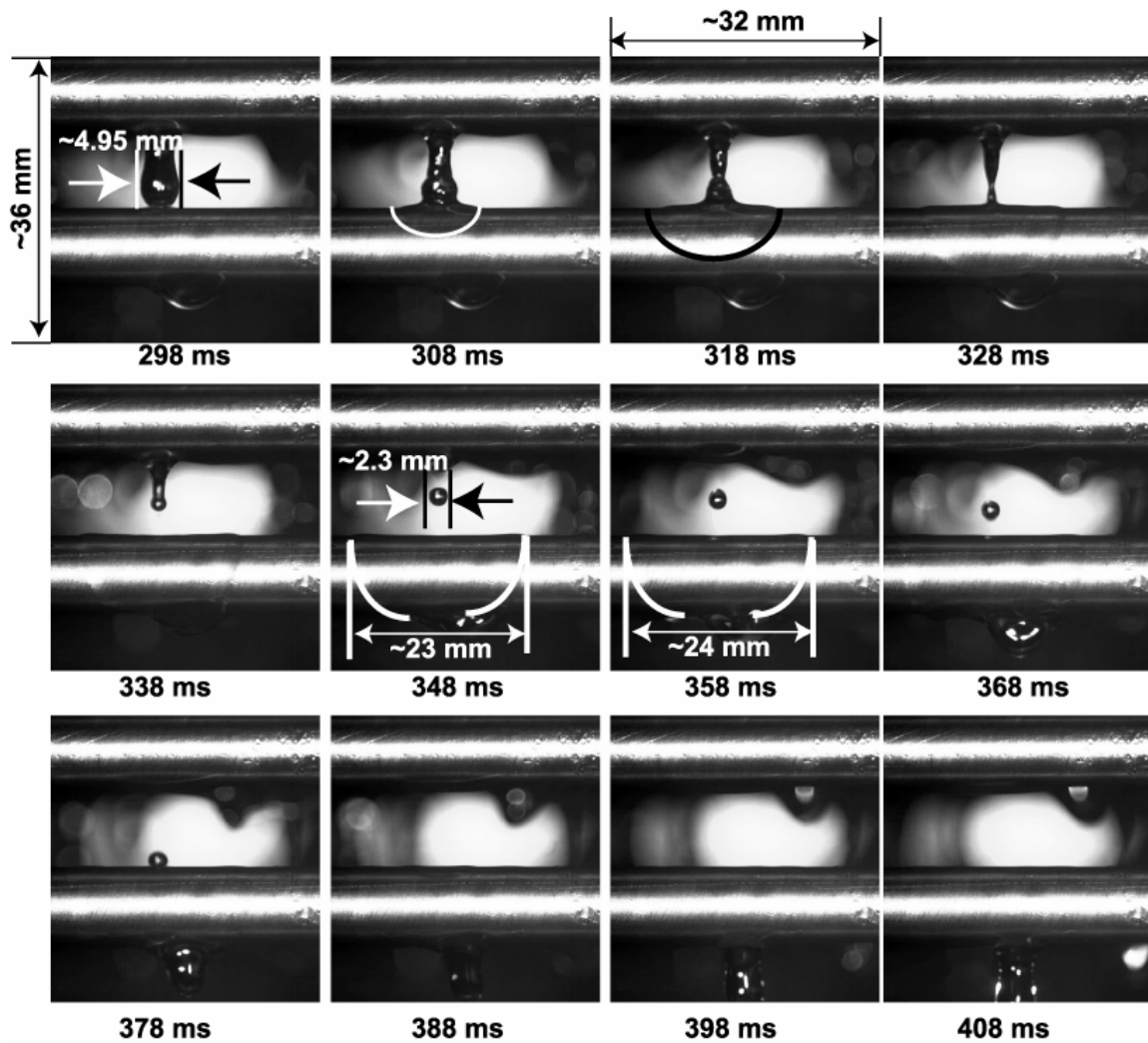
Figure 5.9 Falling-Film Characteristics at P_{abs} of 500 kPa, x_{dil} of 40% and Flow Rate of 0.026 kg/s (Re_l = 71)

It is also seen that the solution on the tube surface is about to start mixing with the droplet hanging below. The liquid-bridge has broken and is recoiling at time step 338 ms, while the solution on the tube is still spreading in width. A further spread in the film is observed from 348 to 358 ms. For this video sequence, the maximum stretch is observed at 358 ms and found to be approximately 24 mm. In these video frames (348 and 358 ms), a satellite drop is also seen. Its diameter is estimated to be approximately 2.3 mm. The maximum width of the liquid-bridge at the beginning of this sequence is about 4.95 mm (298 ms). If this is considered the primary droplet diameter, the satellite droplet diameter is about 45% of the primary droplet. Yung *et al.* (1980) also reported the secondary droplet diameter to vary between 25 and 46% of the primary droplet diameter. It appears that the film on the tube surface stretches a little more in subsequent frames, but is only faintly seen in video frame at 368 ms. At this stage (368 ms), a major portion of the solution is still on the tube surface; however, a significant movement of the solution to the droplet below is also seen. At 378 ms, the satellite droplet impacts on the lower tube. At this instant, a droplet underneath starts developing. Droplet formation and several other characteristics of inter-tube flow are discussed in the next section. The satellite drop mixes with the remaining solution on the tube surface at 388 ms. The last two frames (398 and 408 ms) show the movement of the remaining solution to the tube below. It is assumed that solution no longer remains on the tube surface at 408 ms; therefore, the residence time of film is estimated to be 110 ms (or 0.11 s). For this test condition, equation 5.13 yields a residence time of 0.22 s. Thus, the observed time is only half of the value predicted by the equation from the literature. However, it should be kept in mind that equation 5.13 calculates the residence time of the film on a tube not

susceptible to impact from other droplets at neighboring locations, whereas the behavior in a tube bank with other interactions is likely to lead to a lower residence time on the tube surface.

5.2.4 Inter-Tube Flow

Figure 5.10 shows a sequence of droplet formation, elongation and detachment for a representative case at an absorber pressure of 345 kPa, dilute solution concentration of 25% and solution flow rate of 0.019 kg/s. In this figure, the time, noted on the individual frames, refers to the specific frames after video recording was started. Many of the characteristics are similar to those presented by Killion and Garimella (2003). They documented formation, detachment and fall of the droplets in the flow of water over a vertical column of 12.7 mm OD horizontal tubes with a center-to-center spacing of 38.1 mm. They also discussed waviness of the film surface due to impact and detachment of droplets. Usually, the droplet mode is governed by an interplay of surface tension and gravity forces. As can be seen in the Figure 5.10, the droplet is hanging on the underside of the upper tube at the beginning of the droplet formation phase (168 ms). There are two possible ways in which the droplet grows and eventually detaches. Thus, a droplet can detach when it has grown to a size (either due to absorption or due to axial flow of solution towards the forming drop) where the force due to gravity exceeds surface tension. Alternately, a much accelerated droplet formation occurs if a hanging droplet receives liquid from another droplet impinging on the upper tube.
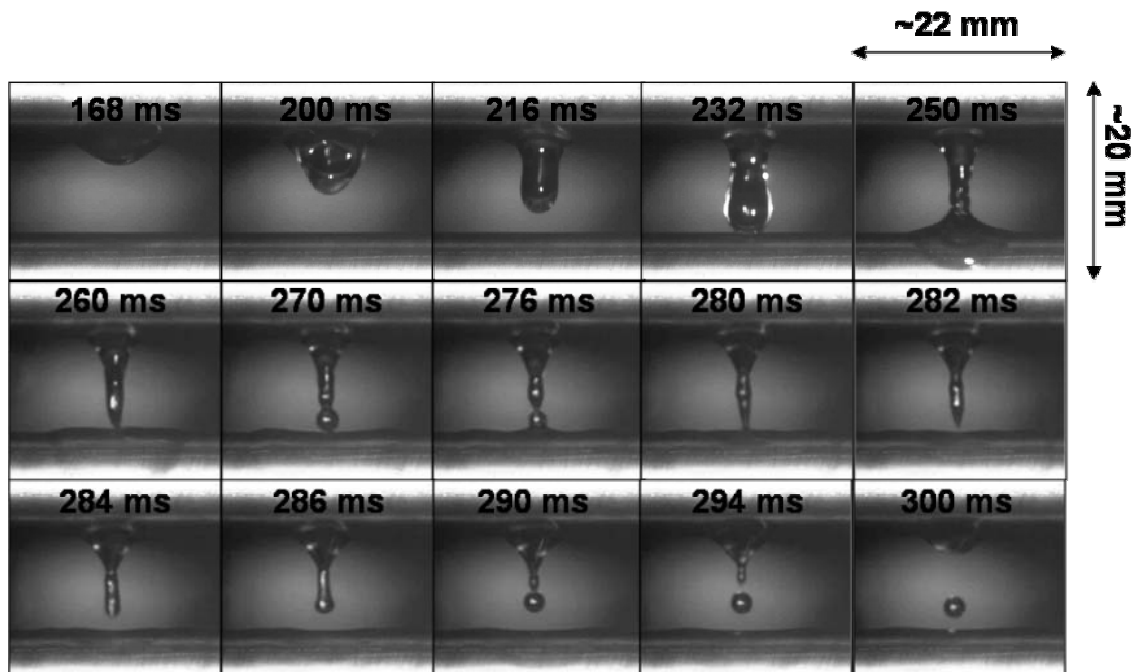
Figure 5.10 Droplet Characteristics (Impacting Droplet) at P_{abs} of 345 kPa, x_{dil} of 25% and Flow Rate of 0.019 kg/s (Re_l = 49) (Note: Frames shown at non-uniform time increments)

Generally, the latter process dominates the droplet mode in such tube banks. The droplet at the underside of the tube starts growing very rapidly as soon as it receives solution from the top (168 – 200 ms). The growing droplet keeps drawing the solution from the droplet formation site decreasing the wetted area in the vicinity of the droplet site (216 ms). At this stage, the droplet shape is almost cylindrical. Once the droplet has grown reasonably in size, the end of droplet starts assuming a spherical shape and necking starts in the solution bridge (232 ms). However, the primary droplet never detaches from this column, and starts touching the next tube, thus forming a liquid bridge between two tubes (250 ms). This is due to the smaller tube spacing in this study as discussed above. This liquid bridge keeps supplying the solution to the tube below and eventually breaks very close to the top of the lower tube (260 ms). However, the liquid bridge does not start

147

recoiling at this stage. At the end of the liquid bridge, a secondary (satellite) droplet starts developing (270 ms). Even this secondary droplet does not fully detach and a continuous solution bridge still exists (276 - 280 ms). The liquid bridge eventually breaks near the lower tube (282 ms) and another secondary droplet begins to develop at the lower end of the hanging column during recoil (284 - 286 ms). During this process, the upper end of the column is almost triangular (276 - 294 ms). The remaining solution bridge recoils very fast and breaks again into smaller droplets. This is also reported by Killion and Garimella (2003). Although many secondary (or satellite) droplets appear to be forming (290 ms), only one or two secondary droplets are actually formed (294, 300 ms). This was true for a majority of the operating conditions in the present study while many studies in the literature have shown several satellite droplets. The absence of many satellite drops could be due to the smaller tube spacing, which prevents formation of a complete droplet and could interfere with the subsequent process of satellite droplet formation. The major secondary droplet diameter was found to be about 2 mm (40%) of the primary droplet diameter. Yung *et al*. (1980) also reported the secondary droplet diameters to be 24 to 46% of the primary droplet diameter. From Figure 5.10, an estimate of droplet formation time can be obtained. The droplet starts growing at 168 ms and keeps growing until 232 ms, when it starts touching the tube below. The total time spent during these time steps (considered as the impacting droplet formation time) is 64 ms (or 0.064 s), which is much shorter than the 0.44 s estimated using equation 5.14. However, this value includes only the time since it starts receiving the solution and not the dormant period that it stays pendant under the tube. The shorter formation time shows the acceleration of the droplet formation regime due to liquid arrival. In fact, the

droplet at this site was found to exist even at 20 ms, so the total time of formation is 212 ms (0.21 s), which closer to the predicted time (0.44 s). Figure 5.11 shows a video frame at 80 ms with the estimated droplet spacing for the same representative case. From this figure, the droplet spacing is found to be approximately 18 mm, while equation 5.15 yields 16.35 mm, which agrees reasonably well with the observed value.

The results for the key parameters in film, droplet formation and fall such as residence time, spacing, droplet sizes and film thickness are summarized in Table 5.2, where the corresponding values predicted by the literature are also shown. Since the droplet never actually detached, and the videos were recorded facing the tube surface, the droplet free-fall time and film thickness could not be obtained experimentally. It appears from these comparisons that the agreement between the observed and estimated values obtained using equations from the literature must be viewed in the context of flow predictions for well controlled flow over a single tube versus flow in a tube bank that is affected by interaction with neighboring tubes and drops. Some of the confounding influences, therefore, are different initial conditions of the flow (a non-zero velocity at the beginning of flow), multiple tube columns as opposed to single-columns typically used in the literature, and errors in defining start and end times for a flow regime in the visual observations conducted here.
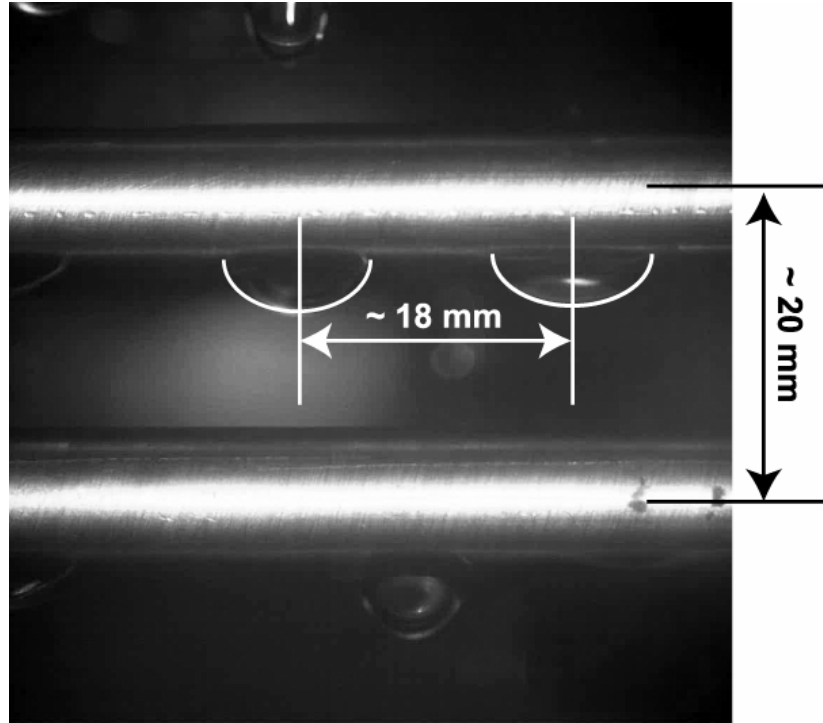
Figure 5.11 Estimation of Droplet Site Spacing (345 kPa, 25%, 0.019 kg/s)

Table 5.2 Comparison of Key Parameters in Flow over Tube Banks (345 kPa, 25%, 0.019 kg/s)

Parameter	Observed Value	Literature Prediction
Droplet Diameter	~ 5 mm	6.2 mm
Droplet Site Spacing (λ_{dp})	~ 18 mm	16.35 mm
Droplet Formation Time ($t_{dp,form}$)	0.21 s	0.44 s
Free-fall Time ($t_{dp,fall}$)	N/A	0.064 s
Film Thickness ($\delta_{film,ave}$)	N/A	0.165 mm
Film Residence Time (t_{film})	~ 0.134 s	0.29 s

5.2.4.1 Axial Movement

Although not shown in Figure 5.10, there were two droplets hanging on the underside of the upper tube, one of which received solution from the top and the other did not. At 300 ms, while the droplet that received solution has gone through the entire sequence of the formation and detachment, the other only increases in size slightly and does not start the detachment process until 506 ms. It can be seen for this droplet as well that the droplet formation time is about 0.34 s (from 168 ms to 506 ms) as opposed to 0.44 s predicted by equation 5.14. This droplet (toward the right at the upper tube) is shown in Figure 5.12. It has grown enough that it starts the detachment process (506 ms). Interestingly, multiple satellite droplets are observed for this droplet (546 ms). When the droplet is formed due to the liquid coming from the top, it is influenced by the momentum carried forward by the impacting droplet. However, a droplet growing primarily by absorption of the vapor and the axial flow of the solution is affected only by the gravity and surface tension effects. Axial movement on the underside of the tubes is also seen in Figure 5.12. Axial movement is illustrated by the increasing distance from the left edge of the video frames. Over a time interval of 40 ms from 506 to 546 ms, the droplet traveled by 2 mm (therefore, with a velocity of 50 mm/s), and over a time interval of 474 ms from 506 ms to 980 ms, it traveled by 6 mm (therefore, with a velocity of 12.5 mm/s). However, these velocities can not be taken as representative of a common or average axial velocity, since not all the test conditions showed axial movement. Also, these axial velocities are expected to vary significantly between the initial and latter stages of droplet formation. Due to the axial movement, a good portion of the tube underside is expected to be completely wetted.
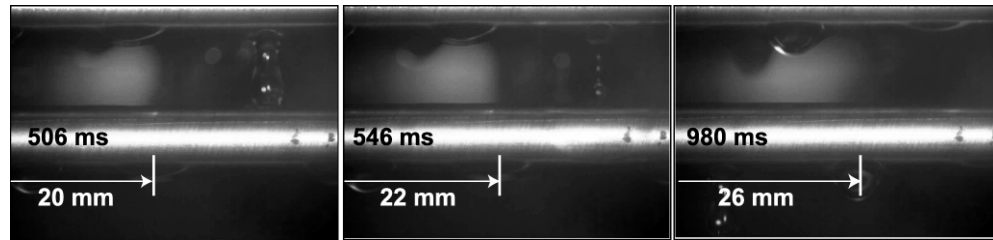
Figure 5.12 Droplet Characteristics (Axial Movement)

5.2.4.2 Droplet Interaction

All the phenomena of droplet formation, liquid bridge elongation, detachment and axial movement enhance the mixing and present fresh surface for the absorption of vapor (Killion and Garimella 2003) and can affect the absorption rates. The axial movement and mixing is further enhanced when two droplet sites are close to each other. As seen in Figure 5.13 for a representative test case of 345 kPa absorber pressure, 25% dilute solution concentration and 0.026 kg/s solution flow rate, two neighboring sites on the upper tube (750 ms) are beginning to merge into each other. The probability of two droplet sites being closer together is higher near the top (Figure 5.14) of the tube array (due to proximity to the drip tray), and at higher flow rates. (The droplet spacing increases towards the bottom of the tube bank due to progressively merging fluid streams at different axial locations.) However, before a new droplet site emerges (Figure 5.12), the solution is drawn in and out of the two sites continuously (770 – 830 ms). Eventually, one droplet site outgrows the other (850 ms), and the droplet elongation and detachment process starts. This interaction also results in mixing which may enhance the absorption rates by presenting a fresh surface to the oncoming vapor (shown by the ovals in Figure 5.14).
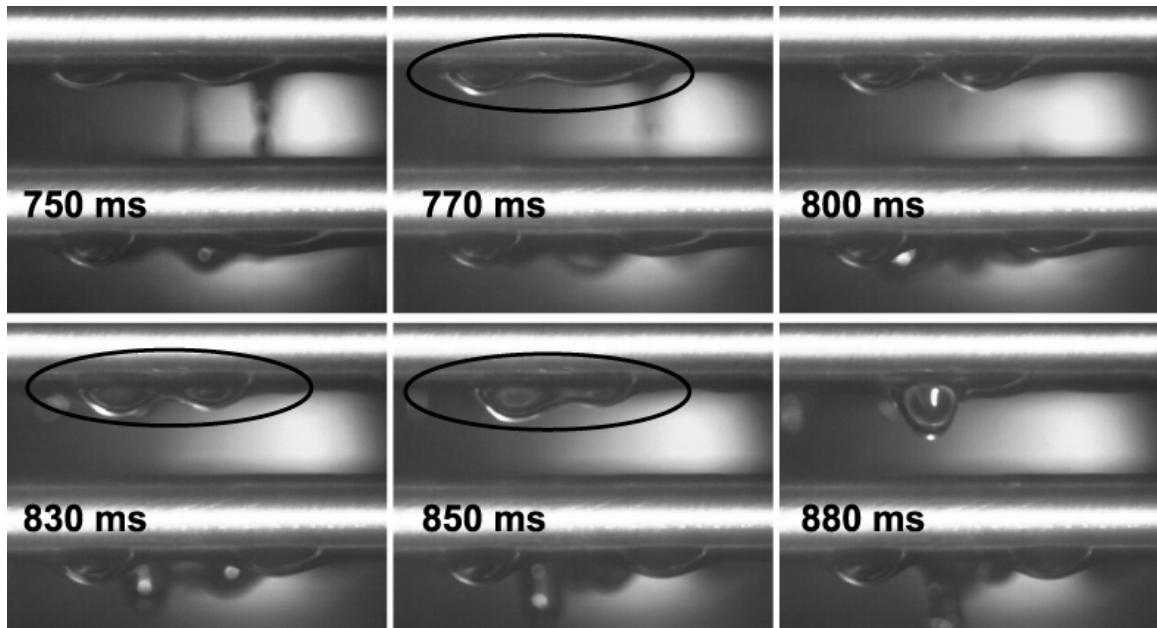
Figure 5.13 Droplet Interaction

Top Segment   Middle Segment
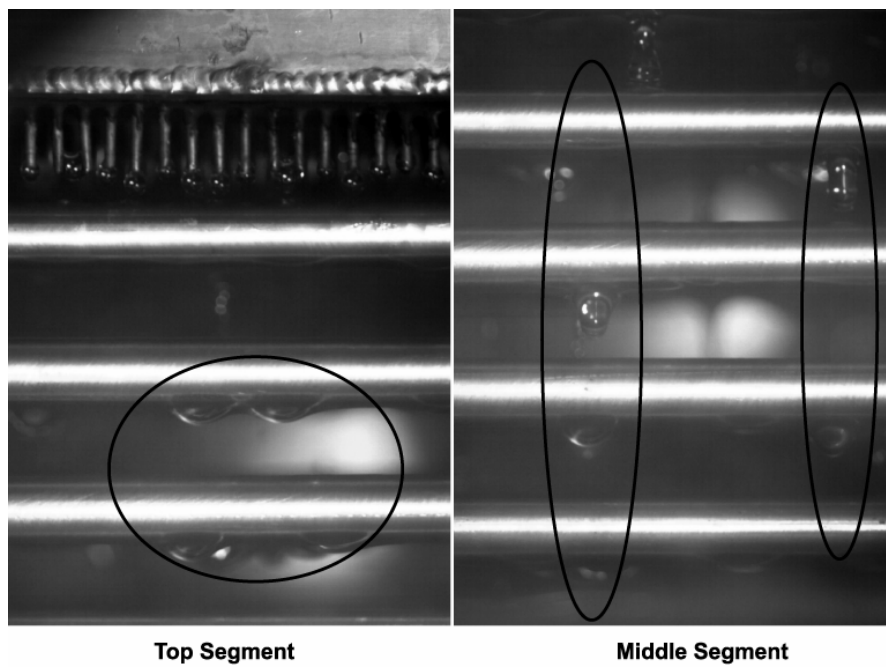
Figure 5.14 Droplet Interaction (Effect of Location)

Droplet interaction is also dependent on the distance between the neighboring sites. If the two sites are far enough apart, as seen on the lower tube in Figure 5.13, they do not merge. The interaction between neighboring sites also affects the formation of newer droplet sites as the solution flows from one tube to the other. It is also possible that as the number of droplet sites increases, the actual mass flux (due to reduced wetting) at the lower tubes is higher when only the wetted portion of the tube surface is considered and results in higher Reynolds numbers at those tubes.

5.2.5 Solution Progression

Figure 5.15 shows the progression of the solution as it flows from the top to the bottom of the tube array. It should be noted that this figure does not show any time because only one camera was used to record the videos at these different locations. This figure combines all the different characteristics of the droplet mode discussed above. While in general the droplet characteristics remain the same, the distance between droplet sites increases (from ~ 20 mm at the top segment to ~ 31 mm at the bottom segment) along the solution flow path (as shown by ovals), resulting in reduced interaction between neighboring sites. Reduced interaction also results in almost inline droplet sites from tube to tube. This also indicates that the droplet sites are predominantly determined by already existing sites in the absence of the droplet interaction. It is also seen that the wetting at the underside of the tubes decreases progressively along the solution flow path (as indicated by the increasing distance between ovals from the top to the bottom of the tube array). It can be seen, therefore, that within a horizontal tube falling-film component, there can be significant differences from one location to another that are governed by the interaction of gravity, surface tension and momentum forces.

154
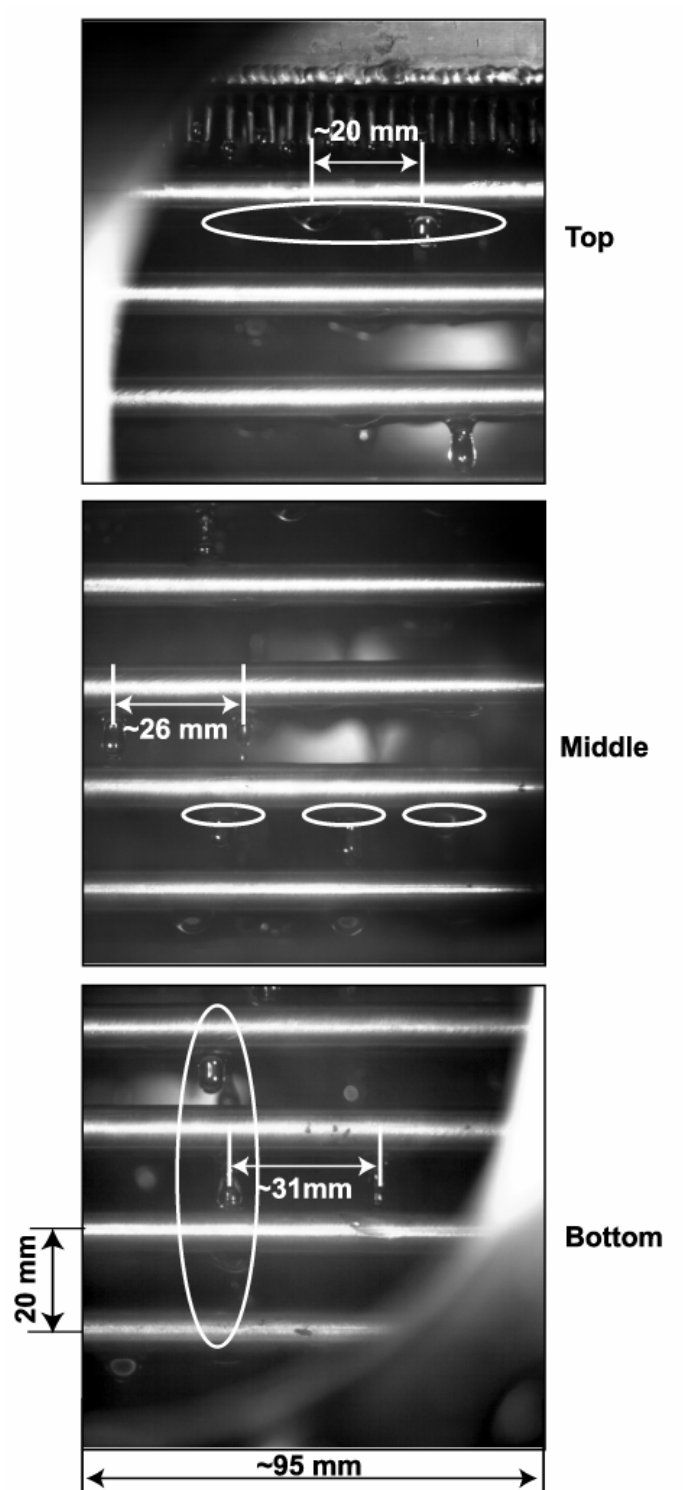
Figure 5.15 Progression of Solution

155

5.2.6 Effect of Solution Flow Rate

Experiments were conducted for three different solution flow rates of 0.019, 0.026 and 0.034 kg/s.   Solution properties remain fairly constant (Table 5.3) for a given absorber pressure and dilute solution concentration.

Table 5.3 Effect of Solution Flow Rate (345 kPa, 25%)

Property	Flow Rate (kg/s)			Effect
	0.019	0.026	0.034	
ρ (kg/m^3)	878.6	878.7	885.8	$\leftrightarrow$
μ (kg/m-s)	6.23×10^{-4}	6.21×10^{-4}	6.46×10^{-4}	$\leftrightarrow$
σ (kg/s^2)	3.72×10^{-2}	3.72×10^{-2}	3.83×10^{-2}	$\leftrightarrow$
Ka	3.05×10^{10}	3.10×10^{10}	2.90×10^{10}	$\leftrightarrow$
Droplet spacing (mm)	16.4	16.0	15.9	$\downarrow$

Figure 5.16 shows the middle visual area for two different solution flow rates (0.019 kg/s and 0.026 kg/s) at an absorber pressure of 345 kPa and dilute solution concentration of 25%. As noted in Section 5.2.2, all the experiments in the present study fall under the droplet mode. The main effect of the increased solution flow rate is found to increase the wetting (shown by ovals in the figure). The improved wetting is also confirmed by reduced droplet spacing (from 16.4 to 16.0 mm as estimated by equation 5.15 and from ~ 61 mm to ~ 26 mm as seen in the video frames) as the solution flow rate increases (from 0.019 kg/s to 0.026 kg/s). Although the droplet spacing at 0.019 kg/s is found to be unusually high, it should not be considered as representative of the entire tube array for this test conditions.
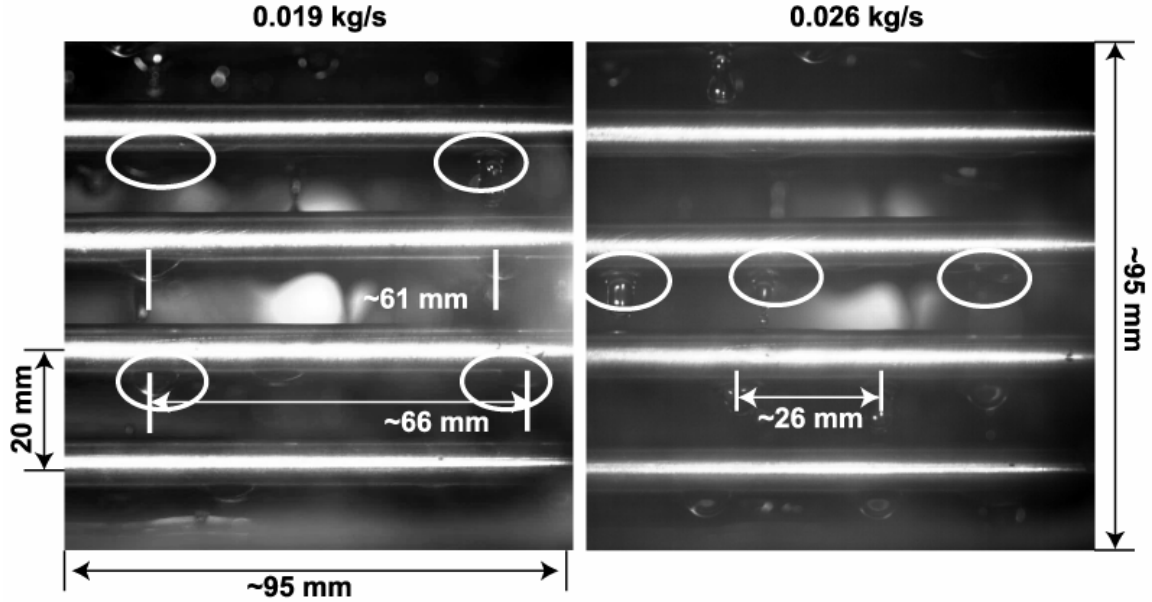
Figure 5.16 Effect of Solution Flow Rate (345 kPa, 25%)

The solution flow is dynamic in nature and its distribution can vary from location to location and over time. Also, both the residence time in the film on the tube surface and the droplet formation time decrease as the solution flow rate increases. For example, according to equation 5.13, the residence time in the falling film reduces from 0.28 to 0.23 s, while from the video, it is found to decrease from 0.144 s to 0.132 s as the solution flow rate increased from 0.019 to 0.026 kg/s for the representative case. Similarly, the droplet formation time as predicted from equation (5.14) reduces from 0.45 to 0.33 s, while it is found to decrease from 0.224 s (including self-growth, before it receives solution from the impacting droplet on the tube above) to 0.162 s in the video.

5.2.7 Effect of Solution Concentration

The nominal dilute solution concentration varied from 15% to 40% in the visualization tests. Table 5.4 shows the variation of solution properties at an absorber pressure of 345 kPa and a solution flow rate of 0.026 kg/s.

Table 5.4 Effect of Solution Concentration (345 kPa, 0.026 kg/s)

Property	Dilute Solution Concentration (%)			Effect
	15	25	40	
ρ (kg/m^3)	895.8	878.7	857.1	↓
μ (kg/m-s)	4.15×10^{-4}	6.21×10^{-4}	8.01×10^{-4}	↑
σ (kg/s^2)	4.17×10^{-2}	3.72×10^{-2}	3.32×10^{-2}	↓
Ka	2.23×10^{11}	3.10×10^{10}	7.77×10^{9}	↓
Re_{trans} (DP-Column) (Mitrovic 1986)	117	71	55	↓
Re_{exp}	51	35	27	↓
Film Thickness (mm)	0.159	0.185	0.205	↑
Droplet Spacing (mm)	16.9	16.0	15.3	↓
Residence Time (s)	0.202	0.227	0.245	↑
α_{Film} (W/m^2-K)	2460	1830	1491	↓

It can be seen that the solution concentration affects the viscosity the most, which increases from 4.15×10^{-4} to 8.01×10^{-4} kg/m-s as the concentration increases from 15 to 40%. Both the density (changes from 896 to 857 kg/m^3) and the surface tension (changes from 0.042 to 0.032 kg/s^2) decrease slightly with the concentration. As a result of this, the Kapitza (Ka) number decreases from 2.23×10^{11} to 7.77×10^{9} as the concentration increases from 15 to 40%. This, in turn, results in a smaller transitional Reynolds number (decreases from 117 to 55 as the concentration changes from 15 to 40%) for transition

from the droplet to the column mode. In other words, the column mode can be obtained at smaller solution Reynolds numbers as the solution concentration increases (due to reduced transitional Re) or the droplet mode can be sustained for larger Reynolds numbers as the solution concentration decreases (due to increased transitional Re). However, the experimental Reynolds number also decreases for a given a flow rate and a given absorber pressure as the solution concentration increases (due to increased viscosity). For example, the solution Reynolds number decreases from 51 to 27 as the concentration increases from 15 to 40% at the absorber pressure of 345 kPa and solution flow rate of 0.026 kg/s (Table 5.4). This means that the actual flow rate (in kg/s) required for transition to the column mode from the droplet mode will not differ significantly at different concentrations while keeping the absorber pressure constant.

It was found that the residence time in the falling-film increases as the concentration increases. Figure 5.17 shows the effect of solution concentration using two video frames of middle section at an absorber pressure of 345 kPa and concentrated solution flow rate of 0.026 kg/s as the dilute solution concentration changes from 25% to 40%. For the representative test condition at 345 kPa and 0.026 kg/s, the residence time increases from 0.132 to 0.144 s based on an analysis of the video frames. One implication of this can be that with a higher residence time, it may be easier to remove the heat of absorption since the solution remains in contact with the coolant for a longer time. The droplet spacing also decreases slightly (e.g., from ~ 26 mm to ~ 25 mm as seen in Figure 5.17) as the concentration increases from 25% to 40%, resulting in increased wetting (shown by ovals).
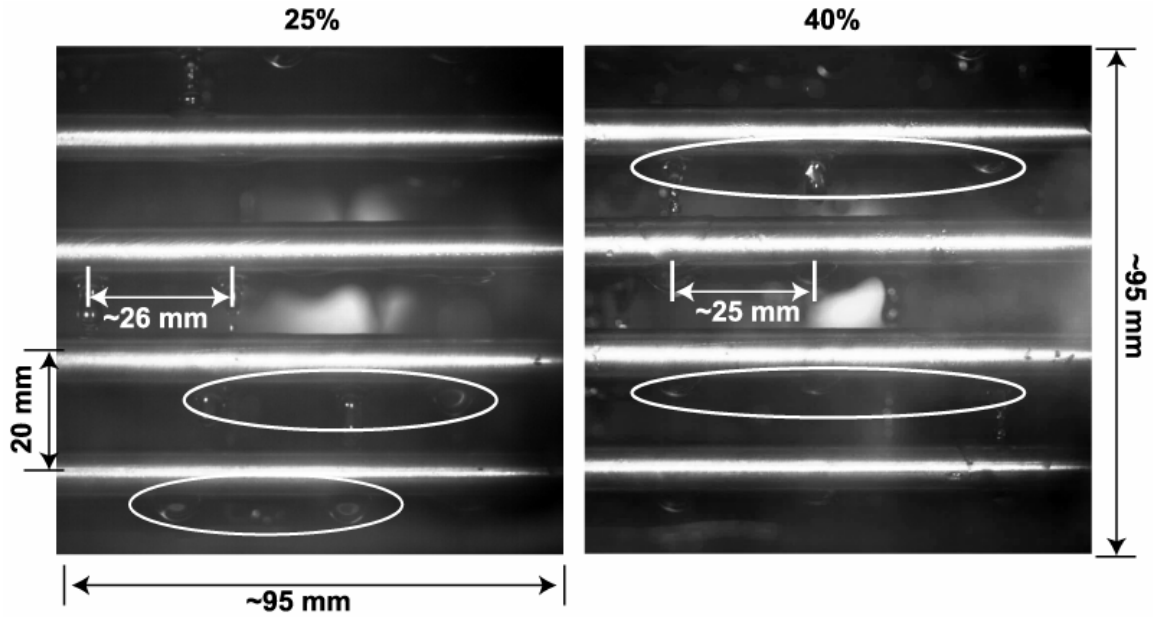
Figure 5.17 Effect of Solution Concentration (345 kPa, 0.026 kg/s)

The solution film thickness should increase (e.g., from 0.159 to 0.205 mm, as estimated using equation 5.10) with increasing concentration. A thicker solution film will, in general, present greater resistance to the heat transfer; however, there can be other effects such as increased turbulence and waviness as the film grows thicker. It can be seen that the film thickness varies in an opposite manner to the droplet spacing and the residence time. Therefore, it may be possible that these two factors partially counter each other's effects on heat and mass transfer. However, both the film thickness (decreases with the solution concentration) and Reynolds number (increase with solution concentration) vary in a manner (thinner film and higher Reynolds number) that enhances the absorption characteristics (at least the heat transfer) at lower concentrations for a given pressure and solution flow rate.

The combined effect of these parameters can also be seen in the observed trends in the heat transfer coefficient (Figure 5.18) where the solution heat transfer coefficient, in general, is found to decrease with the solution concentration (due to a decrease in solution Re for a given flow rate and absorber pressure).
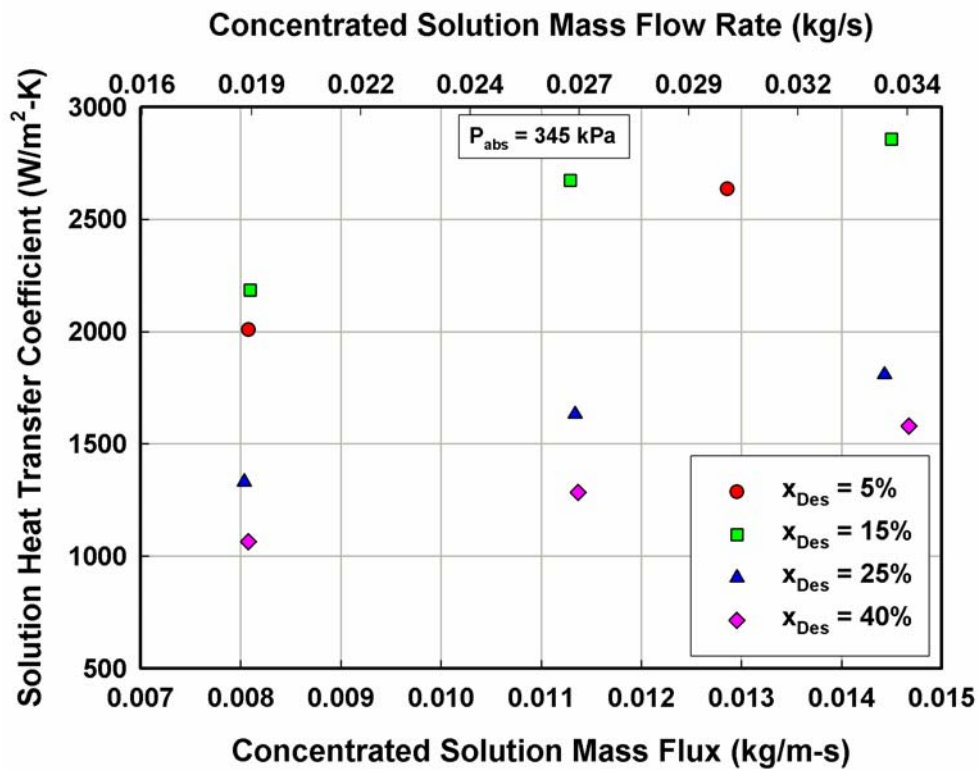
Figure 5.18 Effect of Solution Concentration on $\alpha_{Abs,Film}$ (345 kPa)

5.2.8 Effect of Absorber Pressure

Table 5.5 shows the change in solution properties as the absorber pressure changes from 150 to 500 kPa at a dilute solution concentration of 25% and concentrated

solution flow rate of 0.026 kg/s. As opposed to the effect of the increasing concentration, the density (changes from 898 to 872 kg/m^2), the surface tension (changes from 0.040 to 0.037 kg/s^2) and the viscosity (changes from 7.56×10^{-4} to 4.32×10^{-4} kg/m-s), all decrease with increasing absorber pressure. The net result is an increased solution Kapitza number (from 1.70×10^{10} to 4.32×10^{11}). Therefore, the Reynolds number for transition from droplet to column mode also increases from 69 to 102 with absorber pressure.

Table 5.5 Effect of Absorber Pressure (25%, 0.026 kg/s)

Property	Absorber Pressure (kPa)			Effect
	150	345	500	
ρ (kg/m^3)	898.6	878.7	872.3	↓
μ (kg/m-s)	7.56×10^{-4}	6.21×10^{-4}	4.32×10^{-4}	↓
σ (kg/s^2)	3.97×10^{-2}	3.72×10^{-2}	3.67×10^{-2}	↓
Ka	1.70×10^{10}	3.10×10^{10}	1.27×10^{11}	↑
Re_{trans} (DP-Column) (Mitrovic 1986)	69	71	102	↑
Re_{exp}	29.1	35	50	↑
Film Thickness (mm)	0.196	0.185	0.165	↓
Droplet Spacing (mm)	16.4	16.0	15.9	↓
Residence Time (s)	0.241	0.227	0.199	↓
α_{Film} (W/m^2-K)	1884	1830	1925	↔

Figure 5.19 shows the effect of the absorber pressure using two video frames for two different absorber pressures of 150 and 345 kPa at a dilute solution concentration of

25% and flow rate of 0.026 kg/s. While both the residence time in the falling-film (changes from 0.158 to 0.134 s) and the droplet formation time (changes from 0.206 to 0.184 s, estimated using equation 5.10) are found to decrease with the increasing absorber pressure, the solution film thickness (changes from 0.196 to 0.165 mm, estimated using equation 5.10) also decreases as the absorber pressure increases. The droplet spacing is also found to decrease (from 28 to 26 mm, Figure 5.19) with increasing pressure; however, the variation is small.
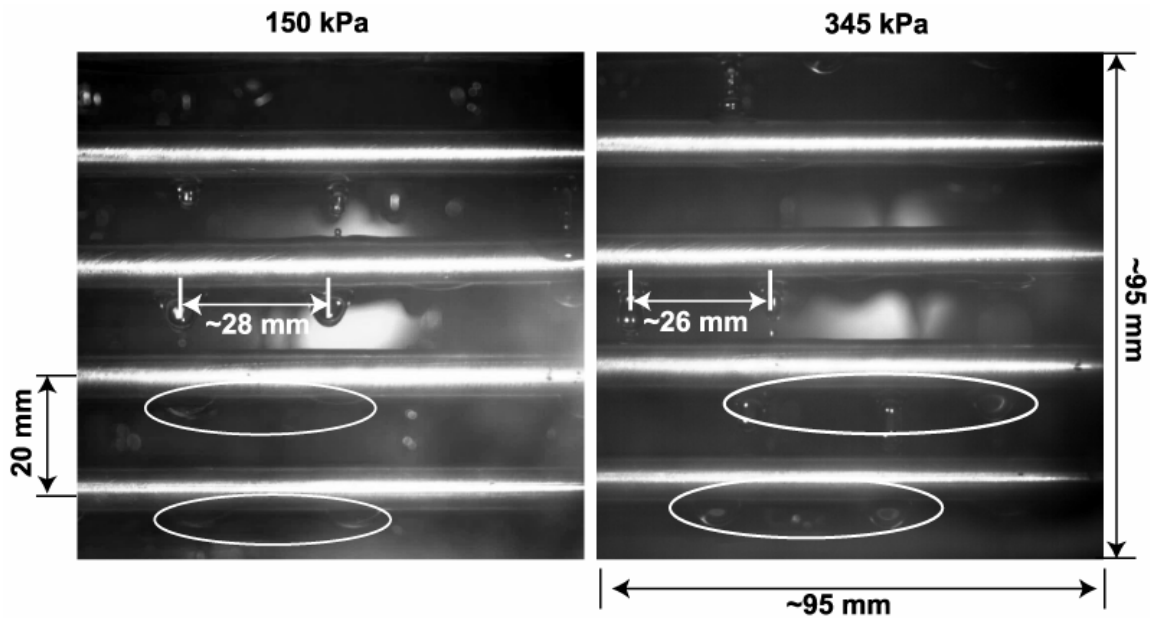
Figure 5.19 Effect of Absorber Pressure (25%, 0.026 kg/s)

It can be seen that as far as the determination of the flow mode is concerned, solution concentration and absorber pressure seem to influence the flow modes in opposite manner (via their influence on Re, i.e., transitional Re decreases with increasing

163

concentration (Table 5.4) while it increases with increasing pressure (Table 5.5)). The relative importance of film thickness, droplet spacing and residence time becomes more important when the effects of the pressure and the concentration are taken into consideration together. For example, at low absorber pressure and high concentration conditions, the effect of both the higher concentration and the lower pressure is to increase the residence time and the film thickness. For example, the residence time increases from 0.2 to 0.24 s (calculated using equation 5.13) when the dilute solution concentration changes from 15 to 40% at an absorber pressure of 345 kPa, or when the absorber pressure changes from 500 to 150 kPa at a dilute solution concentration of 25%. Similarly, the film thickness increases from 0.159 to 0.205 mm (calculated using equation 5.10) when the dilute solution concentration changes from 15 to 40% at the absorber pressure of 345 kPa, and it increases from 0.165 to 0.196 mm when the absorber pressure changes from 500 to 150 kPa at a dilute solution concentration of 25%. The effect of the absorber pressure on the solution heat transfer coefficient (Figure 5.20) at a given concentration is, however, not as significant as the effect of the concentration.

5.3 Summary

An analysis of the videos demonstrated many interesting details of the flow patterns in horizontal-tube falling-film absorbers over a wide range of operating conditions during actual operation of an ammonia-water heat pump. In the visualization experiments, the droplet mode is found to be the dominant mode. It is found that the droplet formation and detachment is strongly affected by the solution arriving from the tube above (as an impacting droplet).
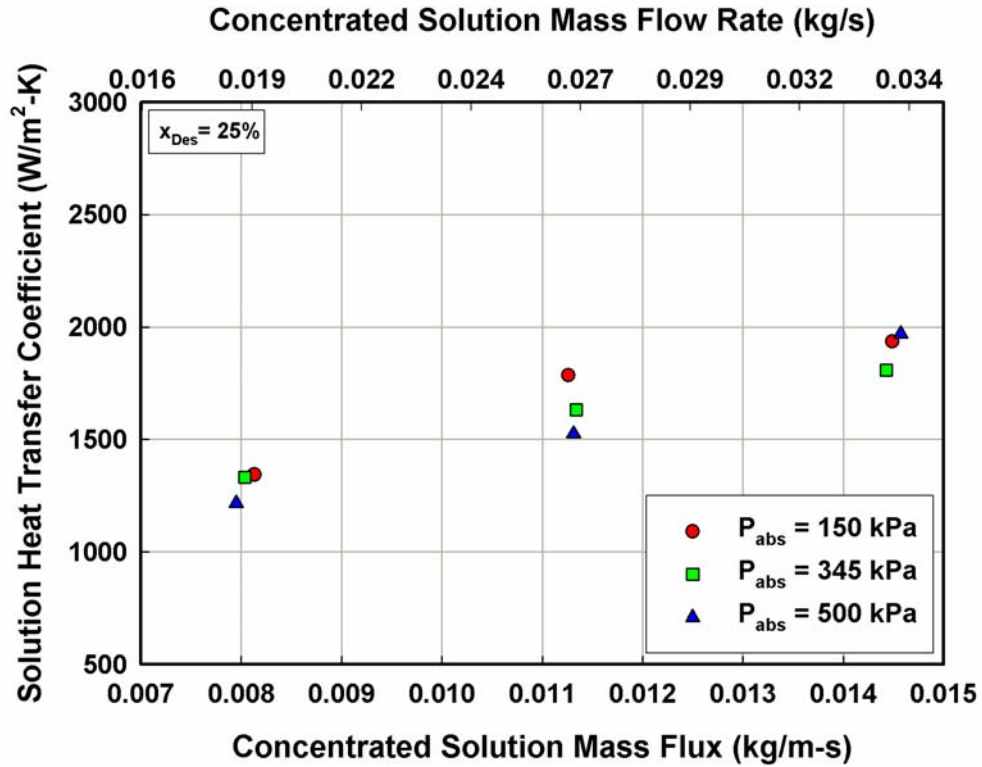
Figure 5.20 Effect of Absorber Pressure on $\alpha_{Abs,Film}$ (25%)

While some of the droplets are found to grow on their own (mostly due to the absorption

of vapor and axial movement of the solution), a majority of the droplets are driven by the

momentum carried forward by the impacting droplets. Droplet sites are found to be

strongly dependent on the already existing sites. However, if two droplet sites are close

enough, a significant interaction between those sites is also observed. Due to the smaller

tube spacing in the present study, the primary droplet never actually detaches from the

solution column before impacting the next tube. In addition, the first secondary (satellite)

drop also does not detach from the solution column. In a majority of tests, only two

major satellite droplets are observed. In some of the cases, axial movement at the

underside of the tubes is also observed. The axial movement not only produces waves

that will enhance mixing, it but also wets a good portion of the underside of the tube, providing a large surface area for heat transfer.

Operating conditions, especially the solution concentration, are found to influence the flow characteristics significantly through their influence on the properties. While complete, uniform wetting is almost non-existent, the wetting of the tube surface increases with the solution flow rate. Assuming complete, uniform wetting of the tubes will result in underestimation of the local heat transfer performance of the *solution film*. This is because for a given heat duty, the actual area available for heat transfer is much smaller than total surface area of the tubes. (Of course, this also implies that the total available tube surface area does not participate in heat transfer, thus tending to decrease overall performance.) The absorber pressure and the solution concentration can affect the absorber performance in a very complex manner through their influence on the film thickness, the residence time in the film and the droplet-site spacing. While absorber pressure and solution concentration affect residence time and film thickness in opposite manner, residence time and film thickness themselves may affect heat transfer in opposite manner. This may further be complicated by the changes in droplet spacing through its effect on the wetting of the tube surface as well the opposite influences of solution concentration and absorber pressure on the solution Reynolds number. Although all these various parameters affect the flow characteristics and, in turn, affect heat and mass transfer performance, the solution Reynolds number is still the most significant parameter. It is, therefore, necessary to give particular attention to the solution Reynolds number variation as the solution concentration and the absorber operating pressure changes.

CHAPTER 6 SEGMENTAL ANALYSIS

The analysis of heat and mass transfer in the absorber at the component level was presented in Chapter 4. Absorber performance was measured in terms of the overall heat duty and transport coefficients. However, these processes can vary from one location to the other within the absorber. During the experiments, solution temperatures at each tube row and the corresponding coolant temperatures in the coolant headers were recorded. The absorber therefore can be subdivided into multiple segments. These measurements are used to study the absorption process at the local level within the absorber. It is also necessary to account for external effects such as heat loss to the ambient and possible heat conduction from the drip tray to the coolant headers and within in the coolant headers. It was also discussed in the previous chapter on Flow Visualization that the solution flows from one tube row to the other in the droplet mode for the range of operating conditions considered here. Therefore, there is possibility of some absorption taking place in between the tubes in the droplets. The relative contributions of the fluid film and the droplets to the overall absorption should be understood. This chapter presents a detailed description of segmental analyses of the absorption process, considering these local aspects.

6.1 Segments in the Absorber

The absorber assembly (discussed in Chapter 3) consists of an outer shell, a tube array and a drip tray. The tube array consists of six tube rows each consisting of four

tubes. During the experiments, solution temperatures at each row of the tube array, at the drip tray, and at the solution pool were measured. On the coolant side, temperatures were measured at the inlet and the outlet headers of each pass (tube row). However, during the experiments, some of the thermocouples malfunctioned. Using the available measurements, it was possible to segment the tube array into three distinct segments. The drip tray is treated separately, and considered as an additional element in the absorber. Similarly, the solution pool at the absorber-shell bottom is also treated separately and constitutes another segment. Also, the solution exiting the drip tray and falling on the top row is analyzed separately. Thus, the entire absorption process is addressed in six segments. Figure 6.1 shows the arrangement of these segments in the absorber assembly.
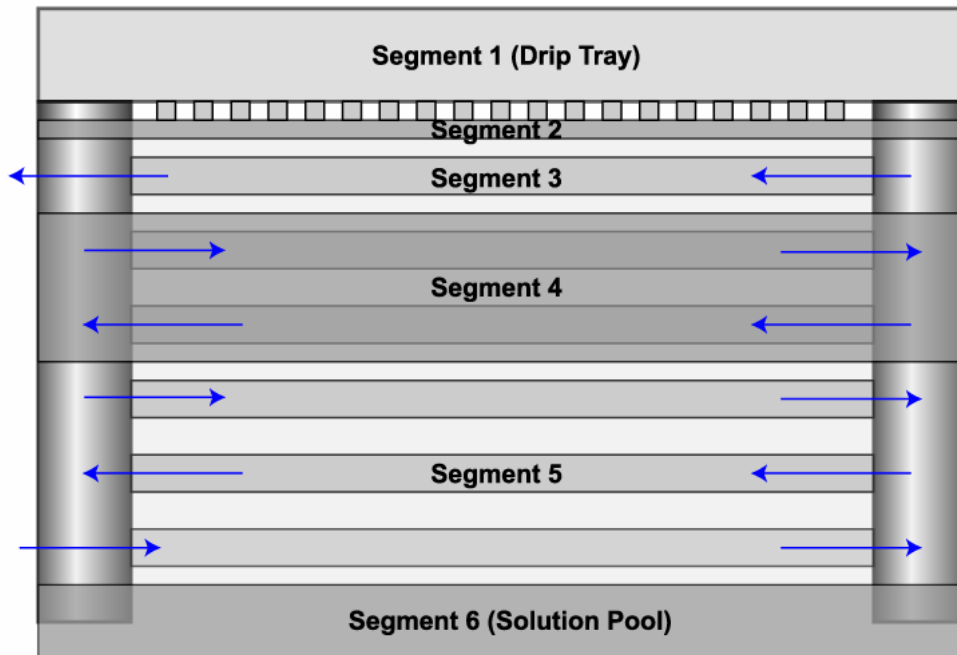
Figure 6.1 Segments in the Absorber

The first segment consists of the drip tray, the second segment extends from the drip tray to the top row of the tube array, the next three segments consist of 1, 2 and 3 coolant tubes respectively, and the final segment consists of the solution pool. Segments 3, 4 and 5 involve heat exchange with the coolant, while the other three segments do not involve any coolant; therefore absorption in these segments is treated as an adiabatic absorption process.

6.2 Temperature Profile

The dilute solution entering the absorber is collected in the drip tray and distributed over the tube array through very small diameter capillary tubes. The dilute solution then flows downward under the influence of gravity from one tube to the next tube below it. To measure the solution temperature at each of the tube rows, thermocouples were attached on one tube of each row. However, the local temperatures measured on the ammonia-water side depend upon whether they are in contact with the liquid phase or the vapor phase during measurement. Further, solution flow patterns are easily influenced by various factors such as gravity, flow rate, and solution property changes. Therefore, due to the dynamic behavior of the solution film, these thermocouples could record a liquid-film temperature or a vapor temperature, or a combination. The measured temperatures were therefore used to develop a smoothed temperature profile along the absorber rows using a 3rd degree polynomial. Appendix C discusses the development and use of temperature profile in detail. Figure 6.2 shows a representative temperature profile, with the individual segment widths representative of the surface area of the tubes in each segment. It shows the measured solution and coolant

169

temperatures, the solution saturation temperatures at the absorber inlet and outlet, and the solution temperature profile used for segmental analysis.
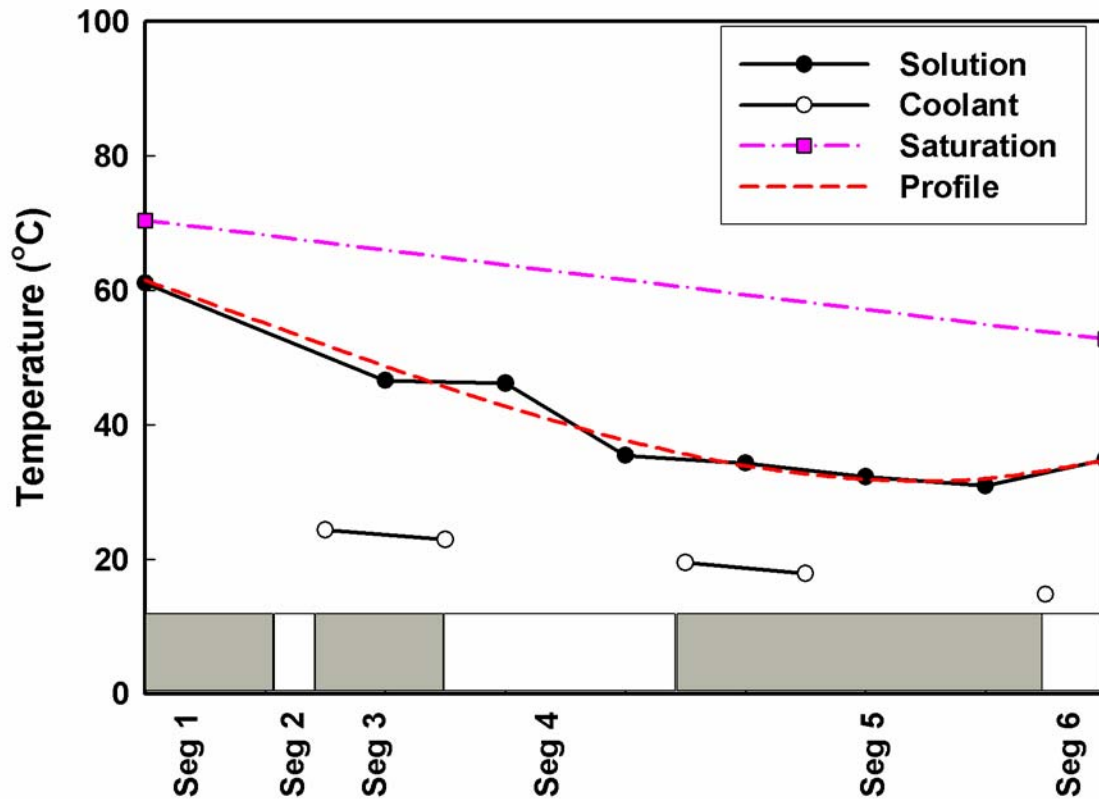
Figure 6.2 Representative Temperature Profile in the Absorber

6.3 Segmental Calculations

At the absorber, the solution inlet, the solution outlet, and the vapor inlet conditions are obtained from the measurements and the overall system analysis (for solution and vapor concentrations). These inlet conditions can be used to initiate segmental calculations at the top segment. Mass, species and energy balances can be

used to obtain the outlet conditions; however, at the outlet, there are four unknowns: solution flow rate, temperature, concentration and enthalpy. Therefore, to proceed with segmental calculation, there is at least one more parameter that should be known at the segment outlet. This is where the temperature profile discussed in the previous section is used. Since the solution temperature at the outlet of each segment is now known (from the temperature profile), and the vapor state is known throughout the absorber (as discussed in Section 4.4.1), mass, species and energy balances can be used to obtain the amount of refrigerant vapor absorbed, the outlet solution flow rate and outlet conditions in each segment. However, for accurate segmental analysis, other external effects must be accounted for. Therefore, two main external effects: conduction between the drip tray and the headers, and heat losses to the ambient, are discussed first, followed by the detailed segmental analysis.

6.3.1 Conduction from Drip Tray to Coolant Headers

The drip tray is located on the top of the coolant headers. Since the solution temperature at the drip tray is higher than the coolant header temperature, it is possible that some heat flows from the drip tray to the coolant headers through conduction in the header walls and the side walls separating the headers. Figure 6.3 shows the arrangement of the coolant header. Only the left coolant header is shown in this figure. Using this schematic, a thermal resistance network (Figure 6.4) is used to calculate the heat flow for each segment. The main heat flow path in the resistance network is from the drip tray to the coolant bulk, while the secondary flow paths are from the drip tray to the side wall of the headers, and from the side wall to the coolant bulk.

171
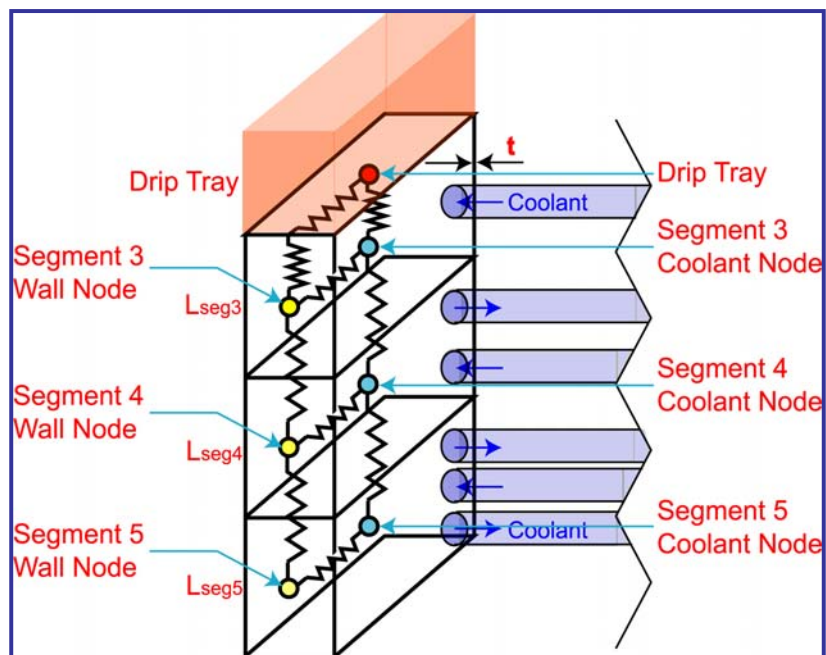
Figure 6.3 Coolant Header Schematic (Only one header shown)

All the three segments shown in the schematic involve heat exchange with the absorber coolant. In this schematic, the drip tray temperature (T_{DT}) and the segmental coolant temperatures (T_C) are obtained from measurements; however, each segmental wall temperature must be obtained through analysis. By formulating the thermal resistance network and iteratively solving the heat balance equations at each node, these segmental wall temperatures are obtained. The coolant nodes are defined at the center of the coolant bulk, while the wall nodes are defined at middle of the header walls. Details of these calculations are presented in Appendix D.

These conduction heat duties are used to modify the measured segmental coolant heat duties, which will be presented where the segmental heat and mass transfer calculations are discussed.

172
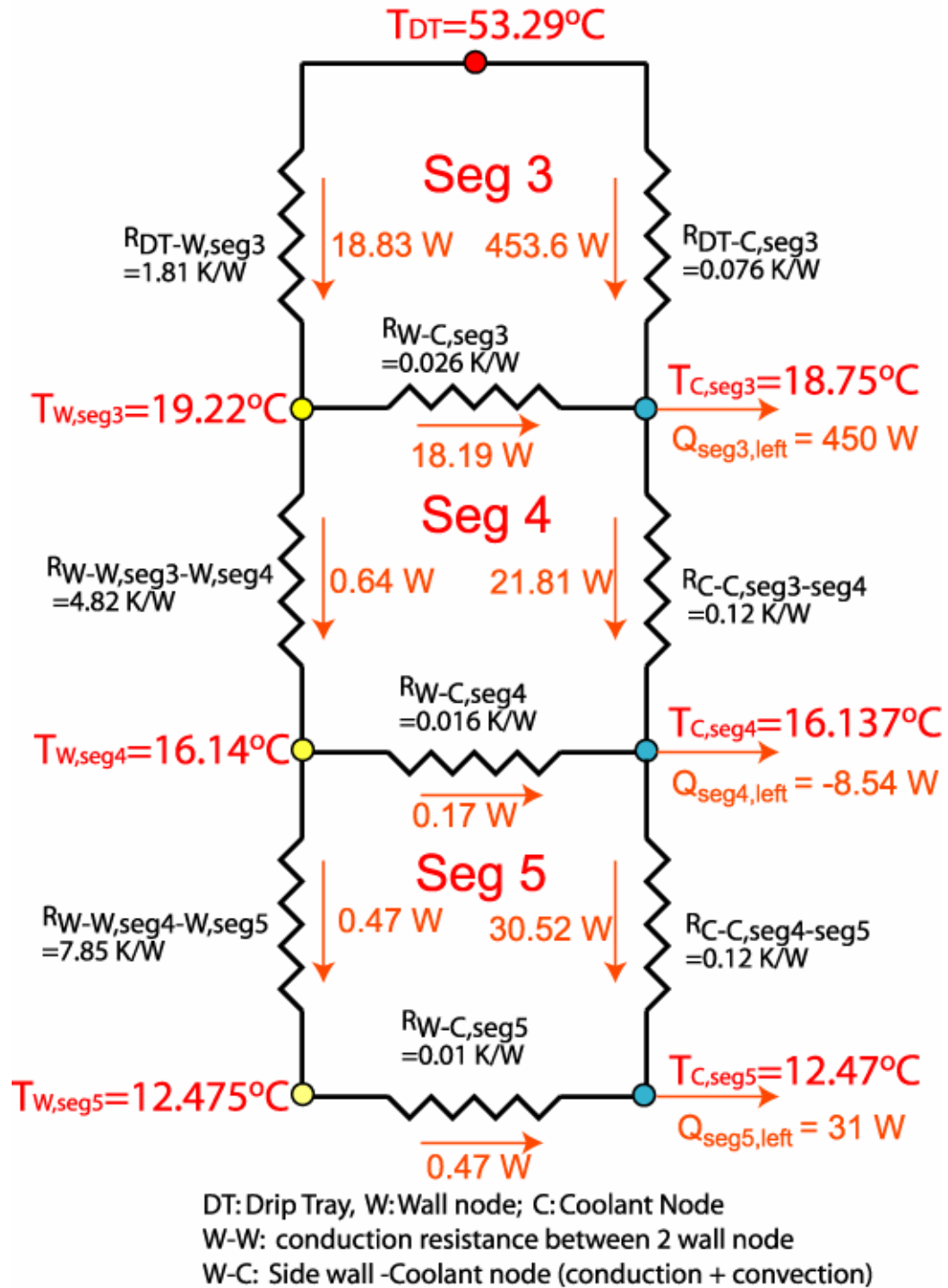
Figure 6.4 Conduction Heat Duties and Thermal Resistances for the Representative case of 345 kPa, 25%, and 0.026 kg/s (Left header only)

Figure 6.4 shows the values of conduction heat duties along with various resistances in the left header for the representative case of 25% dilute solution concentration, 345 kPa absorber pressure and 0.026 kg/s concentrated solution flow rate. Similar values are obtained for the right header also. The coolant-side heat duty for this case is 7.954 kW while the total conduction heat duty (sum of the left and the right headers) is 0.96 kW. By comparing the different segments, it is found that the conduction heat duty for segment 3 (next to the drip tray) is the highest (0.91 kW of the total conduction heat duty of 0.96 kW) due to the large temperature gradient between the drip tray and the coolant headers. The coolant-side heat duties for the segments 3, 4, and 5 are 1.82 kW, 2.977 kW, and 3.154 kW, respectively while the conduction heat duties are 0.91 kW, -0.01 kW and 0.06 kW for these segments.

6.3.2 Heat Loss to Ambient

The absorber is exposed to the ambient and provides a significant surface area for heat transfer. The average temperature inside the absorber is significantly higher than the ambient temperature. Usually the large solution pool, as well as the vapor in the absorber, are in direct contact with the absorber shell. Therefore, the absorber shell is at a higher temperature than the ambient. Although the absorber shell is insulated using ½" thick (t_{ins}) fiber-glass insulation to minimize heat losses (or gain in certain low temperature cases) from the ambient, it is expected that there will be some heat loss from the absorber shell that needs to be accounted for in the heat and mass transfer calculations of the absorber. Heat can be transferred from the outer surface of the absorber shell to the ambient both by convection and radiation. The absorber shell is assumed to be at a temperature that is the average of the absorber inlet and outlet temperatures. The

174

surrounding air properties are calculated at an average of the insulation surface and the ambient temperatures. It should be noted the insulation surface temperature is unknown and calculated iteratively by solving the heat flow equations. The heat flow equations are formulated using thermal resistances and temperature differences. The main thermal resistances accounted for are: conduction resistance of the absorber shell, conduction resistance of the insulation, and natural convection and radiation resistance at the insulation surface (Figure 6.5). The surface emissivity is taken to be 0.85. The ambient temperature is assumed to be 23°C. Details of the heat loss calculations are presented in Appendix E.
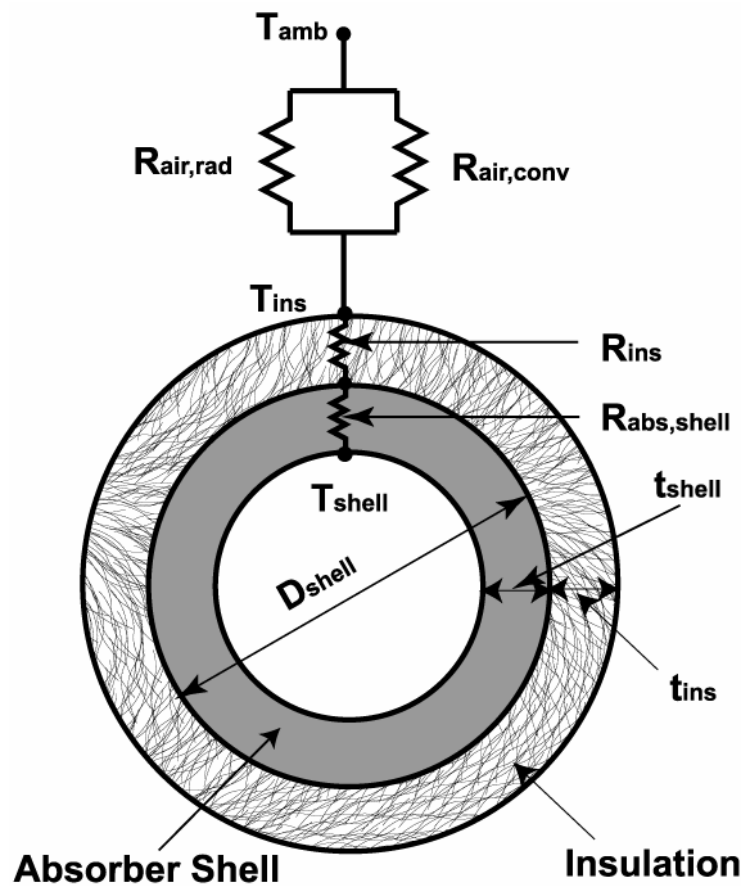
Figure 6.5 Thermal Resistance Network for Heat Loss Calculations

Figure 6.6 shows the estimated heat losses for all the data taken in this study. The maximum heat loss to the ambient is 1.9% of the measured absorber heat duty. The heat losses to the ambient vary from 2.5 W to 76 W for the range of the conditions tested. Heat losses to the ambient for the representative case are only 32 W, while the coolant-side heat duty is 7.954 kW.
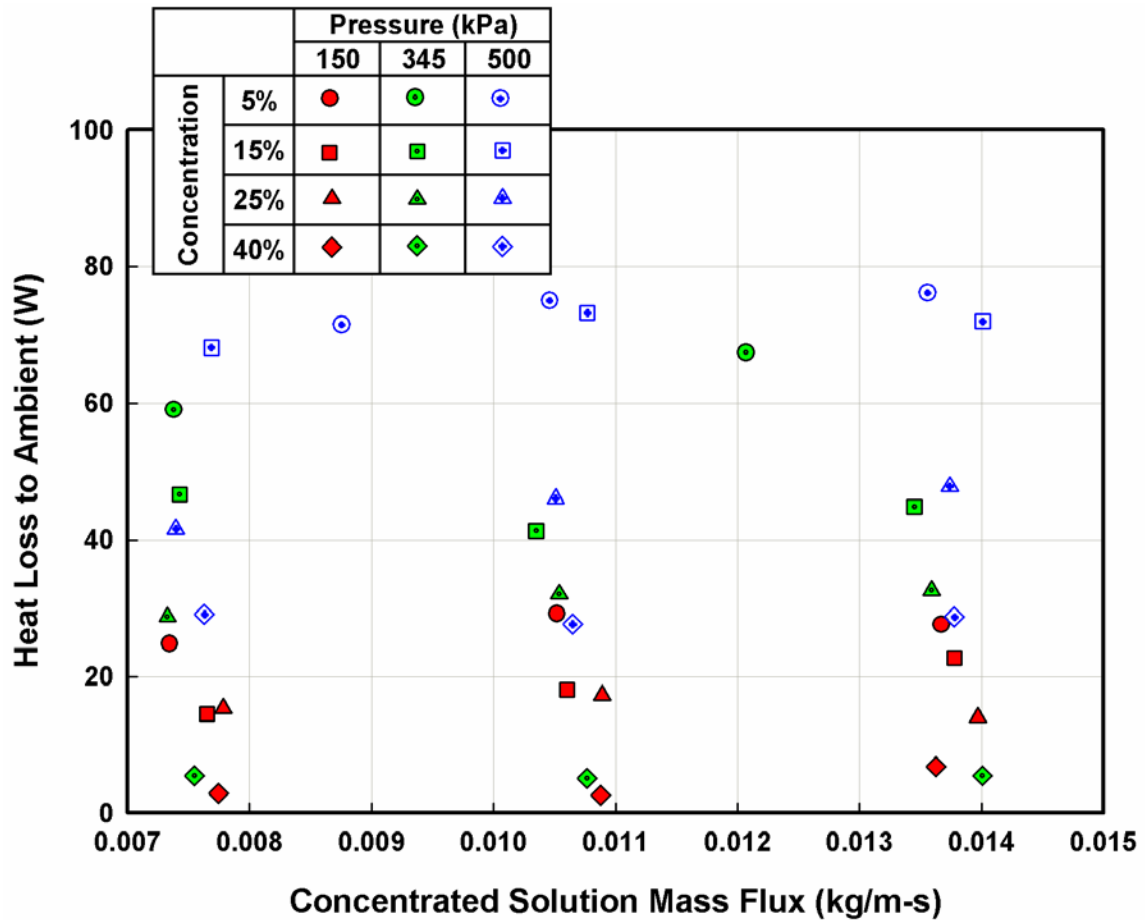
Figure 6.6 Estimated Heat Loss to Ambient

6.3.3 Drip Tray Segment

It was discussed in Chapter 4 that the refrigerant vapor in the absorber changes its state from the measured inlet conditions to those of saturation at the minimum temperature and average absorber pressure. This change in state results in a change in the enthalpy of the vapor and is accounted for at the drip tray segment. It is assumed that entire vapor entering the absorber interacts with the dilute solution in the drip tray, resulting in some heat and mass exchange before the solution falls over the tubes. At the drip tray, considered as the first segment from the top in the absorber, either absorption or desorption can occur depending on inlet conditions. The dilute solution inlet and the vapor inlet conditions are fully specified by measurements and system-level analyses (for solution and vapor concentrations). The entire absorber is considered to be at an average of the inlet and the outlet pressures. At the solution outlet for this drip tray, the temperature is obtained from the solution temperature profile discussed previously. Similarly, the vapor outlet conditions are obtained from the assumption of saturated vapor at the minimum temperature in the absorber. The unknown values at the first segment are therefore the amount of vapor absorbed/desorbed at the drip tray, the solution outlet flow rate, and its concentration. The process at the drip tray segment is shown schematically in Figure 6.7. The amount of vapor absorbed, and dilute solution and vapor outlet flow rates can be calculated by iteratively solving the mass, species and energy balance equations. The transfer process here is adiabatic except for the amount of heat transferred by conduction to the coolant headers.
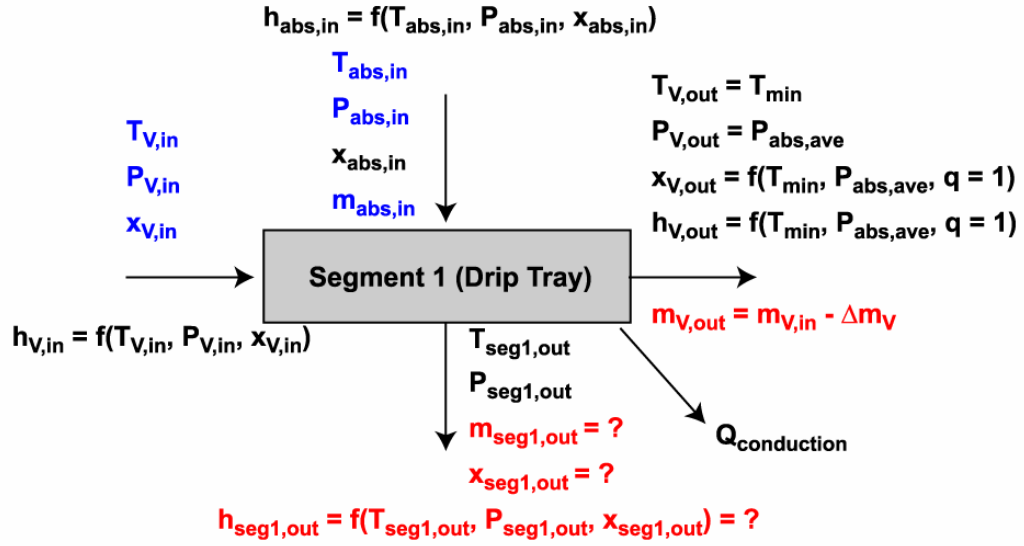
Figure 6.7 Drip Tray Schematic

The equations for mass, species and energy balance are as follows:

$$\dot{m}_{V,out} = \dot{m}_{V,in} - \Delta\dot{m}_V \tag{6.1}$$

$$\dot{m}_{abs,in} + \dot{m}_{V,in} = \dot{m}_{seg1,out} + \dot{m}_{V,out} \tag{6.2}$$

$$\dot{m}_{abs,in} \times x_{abs,in} + \dot{m}_{V,in} \times x_{V,in} = \dot{m}_{seg1,out} \times x_{seg1,out} + \dot{m}_{V,out} \times x_{V,out} \tag{6.3}$$

$$\dot{m}_{abs,in} \times h_{abs,in} + \dot{m}_{V,in} \times h_{V,in} = \dot{m}_{seg1,out} \times h_{seg1,out} + \dot{m}_{V,out} \times h_{V,out} + Q_{conduction} \tag{6.4}$$

For the representative case (25%, 345 kPa and 0.026 kg/s), the amount of vapor absorbed in the drip tray is 2.462×10^{-4} kg/s. The measured vapor flow rate for this case is 2.826×10^{-3} kg/s. Therefore, the decrease (due to near-adiabatic absorption) in the vapor flow rate after its interaction with the drip tray is about 8.7%. This amount of vapor absorbed by the dilute solution changes the dilute solution flow rate falling over the tube

array by approximately 1% from 0.0228 kg/s to 0.023 kg/s. Also, the solution concentration changes from 0.267 to 0.271 (~1.5%).

6.3.4 Segments with Coolant

As mentioned in the previous section, there are a total of six segments in the absorber, and three out of the six segments (segment 3, 4 and 5) involve heat exchange with the absorber coolant. At each of these segments, the solution inlet and the vapor conditions are fully specified. It was mentioned in the beginning of this chapter that there is a possibility of some absorption in the droplets between the tubes. Each coolant segment is therefore further divided in two segments: Falling-film, and droplet. Absorption in the droplets is considered to be adiabatic due to the weak coupling with the coolant. (The absorption in the falling-film region determines the inlet conditions to the droplet absorption phase). At the droplet outlet, the temperature is obtained from the solution temperature profile. Figure 6.8 shows a schematic of such a segment. In these segments, the unknown quantities are the amount of vapor absorbed, the solution outlet flow rate, its concentration, and the droplet inlet temperature. These are calculated using mass, species and energy balance at each of the segments. In the energy balance equation for the film part of the segment, the coolant-side heat duty is modified to account for the contribution of conduction heat transfer from the headers and the drip tray as applicable. The heat generated during the absorption of the vapor is carried away by the absorber coolant flowing inside the tubes. Since the coolant flow rate as well as the segmental coolant inlet and outlet temperatures are measured, the coolant-side absorber heat duty for each segment is readily calculated. Figure 6.9 shows schematically the falling-film part of a segment involving the absorber coolant.

179

Figure 6.8 Cooled Segment (Falling-Film and Droplet Parts)

Figure 6.9 Schematic for Segments with Coolant (Falling-Film Part)

The equations used to calculate the amount of absorbed vapor in the falling-film part (denoted with the subscript FF) of the segment are as follows:

$$\dot{m}_{seg,in} + \dot{m}_{seg,V,FF,in} = \dot{m}_{seg,FF,out} \tag{6.5}$$

$$\dot{m}_{seg,in} \times x_{seg,in} + \dot{m}_{seg,V,FF,in} \times x_{seg,V,in} = \dot{m}_{seg,FF,out} \times x_{seg,FF,out} \tag{6.6}$$

$$Q_{seg,sol} = \dot{m}_{seg,in} \times h_{seg,in} + \dot{m}_{seg,V,FF,in} \times h_{seg,V,in} - \dot{m}_{seg,FF,out} \times h_{seg,FF,out} \tag{6.7}$$

$$Q_{C,FF,seg} = \dot{m}_{C,seg} \times C_{P,C,seg} \times (T_{C,seg,out} - T_{C,seg,in}) \tag{6.8}$$

$$Q_{seg,sol} = Q_{C,FF,seg} - Q_{seg,conduction} \tag{6.9}$$

For the droplet part (denoted with the subscript dp) (Figure 6.10),
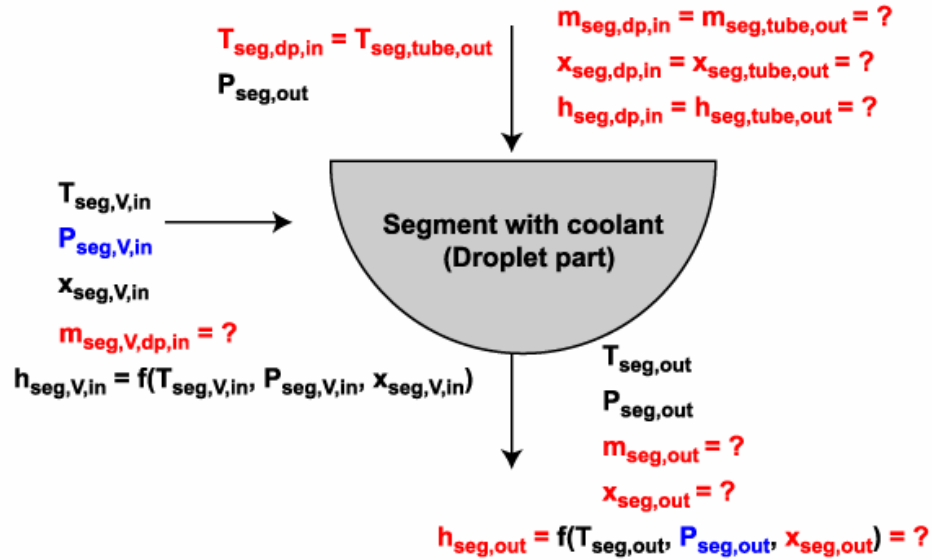
Figure 6.10 Schematic for Segments with Coolant (Droplet Part)

$$\dot{m}_{seg,dp,in} + \dot{m}_{seg,V,dp,in} = \dot{m}_{seg,out} \tag{6.10}$$

$$\dot{m}_{seg,dp,in} \times x_{seg,dp,in} + \dot{m}_{seg,V,dp,in} \times x_{seg,V,in} = \dot{m}_{seg,out} \times x_{seg,out} \tag{6.11}$$

$$\dot{m}_{seg,dp,in} \times h_{seg,dp,in} + \dot{m}_{seg,V,dp,in} \times h_{seg,V,in} = \dot{m}_{seg,out} \times h_{seg,out} \tag{6.12}$$

Other equations connecting the film and droplet absorption phases of the segments are:

$$\dot{m}_{seg,dp,in} = \dot{m}_{seg,FF,out} \tag{6.13}$$

$$x_{seg,dp,in} = x_{seg,FF,out} \tag{6.14}$$

$$h_{seg,dp,in} = h_{seg,FF,out} \tag{6.15}$$

$$T_{seg,dp,in} = T_{seg,FF,out} \tag{6.16}$$

Since the temperature at the droplet inlet (or falling-film outlet) is not known, one additional equation is necessary to solve these equations to obtain the amount of vapor absorbed in the film and droplet parts of the segment. Since it is not practical to accurately measure the temperature of the solution at the intersection of the falling-film and droplet regions, especially in such a full-scale system-level facility, closure is obtained by estimating the amount of vapor absorbed in the droplets based on the relevant information available in the literature. Interface mass transfer in droplets has been studied extensively in both the liquid-liquid and vapor-liquid systems (one phase is noted as continuous and the other as dispersed). Some of the prevalent theories and models for such processes are discussed here before making a choice to estimate the absorption rates in the droplets. The balance of the absorption in each segment is then attributed to the falling-film phase and modeled in terms of the relevant dimensionless parameters.

6.3.4.1 Interface Mass Transfer

Vapor absorption process is an interphase mass transfer process, for which several theories exist in the literature (Asano 2006; Bird *et al.* 2002; Sherwood *et al.* 1975). The primary theories include: film (Nernst 1904), penetration (Higbie 1935), and surface renewal (Danckwerts 1951). Over time, many researchers have modified these theories and developed models to analyze interphase mass transfer in several applications, e.g., vapor absorption/desorption, liquid-liquid extraction. A brief description of these theories is presented first, followed by a description of some models that address interphase mass transfer (specifically in droplets).

Film Theory

This is the oldest theory available for interphase mass transfer, and was originally developed by Nernst (1904). The theory assumes that mass transfer resistance exists only in a thin region (usually a stationary film) near the phase boundary (interface). Transport in this region is primary through diffusion; therefore, the convective term can be neglected in the governing equation. In a simple case of unidirectional transport, the mass flux can be obtained as follows (Asano 2006):

$$N_1 = \rho D_{12} \left(\frac{x_s - x_\infty}{\delta} \right) \tag{6.17}$$

Here, x_s and x_∞ are the concentrations at the interface and in the bulk of the absorbing phase, respectively. A mass transfer coefficient is usually defined as:

$$\beta = \frac{D_{12}}{\delta} \tag{6.18}$$

Whitman (1923) developed a two-film theory for gas absorption (later presented by (Lewis and Whitman 1924)) that considers thin regions of mass transfer resistance

(stationary films) in both liquid and vapor phases; however, Lewis and Whitman (1924) also noted that usually a sharp line of demarcation does not exist between stationary films and the bulk of the fluid. It is assumed that the actual amount of the solute contained in the films is very small because the films are very thin; therefore, the solute flow rate must be the same in the two films. For this reason, the two films are considered as two diffusional resistances in series. They further noted that depending upon the solubility of the gas in the liquid, either of the phases can control the absorption process, i.e. vapor-phase controlled (high solubility) and liquid-phase controlled (low solubility).

Film theory yields mass flux proportional to D_{12} while experimental investigations have suggested D_{12}^{a}; where a is usually less than 1 (Sherwood *et al.* 1975). The theory also does not suggest any method to calculate the film thickness (δ). Despite its limitations, this theory predicts the mass transfer in simple situations satisfactorily, e.g., evaporation of a pure liquid in a diffusion cell and absorption of pure gas in an agitated vessel (Asano 2006).

Penetration Theory

Film theory assumes a steady-state condition. However, in many industrial processes, the two phases come in contact for only a brief amount of time. This may be insufficient for the phases in contact to reach steady state. Higbie (1935) proposed that "the first stage in the absorption process must be the penetration of the liquid film by the dissolved gas". He developed the penetration theory by solving the transient diffusion equation and neglecting the convective term. This treatment is similar to transient heat conduction. According to this theory, a time-averaged liquid-phase mass-transfer ($\beta_{l,Hg}$) coefficient can be obtained as:

$$\beta_{l,Hg} = 2\sqrt{\frac{D_{12}}{\pi t}} \tag{6.19}$$

Here, t is the time of contact (exposure time) for the two phases. Penetration theory predicts that the mass transfer coefficient will vary as $D_{12}^{0.5}$, which is closer to many experimental observations than proportional to D_{12} (Sherwood *et al.* 1975). It also predicts a decreasing mass transfer rate as the exposure time increases. The theory yields satisfactory results only for short exposure times. However, obtaining the exposure time is not trivial. It assumes that the liquid film is laminar; therefore, in the case of droplets, internal circulation is neglected.

Surface Renewal Theory

Higbie's (1935) penetration theory is applicable for short exposure times where the penetration into the liquid film is small. Danckwerts (1951) argued that this model is of limited use, especially when the liquid film is turbulent. In this case, there are large eddies that continuously bring fresh liquid to the surface, and sweep away and mix the surfaces (which have been in contact with the vapor) with the bulk liquid. Therefore, the vapor phase continually comes in contact with fresh liquid. According to this theory, a liquid-phase mass transfer coefficient can be calculated as:

$$\beta_{l,Dk} = \sqrt{D_{12}s} \tag{6.20}$$

Here, s is the surface renewal rate. This theory also predict that the mass transfer coefficient varies as $D_{12}^{0.5}$, which is again closer to experimental observations than proportional to D_{12} (Sherwood *et al.* 1975). This theory is also difficult to apply, since the data on surface renewal rates are not available usually.

6.3.4.2 Mass Transfer in Droplets

Droplets are widely used in many absorption/extraction applications. Even in the falling-film type of absorber, the solution flow rate is maintained such that the flow from one tube row to the next is in the form of droplets. Mass transfer in droplets is influenced by a wide variety of parameters, e.g., droplet size and shape, fluid properties in the various phases, exposure time of the phases, drop oscillation, and internal circulation if present. A majority of the available studies developed models for droplet mass transfer in liquid-liquid extraction applications. Furthermore, not all of these studies have accounted for internal circulation in the droplets. Ryan (1994) presented a summary of several such models. Studies by Skelland and Minhas (1971) and Shih *et al*. (1995) summarize various mass transfer models for droplets. Some of these models, which can be used to estimate representative liquid-phase droplet mass-transfer coefficients for ammonia-water absorption, are briefly discussed here.

Liquid-Liquid Systems

Kronig and Brink (1950)

Kronig and Brink (1950) studied extraction from drops falling (or rising, depending upon the density difference) under the influence of gravity (low Reynolds number) in another immiscible liquid. Laminar internal circulation was expressed using Hadamard's (1911) circulation patterns for the internal flow field developed for spherical drops falling/rising at a steady state (i.e., at terminal velocity). Their model assumed that the concentration gradients follow the internal circulation. They obtained an eigenvalue solution to the governing differential equation formed by combining the effects of diffusion and convection.

Heertjes *et al.* (1954)

Heertjes *et al.* (1954) studied liquid-phase mass transfer in droplets using isobutanol and water as the working fluids in a spray-column. Experiments were conducted both on water drops falling in isobutanol and vice-versa. They compared their results with the model of Kronig and Brink, which appeared to predict the data adequately for isobutanol droplets falling in water; however, the Kronig and Brink model predictions were not good for water droplets falling in isobutanol. The disagreement in the case of water droplets was attributed to the effect of floating of water droplets in isobutanol. They suggested a liquid-phase mass transfer correlation in the following form:

$$\beta_{l,Hj} = \frac{24}{7}\sqrt{\frac{D_{12,d}}{\pi t}} \qquad (6.21)$$

Here, $D_{12,d}$ is the binary diffusivity in the dispersed (droplet) phase, and t is the droplet rise/fall time in the continuous phase. In a later study, Heertjes and DeNie (1966) presented a mass transfer correlation based on the fresh surface (surface renewal) theory for isobutanol drops forming in a continuous phase of water.

$$\beta_{l,HdN} = \left(2\frac{A_R}{V_{dr}} + \frac{4}{3}B\right)\sqrt{\frac{D_{12,d}}{\pi t}} \qquad (6.22)$$

Here, A_R is the surface of the rest drop (before a new surface is formed due to absorption), V_{dr} is the volume of the released drop, and B is the surface-to-volume ratio of the drops.

Handlos and Baron (1957)

Handlos and Baron (1957) studied mass transfer from drops rising/falling in a continuous phase of another liquid. They pointed out that using Hadamard's (1911) circulation patterns to describe the internal circulation does not improve the mass transfer

performance predictions significantly because it changes the effective diameter of the droplet to a characteristic length defined by the circulation pattern, which is smaller by a factor of approximately 2. The model is good for high Reynolds numbers (greater than 1000) when the internal circulation is turbulent. They developed a correlation of the following form:

$$\beta_{l,HB} = \frac{0.00357u}{1+\dfrac{\mu_d}{\mu_c}}$$

(6.23)

Here, u is the drop velocity, and μ_d and μ_c are viscosities in the dispersed and continuous phases, respectively. They also pointed out that the concentration gradient may not be the best driving potential for mass transfer; rather chemical activity appears to be the more suitable driving potential.

Olander (1966)

Olander (1966) re-derived the Handlos and Baron (1957) equation numerically and extended their model to shorter exposure times and larger drops. He proposed the following equation for the droplet mass-transfer coefficient:

$$\beta_{l,Ol} = 0.972\beta_{l,HB} + \frac{0.075d_{dp}}{t}$$

(6.24)

Angelo et al. (1966)

Angelo et al. (1966) generalized Higbie's penetration theory (1935) by adding the effect of stretching surfaces during drop formation and oscillation. They refined the Rose and Kintner (1966) model for large oscillating drops and suggested a new time-averaged (for one cycle of oscillation) mass transfer coefficient correlation.

$$\beta_{l,Ag} = \frac{2}{\sqrt{\pi}}\left[fD_{12,d}\left(1+\varepsilon+\frac{3\varepsilon^2}{8}\right)\right]^{1/2}$$

(6.25)

Here, f is the frequency of oscillation that can be found using the equation given by Lamb (Clift *et al.* 1978), and ε is a dimensionless amplitude factor of the surface-time correlation for the system under consideration.

$$f = \left[\frac{8\sigma}{3\pi m_{dp}}\right]^{1/2}$$
(6.26)

Here, σ is the surface tension and m_{dp} is the mass of the droplet.

Ruckenstein (1967)

Ruckenstein (1967) studied mass transfer between a single drop and a continuous phase for small Reynolds numbers (~ 100 or smaller). His model assumed a well mixed drop interior with mass transfer resistance in a liquid boundary layer only. He obtained a mass transfer correlation of the following form:

$$\beta_{l,Rck} = 2\left(\frac{uD_{12,d}}{\pi d_{dp}}\right)^{1/2}$$
(6.27)

Here, u is the velocity of the falling drop and d is the droplet diameter.

Skelland and Minhas (1971)

Skelland and Minhas (1971) measured the mass transfer coefficient for three dispersed-phase controlled (droplet phase) liquid-liquid systems. They compared their results with those predicted by several models (Coulson and Skinner 1952; Groothuis and Kramers 1955; Heertjes and de Nie 1966; Heertjes *et al.* 1954; Licht and Pansing 1953). These models, however, did not predict their experimental data satisfactorily. Based on their measurements, they suggested a new droplet mass-transfer coefficient correlation as follows:

$$\beta_{l,SM} = 0.0432 \frac{d}{t}\left(\frac{u^2}{d_{dp}g}\right)\left(\frac{d_{dp}^2}{tD_{12,d}}\right)\left(\frac{\mu_d}{\sqrt{\rho_d d_{dp}\sigma_d}}\right)$$
(6.28)

Here, g is the acceleration due to gravity and all the symbols have their usual meaning.

Liquid-Vapor Systems

The studies summarized above considered droplets as a dispersed-phase in a continuous-phase of another liquid. A liquid-liquid system can differ significantly from a liquid-vapor system due to the large differences in properties, e.g., diffusivity, viscosity, density, and surface tension, between the phases. Some of the studies that address droplet mass transfer in vapor-liquid systems are summarized here.

Garner and Lane (1959)

Garner and Lane (1959) conducted experiments on droplet mass transfer during absorption of CO_2 into water and hydrocarbons, and absorption of water into glycols and an amine. They studied droplets diameters of 4.22 and 5.85 mm. The observed mass transfer rates in their experiments were found to be larger (up to 2.5 times) than those predicted by Kronig and Brink (1950).

Groothuis and Kramers (1955)

Groothuis and Kramers (1955) measured the amount of SO_2 absorbed by individual drops of water and hydrocarbons during formation at the tip of a capillary tube. Based on penetration theory combined with a surface renewal assumption, they derived a mass transfer coefficient equation during droplet formation.

$$\beta_l = \frac{4}{3}\sqrt{\frac{D_{12,d}}{\pi t}}$$
(6.29)

They found that the rate of absorption was higher for shorter formation times due to the mixing produced by the liquid leaving the capillary; however, the total amount of absorption was greater for longer formation times, partly due to convection. The effects

of mixing and convection decrease as the viscosity of the solution increases. The droplet formation time varied between 1 and 40 seconds.

Altwicker and Lindjem (1988)

Altwicker and Lindjem (1988) conducted experiments to investigate liquid-side mass transfer in forming droplets during the absorption of CO_2 by water drops. Their work focused on drop sizes of 0.6 and 1.2 mm diameter at very short formation times (< 0.1 s). Kronig and Brink's model (1950) underpredicted their results; however, the data showed absorption rates similar to those of Garner and Lane (1959) for larger diameter drops. They attributed larger absorption rates than those predicted by Kronig and Brink model to unsteady internal circulation during formation. The model of Angelo *et al.* (1966) predicted their results satisfactorily for all drop sizes.

Shih *et al.* (1995)

Shih *et al.* (1995) studied absorption of SO_2 vapor into drops of HCl solution to determine the liquid-phase mass transfer coefficient. The drop generator consisted of an injection bottle, needle, and a flow regulator. Drops of diameters of 2.79 and 4.44 mm were allowed to fall in the absorption column while absorbing the SO_2 vapor at room temperature ranging from 20 - 30°C. They found the liquid-phase mass transfer coefficient to be independent of falling velocity, contact time, and vapor-phase concentration, depending only on the liquid-phase diffusivity and the frequency of drop oscillation. In their comparison with models of other researchers, they found that the models of Ruckenstein (1967) and Olander (1966) did not predict the results satisfactorily; however, the models of Handlos and Baron (1957) and Angelo *et al.* (1966) predicted the data better.

6.3.4.3 Application to Growing Droplets in Horizontal Tube Flow

A majority of the droplet absorption/extraction models discussed above were developed for fully-formed droplets traveling through a continuous phase of liquid or vapor. These droplets were produced using spray nozzles or similar mechanisms and moved through the continuous phase mostly under the influence of gravity. The droplets formed during gravity-driven flow over horizontal tube banks differ substantially from those produced using spray nozzles and other similar means. Droplet hydrodynamics in horizontal falling-film absorbers are primary governed by solution properties and the flow rate of the solution. Furthermore, irrespective of the size of the droplet, there will always be significant internal circulation during droplet formation on the underside of the tubes.

The studies on vapor-liquid systems discussed above were also for sparingly soluble gases. Therefore, absorption in a majority of these studies is liquid-side controlled. However, for the ammonia-water fluid pair, ammonia is highly soluble in water (89.9 g/100 ml of water at 0°C). While the studies discussed above focus on drops moving at terminal velocities, i.e., at steady state, droplets in a horizontal-tube falling-film absorbers rarely reach steady state. Some studies (Jeong and Garimella 2002; Kyung *et al.* 2007) have demonstrated that between droplet formation and free fall, only the droplet formation regime shows any significant amount of vapor absorption. It was also noted in the previous chapter that the droplet free-fall time was very small (0.06 s) compared to droplet formation, which varied from 0.22 to 0.51 s, in the present study. In addition, droplet free-fall was rarely seen in this study due to the smaller tube spacing.

In the case of the ammonia-water mixture, the relative importance of liquid- and vapor-phase mass transfer resistances will depend upon operating conditions because the properties can vary with solution temperature and concentration. Nevertheless, to obtain an estimate of the vapor mass absorbed in the droplets, the droplet mass transfer coefficient in the liquid-phase was obtained using several correlations discussed in the previous section. For a representative case of dilute solution concentration of 25%, absorber pressure of 345 kPa, and a solution flow rate of 0.026 kg/s, the liquid-phase mass-transfer coefficient for the bottom segment (consisting of 3 tubes) obtained using these models is summarized in Table 6.1. It can be seen that many models (Angelo *et al.* 1966; Heertjes *et al.* 1954; Olander 1966; Ruckenstein 1967) yield similar values of liquid-phase mass transfer coefficient on the order of 10^{-4} m/s. The Handlos and Baron (1957) correlation, however, yields a very small mass transfer coefficient. This is due to the large viscosity difference between liquid and vapor phases. Their model was developed for liquid-liquid extraction applications. The model of Groothius and Kramers (1955) (developed for vapor-liquid systems) yields smaller mass transfer coefficients than the others (except for that of Handlos and Baron). The mass transfer coefficient from the Groothius and Kramers model was then used with the Colburn-Drew method to estimate the amount of the vapor absorbed in the droplets.

$$\dot{n}_T = -C_{T,l} \times \beta_{l,GK} \times \ln\left(\frac{\tilde{z} - \tilde{x}_{l,bulk}}{\tilde{z} - \tilde{x}_{l,int}} \right) \tag{6.30}$$

This, however, results in unrealistically high absorption rates in the droplet. For the representative condition (345 kPa, 25% and 0.026 kg/s), the amount of vapor absorbed in the bottom segment was predicted to be 0.014 kg/s, which is about 50% of measured refrigerant flow rate of 0.0028 kg/s, and more than 100% of the total amount absorbed in

the bottom segment, 0.0134 kg/s (obtained without accounting for droplet absorption). This also implies that the use of other models in Table 6.1 would yield even higher, and therefore, unacceptable absorption rates. It should also be noted that for a given liquid-phase mass transfer coefficient, absorption rates in the liquid-phase are much larger than those in the gas phase because of the larger molar concentrations in the liquid-phase.

Table 6.1 Representative Mass Transfer Coefficients in Droplets (345 kPa, 25% and 0.026 kg/s)

Study	Type	β_l Correlation	Value
Heertjes *et al.* (1954)	Liquid-Liquid	$\beta_{l,HJ} = \dfrac{24}{7}\sqrt{\dfrac{D_{12,d}}{\pi t}}$	2.23×10^{-4} m/s
Groothius and Kramers (1955)	Liquid-Vapor	$\beta_{l,GK} = \dfrac{4}{3}\sqrt{\dfrac{D_{12,d}}{\pi t}}$	8.679×10^{-5} m/s
Handlos and Baron (1957)	Liquid-Liquid	$\beta_{l,HB} = \dfrac{0.00357u}{1+\mu_d/\mu_c}$	2.24×10^{-6} m/s
Olander (1966)	Liquid-Liquid	$\beta_{l,Ol} = 0.972\beta_{l,HB} + \dfrac{0.075d_{dp}}{t}$	1.17×10^{-4} m/s
Angelo *et al.* (1966)	Liquid-Liquid	$\beta_{l,Ag} = \dfrac{2}{\sqrt{\pi}}\left[fD_{12,d}\left(1+\varepsilon+\dfrac{3\varepsilon^2}{8}\right)\right]^{1/2}$	2.79×10^{-4} m/s
Ruckenstein (1967)	Liquid-Liquid	$\beta_{l,Rck} = 2\left(\dfrac{uD_{12,d}}{\pi d}\right)^{1/2}$	2.08×10^{-4} m/s
Skelland and Minhas (1971)	Liquid-Liquid	$\beta_{l,SM} = 0.0432\dfrac{d}{t}\left(\dfrac{u^2}{dg}\right)\left(\dfrac{d^2}{tD_{12,d}}\right)\left(\dfrac{\mu_d}{\sqrt{\rho_d d\sigma_d}}\right)$	8.65×10^{-4} m/s

It should be noted, however, that the above calculation accounts only for the mass transfer resistance presented by the liquid phase in the droplet. The other resistance encountered by the vapor is in the gas phase, as it moves from the bulk condition to the interface. To evaluate the relative importance of liquid- and vapor-phase mass-transfer resistances, comparisons were made based on Higbie'e penetration theory as illustrated in Bird *et al.* (2002). The ratio of the liquid-phase only to the liquid-phase-based overall mass transfer conductance can be obtained as:

$$\frac{k_l}{K_l} = 1 + \frac{k_l}{m_{eq} k_V} \tag{6.31}$$

For the liquid-phase mass transfer resistance to be dominant, $\dfrac{k_l}{m_{eq} k_V}$ should be much less than 1. In this case, the overall conductance will be same as the liquid-phase conductance. However, if this ratio is greater than 10, then the mass transfer will be vapor-phase dominated. If the ratio lies between 0.1 and 10, mass transfer resistances in both phases should be considered. Assuming the penetration theory to be valid in both the phases, this ratio can be calculated as,

$$\frac{k_l}{m_{eq,x} k_V} = \frac{C_{T,l}}{C_{T,V}} \sqrt{\frac{D_{aw,l}}{D_{aw,V}}} \frac{1}{m_{eq,x}} \tag{6.32}$$

Here, $C_{T,l}$ and $C_{T,V}$ are the molar concentrations, $D_{aw,l}$ and $D_{aw,V}$ are the binary diffusion coefficients of ammonia-water mixture in the liquid and vapor phases respectively, and $m_{eq,x}$ is the slope of the equilibrium curve. For the representative case at dilute solution concentration of 25%, absorber pressure of 345 kPa and solution flow rate of 0.026 kg/s, the second term in equation 6.31 is 75, as shown below

$$\frac{k_l}{m_{eq,x}k_V} = \frac{51.53(\text{kmol/m}^3)}{0.1392(\text{kmol/m}^3)}\sqrt{\frac{5.027\times10^{-9}(\text{m}^2/\text{s})}{8.312\times10^{-6}(\text{m}^2/\text{s})}}\frac{1}{0.1203} = 75.46 \qquad (6.33)$$

For the range of operating conditions considered in the present study, this ratio is significantly high except for cases at low dilute solution concentrations and high absorber pressures. The ratio varies between 30 and 590, except for the cases at the dilute solution concentrations of 5 and 15% at the absorber pressure of 500 kPa, where it varies between 15 and 20. Erickson *et al.* (1998) have also showed that for similar operating conditions, high pressure and low concentration (560 kPa and 9%), it is necessary to account for the mass transfer resistance in both phases. In this study, however, for majority of the test cases, the mass transfer appears to be dominated by vapor-phase mass transfer. Based on these comparisons, the vapor mass absorbed during the droplet formation regime is calculated using the Colburn-Drew method in the vapor phase. In the absence of an appropriate correlation for the vapor-phase mass transfer coefficient, it is calculated using a heat and mass transfer analogy in the vapor phase.

6.3.4.4 Estimation of Vapor Mass Absorbed during Droplet Formation

The amount of vapor absorbed in the droplets is obtained using the Colburn-Drew (Colburn and Drew 1937) method as follows:

$$\dot{n}_T = -C_{T,V}\times\beta_V\times\ln\left(\frac{\tilde{z} - \tilde{x}_{V,int}}{\tilde{z} - \tilde{x}_{V,bulk}}\right) \qquad (6.34)$$

$$\dot{m}_{dp,NH_3} = \dot{n}_T\times\tilde{z}\times M_{NH_3}\times A_{dp} \qquad (6.35)$$

$$\dot{m}_{dp,H_2O} = \dot{n}_T\times(1 - \tilde{z})\times M_{H_2O}\times A_{dp} \qquad (6.36)$$

$$\dot{m}_{dp} = \dot{m}_{dp,NH_3} + \dot{m}_{dp,H_2O} \qquad (6.37)$$

Here, $\tilde{x}_{V,int}$ and $\tilde{x}_{V,bulk}$ are the molar vapor concentrations at the interface and in the bulk. The vapor-liquid interface is assumed to be at equilibrium at the bulk solution temperature and the absorber pressure. Therefore,

$$x_{V,int} = f\left(T_{int} = T_{l,bulk}, P_{abs,ave}, q = 1\right) \tag{6.38}$$

Since the ammonia-water fluid pair has a volatile absorbent, the actual concentration of the condensing flux (z) is different from both the interface and bulk concentrations of the vapor. This is calculated using an interface energy balance as follows:

$$\Delta h_{int} = z \times h_{fg,NH_3} + \left(1 - z\right) \times h_{fg,H_2O} \tag{6.39}$$

In the Colburn-Drew equation, there are still two unknowns that need to be determined to estimate the amount of vapor absorbed in the droplets. These are the mass transfer coefficient (β_V) and the surface area A_{dp}. The mass transfer coefficient is calculated using the heat and mass transfer analogy as mentioned above. Since the vapor is essentially quiescent, a natural-convection heat-transfer coefficient is obtained for flow around a sphere using the following correlation (Incropera and DeWitt 2002),

$$Nuss_V = 2 + \frac{0.589 \times Ra_V^{1/4}}{\left(1 + \left(0.469/Pr_V\right)^{9/16}\right)^{4/9}} \tag{6.40}$$

$$Sh_V = Nuss_V \times \left(\frac{Sc_V}{Pr_V}\right)^{1/3} \tag{6.41}$$

$$\beta_V = Sh_V \times \frac{D_{aw,V}}{d_{pd}} \tag{6.42}$$

Here, $D_{aw,V}$ is the binary diffusion coefficient in the vapor-phase, and d_{pd} is the diameter of the primary droplet ($d_{pd} = 3 \cdot \left(\sigma/\rho g\right)^{1/3}$ (Yung et al. 1980)).

During droplet formation, the droplets are hanging at the underside of the tubes. For the calculation of the surface area, these droplets are idealized as hemispheres (Figure 6.8). The diameter of this hemispherical droplet is, however, different from the primary droplet diameter. As the droplet attached to the tube grows to a critical size, it starts descending and quickly detaches thereafter from the tube and falls on to the next tube. This diameter can be calculated by equating the volume of this half sphere to the primary droplet volume (Jeong and Garimella 2002). Therefore, the critical diameter is given as:

$$d_{pd,C} = 2^{1/3} \times d_{pd} \tag{6.43}$$

The number of such droplets per tube-row (each row consists of 4 tubes, since there are 4 columns in the tube array) is found using the total mass flow rate and the mass of the primary droplet as follows:

$$N_{dp} = \frac{\dot{m}}{(4\pi/3)(d_{pd}/2)^3 \rho} \tag{6.44}$$

For the representative test condition (345 kPa, 25% and 0.026 kg/s), the primary droplet diameter was found to be approximately 6 mm and its mass to be 0.104×10^{-3} kg. This results in about 240 droplets per second underneath a tube row for a solution flow rate of 0.026 kg/s. The number of droplets per tube-row was also found based on the droplet site spacing (λ_{dp}, (Armbruster and Mitrovic 1998)), dividing the tube length by the droplet site spacing.

$$N_{dp,\lambda} = 4 \times L_t / \lambda_{dp} \tag{6.45}$$

In the equation above, the factor of 4 accounts for the fact that there are 4 tubes in a tube row. For this representative test condition, the number of droplets per tube-row found using this method was about approximately 75. However, this is at any given instant.

For the representative test condition, the time of droplet formation is 0.28 s; therefore on average, at a given droplet site, three droplets will be formed. Therefore, the total number of droplets for a 1 second duration is 3 times the value predicted using equation 6.45 and is approximately 225 per second for the given flow rate. This value is in good agreement with the value calculated using equation 6.44.

The droplet surface area per tube row is calculated based on the droplet critical diameter as follows (it is divided by 2 because the droplet underneath the tube is a hemisphere),

$$A_{dp} = N_{dp} \times 4\pi \left(d_{pd,C}/2 \right)^2 /2 \tag{6.46}$$

It should be noted that this surface area is at the bottom of one tube row. In case of an absorber segment with multiple tube rows, the droplet area is multiplied by number of tube rows in that segment. For the representative case, the droplet critical diameter is approximately 7.7 mm and the droplet surface area per tube-row is 0.023 m^2. The solution properties in the droplet mode are calculated at droplet inlet conditions (exit of the tube row above). However, in the segment with multiple tube rows, the properties are calculated at the average conditions for that segment. With all the parameters known, the amount of vapor absorbed can be calculated using the Colburn-Drew equation.

6.3.4.5 Results for Segments involving Coolant

Using the methodology outlined above, the amount of vapor absorbed in the film and droplet parts of segments 3, 4 and 5 is obtained. Table 6.2 summarizes the results for these segments. The total amount of vapor absorbed in the film and droplet modes is found to be 2.42×10^{-4} kg/s (8.5% of the measured vapor flow rate), 1.34×10^{-3} kg/s (47.5%) and 1.32×10^{-3} kg/s (46.9%), in segments 3, 4 and 5 respectively for the representative case (25%, 345 kPa and 0.026 kg/s). Thus, it can be see that almost the

entire vapor flow rate (102% of the measured flow rate; this is higher than 100% as there is some desorption in segments 2 and 6 which is discussed in the next section) is absorbed in the segments involving heat exchange with the coolant. Table 6.2 also shows the relative contribution of the film and droplet modes to the absorption in these segments.

Table 6.2 Summary of Segmental Vapor Mass Absorbed in Coolant Segments for the Representative case (345 kPa, 25% and 0.026 kg/s)

Segment	$\dot{m}_{FF}$ (kg/s)	$\dot{m}_{dp}$ (kg/s)	$\dot{m}_{total,seg}$ (kg/s)	$\dot{m}_{dp}/\left(\dot{m}_{dp}+\dot{m}_{FF}\right)\%$	$\left(\dot{m}_{dp}+\dot{m}_{FF}\right)/\dot{m}_{Meas}\%$
Seg 3	2.173×10^{-04}	2.48×10^{-05}	2.42×10^{-04}	10.25	8.5
Seg 4	1.310×10^{-03}	3.29×10^{-05}	1.34×10^{-03}	2.45	47.5
Seg 5	1.312×10^{-03}	1.33×10^{-05}	1.33×10^{-03}	1.01	46.9

It can also be seen that the amount of vapor absorbed in the droplets is significant only in segment 3 (~ 10% of that segment). This fraction decreases further as the solution flows to the lower segments (Segments 4 and 5). This is probably due to a lower driving potential (solution concentration increases and temperature decreases) between the solution and the vapor in the lower segments. Figure 6.11 also shows the relative contributions of the falling-film and droplet modes in the cooled segment for this representative test condition. For this case, without accounting for the contribution of conduction described above, the amount of vapor absorbed would have been 7.62×10^{-4} kg/s (26.9%), 1.33×10^{-3} kg/s (47%) and 1.35×10^{-3} kg/s (47.5%) in segments 3, 4 and 5 respectively. It can be seen that if the contribution of conduction had not been accounted for, the amount of the vapor absorbed would have been over predicted (especially in segment 3, which is adjacent to the drip tray).
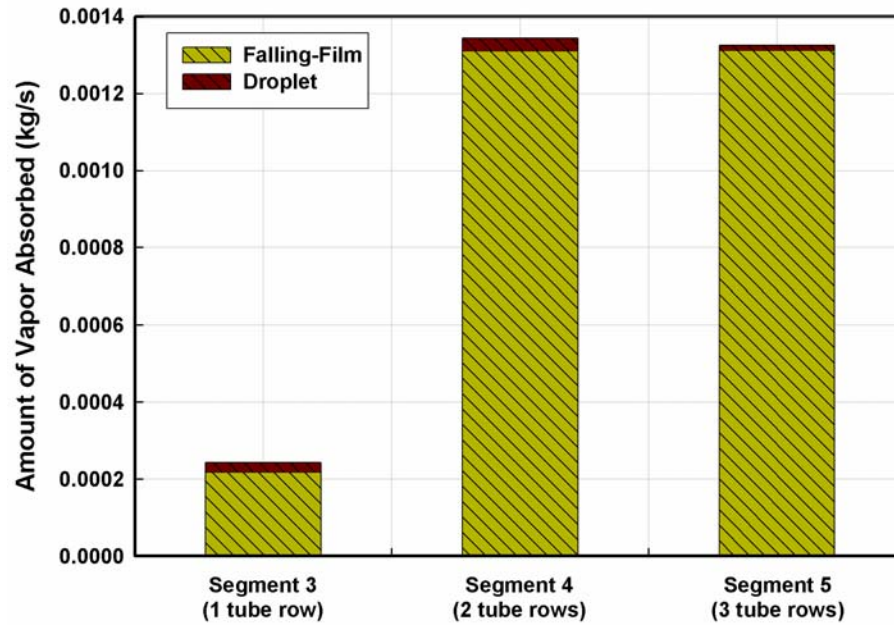
Figure 6.11 Relative Contributions of the Falling-Film and Droplet modes in the Cooled Segments (345 kPa, 25% and 0.026 kg/s)

Figure 6.12 shows the variation of solution temperature for the representative case in the coolant segment. It can be seen that due to near-adiabatic absorption in the droplets, the solution temperature rises at the exit of the falling-film phase on each tube row. The solution temperature increased from 47.16 to 47.59 (0.43°C) at the outlet of segment 3, from 39.7 to 40.22 (0.52°C) at the outlet of segment 4, and from 31.56 to 31.76°C (0.2°C) at the outlet of segment 5, for this test condition. The distance between segments in this figure is indicative of the lengths of these segments (i.e, segment 3 consists of one, segment 4 consists of two, and segment 5 consists of 3 tube rows, respectively).
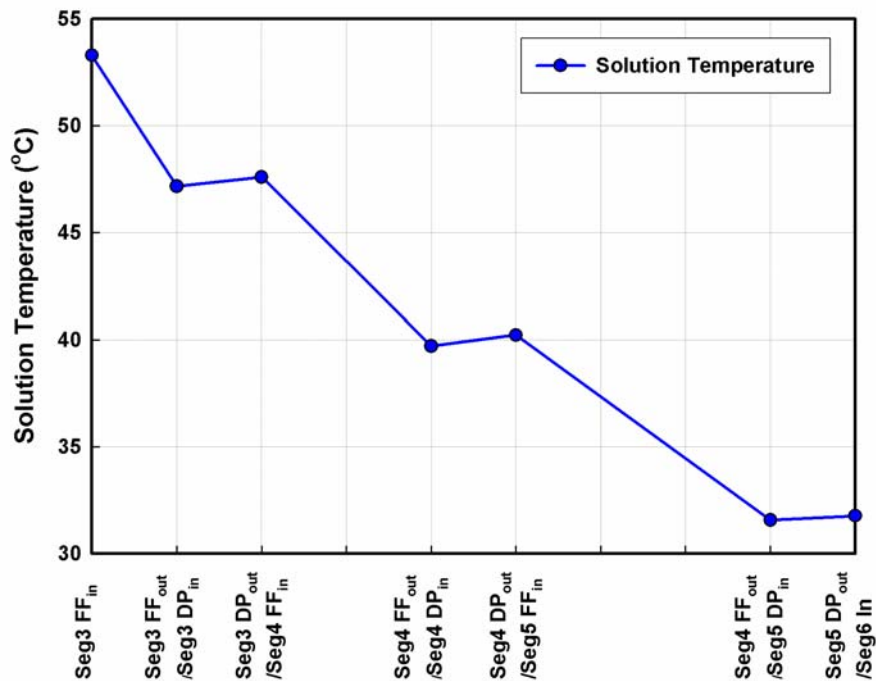
Figure 6.12 Variation of Solution Temperature in Cooled Segment (345 kPa, 25% and 0.026 kg/s)

6.3.5 Segments without Coolant

There are 3 segments that do not involve any absorber coolant (including the drip tray segment). Since the absorber coolant is not involved in these segments, the absorption/desorption process for these segment is considered adiabatic. The drip tray segment was discussed in the previous section (Section 6.3.3). The other two segments (segment 2 and 6) are discussed here.

6.3.5.1 Second Segment

The segment 2 extends from the outlet of the drip tray to just before the top of the tube row. This segment consists of the dilute solution droplets that are hanging at the exit

of the capillary tubes before falling on the first row of tubes. These droplets are considered to participate in the mass transfer process; therefore this transfer process is treated as a separate segment. The use of this segment also enables calculation of a more representative solution temperature at a vertical location halfway between the bottom of the drip tray and the top of the first row of tubes. The absorption/desorption process for this segment is adiabatic. At this segment, the solution inlet conditions are known from calculations at the drip tray segment, and the vapor conditions are also specified based on the uniform vapor conditions in the absorber. The solution outlet temperature is obtained from the solution temperature profile. The unknown values are the amount of the absorbed vapor, the solution outlet flow rate and the outlet concentration, which are calculated using mass, species and energy balances at the segment. The schematic for this segment is shown in Figure 6.13.
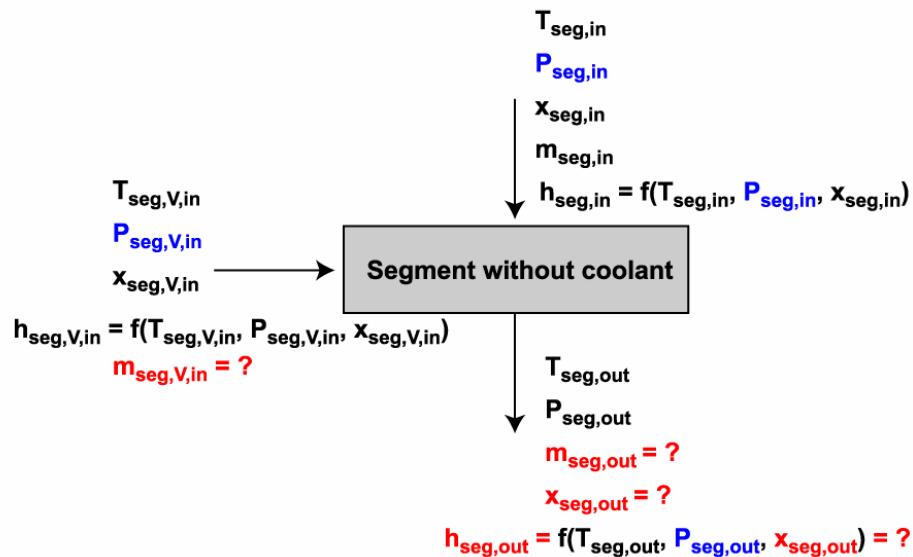
Figure 6.13 Schematic for Segments without Coolant (Segment 2)

The mass and species balance equations are similar to those used in the segments involving the absorber coolant; however, the energy balance equation is modified as follows:

$$\dot{m}_{seg,in} \times h_{seg,in} + \dot{m}_{seg,V,in} \times h_{seg,V,in} = \dot{m}_{seg,out} \times h_{seg,out} \qquad (6.47)$$

It should be noted that this segment does not involve any conduction heat transfer terms, either with the drip tray or with the headers. For several of the test conditions, some desorption was observed at this segment. For the representative case (25%, 345 kPa and 0.026 kg/s), the amount of vapor desorbed at this segment is 2.14×10^{-4} kg/s (approximately 7.5% of the measured vapor flow rate). This may be due to a higher dilute solution temperature or a larger solution concentration than that of the interface liquid concentration in the absence of any heat removal. It should also be remembered that this solution inlet temperature is based on a curve-fit of the thermocouple readings along the absorber, and in cases with the curve-fit values higher than the measured value, some desorption can be predicted to fit the profile, even if it does not actually occur.

6.3.5.2 Solution Pool

The solution pool is the last segment of the absorber, and is also an adiabatic segment similar to segment 2, except that the heat loss to the ambient is accounted for in this segment. Again, the solution inlet and the vapor conditions are fully specified, with the solution outlet temperature obtained from the solution temperature profile. The amount of the absorbed vapor is calculated using mass, species and energy balance equations. The schematic for this segment is shown in Figure 6.14. The mass and species balance equations are identical to those for the other segments involving absorber

coolant. However, the energy balance equation contains a term for heat loss to the ambient. The details of the heat loss calculation were discussed in the previous section. The energy balance equation is:

$$\dot{m}_{seg,in} \times h_{seg,in} + \dot{m}_{seg,V,in} \times h_{seg,V,in} = \dot{m}_{seg,out} \times h_{seg,out} + Q_{loss} \qquad (6.48)$$

For the representative case (25%, 345 kPa and 0.026 kg/s), the amount of vapor desorbed at the solution pool segment is 1.05×10^{-4} kg/s (approximately 3.7% of the measured vapor flow rate). Again, it can be seen that this amount is very small compared to the amount of vapor absorbed in the cooled segments.
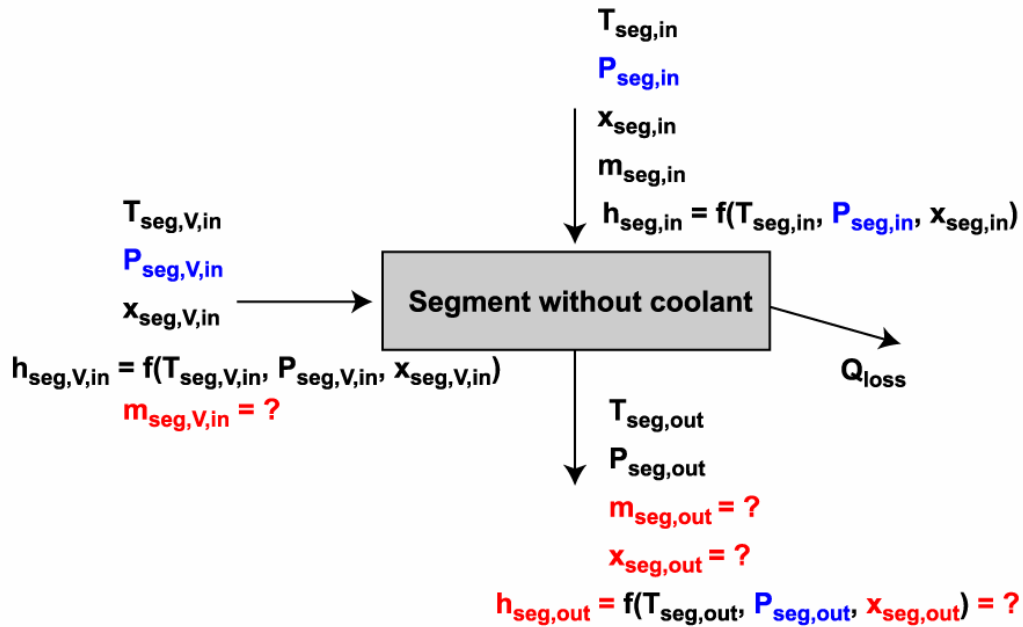
Figure 6.14 Schematic for Solution Pool Segment

6.4 Segment Heat and Mass Transfer Coefficients

The previous section discussed procedures to obtain segment heat duties and the mass absorbed in the various segments of the absorber. The cooled segments were further sub-divided into falling-film and droplet parts to obtain the relative contributions of these flow modes to the total absorption rates, i.e., $\Delta \dot{m}_{V,FF}$ and $\Delta \dot{m}_{V,dp}$. The analysis outlined also yielded solution temperatures at the outlet of the falling film on the tube surface. With these values, segmental film heat and mass transfer coefficients are calculated using the methodology outlined in Chapter 4 for obtaining overall film heat and mass transfer coefficients.

6.4.1 Segment Heat Transfer Coefficient

Segments 3, 4 and 5 contain 1, 2 and 3 tube rows respectively from the top of the absorber tube array. At each of the segments, the solution- and the coolant-side heat duties, the solution-film inlet and outlet temperatures, and the coolant inlet and outlet temperatures are specified or calculated based on the analyses described above. The overall heat transfer coefficient is calculated using the average segmental heat duty and an LMTD defined using the solution-film and coolant temperatures. Similarly, the segmental solution heat transfer coefficient is calculated using the segmental coolant-side heat duty, and an LMTD defined as the temperature difference between estimated solution-film temperatures obtained from the solution temperature profile and the analysis in the previous section, and the measured coolant temperatures. In addition to the above, conduction heat duties from the drip tray for each segment are used to modify the segmental coolant-side heat duties, as described in the previous section. The coolant-

side heat transfer coefficient is obtained from the literature using Churchill's (1977a; 1977b) correlation. It was discussed in Chapter 4 that four heat distinct regions were defined for the vapor absorption process. For each segment, the heat duties for the different heat regions are computed as explained in Chapter 4.

6.4.2 Segment Mass Transfer Coefficient

From the segmental analysis, the amount of the vapor absorbed in each segment and other parameters such as temperature, pressure and concentration are obtained. As discussed in Chapter 4, segmental vapor mass transfer coefficients are obtained using the Colburn-Drew (1937) methodology for each segment. The interface conditions are assumed as saturated liquid and vapor at the average solution bulk temperature for each segment, and the average absorber pressure. The liquid and vapor equilibrium concentrations at the interface are obtained from the above conditions. The amount of the absorbed vapor is obtained from the mass, species and energy balance equations and converted into a molar flux. The condensing flux concentration is computed from the latent heat balance for the binary mixture, and then a vapor mass transfer coefficient for each segment is obtained. These details were presented in connection with the overall absorber analysis in Chapter 4.

6.5 Segmental Results

This section presents results for a representative case of 25% dilute solution concentration at the desorber, 345 kPa (50 psi) absorber pressure and 0.026 kg/s (3.5 lb_m/min) concentrated solution flow rate. These conditions were also used in Chapter 4 to illustrate the single-point absorber analysis.

6.5.1 Comparison of Measured and Calculated Vapor Flow Rates

Figure 6.15 shows a comparison of the measured refrigerant vapor flow rate and the sum of the vapor absorbed in each of the segments, based on the above analysis. The figure also includes ±15% error bands. The total calculated amount of vapor absorbed is, therefore,

$$M_{Total,V,in} = \dot{m}_{seg1,V,in} + \dot{m}_{seg2,V,in} + \dot{m}_{seg3,V,FF,in} + \dot{m}_{seg3,V,dp,in} + \dot{m}_{seg4,V,FF,in} + \dot{m}_{seg4,V,dp,in} \\ + \dot{m}_{seg5,V,FF,in} + \dot{m}_{seg5,V,dp,in} + \dot{m}_{seg6,V,in} \tag{6.49}$$
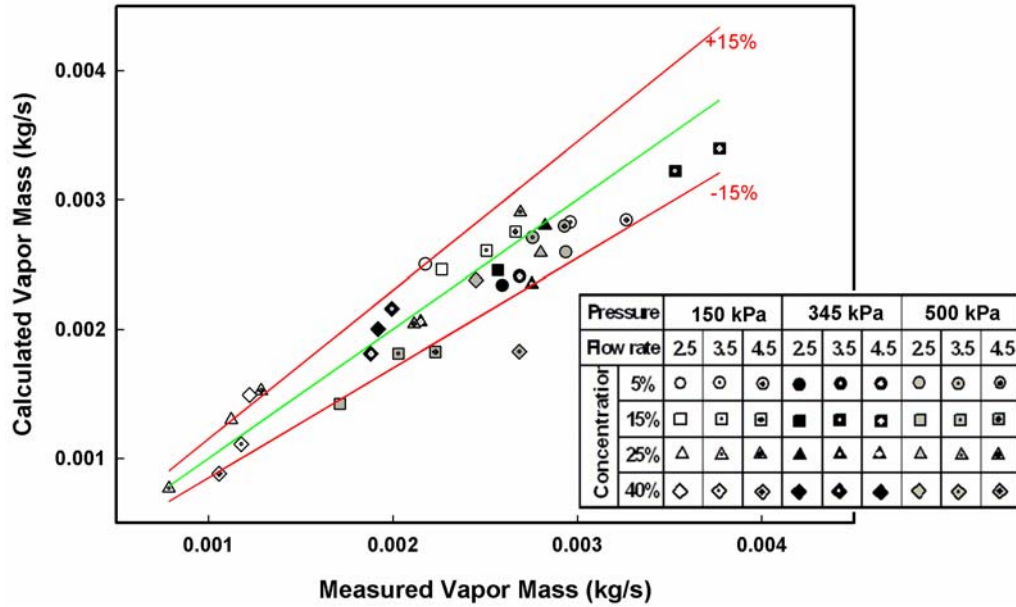
Figure 6.15 Comparison of Measured and Calculated Absorption Rates

It should be noted here that the droplet absorption contributions are obtained from the models in the literature discussed above while the local film absorption contributions and other adiabatic absorption components are directly obtained from the measured local

temperatures and the mass, species, and energy balances. The disagreement between the measured and calculated values is defined as follows:

$$\text{Frac}(\%) = \left(\left(\dot{M}_{\text{Total,V,in}} - \dot{m}_{V,in} \right) \right) \Big/ \dot{m}_{V,in} \times 100 \qquad (6.50)$$

As can be seen in Figure 6.15, there is good agreement between measured and computed vapor mass flow rates. The calculated total absorbed vapor mass is predicted within 15% of the measured vapor masses for 29 out of 36 data points (81%). Also, 25 of these 29 data points are predicted within 10% of the measured vapor masses. The larger discrepancies correspond to cases that are difficult to maintain experimentally due to combinations of low absorber pressure and high dilute solution concentration as described in Chapter 3.

6.5.2 Segmental Heat Duty and Heat Transfer Coefficient

Figure 6.16 shows the segmental heat transfer results for a representative case (0.026 kg/s, 25% and 345 kPa). Similar results are obtained for other test conditions. The heat duties for the different regions during absorption, and the segmental heat transfer coefficients are shown in this figure. It can be seen from the figure that the sensible heat terms representing the cooling of the vapor and the cooling of the condensed vapor are the smallest among all the heat duty terms. The negative values imply that the vapor as well as the condensed vapor are slightly heated by the absorption process at the vapor/liquid interface, although the effect is minimal. In segment 1 (the drip tray), the latent heat duty is positive (0.29 kW) showing that the vapor is absorbed in the drip tray as discussed in the previous section.
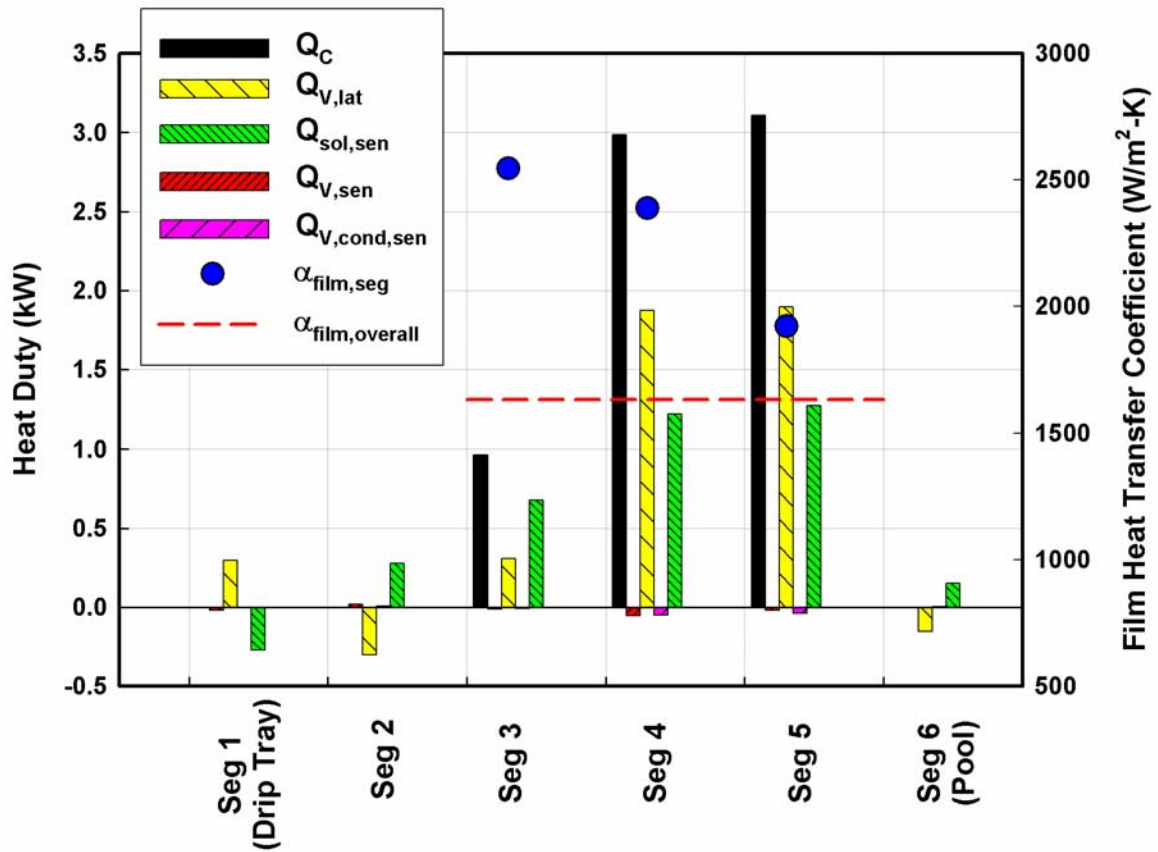
Figure 6.16 Segmental Heat Duty and Segmental Heat Transfer Coefficient (345 kPa, 25% and 0.026 kg/s)

However, it should be noted that depending on the test conditions, either desorption or absorption can take place at the drip tray. The vapor sensible heat duty is -0.02 kW while the condensed-vapor sensible heat duty is -0.006 kW. Clearly, these values are insignificant compared to the latent and solution sensible heat duties. For segment 2, the latent heat duty is negative (-0.3 kW) resulting in desorption at this segment. For the cooled segments (segments 3, 4 and 5), both the vapor latent heat and the solution sensible heat duties are large fractions of the coolant-side heat duty. Positive values of the latent heat duties imply absorption. It should be kept in mind that these three

segments have different heat transfer areas due to different numbers of tube rows, therefore conclusions can not be drawn about the heat transferred per unit area just based on these heat duties. As expected, absorption occurs most prominently in the segments cooled by the absorber coolant. For segment 3, the latent heat duty is 0.31 kW (32% of the coolant duty, 0.96 kW, for this segment) while the solution sensible heat duty is 0.68 kW (71% of the coolant duty). Similarly for segment 4, the latent heat duty is 1.87 kW (62.5% of the coolant duty, 2.99 kW, for this segment) while the solution sensible heat duty is 1.22 kW (40% of the coolant duty). And for segment 5, the latent heat duty is 1.89 kW (61% of the coolant duty, 3.1 kW, for this segment) while the solution sensible heat duty is 1.27 kW (40% of the coolant duty). For all these three segments, the vapor sensible and condensed vapor sensible heat duties are 1-2% of the respective coolant duties in the segment. Segment 6 represents the solution pool. The solution pool has the largest mass transfer area; therefore, some vapor may be absorbed or desorbed at the pool to maintain liquid–vapor equilibrium in the absorber. In this segment, some of the test cases show absorption, while others show desorption; however, these values are very small. For the representative case, the latent heat duty at segment 6 is -0.15 kW, resulting in a small amount of vapor (1.05×10^{-4} kg/s, approximately 3.7% of the measured vapor flow rate) being desorbed.

The overall film heat transfer coefficient (horizontal dotted line) and segmental heat transfer coefficients (circles) for this case are also shown in Figure 6.16 (read y-axis on right). It can be seen that the segmental solution heat transfer coefficients are significantly higher than the overall solution heat transfer coefficient. The overall solution heat transfer coefficient is calculated using the LMTD based on the absorber

211

inlet and outlet temperatures, which results in a relatively higher LMTD, because it includes the sub-cooling at the solution pool and the drip tray. However, higher segmental heat transfer coefficients are obtained from a relatively small LMTD, because the entire heat of absorption is carried away by the absorber coolant at segment 3, 4 and 5.

6.5.3 Segmental Vapor Mass Absorbed and Mass Transfer Coefficient

Figure 6.17 shows the mass absorbed in each segment and the mass transfer coefficient for a representative case (345 kPa, 25% and 0.026 kg/s).
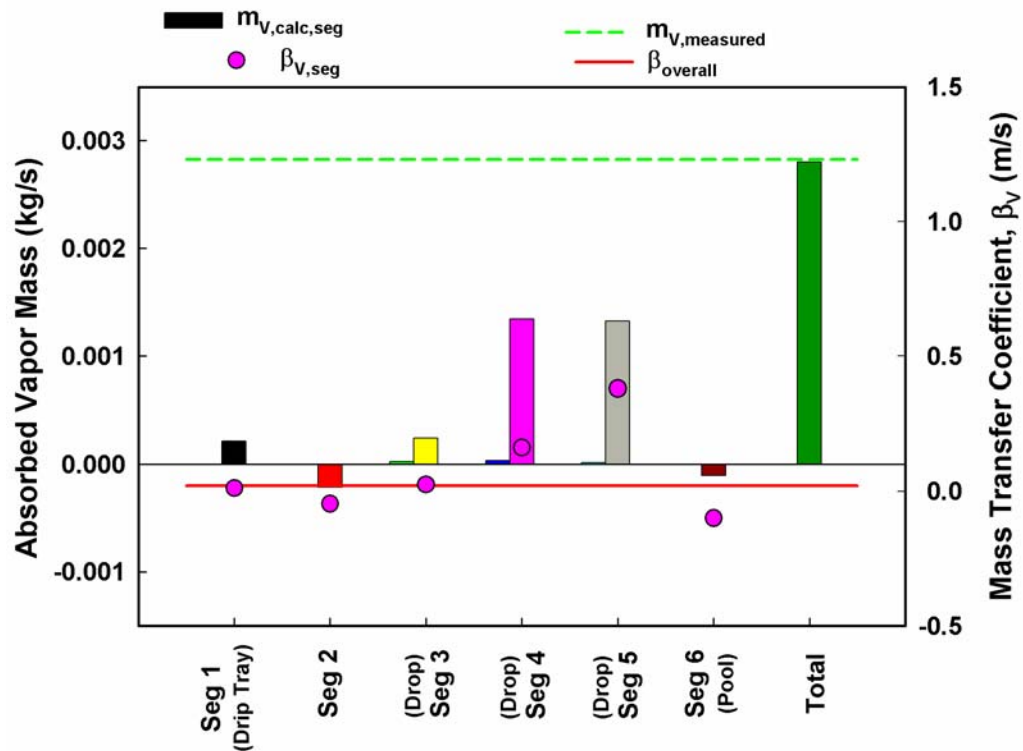
Figure 6.17 Segmental Vapor Mass Absorbed and Mass Transfer Coefficient (345 kPa, 25% and 0.026 kg/s)

Good agreement is seen between the measured (2.826×10^{-3} kg/s) and the calculated (2.804×10^{-3} kg/s) total vapor flow rates. At the drip tray segment, some absorption (2.125×10^{-4} kg/s) can be seen. This is a calculated value to account for the change in the vapor condition. As mentioned in the previous section, desorption is observed at segment 2 (-2.14×10^{-4} kg/s) and the solution pool segment (-1.05×10^{-4} kg/s), which are the segments with negative latent heat duty. A majority of the ammonia vapor is absorbed in segments 3 (2.42×10^{-4} kg/s, 8.5% of the measured), 4 (1.34×10^{-3} kg/s, 47.5% of the measured) and 5 (1.32×10^{-3} kg/s, 47% of the measured), where the absorption heat is removed by the absorber coolant. Since the mass transfer areas for each segment are not equal, the amount of absorbed vapor mass for each segment cannot be compared directly. The amount of vapor absorbed in segment 4 (1.34×10^{-3} kg/s) and 5 (1.32×10^{-3} kg/s) are relatively similar, although the area of segment 4 is 0.07 m^2 and that of segment 5 is 0.105 m^2. The mass absorbed per unit area decreases from segment 4 (1.91×10^{-2} kg/m^2-s) to segment 5 (1.35×10^{-2} kg/m^2-s). This is because of the relatively lower driving temperature differences in the lower segments. For example, the LMTD in segment 3 is 32.4°C while those in segment 4 and segment 5 are 27.42°C and 22.03°C, respectively. Figure 6.17 also shows the estimated amount of vapor absorbed in the droplets. It can be seen that this amount is very small compared to the vapor absorbed in the tube part of the coolant segment. Except for some test cases of 5% and 15% dilute solution concentration at an absorber pressure 500 kPa, and of 5% dilute solution concentration at the absorber pressure of 345 kPa, the estimated amount of vapor absorbed is less than 6%. In the extreme of high pressure and low concentration cases, some cases showed an estimated amount of 30%. This is probably due to the low solution concentration that provides a

large potential for absorption (concentration difference between the vapor and solution) without additional cooling. However, it should be kept in mind that these were the most difficult cases to obtain and experimental uncertainties could be high. Therefore, these estimates may not be as accurate as those at other conditions. In the discussion of the segmental heat transfer results, it was found that the segmental heat transfer coefficients are higher than the overall solution heat transfer coefficient for the whole absorber. However, this is not true for all the segments for the vapor mass transfer coefficient as the mass transfer coefficient is negative for the segments where desorption is taking place. It should be noted that these coefficients could also be shown as positive values with a change in sign of the mass flow rate depicting desorption. For the segments cooled by the absorber coolant, the mass transfer coefficient increases as the solution flows from the top ($\beta_{v,seg3}$ = 0.024 m/s) to the bottom ($\beta_{v,seg5}$ = 0.379 m/s) of the tube array and is higher than the overall mass transfer coefficient (0.02 m/s (Lee 2007)).

6.5.4 Droplet Absorption Rates

For the cooled segments, contributions of the falling-film and droplet mode were also obtained for the range of experiments conducted. Figure 6.18 shows the fraction of vapor absorbed in droplets in the present study. In general, the fraction of vapor absorbed in droplets is larger at higher solution flow rates at any given absorber pressure and dilute solution concentration. In some cases, however, the solution flow rate of 0.011 kg/m-s (0.026 kg/s or 3.5 lb$_m$/min) shows larger fractions than at the highest flow rate of 0.0135 kg/m-s (0.034 kg/s or 4.5 lb$_m$/min). Jeong and Garimella (2002) also reported an increasing fraction of vapor absorbed in droplets at higher solution flow rates during absorption of water vapor by aqueous LiBr solution.

214
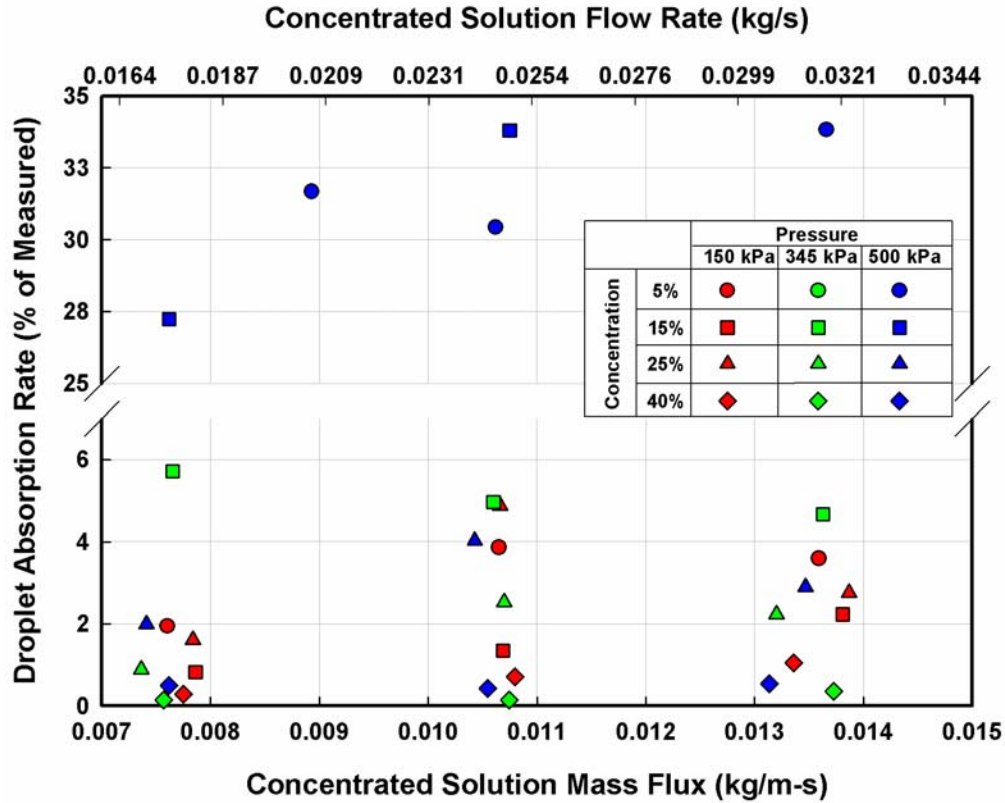
Figure 6.18 Fraction of Absorption Rate in the Droplet Mode

In their simulation results, they found that about 14% of water vapor was absorbed in droplet formation mode for a mass flux of 0.006 kg/m-s. For a similar mass flux of 0.0075 kg/m-s, the highest fraction of vapor absorbed in droplets in the present study is about 6%. Because of higher liquid-phase diffusivities, the amount of vapor absorbed in the droplets will be smaller for the ammonia-water fluid pair. The highest mass flux of 0.0135 kg/m-s in the present study is smaller than the highest mass flux of 0.106 kg/m-s in the work of Jeong and Garimella (2002). As discussed above, the amount of vapor absorbed in droplets was estimated using a surface area based on the critical diameter of the primary droplet. To investigate the effect of using a different area, the amount of vapor absorbed was also estimated using a surface area based on the diameter of primary

droplet. Equation 6.43 provides the relationship between these two diameters (Please also refer to Figure 6.8). For the representative case (25%, 345 kPa and 0.026 kg/s), the fraction of vapor absorbed in droplets changed from 2.53 to 3.17%, when the mass transfer area changed from 0.13 m^2/s for a critical drop diameter of 7.64 mm to 0.16 m^2/s for a primary droplet diameter of 6.06 mm (~ 23% change). The mass transfer area based on the critical drop diameter is smaller than the area based on the primary droplet diameter because the critical diameter droplets were considered as hemispheres at the bottom of the tubes (therefore, only half the surface area participates in mass transfer). Similarly, the largest fraction changed from 6 to 7%. Thus, the amount of vapor absorbed in droplets still remains relatively negligible compared to the amount absorbed in the falling-film region.

The effect of the absorber pressure is mixed and direct conclusions can not be drawn from the data. It appears that the relative absorption in droplets increases slightly as the absorber pressure increases at a given solution flow rate and dilute solution concentration. Dilute solution concentration, however, seems to affect the droplet absorption rate significantly. In general (leaving out a few exceptions), the absorption rate in the droplets is larger at smaller dilute solution concentrations. In Figure 6.18, for any given absorber pressure, the 40% concentration cases (represented by diamonds) show the lowest fractions (located towards the bottom of the graph) while the 5 and 15% cases (represented by circles and rectangles, respectively) show the highest fractions. Since the actual dilute solution concentration entering the absorber for the 5 and 15% nominal cases was similar, these two concentration cases show somewhat similar results for droplet absorption rates. Test cases at 25% dilute solution concentration show

droplet-mode absorption fractions between those for the 40% and 15% solution concentration cases, except at the 150 kPa where the 25% solution concentration cases show larger fractions than those for the 15% solution concentration cases. The reason for this behavior is not apparent; however, these cases had the smallest amount of vapor absorbed among all the test cases. One possible explanation for the larger fractions of vapor absorbed in droplets at smaller concentrations could be the larger concentration differences between vapor and liquid at these conditions. Since the solution contains a very small amount of ammonia at these conditions, a larger amount of vapor can be absorbed by the solution without additional cooling, i.e., in droplet-mode adiabatic absorption. In addition, the 5 and 15% solution concentration cases at 500 kPa are also the cases where the mass transfer resistances in both phases were found to be significant (discussed in the previous section on interface mass transfer). Based on these trends, it could be said that the amount of vapor absorbed in droplets increases with increasing absorber pressure and decreasing dilute solution concentration.

6.6 Segmental Results in Non-dimensional Form

Both the overall results in Chapter 4 and the segmental results above are presented in terms of the measured heat and mass transfer coefficients as a function of the measured solution flow rate. These results can be generalized using the appropriate non-dimensional parameters such as the Nusselt number and the Sherwood number, which are discussed below.

6.6.1 Relevant Non-dimensional Parameters for Heat Transfer

The primary non-dimensional parameters pertinent to heat transfer phenomena are the Nusselt, Prandtl and Reynolds numbers. The solution Reynolds number ($Re_{seg,l}$) is defined using the normalized concentrated solution flow rate ($\Gamma_{seg,l}$) and the dynamic viscosity of the solution as follows (the segmental value of $Re_{seg,l}$ is calculated by substituting appropriate values of the mass flux and viscosity for that segment; the same is true for the other non-dimensional parameters):

$$Re_{seg,l} = \frac{4 \times \Gamma_{seg,l}}{\mu_{seg,l}} \qquad (6.51)$$

where $\Gamma_{seg,l} = \dfrac{\dot{m}_{seg,l}}{N_{t,pr} \cdot L_t \cdot 2}$, and $\dot{m}_{seg,l}$ is the average (of the inlet and outlet) segmental solution mass flow rate, $N_{t,pr}$ is the number of tubes in each row of the tube array, and L_t is the length of the tubes. The solution flow rate is divided by 2 because the solution flows on two sides of the tubes. The solution Prandtl number ($Pr_{seg,l}$) is defined as follows:

$$Pr_{seg,l} = \frac{\mu_{seg,l} \times C_{p,seg,l}}{k_{seg,l}} \qquad (6.52)$$

The solution heat transfer coefficient is non-dimensionalized to obtain the solution Nusselt number as follows:

$$Nu_{seg,l} = \frac{\alpha_{seg,l} \times \delta_{seg,l}}{k_{seg,l}} \qquad (6.53)$$

Here, to define the solution Nusselt number ($Nu_{seg,l}$), the solution film thickness is used as the characteristic dimension. The solution film thickness is the preferred characteristic dimension in falling-film flow. Figure 6.19 shows a schematic of the falling-film on a horizontal tube. (It should be noted that the solution film thickness is obtained assuming a uniform thickness film around the tube).
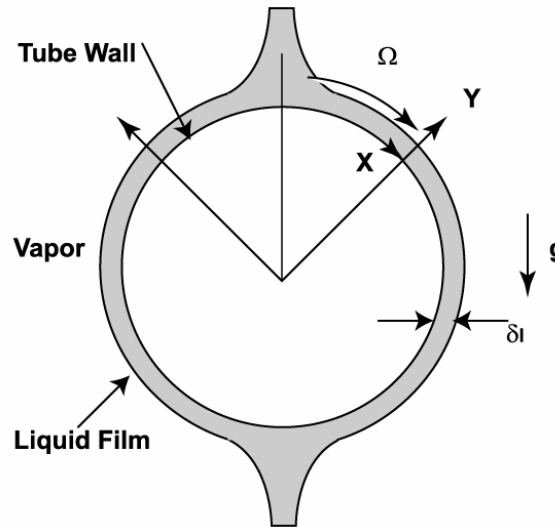
Figure 6.19 Falling-Film around the Tube

The Nusselt condensation film thickness definition (Bird *et al.* 2002) is used in this study for the solution film thickness.

$$\delta_{seg,l} = \left[\frac{3 \times \mu_{seg,l} \times \Gamma_{seg,l}}{g \times \rho_{seg,l}^2} \right]^{1/3} \times \frac{2}{\pi} \times \int_0^{\pi/2} \sin^{-1/3}\Omega \times d\Omega \tag{6.54}$$

Since the solution flows on the two sides of the cylinder, to obtain the average film thickness, the above equation is integrated from 0 to $\pi/2$.

$$\delta_{seg,l} = \left[\frac{3 \times \mu_{seg,l}^2 \times Re_{seg,l}}{4 \times g \times \rho_{seg,l}^2} \right]^{\frac{1}{3}} \times \frac{2}{\pi} \times (2.103) \qquad (6.55)$$

Once the film thickness is obtained, the solution $Nu_{seg,l}$ is obtained using the solution heat transfer coefficient, the solution thermal conductivity, and the film thickness.

6.6.2 Segmental Solution Nusselt Number ($Nu_{seg,l}$)

Figure 6.20 shows segmental Nusselt numbers for segment 4 as a function of the solution Reynolds number ($Re_{seg,l}$). The higher $Re_{seg,l}$ can be obtained either with a higher mass flux or with a lower viscosity. The $Nu_{seg,l}$ increases as the $Re_{seg,l}$ increases at a constant absorber pressure. It can also be seen that absorber pressure has a significant effect on the $Nu_{seg,l}$. At a higher pressure, a similar $Nu_{seg,l}$ is obtained at a much higher $Re_{seg,l}$ (as can be seen with a rightward shift with an increase in the absorber pressure). In other words, as the absorber pressure increases, the Nusselt numbers for a given $Re_{seg,l}$ are smaller. Ammonia-water solution viscosity increases with concentration (4.14×10^{-4} kg/m-s at 20% to 9.74×10^{-4} kg/m-s at 40%); therefore, at a constant absorber pressure, for the same solution mass flux, the solution $Re_{seg,l}$ is smaller at the higher concentrations, which would yield a lower $Nu_{seg,l}$. This means that a $Re_{seg,l}$ dependence could address the effect of the mass flow rate and the effect of the concentration change through the viscosity on $Nu_{seg,l}$. However, the pressure effect cannot be accounted for by $Re_{seg,l}$ alone.
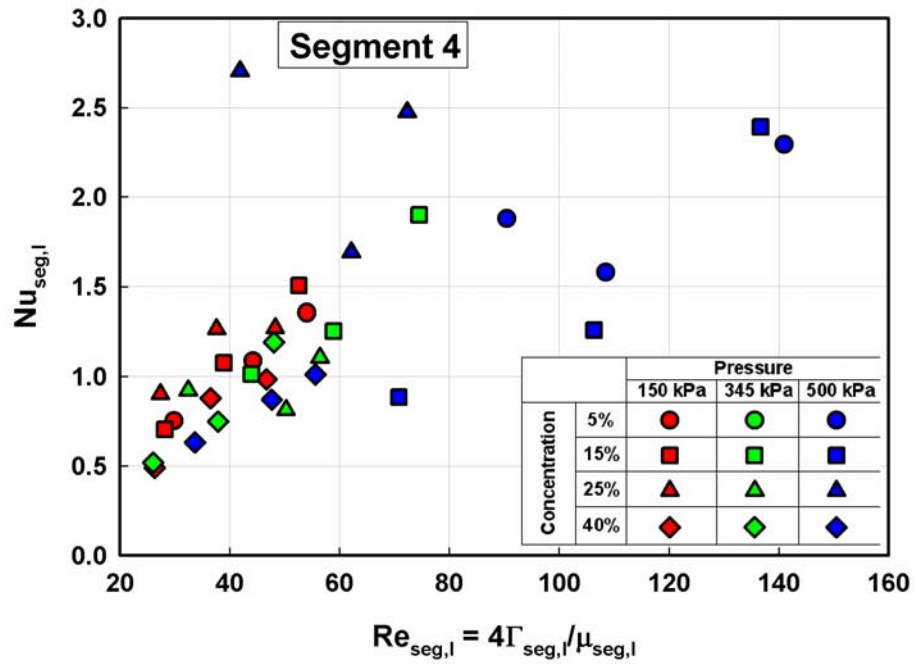
Figure 6.20 Segment 4 Nu vs Re

Figure 6.21 shows the segmental Nusselt number for the segment 4 as function of the solution Prandtl number ($Pr_{seg,l}$). Although the trends in $Nu_{seg,l}$ as $Pr_{seg,l}$ varies are not very clear, it can be seen that $Nu_{seg,l}$ decreases slightly at a constant absorber pressure and dilute solution concentration as the solution $Pr_{seg,l}$ increases. The influence of the absorber pressure can be seen in this figure also, as the higher pressure cases are located towards the smaller $Pr_{seg,l}$, while the lower pressure cases are located towards higher $Pr_{seg,l}$. Similar trends are observed for other segments also.
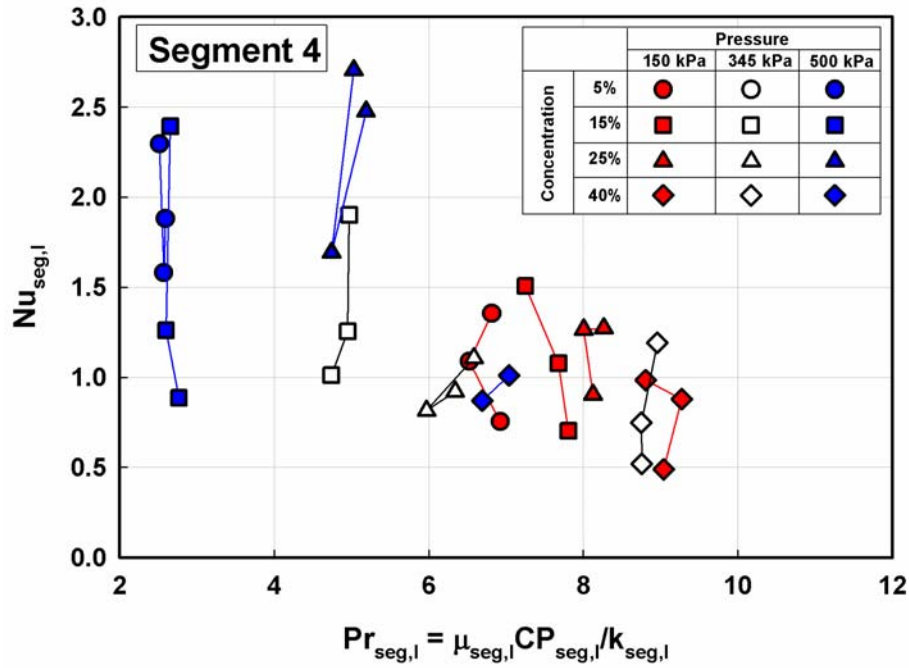
Figure 6.21 Segment 4 Nu vs Pr

6.6.3 Comparison with the Heat Transfer Literature

There are very few studies in the literature that provide correlations for Nu_l in the horizontal-tube falling-film configuration for ammonia-water absorption. The available correlations with any relevance to the present study are used for comparison with the present data. It should be noted that these studies use different definitions for some of the parameters such as the solution Re, mass flux and the film thickness. The differences in these definitions were appropriately accounted for while using these correlations to predict the present data. To avoid confusion due to the different definitions, the falling-film heat transfer coefficients from this study, rather than the Nusselt numbers, are compared with the predictions from the literature.
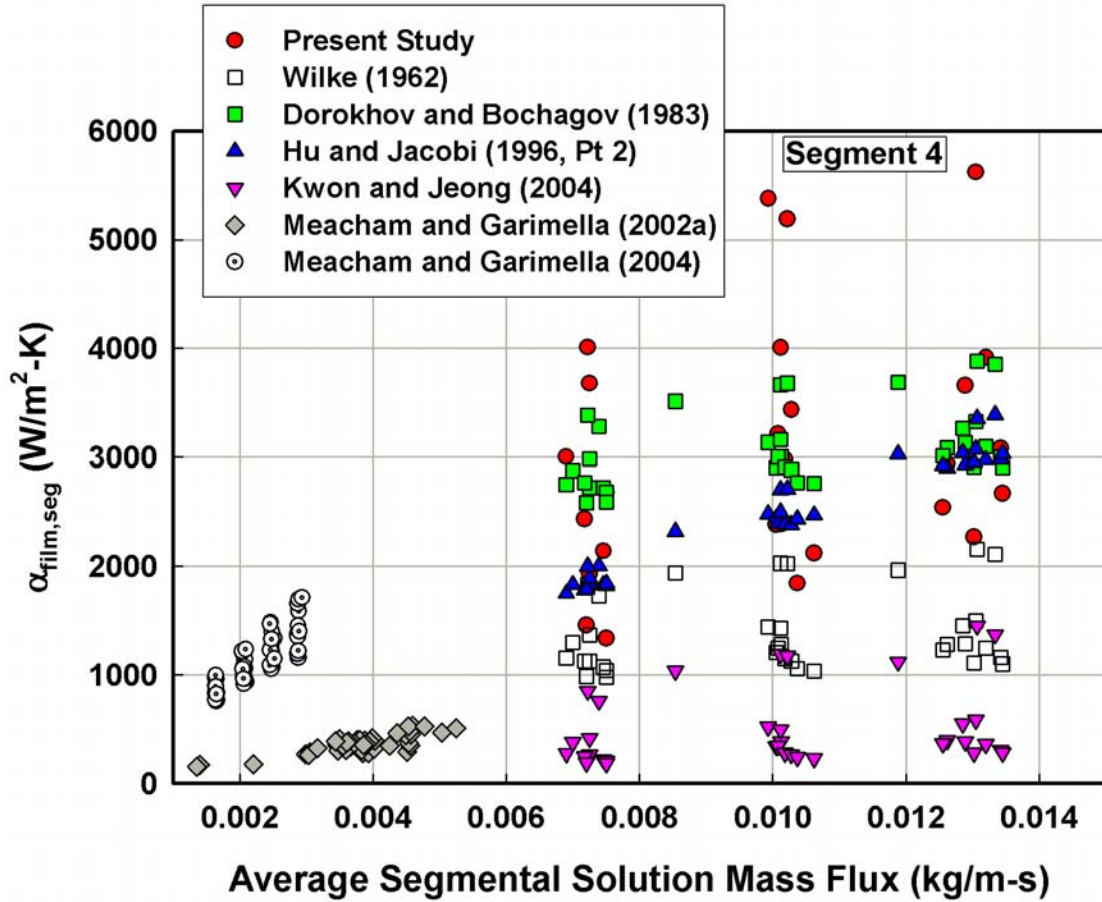
Figure 6.22 Comparison of $\alpha_{Film,seg}$ with the Literature (Segment 4)

Figure 6.22 shows a comparison of the heat transfer coefficients for segment 4 obtained in the present study with the predictions from Wilke (1962), Dorokhov and Bochagov (1983), Hu and Jacobi (1996b), Kwon and Jeong (2004), and the data of Meacham and Garimella (2002a) and Meacham and Garimella (2004). Similar results were obtained for other segments as well. A summary of the correlations is provided in Table 6.3. It should be noted that none of these correlations was developed for a horizontal falling-film tube absorber in an ammonia-water system (except for the data of Meacham and Garimella, which were on horizontal tube banks with tubes of 1.575 mm O.D.). Wilke (1962) developed Nusselt number correlations for the flow of a water-

glycol mixture over a vertical tube (42 mm O.D. and 2.4 m long) for different ranges of the solution Reynolds number ($Re_l < 400$; $400 < Re_l < 800$; $Re_l > 800$). It can be seen that this correlation predicts smaller values of the segmental heat transfer coefficient compared to the present data. The disagreement between his predictions and the present data may be due to the differences in geometry and the range of Reynolds numbers. For most of the data from the present study, the solution Re is less than 100. Also, his study did not involve any gas absorption and was simply a study of single-phase heat transfer in a falling film. Dorokhov and Bochagov (1983) developed a Nu correlation as a function of the solution Peclet number ($Pe_l = Re_l \cdot Pr_l$), film thickness and a characteristic length (half of the tube periphery in the case of a cylindrical tube) for the flow of water/LiBr (57% LiBr by weight) over a column of six horizontal tubes, where the heat duties were measured only for the last two tubes. It should be noted that Dorokhov and Bochagov correlation predicted much higher values of the heat transfer coefficient at the component level (Lee 2007). However, as seen here at the segmental level, the disagreement is relatively smaller. This is probably due to the fact that Dorokhov and Bochagov developed the correlation at the local level, which considers the mixing in the solution film caused by break-up of the film between consecutive tubes. The disagreement between their predictions and some of the present data may be due to the very small absorber pressures (~ 10 kPa) characteristic of LiBr-H_2O systems and the higher solution mass flux in their study. It should be also noted that LiBr-H_2O is a fluid pair with a non-volatile absorbent whereas NH_3-H_2O has a volatile absorbent. Their solution mass flux varies between $0.05 - 0.25$ kg/m-s, which is significantly higher than the highest mass flux (0.015 kg/m-s) in the present study. In addition, their correlation is valid for $1 <$

$2 \cdot Pe_l \cdot \delta_l / (\pi \cdot d) < 20$; and the data from the present study are towards the lower limit

$(2 \cdot Pe_{l,seg} \cdot \delta_{l,seg} / (\pi \cdot d) \sim 1)$ of the validity of their correlation. Hu and Jacobi (1996b)

developed   Nu   correlations   using Re_l, Pr_l,   Archimedes   number

($Ar_l = \left(\sigma_l^3 \Big/ \left(\nu^4 \cdot \rho^2 \cdot g \cdot (\rho_l - \rho_v) \right) \right)^{1/2}$), tube spacing, and the tube diameter as the

parameters for the flow of a Water/Glycol mixture and several other fluids on a

horizontal tube. Different flow regimes were defined based on the modified Galileo

number ($Ga_l = \left(\rho_l \cdot \sigma_l^3 \right) \Big/ \left(\mu_l^4 \cdot g \right)$). All the data from the present study fall under the

droplet flow regime according to their flow regime map. Therefore, the correlation

developed for the droplet mode is used here to predict the film heat transfer coefficient

from the present study. For a majority of the test conditions, their correlation predicts

smaller segmental heat transfer coefficients for the range of conditions tested in the

present study. The lower predictions of the segmental heat transfer coefficients may be

due to the different film thickness definition used by them. This definition, $\delta = \left(\dfrac{\nu^2}{g} \right)^{\!\!\frac{1}{3}}$,

makes the film thickness independent of the solution flow rate. In addition, their

correlation does not account for gas absorption and is only for single-phase heat transfer

in films falling around horizontal tubes. Kwon and Jeong (2004) developed Nu_l

correlations for a helical coil absorber used in ammonia/water absorption for both

counter-current and parallel flow arrangements using the solution Re and liquid-vapor

interfacial shear stress ratio. They used a 12.7 mm diameter tube coiled over an 82.7 mm

diameter for this study. The absorber was 600 mm long with a shell diameter of 114 mm.

The solution mass flux varied from 4.43×10^{-3} kg/m-s to 90.9×10^{-3} kg/m-s at dilute

solution concentrations of 3.13%, 14% and 30.0%. They noted that Nu_l is primarily

affected by the solution Re and the effect of liquid-vapor interfacial shear stress can be

neglected in the parallel flow arrangement. As can be seen in Figure 6.22, their

correlation predicts much smaller solution heat transfer coefficients than the present

values. This may be due to the different driving temperature differences used in the two

studies. Their solution temperatures are close to saturation temperatures corresponding to

the absorber pressure and solution concentrations in their study, while the solution is

considerably sub-cooled in the present study (in certain instances, the degree of outlet

sub-cooling is as high as 33°C). In addition, the absorber pressures are also low in their

study (17 - 193 kPa). Meacham and Garimella (2002a) conducted absorption

experiments on a micro-channel falling-film absorber. The absorber geometry consists of

short lengths (14 mm) of microchannel tubes (1.575 O.D.) arranged in a square array.

These tubes were arranged in 5 passes, where each pass consists of 16 tube rows. Each

of the tube rows had 27 tubes. The total surface area of the absorber was 1.5 m^2. Their

solution mass flux varied in the range 0.0014 – 0.0053 kg/m-s and the vapor

concentration varied in the range 5 – 50%. The average absorber heat duties transferred

were 4.86 - 16.23 kW with solution heat transfer coefficients of 155 - 530 W/m^2-K

(corrected for the difference in the LMTD definitions used in the two studies). The data

of Meacham and Garimella (2002a) show much smaller experimental heat transfer

coefficients; however, it should be kept in mind that the mass fluxes in their study are

much smaller than those in the present study. This is because, although the mass flow

rates used by them were similar (0.010 to 0.040 kg/s) to those in the present study (0.019

- 0.034 kg/s), the solution was distributed over 27 tubes, 0.140 m long for a total length

of 3.78 m, whereas in the present study the total tube length per row was 1.17 m. The data of the Meacham and Garimella (2004) show much higher film heat transfer coefficients compared to the results from their previous study (Meacham and Garimella 2002a).   The increase was attributed to significant improvement in the solution distribution over the tube array. It can also be seen that their newer data have heat transfer coefficients comparable to those from the present study even at much smaller solution mass fluxes. The differences between their experimental values and the present data may be due to the microchannel geometry used by them. In addition, their heat transfer coefficients are those obtained at the component level.

Table 6.3 Summary of Relevant Heat Transfer Studies

	Type and Fluid	Mass Transfer /Phase Change	Geometry	Test Conditions	Γ_l (kg/m–s)	Film Thickness δ (m)	Re_l	Nu_l	Applicability
Wilke (1962)	Vertical Tube (H_2O/ Glycol mixture)	No	Tube Length: 2.5 m Tube OD: 42	Water /Glycol 0, 16%, 55.5%, 77.1%, 95% (%Glycol)	$\dfrac{\dot{m}}{N_t \cdot L_t \cdot 2}$	$\left[\dfrac{3 \cdot \mu_l \cdot \Gamma_l}{g \cdot \rho_l^2}\right]^{1/3} \cdot \dfrac{2}{\pi} \cdot \int_0^{\pi/2} \sin^{-1/3}\Omega \cdot d\Omega$	$\dfrac{\Gamma}{\mu}$	$0.0614 \cdot Re^{8/15} Pr^{0.344}$ $0.00112 \cdot Re^{6/5} Pr^{0.344}$ $0.0066 \cdot Re^{14/15} Pr^{0.344}$	$Re < 400$ $400 < Re < 800$ $Re > 800$
Dorokhov and Bochagov (1983)	Horizontal Tube (H_2O/ LiBr)	Yes	Tube OD:19 Tube Length: 240 Tube Spacing: 28.12	57% LiBr Pressure: –10 kPa Flow Rate: 0.05 – 0.25 kg/m–s	$\dfrac{\dot{m}}{N_t \cdot L_t \cdot 2}$	$\left[\dfrac{3 \cdot \mu_l \cdot \Gamma_l}{g \cdot \rho_l^2}\right]^{1/3} \cdot \dfrac{2}{\pi} \cdot \int_0^{\pi/2} \sin^{-1/3}\Omega \cdot d\Omega$	$\dfrac{\Gamma}{\mu}$	$1.03 \cdot \left(\dfrac{2 \cdot Pe \cdot \delta}{\pi \cdot d_{o,t}}\right)^{0.44}$	$1 < \dfrac{2 \cdot Pe \cdot \delta}{\pi \cdot d_{o,t}} < 20$
Hu and Jacobi (1996b)	Horizontal Tube (H_2O and Glycol and mixtures)	No	Tube OD:15.88, 19.05, 22.22 Tube Spacing: 5–50 Groove Depth : 0.51, 0.76 Groove Width : 2.54, 0.81	Flow Rate: ~ 0.72 kg/m–s T_{in}: 20–40ºC Heat Flux: ~1.15×10⁵ W/m²	$\dfrac{\dot{m}}{N_t \cdot L_t}$	$\delta = \left(\dfrac{\nu^2}{g}\right)^{1/3}$, $Ar = \dfrac{d_{o,t}^3 \cdot g}{\nu^2}$	$\dfrac{2\Gamma}{\mu}$	$2.194 \cdot Re^{0.28} Pr^{0.14} Ar^{-0.20} \left(s/d_{o,t}\right)^{0.07}$ $1.387 \cdot Re^{0.42} Pr^{0.26} Ar^{-0.23} \left(s/d_{o,t}\right)^{0.08}$ $0.113 \cdot Re^{0.85} Pr^{0.85} Ar^{-0.27} \left(s/d_{o,t}\right)^{0.04}$	Sheet Mode Jet Mode Droplet mode
Meacham and Garimella (2002a)	Horizontal Tube Micro– channel (NH_3 /H_2O)	Yes	Tube OD:1.575 Tube Length: 0.14 m Tube Pitch : 4.76 Tube Row Vertical Pitch: 4.76 Tubes per Row: 27 Rows per Pass: 16 Number of Passes: 5 Height: 0.508 m Absorber Area: 1.50 m²	Solution FR: 0.010 – 0.040 kg/s Vapor Generation Fraction: 10 – 50% x_{vapor}= 0.8697 $x_{concentraed}$ = 0.3807 x_{dilute} = 0.2289	$\dfrac{\dot{m}}{N_t \cdot L_t}$	$\left[\dfrac{3 \cdot \mu_l \cdot \Gamma_l}{g \cdot \rho_l^2}\right]^{1/3} \cdot \dfrac{2}{\pi} \cdot \int_0^{\pi/2} \sin^{-1/3}\Omega \cdot d\Omega$	$\dfrac{4\Gamma}{\mu}$		
Meacham and Garimella (2004)	Horizontal Tube Micro– channel (NH_3 /H_2O)	Yes	Tube OD:1.575 Tube Length: 0.137 m Tube Pitch: 7.94 Tube Row Vertical Pitch: 7.94 Tubes per Row: 33 Rows per pass: 2 Number of Passes: 10	Solution FR: 1.51×10⁻²– 2.66×10⁻² kg/s Vapor Fraction: 15%, 20%, 25%, 30% x_{vapor}= 0.93–0.98 T_{in} and (Pressure) 52ºC (355 kPa) 81ºC (680 kPa)	$\dfrac{\dot{m}}{N_t \cdot L_t}$	$\left[\dfrac{3 \cdot \mu_l \cdot \Gamma_l}{g \cdot \rho_l^2}\right]^{1/3} \cdot \dfrac{2}{\pi} \cdot \int_0^{\pi/2} \sin^{-1/3}\Omega \cdot d\Omega$	$\dfrac{4\Gamma}{\mu}$		

Table 6.3 Summary of Relevant Heat Transfer Studies (Continued)

	Type and Fluid	Mass Transfer /Phase Change	Geometry	Test Conditions	Γ_l (kg/m–s)	Film Thickness δ (m)	Re_l	Nu_l	Applicability
			Height: 0.15 m Absorber Area: $0.45 m^2$						
Kwon and Jeong (2004)	Helical Coil (NH_3/ H_2O)	Yes	OD: 12.7 L_{abs}: 600 Coil OD: 82.7 Coil Windings: 30	Solution Flow Rate 4.43–90.0 g/s–m x_{dilute} = 3.13%, 14%, 30% T_{in} = 45 °C, 55 °C, 60 °C $T_{Coolant}$ = 30 °C P = 0.17–1.93 bar	$\dfrac{\dot{m}}{N_t \cdot L_t}$	$\delta = \left(\dfrac{v^2}{g}\right)^{1/3}$	$\dfrac{2\Gamma}{\mu}$	$1.975 \times 10^{-3} \cdot Re^{0.6895} \, \tau^{-0.0249}$ $1.683 \times 10^{-4} \cdot Re^{0.8672} \, \tau^{-0.3018}$	Parallel Flow 10 < Re < 250 Counter Flow 10 < Re < 250

229

6.6.4 Segmental Heat Transfer Correlation

As discussed above, the segmental heat transfer coefficient ($Nu_{seg,l}$) is affected by the solution Reynolds number and the Prandtl number. Based on these observations and because the absorber pressure is found to influence $Nu_{seg,l}$, the influences of $Re_{seg,l}$, $Pr_{seg,l}$ and the absorber pressure are combined in the following form to develop a correlation for the present data.

$$Nu_{l,segment} = a \times Re_{seg,l}^{b} \times Pr_{seg,l}^{c} \times \left(\frac{P_{abs}}{345\,kPa} \right)^{d} \tag{6.56}$$

Here, the constant a, and the exponents b, c and d are determined using regression analysis. The last term accounts for the pressure dependence seen in the data. An absorber pressure of 345 kPa is chosen as the reference pressure because this is the intermediate pressure tested in the present study and represents the normal ambient heat pump mode. The regression analysis yields the following Nusselt number correlation:

$$Nu_{l,segment} = 7.589 \times 10^{-3} \times Re_{seg,l}^{1.043} \times Pr_{seg,l}^{0.455} \times \left(\frac{P_{abs}}{345\,kPa} \right)^{-0.145} \tag{6.57}$$

Figure 6.23 shows a comparison of the measured and predicted $Nu_{seg,l}$ along with $\pm25\%$ error bands. The predicted Nu_{seg} are within $\pm25\%$ of the measured Nu_{seg} for 62 of the 94 data points, with an average absolute deviation of 24%. However, it should be noted that the segmental results are obtained based on several assumptions and approximations, such as the development of a solution temperature profile from solution-side thermocouple readings in which it is not immediately obvious whether liquid or vapor phase temperatures are being recorded. Also, these values depend on the proper

accounting of the contributions to the heat and mass transfer from the drip tray, solution

pool, and header walls.
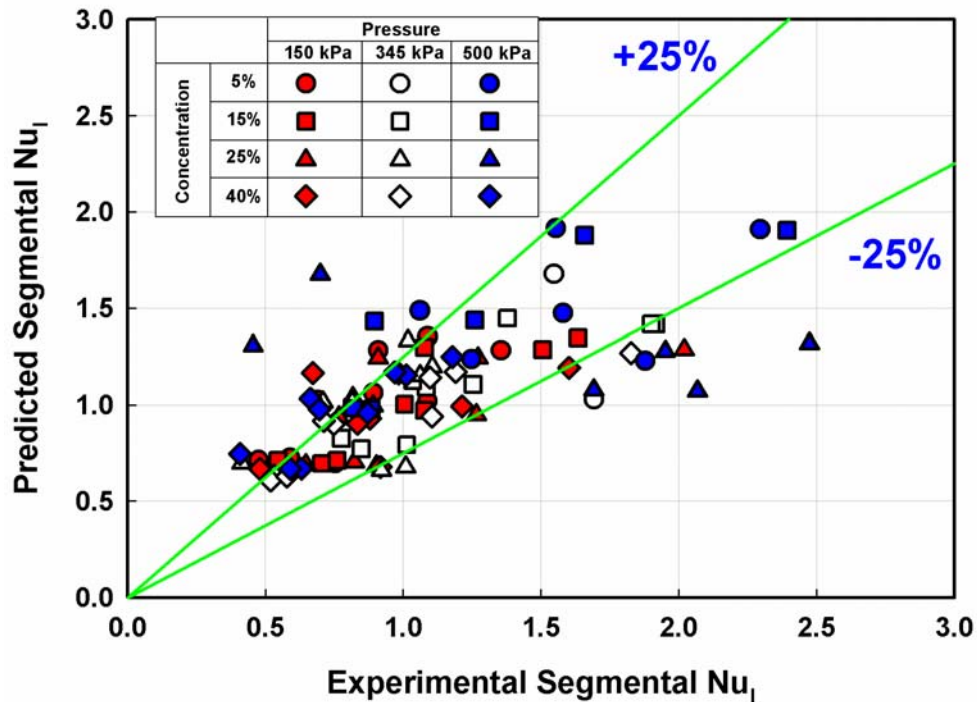
Figure 6.23 Experimental vs Predicted Nu

Figures 6.24 – 6.26 show the measured and predicted segmental $Nu_{seg,l}$ as a

function of $Re_{seg,l}$. Good agreement can be seen between the two values for a majority of

the segmental data. In general, extreme conditions, such as those with 5% and 15%

dilute solution concentration at 500 kPa, show larger discrepancies at all the segments;

however, segment 3 (which includes only the top row) shows the largest discrepancies

among all the three segments. As stated above, these extreme conditions were the most

difficult conditions to obtain and maintain, and different configurations of the test facility were used (i.e., using electric heat for the 5 and 15% cases at higher pressures; use of a sub-cooler for the 25 and 40% cases at lower pressures); therefore larger uncertainties can be expected at these conditions. In addition, segment 3 is affected the most by conduction from the drip tray, and also perhaps reflects the greatest influence of inlet sub-cooling, solution impingement patterns from the drip tray, and other entrance phenomena.
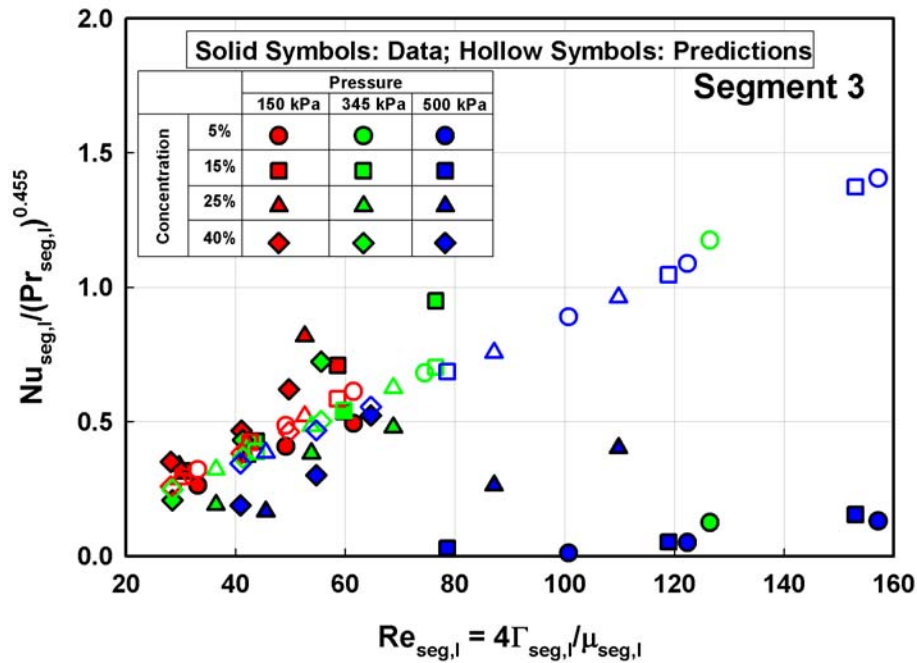
Figure 6.24 Experimental vs Predicted $Nu_{seg,l}$ for Segment 3
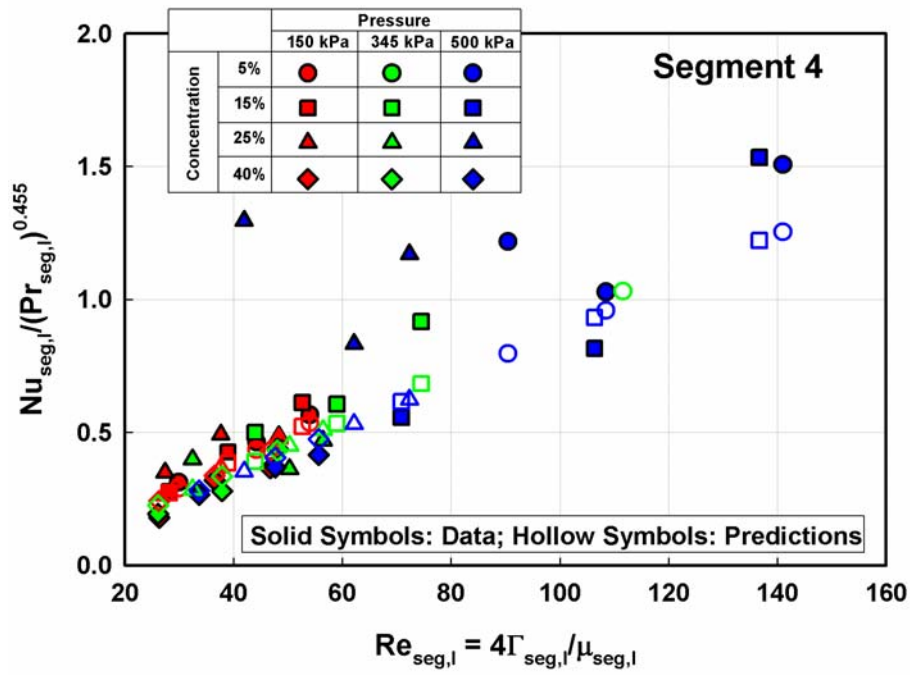
Figure 6.25 Experimental vs Predicted $Nu_{seg,l}$ for Segment 4
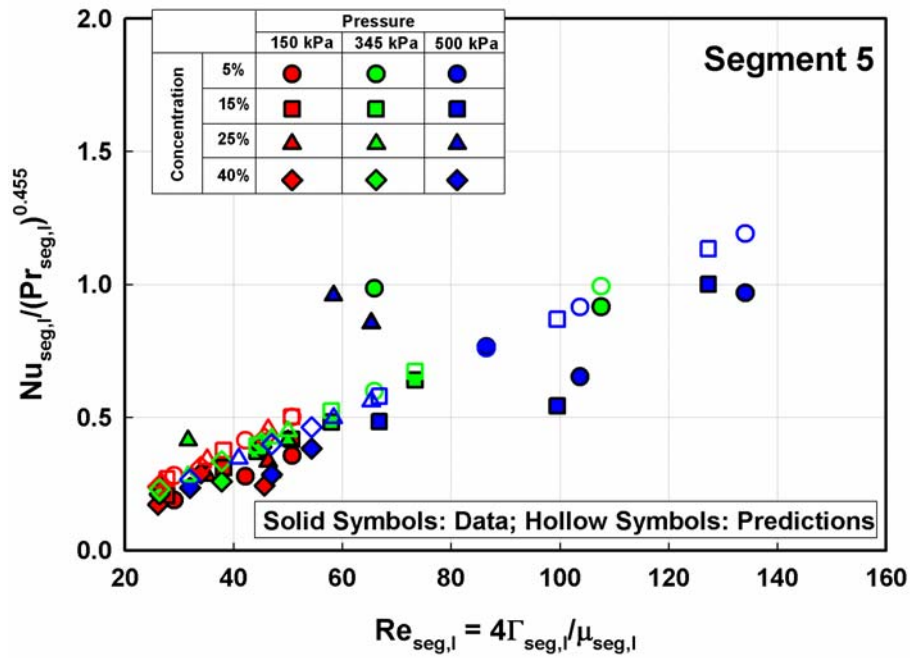
Figure 6.26 Experimental vs Predicted $Nu_{seg,l}$ for Segment 5

6.6.4.1 Comparison with Overall Heat Transfer Correlation

In general, the overall heat transfer coefficient showed similar dependence on the operating conditions; however, the degree of the dependence was different from that seen in the segmental results. Lee (2007) discussed the system level performance in greater detail and also developed a correlation for the overall Nusselt number in the entire absorber as follows:

$$Nu_{l,overall} = 3.22 \times 10^{-3} \times Re_l^{0.945} \times Pr_l^{0.743} \times \left(\frac{P_{abs}}{345\,kPa} \right)^{-0.269} \tag{6.58}$$

It can be seen that while the functional dependence is similar, the constants and exponents are somewhat different. The effect of the Reynolds number is slightly less pronounced (an exponent of 0.945) at the overall level compared to the segment level (an exponent of 1.043). Dependence on the solution Prandtl number is, however, more pronounced at the overall level (an overall exponent of 0.743 compared to a segmental exponent of 0.455). A similar difference is also seen in the pressure correction term (an overall exponent of -0.269 compared to a segmental exponent of -0.145).

6.6.4.2 Parametric Evaluation of Nu_{seg} Correlation

The Nu_{seg} correlation developed in the previous section can be used to study the effects of several parameters on absorption heat transfer. Figures 6.27 and 6.28 show the variation of Nu_{seg} as a function of Re_{seg} with Pr_{seg} and P_{abs} as the parameters. In these figures, the abbreviation PR stands for the pressure ratio (P_{abs}/345 kPa). Some apparent trends can be observed in these graphs. In general, Nu_{seg} increases with increasing Re_{seg}. In Figure 6.27, for a given Re_{seg}, the Nu_{seg} is found to increase as the Pr_{seg} increases.

234
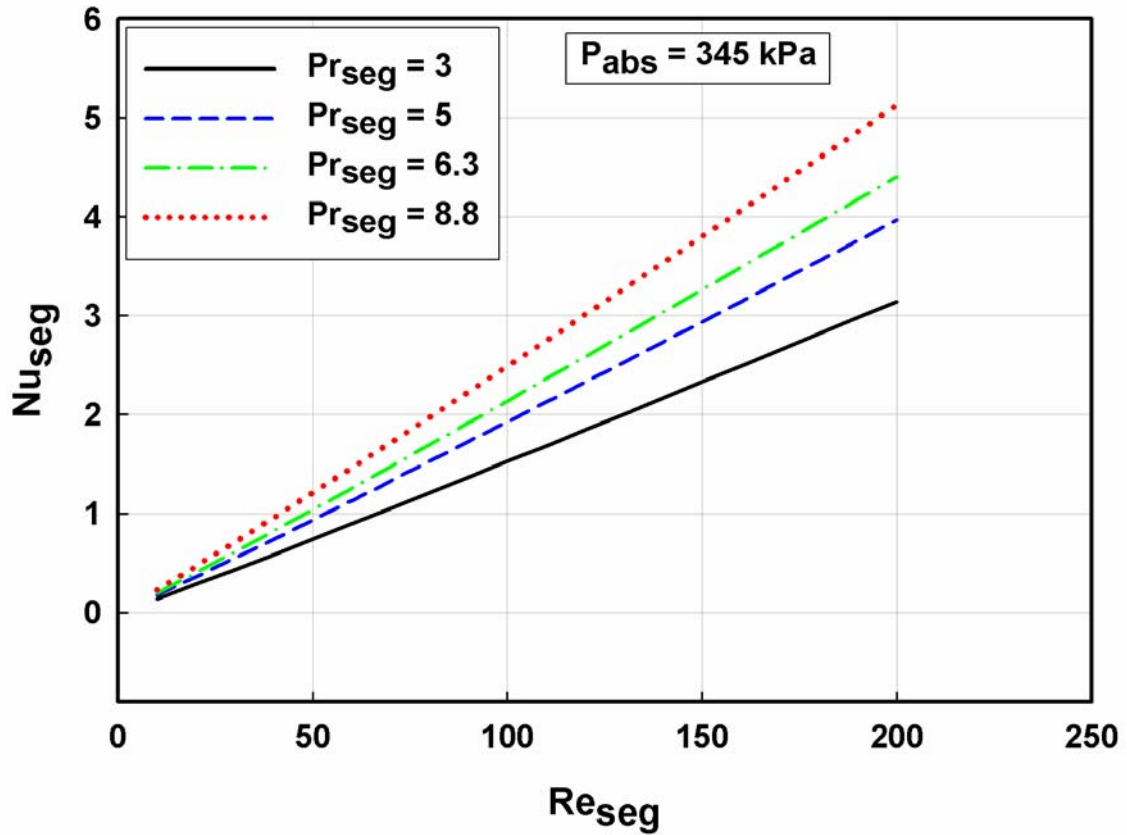
Figure 6.27 Effect of Re_{seg} and Pr_{seg} on Nu_{seg}

Similarly, in Figure 6.28, for a given Re_{seg} and Prandtl number of 6.7, the Nu_{seg} is found to decrease as the P_{abs} (or Pressure Ratio, PR) increases. While these trends demonstrate the capability of the correlation to predict absorption heat transfer characteristics, these may not explain the effects of operating conditions directly. This is because of the confounding influence of operating conditions on the solution properties in a binary mixture, which in turn, determine the Re ($4 \cdot \Gamma / \mu$) and Pr ($\mu \cdot C_P / k$). Therefore, it is typically not possible in practice to vary only the Pr_{seg} or P_{abs} while keeping all the other parameters (e.g., the solution temperature, concentration) constant.
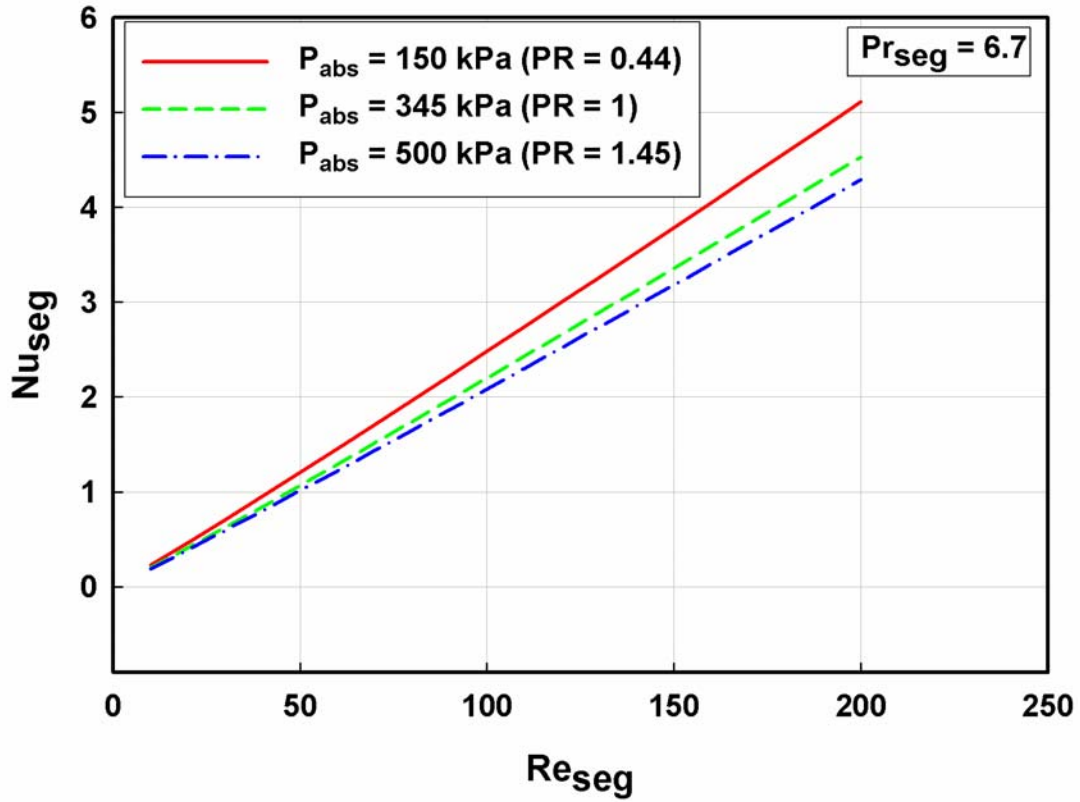
Figure 6.28 Effect of P_{abs} on Nu_{seg}

The effect of the operating conditions on the Re_{seg} and Pr_{seg} for segment 4 is illustrated in Tables 6.4 and 6.5. Table 6.4 shows the variation of average Pr_{seg} (at a given dilute solution concentration and absorber pressure, the variation in Pr_{seg} with the solution flow rate was found to be insignificant) with the absorber pressure and dilute solution concentration. From this table, it can be seen that the combinations of 5% and 150 kPa; 25% and 345 kPa; and 40% and 500 kPa result in similar Pr_{seg}. For a given solution flow rate (0.034 kg/s), similar trends are also seen for Re_{seg} (Table 6.5). Therefore, both the dilute solution concentration and the absorber pressure have a combined effect on the absorption heat transfer characteristics.

236

Table 6.4 Variation of Average Pr_{seg} with Dilute Solution Concentration and Absorber Pressure (0.026 kg/s)

	Pr_{seg}		
	150 kPa	**345 kPa**	**500 kPa**
5%	6.76	2.98	2.56
15%	7.58	4.89	2.68
25%	8.13	6.29	4.98
40%	9.04	8.82	6.81

Table 6.5 Variation of Re_{seg} with Dilute Solution Concentration and Absorber Pressure (0.034 kg/s)

	Re_{seg}		
	150 kPa	**345 kPa**	**500 kPa**
5%	54	111	141
15%	52	75	137
25%	48	56	72
40%	46	48	56

To gain a further understanding on the effect of the operating conditions on the absorption heat transfer, the Nu_{seg} correlation can also be expanded using the definitions of the Re_{seg} and Pr_{seg} as follows:

$$Nu_{l,segment} = 7.589 \times 10^{-3} \times \left(\frac{4 \times \Gamma_{seg}}{\mu_{seg}} \right)^{1.043} \left(\frac{\mu_{seg} C_{p,seg}}{k_{seg}} \right)^{0.455} \left(\frac{P_{abs}}{345\,kPa} \right)^{-0.145} \quad (6.59)$$

It can be seen in the above equation that the solution viscosity appears in both the Re_{seg} and Pr_{seg} definitions affecting the two parameters in an inverse manner. This equation is further modified as follows:

$$Nu_{l,segment} = 7.589 \times 10^{-3} \times \left(4 \times \Gamma_{seg} \right)^{1.043} \left(\frac{1}{\mu_{seg}} \right)^{0.588} \left(\frac{C_{p,seg}}{k_{seg}} \right)^{0.455} \left(\frac{P_{abs}}{345\,kPa} \right)^{-0.145} \quad (6.60)$$

In the present study, the solution heat capacity (C_P) varied only over a small range, e.g, between 4.24 and 4.43 kJ/kg-K for segment 4. Similarly, the solution thermal conductivity also varied over a relatively narrow range, e.g., between 0.55 and 0.62 W/m-K for the segment 4. The largest effect of the operating conditions was seen on the solution viscosity, which varied between 3.7×10^{-4} kg/m-s and 1.16×10^{-3} kg/m-s. Table 6.6 shows the variation of the segment 4 solution viscosity for the range of experiments conducted.

Table 6.6 Variation of Average μ_{seg} with Dilute Solution Concentration and Absorber Pressure (0.026 kg/s)

	μ_{seg} (kg/m-s)		
	150 kPa	345 kPa	500 kPa
5%	9.40×10^{-4}	4.25×10^{-4}	3.71×10^{-4}
15%	1.04×10^{-3}	6.81×10^{-4}	3.92×10^{-4}
25%	1.10×10^{-3}	8.50×10^{-4}	6.72×10^{-4}
40%	1.14×10^{-3}	1.11×10^{-3}	8.69×10^{-4}

It can be seen from the table that for a given absorber pressure, the solution viscosity increases as the dilute solution concentration increases. Using the solution viscosity as a parameter, the variation of Nu_{seg} with the solution mass flux for a given absorber pressure of 345 kPa (PR = 1), a thermal conductivity of 0.58 W/m-K and a solution heat capacity of 4.2 kJ/kg-K is shown in Figure 6.29. It can be seen that for a given solution mass flux (of segment 4), the Nu_{seg} increases as the solution viscosity decreases. This is because of an inverse relationship of the solution viscosity with the Nu_{seg} as shown in the equation above. It should be noted that the smaller viscosity, the larger the Reynolds number for a given mass flux. Therefore, larger Re_{seg} are observed at higher absorber pressures and

lower solution concentrations. This also explains the larger Nu_{seg4} observed for the 5 and

15% nominal solution concentration test cases at an absorber pressure of 500 kPa in the

previous section.   It can therefore be said that the Nu_{seg} correlation developed here

provides insights into absorption heat transfer and can be used to study the influence of

the operating conditions.
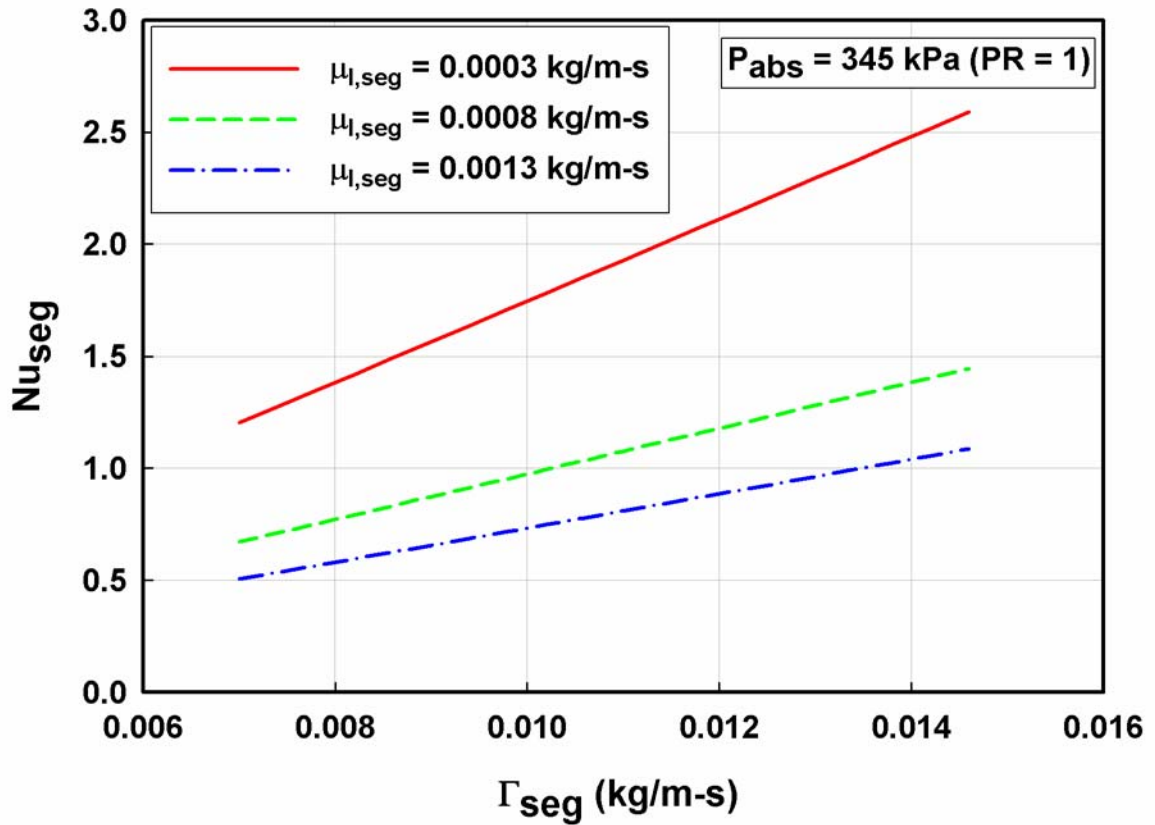
Figure 6.29 Effect of μ_{abs} on Nu_{seg}

6.6.5 Relevant Non-dimensional Parameters for Mass Transfer

Vapor-phase mass transport can be affected by several properties such the viscosity, density, specific heat, and binary diffusion coefficient. The primary non-dimensional groups for the vapor-phase transport properties are the Prandtl number ($Pr_{seg,v}$), and the Schmidt number ($Sc_{seg,v}$). These are defined as:

$$Pr_{seg,v} = \frac{\mu_{seg,v} \times C_{P,seg,v}}{k_{seg,v}} \tag{6.61}$$

$$Sc_{seg,v} = \frac{\mu_{seg,v}}{\rho_{seg,v} \times D_{aw,seg,v}} \tag{6.62}$$

The vapor phase mass transfer coefficient is non-dimensionalized to obtain the Sherwood number ($Sh_{seg,v}$) as follows:

$$Sh_{seg,v} = \frac{\beta_{seg,v} \times d_{o,t}}{D_{aw,seg,v}} \tag{6.63}$$

As mentioned in the earlier sections, the vapor inside the large absorber chamber is relatively quiescent; therefore, the heat transfer is considered to be taking place through natural convection because of the difference between liquid and vapor-phase temperatures, while the mass transfer occurs due to the corresponding concentration differences. To account for natural convection, the segmental Grashof number is defined as follows:

$$Gr_{seg,v} = \frac{g \times \left(T_{seg,int} - T_{seg,v,bulk}\right) \times d_{o,t}^3}{\left(T_{seg,v,bulk} + 273.15\right) \times v_{seg,v}^2} \tag{6.64}$$

The absorption process also involves phase change that needs to be accounted for. The segmental Jakob number ($Ja_{seg,v}$), which accounts for the relative importance of sensible to latent heat during phase change is defined as,

$$Ja_{seg,v} = \frac{C_{P,seg,v}(T_{seg,int} - T_{seg,v,bulk})}{h_{seg,v,int} - h_{seg,l,int}} \tag{6.65}$$

6.6.6 Segmental Vapor Sherwood Number ($Sh_{seg,v}$)

The effects of the vapor Prandtl, Grashof and Jakob numbers can be combined into a single parameter ($\frac{Gr_{seg,v} \times Sc_{seg,v}}{Ja_{seg,v}}$). A similar parameter, $\frac{Gr \times Pr}{Ja}$, is also reported in Carey (1992) on page 369 for film condensation heat transfer. Figure 6.30 shows the dependence of $Sh_{seg,v}$ on $\frac{Gr_{seg,v} \times Sc_{seg,v}}{Ja_{seg,v}}$ for segment 4. Similar trends are observed for other segments also. It can be seen from this figure that $Sh_{seg,v}$ increases as $\frac{Gr_{seg,v} \times Sc_{seg,v}}{Ja_{seg,v}}$ increases. In addition to this dependence, effects of absorber pressure and dilute solution concentration can also be seen in this figure. These trends are similar to those observed for the overall mass transfer coefficient.

It was found that liquid-side properties also influence the vapor-side mass transfer coefficient. The effect of heat and mass transfer as the condensed vapor is transported through the solution film is accounted for using the Lewis number ($Le_{seg,l}$), which relates thermal and mass diffusivities.

$$Le_{seg,l} = \frac{Sc_{seg,l}}{Pr_{seg,l}} \tag{6.66}$$

241
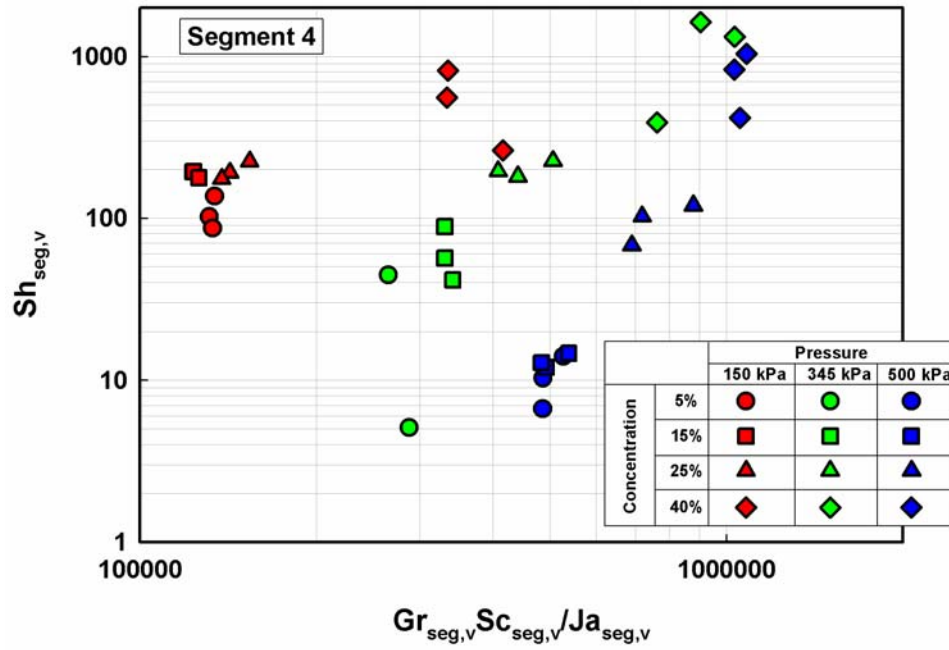
Figure 6.30 Variation of Sh$_{seg,v}$ with $\dfrac{Gr_{seg,v} \times Sc_{seg,v}}{Ja_{seg,v}}$ **for Segment 4**

Figure 6.31 shows the effect of liquid side Le$_{seg,l}$ on Sh$_{seg,v}$. This ratio is the ratio

of the liquid-side thermal and mass diffusivities ($\dfrac{Sc_{seg,l}}{Pr_{seg,l}} = \dfrac{\alpha_{th,seg,l}(= k_{seg,l}/\rho_{seg,l} \cdot C_{P,seg,l})}{D_{aw,seg,l}}$).

It can be seen from the figure that Sh$_{seg,v}$ increases as the Le$_{seg,l}$ increases. A larger Le$_{seg,l}$

implies a higher thermal diffusivity ($\alpha_{th,seg,l}$) or a smaller mass diffusivity (D$_{aw,seg,l}$). The

Sh number is inversely proportional to the mass diffusivity; therefore a smaller D$_{aw,seg,l}$

results in higher Sh$_{seg,v}$. A larger thermal diffusivity facilitates removal of the heat of

absorption, perhaps leading to an increase in the mass transfer coefficient. Since Sh$_{seg,v}$ is

directly proportional to the mass transfer coefficient, a higher thermal diffusivity results

in higher Sh$_{seg,v}$.
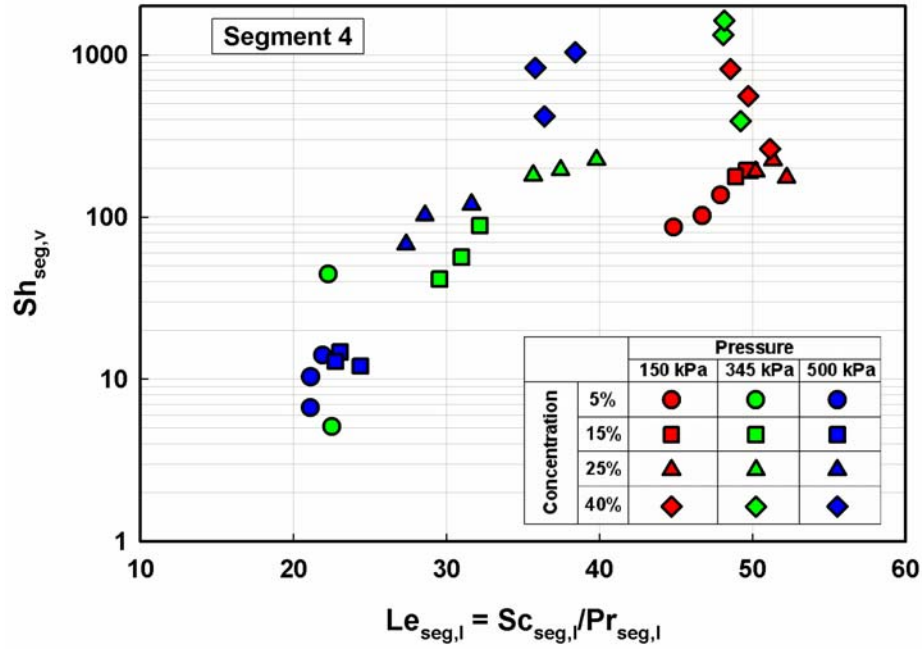
Figure 6.31 Variation of Sh$_{seg,v}$ with $Le_{seg,l} = \dfrac{Sc_{seg,l}}{Pr_{seg,l}}$ for Segment 4

In addition, the data indicate that other liquid and vapor-phase properties could account for some of the variation in the mass transfer coefficient. Among the several properties, the difference between the liquid- and vapor-side viscosities has largest influence on Sh$_{seg,v}$. The Sh$_{seg,v}$ is found to increase with the ratio $\dfrac{\mu_{seg,l} - \mu_{seg,v}}{\mu_{seg,v}}$. Figure 6.32 shows the effect of $\dfrac{\mu_l - \mu_v}{\mu_v}$ on the Sh$_{seg,v}$. It can be seen that Sh$_{seg,v}$ increases as this ratio increases. The increase in this ratio is mostly due to an increase in liquid viscosity (For the range of conditions tested, the liquid-phase viscosity varies from 3.21×10^{-4} - 1.042×10^{-3} kg/m-s, while the vapor-phase viscosity varies from 1.006×10^{-5} - 1.204×10^{-5} kg/m-s).
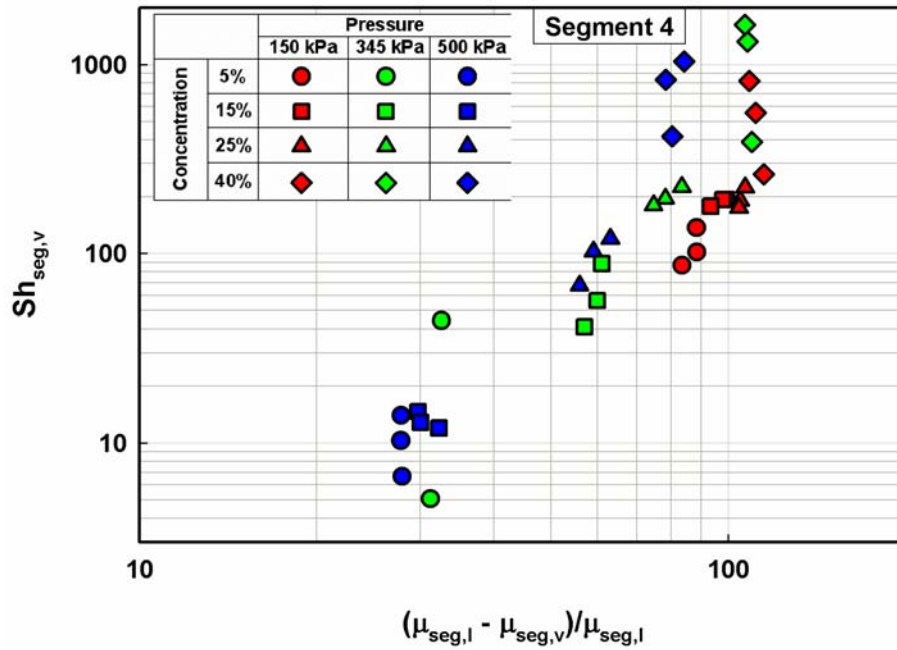
Figure 6.32 Variation of $Sh_{seg,v}$ with $\dfrac{\mu_{seg,l} - \mu_{seg,v}}{\mu_{seg,v}}$ for Segment 4

The liquid viscosity increases as the dilute solution becomes concentrated by absorbing ammonia vapor. The difference in viscosities affects the shear stresses at the interface as well within the solution film, which in turn affects the mass transfer coefficients. The shear stresses at the interface can influence the movement of the vapor towards the interface while the shear stress in the liquid can influence mixing within the liquid-phase, thereby affecting the mass transfer. The higher viscosities are observed for the higher dilute solution concentration cases. As the dilute solution concentration increases, the specific volume of the vapor in equilibrium with the solution decreases. The smaller specific volume implies smaller velocities and therefore smaller shear stresses. The smaller vapor shear can improve mass transfer in counter flow, because it

does not result in a thickening of the liquid film, resulting in higher Sh_v. Kwon and Jeong (2004) also observed similar trends for solution-side Nusselt number in the counter-flow arrangement where Nu_l decreases as the vapor shear increases.

6.6.7 Comparison with the Vapor-phase Mass Transfer Literature

There are again few studies in the literature that provide correlations for mass transfer in ammonia-water absorption. The segmental mass transfer coefficients from this study are therefore compared with those obtained using a heat and mass transfer analogy and those reported by Onda *et al.* (1968). In general, the heat and mass transfer analogy is used to address the coupled heat and mass transfer process in analytical studies. However, the use of the heat and mass transfer analogy and correlations from the literature require the vapor-phase heat transfer coefficient, which in turn requires a vapor-phase Reynolds number (Re_v). Although due to the large absorption chamber occupied by the vapor in this study, no obvious definition of vapor-phase Re emerges, for the purpose of comparison, $Re_{v,max}$ for the present study is defined based on the minimum flow area in the tube array along the solution flow path. The vapor velocity is calculated first as follows:

$$V_{v,seg,frontal} = \frac{\dot{m}_{v,seg,in}}{\rho_v \times A_{seg,frontal}} \tag{6.67}$$

$$V_{v,seg,effective} = \frac{A_{seg,frontal}}{A_{seg,free}} \times V_{v,seg,frontal} \tag{6.68}$$

where $A_{seg,frontal}$ is taken as the bottom area of the tube array and $A_{seg,free}$ is the area excluding the projected tube area of tubes $d_{o,t} \times L_t \times N_{t,pr}$. Also, $\dot{m}_{v,seg,in}$ is the mass

flow rate of the vapor-phase absorbed in the segment. Once the effective vapor velocity

is obtained, the vapor-phase Re is calculated as follows:

$$Re_{v,seg,max} = \frac{\rho_v \times V_{v,seg,effective} \times d_{o,t}}{\mu_v} \qquad (6.69)$$

The vapor-phase Sh_v is calculated from the heat and mass transfer analogy, where

the heat transfer coefficient is estimated using the correlation of Churchill and Bernstein

(1977) for cross flow over cylinders.

$$Sh_{v,seg} = \frac{\beta_{v,seg} \times d_{o,t}}{D_{aw,v}} = Nu_{v,seg} \times \left(\frac{Sc_v}{Pr_v}\right)^{1/3} \qquad (6.70)$$

$$Nu_{v,seg} = 0.3 + \frac{0.62 \times Re_{v,seg,max}^{1/2} \times Pr_v^{1/3}}{\left[1 + \left(0.4/Pr_v\right)^{2/3}\right]^{1/4}}; \qquad Re_{v,seg,max} < 10^4 \quad (6.71)$$

Onda et al. (1968) developed a correlation for mass transfer coefficient between

gas and liquid phases in packed columns during gas absorption and desorption. The

packed column used various random packing, such as Raschig rings and Berl Saddels,

with a nominal size of 6 – 50 mm. The liquid-side mass transfer correlation was

developed for gas absorption and desorption with water and organic solvents such as

methanol and carbon tetrachloride, while the gas-side mass transfer correlation was

developed for gas absorption and vaporization with an air-water system. Again, solely

for the purpose of comparison, the tube array under consideration is approximated to be

analogous to the metal Raschig rings investigated by Onda *et al* (1968).

$$Sh_{v,seg} = \frac{\beta_{v,seg}}{D_{aw,v} \times a} = 2.0 \times \left(a \times d_{o,t}\right)^{-2.0} \times Re_{v,seg,max}^{0.7} \times Pr_v^{1/3} \qquad (6.72)$$

where a^{-1} is the inverse of the characteristic length of the packing. The characteristic lengths for various commercial packings of different sizes are tabulated in Mills (1995). From these values, the characteristic length was approximated using a curve-fit for the tube size of the present study.
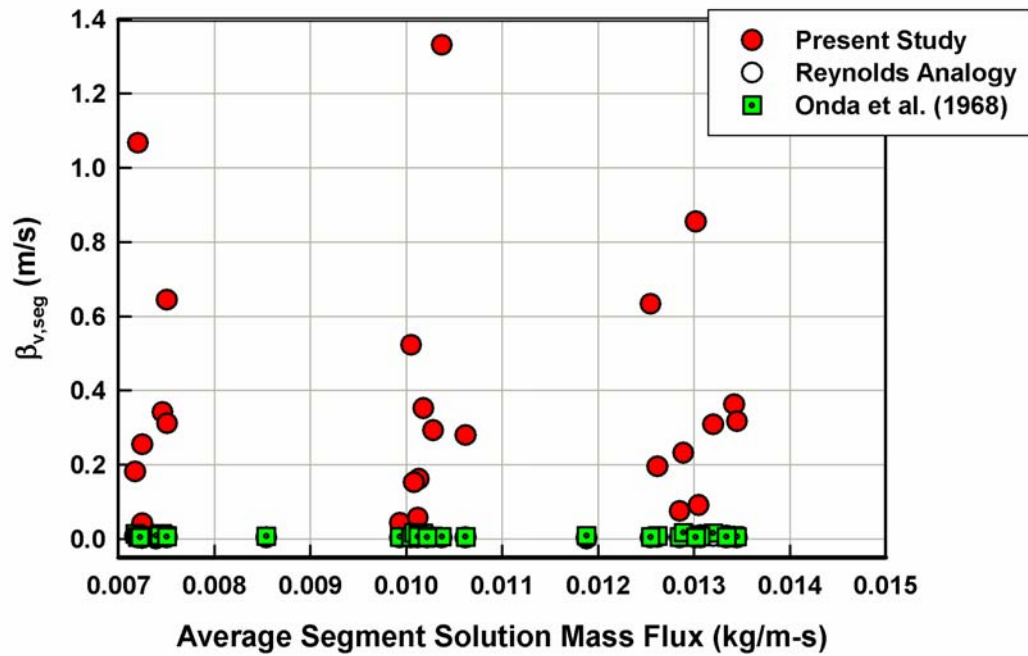
Figure 6.33 Comparison of $\beta_{v,seg}$ with other Studies (Segment 4)

Figure 6.33 shows a comparison of β_v obtained from the data, the heat and mass transfer analogy, and from the correlation of Onda *et al.* (1968). As seen in Figure 6.33, the mass transfer coefficients from the heat and mass transfer analogy and Onda *et al.* (1968) are significantly lower compared with the data from present study. The discrepancies may be due to an inadequate definition of vapor Re for the sake of comparison, because the vapor is essentially deemed to be quiescent in the present study.

The predictions of Onda *et al.* (1968) can also differ from the data from the present study due to differences in geometry and the fluids investigated in their study. It is also seen that the predicted mass transfer coefficients from the literature are relatively similar for all the data and do not show appreciable effects of absorber pressure or dilute solution concentration, although the data from the present study do show large variations with pressure and concentration. Therefore, it is necessary to study the influence of vapor and liquid-phase properties and develop correlations in terms of property variations.

6.6.8 Segmental Vapor-phase Mass Transfer Correlation

As seen in the previous section, several parameters lead to the trends observed trends in the mass transfer coefficient. A correlation that combines the effects of $\frac{Gr_{seg,v} \times Sc_{seg,v}}{Ja_{seg,v}}$, $Le_{seg,l} = \frac{Sc_{seg,l}}{Pr_{seg,l}}$ and $\frac{\mu_{seg,l} - \mu_{seg,v}}{\mu_{seg,v}}$ is developed here to predict the segmental non-dimensional mass transfer coefficient ($Sh_{seg,v}$).

$$Sh_{seg,v} = a \times \left(\frac{Gr_{seg,v} \times Sc_{seg,v}}{Ja_{seg,v}} \right)^{b} \times \left(\frac{Pr_{seg,l}}{Sc_{seg,l}} \right)^{c} \times \left(\frac{\mu_{seg,l} - \mu_{seg,v}}{\mu_{seg,v}} \right)^{d} \qquad (6.73)$$

Here, constant a, and exponents b, c and d are obtained using regression analysis. It was, however, realized that a separate regression using only the segmental data did not result in any significant improvement over the correlation developed by Lee (2007) for the overall mass transfer coefficient. Furthermore, because of the vapor-phase flow configuration in this study, as stated above, it is idealized as a quiescent fluid, which implies that segmental differences in vapor conditions are not appreciable. The

segmental mass transfer correlation; therefore, uses same coefficients/exponents of the correlation developed by Lee (2007):

$$Sh_{seg,v} = 2.708 \times 10^{-11} \times \left(\frac{Gr_{seg,v} \times Sc_{seg,v}}{Ja_{seg,v}} \right)^{1.256} \times \left(\frac{Pr_{seg,l}}{Sc_{seg,l}} \right)^{-1.681} \times \left(\frac{\mu_{seg,l} - \mu_{seg,v}}{\mu_{seg,v}} \right)^{1.426} \quad (6.74)$$

To evaluate the accuracy of the overall correlation to predict the segmental mass transfer coefficient, the overall mass transfer correlation is used to predict the segmental data. Figures 6.34 - 6.36 show the measured and predicted mass transfer coefficients for segments 3, 4 and 5 (involving heat exchange with coolant) respectively using the overall mass transfer correlation.
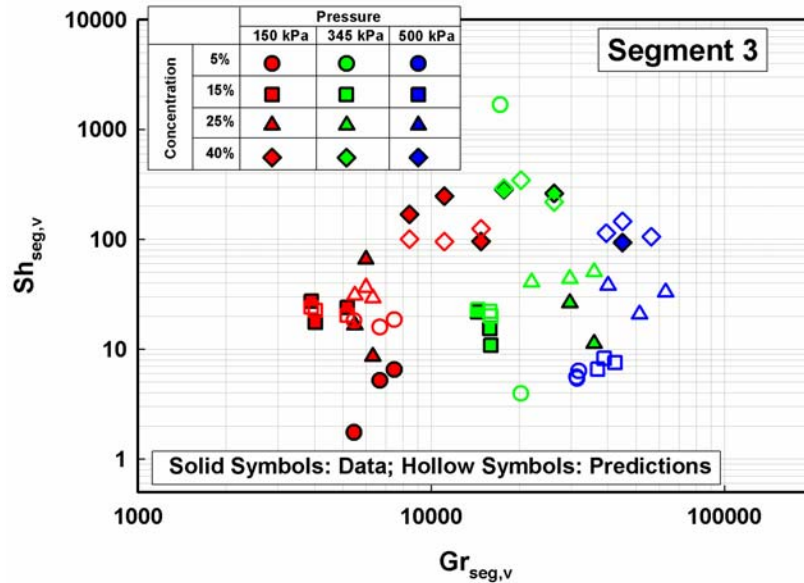
Figure 6.34 Comparison of Experimental and Predicted Sh$_{v,seg}$ for Segment 3
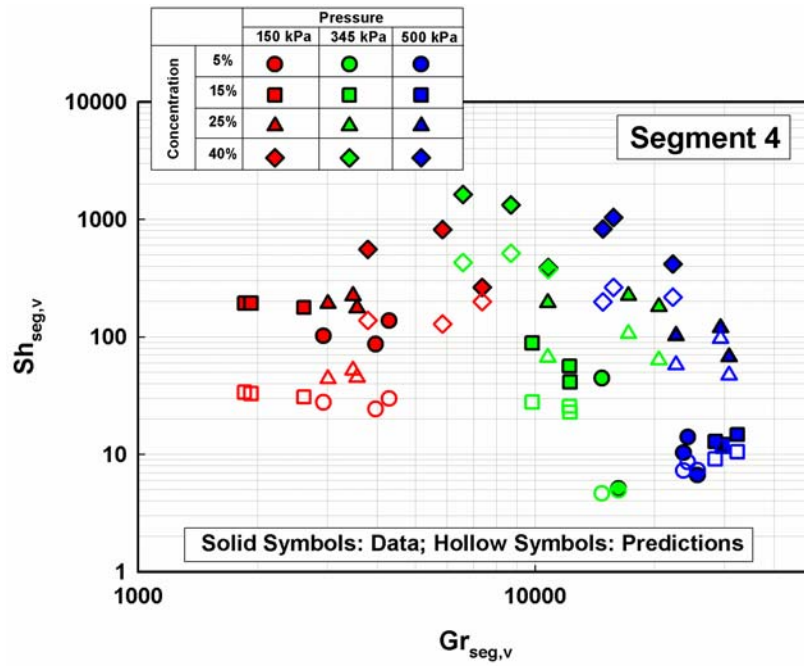
Figure 6.35 Comparison of Experimental and Predicted $Sh_{v,seg}$ for Segment 4
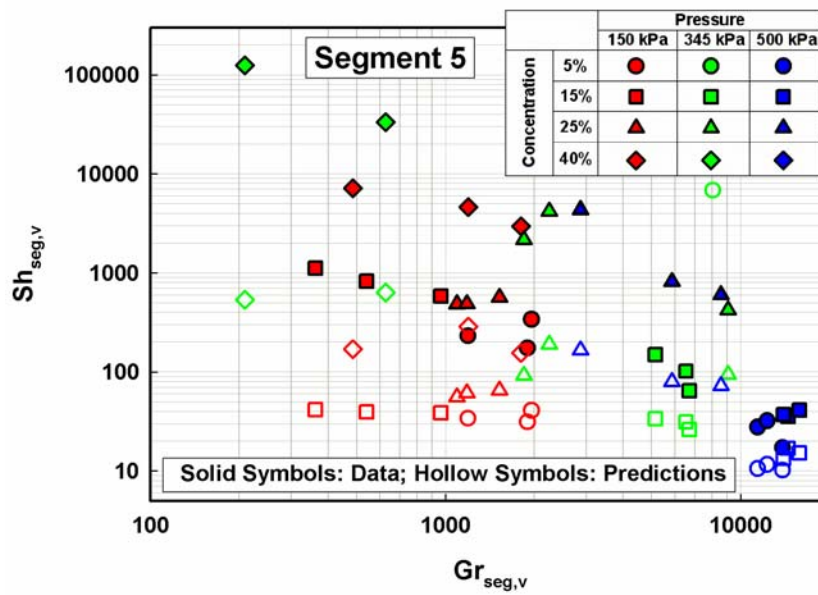
Figure 6.36 Comparison of Experimental and Predicted $Sh_{v,seg}$ for Segment 5

It can be seen that the overall correlation also predicts the segmental data reasonably well. In Figure 6.34, for some test conditions, only predicted values are shown. These are the cases where some desorption is observed from the segmental calculations. In Figures 6.35 and 6.36, relatively better predictions are observed for the 350 and 500 kPa absorber pressure cases as compared to the 150 kPa cases.

6.6.9 Segmental Liquid Sherwood Number ($Sh_{seg,l}$)

Section 4.4.5 presented a methodology to obtain the liquid-phase mass transfer coefficient. This methodology is applied at the segment level to obtain segmental liquid-phase mass transfer coefficients for the falling-film regions of the cooled segments. This section discusses the variation of liquid-phase mass transfer coefficient in non-dimensional form with several parameters. The primary non-dimensional groups for liquid-phase mass transport are the Reynolds number ($Re_{seg,l}$) and the Schmidt number ($Sc_{seg,l}$). The Schmidt number in the liquid phase is defined as follows:

$$Sc_{seg,l} = \frac{\mu_{seg,l}}{\rho_{seg,l} \times D_{aw,seg,l}} \tag{6.75}$$

The segmental liquid-phase mass transfer coefficient ($\beta_{seg,l}$) is non-dimensionalized to obtain the segment Sherwood number ($Sh_{seg,l}$) as follows:

$$Sh_{seg,l} = \frac{\beta_{seg,l} \times \delta_{seg,l}}{D_{aw,seg,l}} \tag{6.76}$$

Figure 6.37 shows the dependence of $Sh_{seg,l}$ on $Re_{seg,l}$ for segment 5. Similar results were obtained for the other segments also. It can be seen from this figure that concentration and pressure affect $Sh_{seg,l}$ through changes in solution viscosity. $Sh_{seg,l}$

decreases as $Re_{seg,l}$ increases, with some variation introduced due to changes in pressure and dilute solution concentration.
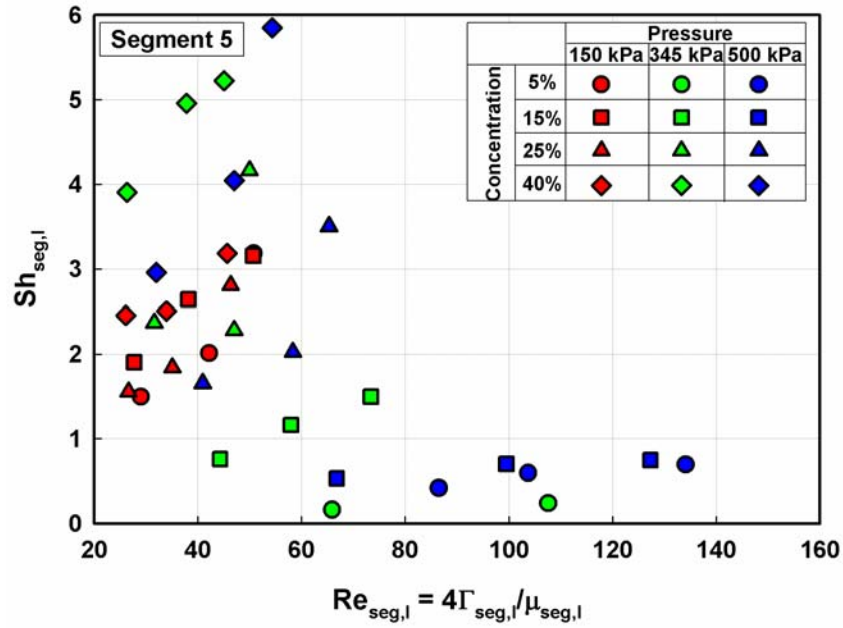
Figure 6.37 Variation of $Sh_{seg,l}$ with $Re_{seg,l}$ for Segment 5

Figures 6.38 and 6.39 show the dependence of $Sh_{seg,l}$ on $Sc_{seg,l}$ and $Pr_{seg,l}$, respectively. It can be seen from these figures that the dependence of $Sh_{seg,l}$ on $Sc_{seg,l}$ and $Pr_{seg,l}$ is very similar, illustrating the coupled nature of liquid-phase heat and mass transfer. For the 345 and 500 kPa cases, $Sh_{seg,l}$ increases as the dilute solution concentration increases, however, there is no clear effect of concentration on $Sh_{seg,l}$ for the 150 kPa cases. In Figures 6.37 – 6.39, the effect of absorber pressure can clearly be seen.
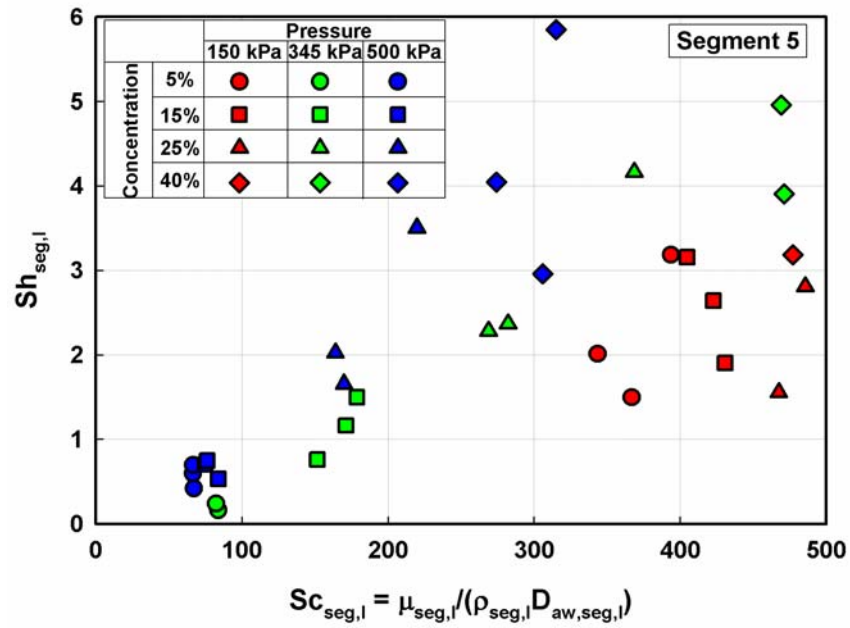
Figure 6.38 Variation of $Sh_{seg,l}$ with $Sc_{seg,l}$ for Segment 5
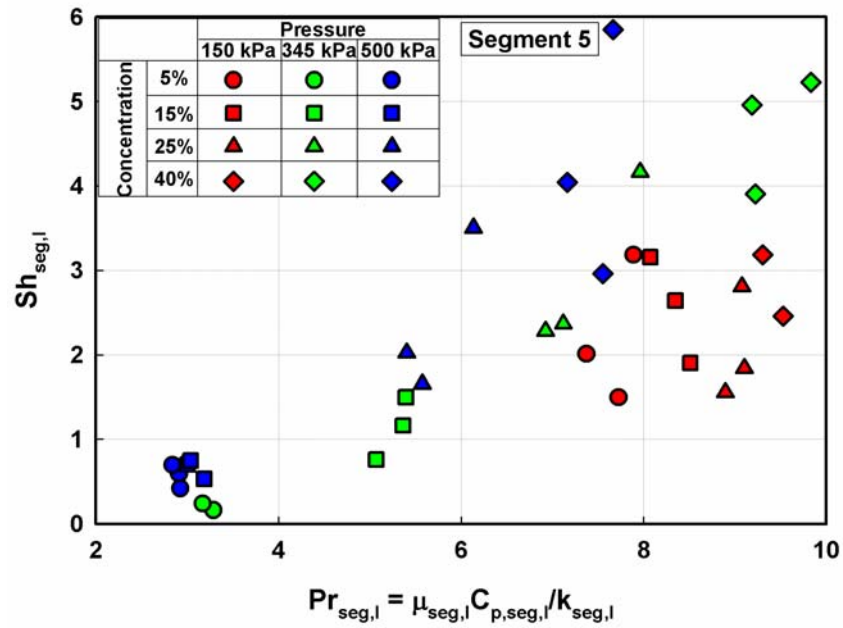
Figure 6.39 Variation of $Sh_{seg,l}$ with $Pr_{seg,l}$ for Segment 5

It can be seen in Figure 6.37 that the liquid-phase $Sh_{seg,l}$ shifts towards the right in the graph as the absorber pressure increases. In Figures 6.38 and 6.39, an opposite trend is observed. As the absorber pressure increases, the liquid-phase $Sh_{seg,l}$ shifts towards the left in these graphs. These reverse trends are probably due to the inverse dependence of the Re and Sc (or Pr) on the solution viscosity. For example, at a constant dilute solution concentration of 15% and concentrated solution flow rate of 0.034 kg/s, with an increase in absorber pressure from 150 kPa to 500 kPa, the viscosity decreases from 0.826×10^{-3} kg/m-s to 0.344×10^{-3} kg/m-s. This results in an increase in the solution Re from 66 to 128, but a decrease in the solution Sc from 228 to 49.

6.6.10 Comparison with the Liquid-phase Mass Transfer Literature

There are few studies in the literature that provide correlations for convective mass transfer coefficient in the liquid phase. Therefore, the mass transfer coefficients from this study are compared with those obtained using a heat and mass transfer analogy, and with a correlation developed by Inoue *et al.* (2004).

The heat and mass transfer analogy in the liquid-phase can be written as follows:

$$ Sh_{seg,l} = \frac{\beta_{seg,l} \times \delta_{seg,l}}{D_{aw,seg,l}} = Nu_{seg,l} \times \left(\frac{Sc_{seg,l}}{Pr_{seg,l}} \right)^{\frac{1}{3}} \qquad (6.77) $$

where $\beta_{seg,l}$ is the mass transfer coefficient in the liquid-phase, and $\delta_{seg,l}$ is the film thickness used in the Nusselt number $Nu_{seg,l}$ described previously.

Inoue *et al.* (2004) developed heat and mass transfer correlations for falling liquid films formed by distilled water on a horizontal tube during ammonia absorption. The absorber consisted of a steel shell with an inner diameter of 200 mm and length of 600

mm; the tubes had an outer diameter of 17.3 mm and length of 600 mm. The absorber coolant flow rate was 1.0×10^{-4} m^3/s with an inlet temperature of 288 K. The flow rate of distilled water (absorbent) ranged from 1.64×10^{-3} to 4.17×10^{-3} kg/s at temperatures between 288 and 303 K. Tests were conducted at pressures between 11.2 and 14.7 kPa with an ammonia vapor concentration of 100%. Heat transfer coefficients were correlated with the liquid Reynolds number and a temperature ratio (the ratio of temperature differences between the solution inlet and the tube wall, and between the vapor temperature and the tube wall temperature). Mass transfer coefficients in the vapor-phase were correlated with the Schmidt number and Reynolds number of the vapor phase and the ratio between the density of the vapor at the interface and the bulk vapor. Although they developed a heat transfer correlation for the liquid phase and a mass transfer correlation for the vapor phase, these correlations were not compared in earlier sections with the corresponding results from the present study, because these correlations of Inoue *et al.* (2004) were expressed in terms of the wall temperature and the vapor-phase Reynolds number, which would be inapplicable for the present study, because a quasi-quiescent vapor assumption is made here.

Inoue *et al.* (2004) did report a correlation for the mass transfer coefficient in the liquid phase in terms of the Reynolds and the Schmidt number of the liquid phase as follows:

$$\text{Sh}_{\text{seg,l}} = \frac{\beta_{\text{seg,l}} \times \delta_{\text{seg,l}}}{D_{\text{aw,seg,l}}} = 0.26 \times \text{Re}_{\text{seg,l}}^{-0.09} \text{Sc}_{\text{seg,l}}^{0.005} \tag{6.78}$$

where $\delta_{seg,l}$ is $\delta_{seg,l} = \left(\frac{v_{seg,l}^{2}}{g} \right)^{\frac{1}{3}}$ in the above equation.

Figure 6.40 shows a comparison of $\beta_{seg,l}$ obtained in the present study for segment 4, and those obtained from the heat and mass transfer analogy and from the correlation of Inoue *et al.* (2004).
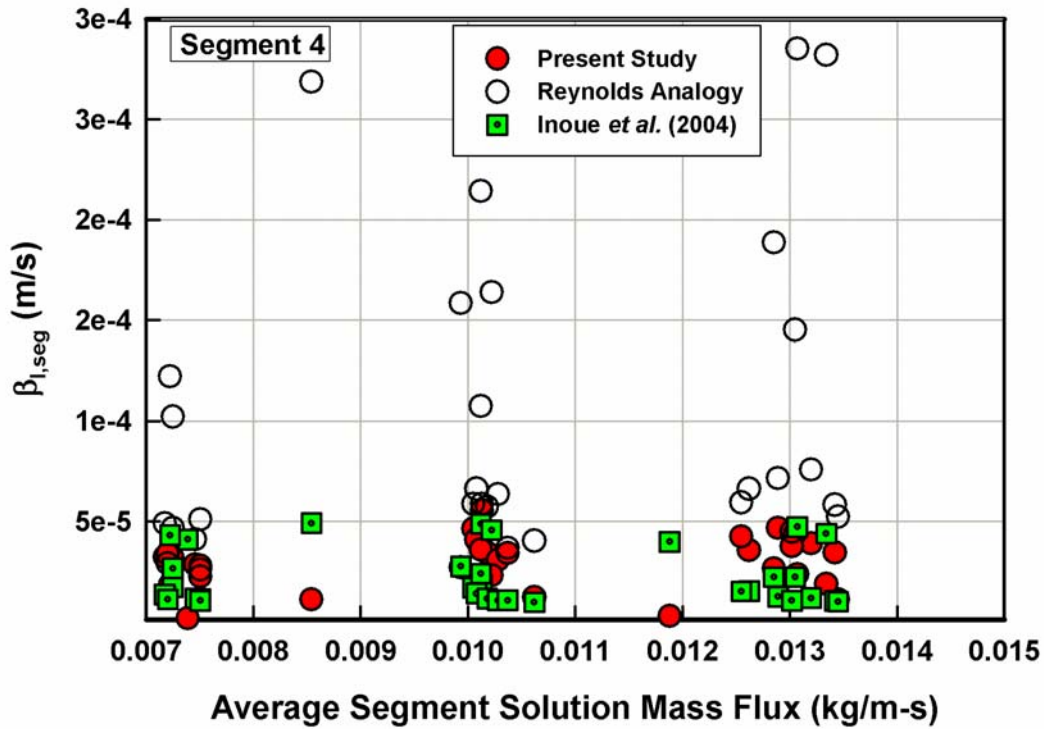
Figure 6.40 Comparison of $\beta_{l,seg}$ with other Studies (Segment 4)

As seen in Figure 6.40, the mass transfer coefficients from the heat and mass transfer analogy are higher than the data from the present study. The deviations in the mass transfer coefficient predicted by the analogy and the data from the present study increase as the flow rate increases. This is because the mass transfer coefficients from the present study did not increase proportionately with an increase in Nusselt number, while the mass transfer coefficient predicted by the analogy does so. This implies that mass transfer

coefficients were not affected significantly by an increase in the solution flow rate, although the Nusselt numbers are affected by the solution mass flow rate. Values predicted by the correlation of Inoue *et al.* (2004) show somewhat better agreement with the results from the present study. Some disagreement of the present data with those of Inoue *et al.* (2004) could be due to the fact that they conducted tests at a single pressure without a change in solution concentration; however, tests in the present study were conducted at three different pressures and four different dilute solution concentrations.

6.6.11 Segmental Liquid-phase Mass Transfer Correlation

Based on the observations from the previous sections, and because the absorber pressure is found to influence $Sh_{seg,l}$, the influences of $Re_{seg,l}$, $Sc_{seg,l}$ and the absorber pressure are combined in the following form to develop a correlation for the present data.

$$Sh_{seg,l} = a \times \left(Re_{seg,l}\right)^{b} \times \left(Sc_{seg,l}\right)^{c} \times \left(\frac{P_{abs}}{345\,kPa}\right)^{d} \qquad (6.79)$$

Here, constant a, and exponents b, c and d are obtained using regression analysis. The resulting correlation is,

$$Sh_{seg,l} = 1.298 \times 10^{-4} \times \left(Re_{l}\right)^{0.566} \times \left(Sc_{l}\right)^{1.32} \times \left(\frac{P_{abs}}{345\,kPa}\right)^{0.644} \qquad (6.80)$$

Figure 6.41 shows a comparison of the measured and predicted $Sh_{seg,l}$. It can be seen in this figure that only fair agreement is obtained between these predictions and the data. It should be noted that the segmental calculations are affected by the uncertainties in determination of the segmental absorption rates, segmental driving temperature

differences, and also due to the uncertainties in the properties and temperature measurements.
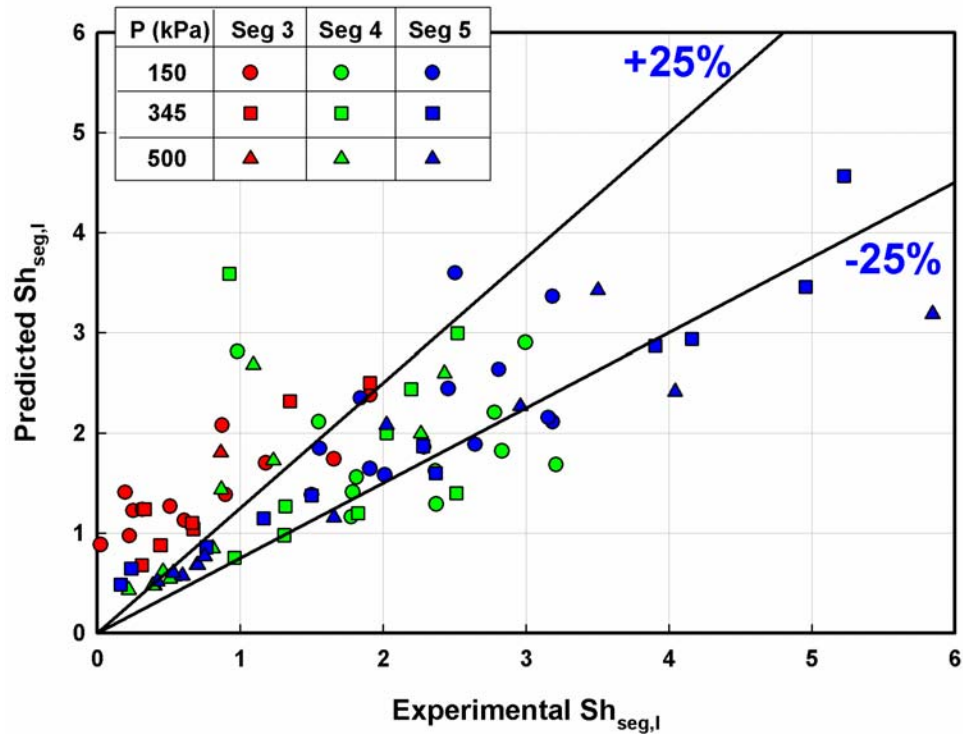
Figure 6.41 Experimental and Predicted Sh$_{seg,l}$

Among the various segments, segment 3 shows the largest discrepancy. The uncertainties in heat and mass transfer calculations at this segment are further affected by the uncertainties in calculation of the conduction heat duty, solution impingement patterns from the drip tray, and other entrance phenomena. Although the scatter is large (partly due to the fact that the liquid-phase mass transfer resistance is not dominant), this correlation captures the trends governing the liquid-phase mass transfer reasonably well. For example, by comparison of the exponents of the Re and Sc, it can be seen that the

exponent of Sc is higher, which implies that the liquid-phase properties have a larger influence in the determination of $Sh_{seg,l}$ than the Re (which is also influenced by the solution flow rate). Similar trends were seen in the data where the effect of solution flow rate was found to be minimal.

6.6.11.1   Comparison with Overall Sh_l Correlation

Lee (2007) discussed the system level performance in greater detail and also developed a correlation for the overall liquid-phase Sherwood number in the entire absorber as follows:

$$Sh_l = 7.437 \times 10^{-4} \times \left(Re_l\right)^{0.397} \times \left(Sc_l\right)^{1.04} \times \left(\frac{P_{abs}}{345kPa}\right)^{0.884} \tag{6.81}$$

In general, the overall liquid-phase mass-transfer coefficient (Lee 2007) showed similar dependence on the operating conditions as seen in the segmental correlation developed here; however, the degree of the dependence was different from that seen in the segmental results. It can be seen that while the functional dependence is similar, the constants and exponents are somewhat different. The effect of Reynolds number is slightly less pronounced (an exponent of 0.397) at the overall level compared to the segment level (an exponent of 0.566). The same is true for the Schmidt number as well, where the segment level exponent is 1.32 compared to the overall level exponent of 1.04. Dependence on the pressure ratio is, however, more pronounced at the overall level (an overall exponent of 0.884 compared to a segmental exponent of 0.644).

6.6.11.2 *Parametric Evaluation of Sh$_{seg,l}$ Correlation*

The Sh$_{seg,l}$ correlation developed in the previous section can be used to study the effects of several parameters on liquid-phase absorption mass transfer. Figures 6.42 and 6.43 show the variation of Sh$_{seg,l}$ as a function of Re$_{seg,l}$ with P$_{abs}$ and Sc$_{seg,l}$ as the parameters.
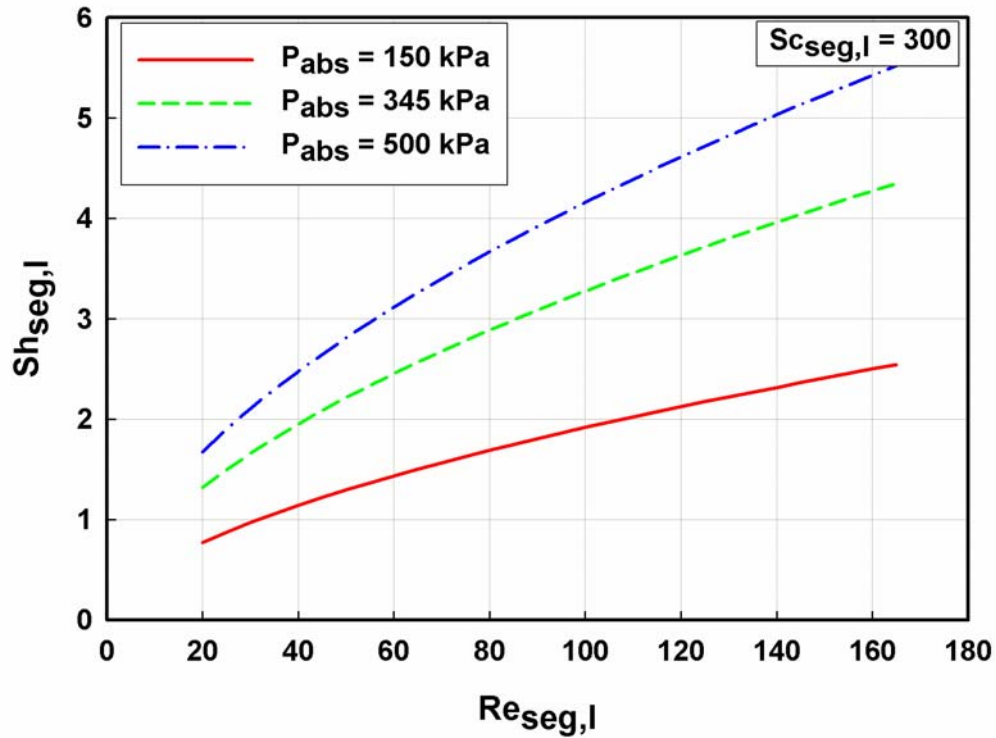
Figure 6.42 Effect of Re$_{seg,l}$ and P$_{abs}$ on Sh$_{seg,l}$

In general, Sh$_{seg,l}$ increases with increasing Re$_{seg,l}$. The Sh$_{seg,l}$ is also found to increase with increasing pressure at any given Re$_{seg,l}$. In Figure 6.43, the Sh$_{seg,l}$ is found to

increase with increasing $Sc_{seg,l}$. As discussed earlier for the segmental Nu correlation, these trends demonstrate the capability of the $Sh_{seg,l}$ correlation to predict the liquid-phase absorption mass transfer; however, they may not explain the effects of the operating conditions directly. This is because of the simultaneous effect of the operating conditions on several solution properties in a binary mixture, which in turn, lead to different variations in the Re ($4\Gamma/\mu$) and Sc ($\mu/\rho D_{aw}$).
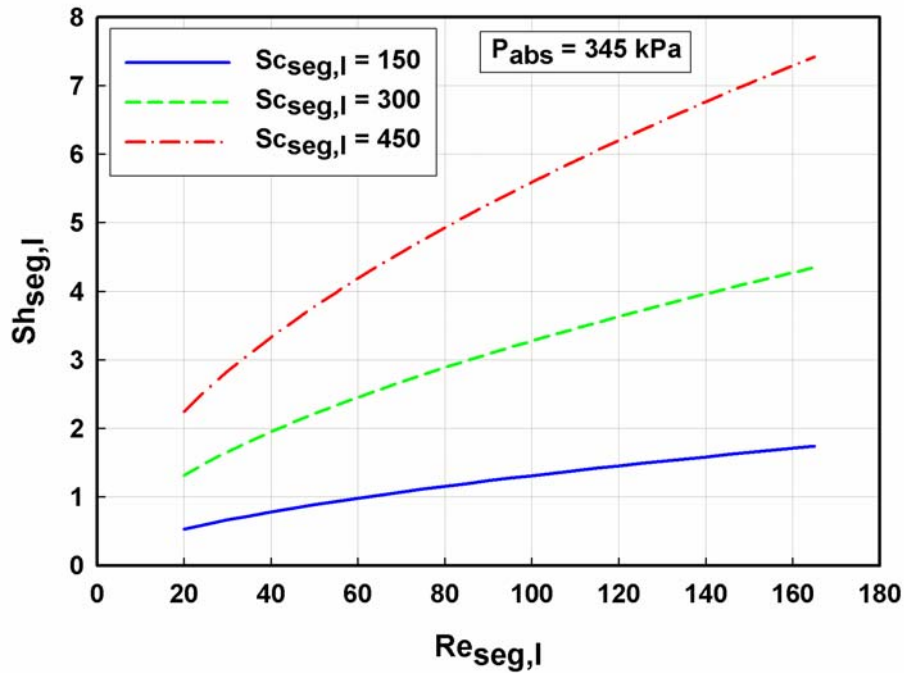
Figure 6.43 Effect of $Re_{seg,l}$ and $Sc_{seg,l}$ on $Sh_{seg,l}$

It was also noted in Section 6.6.4.2 that several combinations of absorber pressure and dilute solution concentration can result in similar Pr. This is also true for the case of Sc.

For example, the combinations of 345 kPa and 25%, and 500 kPa and 40% results in a Sc value of about 260. Therefore, to gain a further understanding on the effects of operating conditions on the liquid-phase mass transfer, the $Sh_{seg,l}$ correlation is expanded using the definitions of the non-dimensional groups as follows:

$$Sh_l = 1.298 \times 10^{-4} \times \left(\frac{4\Gamma_l}{\mu_l}\right)^{0.556} \times \left(\frac{\mu_l}{\rho_l D_{aw,l}}\right)^{1.32} \times \left(\frac{P_{abs}}{345\,kPa}\right)^{0.644} \qquad (6.82)$$

This equation is further modified as follows:

$$Sh_l = 1.298 \times 10^{-4} \times \left(4\Gamma_l\right)^{0.556} \left(\frac{1}{\rho_l}\right)^{1.32} \times \left(\frac{\mu_l^{0.764}}{D_{aw,l}^{1.32}}\right) \times \left(\frac{P_{abs}}{345\,kPa}\right)^{0.644} \qquad (6.83)$$

In the present study, the solution density varied over a relatively small range, e.g., 840 – 907 kg/m^3. However, the variations in the solution viscosity and the diffusion coefficient were significant. The solution viscosity varied between 3.7×10^{-4} and 1.16×10^{-3} kg/m-s, while the diffusion coefficient varied between 3.29×10^{-9} and 8.23×10^{-9} m^2/s. Therefore, the effects of these two solution properties are investigated in Figures 6.44 and 6.45. It can be seen that the solution Sh_{seg} increases with the increasing viscosity as predicted by the equation above, while the solution Sh_{seg} decreases as the diffusion coefficient increases because of its inverse relationship with the $Sh_{seg,l}$. It should be noted that the solution Re decreases as the viscosity increases while the solution Sc may increase or decrease depending upon the relative changes in the viscosity and the diffusion coefficient. Therefore, it can be said the liquid-phase mass transfer coefficient will be determined by the combined influences of the operating conditions on the liquid-phase transport properties.
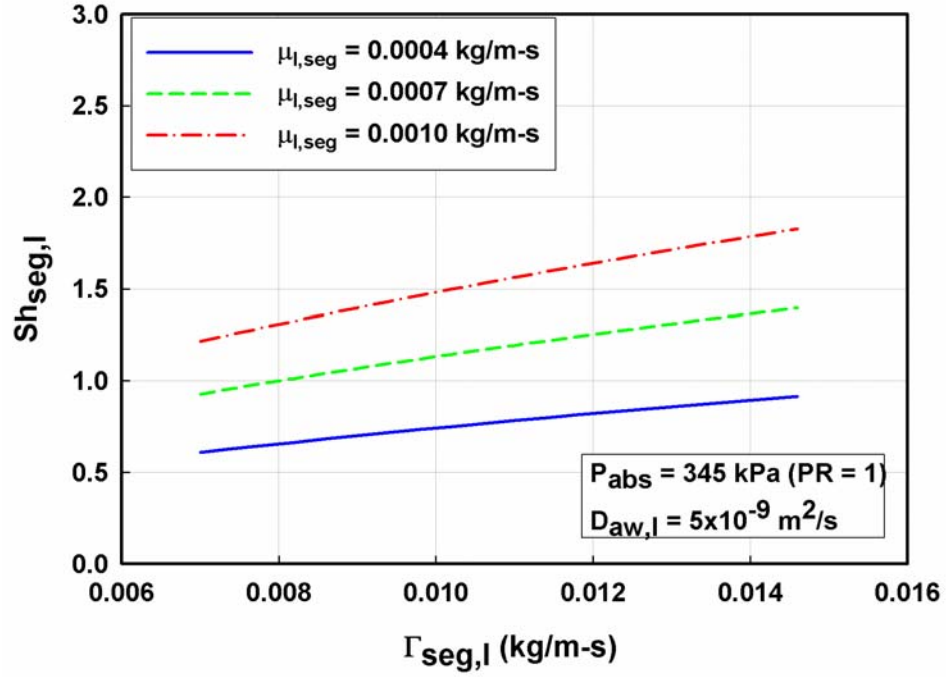
Figure 6.44 Effect of $\mu_{seg,l}$ on $Sh_{seg,l}$
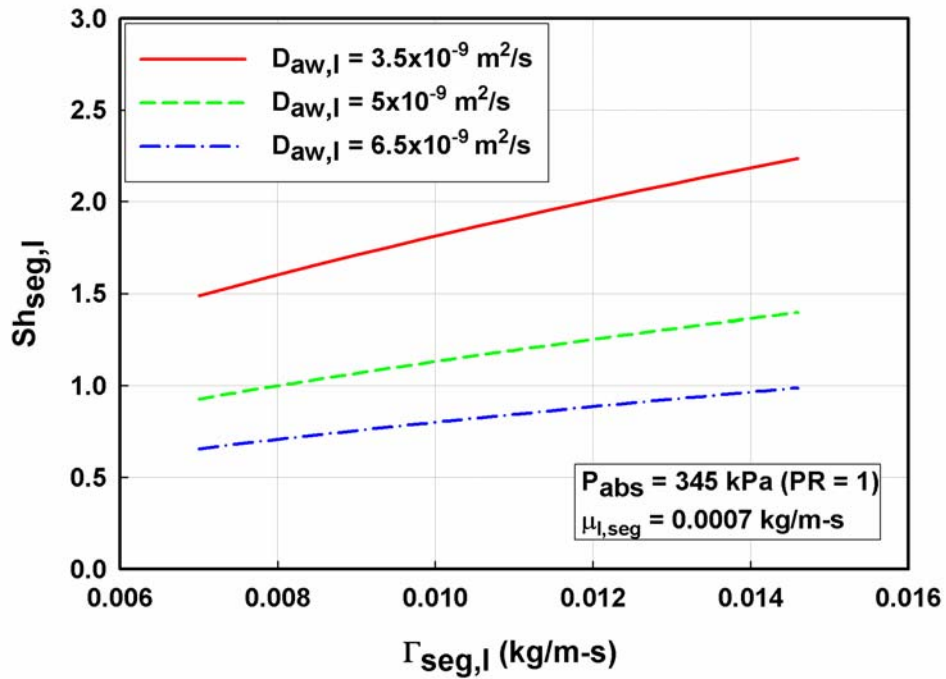
Figure 6.45 Effect of $D_{aw,l}$ on $Sh_{seg,l}$

6.7 Summary

This chapter discussed the variation of heat and mass transfer rates within the absorber in detail. The entire is absorber is divided in six segments. Three of these involve heat exchange with the coolant while the other three are adiabatic; however, all the six segments involve mass transfer. The vapor state within the absorber is idealized to that of saturation corresponding to the minimum temperature and average absorber pressure. Using measured temperatures on the individual tube rows, in the drip tray and the solution pool, a solution temperature profile is developed. Mass, species and energy balances are used to compute segmental heat and mass transfer rates while accounting for the extraneous effects, mainly, heat conduction between the drip tray and the coolant headers, and the heat losses to the ambient. The segments exchanging heat with the coolant were further sub-divided into film and droplet segments. For a majority of the test conditions, the contribution of the droplet mode to the total absorption rate is found to be very small. However, as the dilute solution concentration decreases and the operating pressure increases, the contribution of the droplet mode may not be negligible. The droplet mode absorption rates estimated from models in the literature were subtracted from the total absorption rates in each segment to obtain the film contribution to absorption. These film absorption rates were then used to compute the experimental film heat and mass transfer coefficients. The segmental heat and mass transfer coefficients were then represented by the relevant non-dimensional numbers. The effects of the operating conditions on the non-dimensional heat and mass transfer coefficients, Nusselt number and Sherwood number respectively, through the liquid and vapor properties were discussed.

Based on the insights gained from these trends, empirical correlations were developed for predicting the Nusselt and Sherwood numbers. Their applicability is limited to the ranges of parameters shown in Table 6.7. Use of these correlations beyond these ranges is likely to lead to less reliable predictions. It should be noted that the vapor-phase mass transfer correlation is also subject to additional uncertainty due to the approximate nature of the evaluation of vapor-phase transport properties, as discussed in Appendices A and B.

Table 6.7 Range of Applicability of Heat and Mass Transfer Correlations

Absorber Mass Flow Rate	
Concentrated Solution	$1.86 \times 10^{-2} - 3.43 \times 10^{-2}$ kg/s
Inlet Vapor	$7.86 \times 10^{-4} - 3.77 \times 10^{-3}$ kg/s
Absorber Temperature	
$T_{Abs,in}$	$34.7 - 105.4\,^{\circ}$C
$T_{Abs,out}$	$14.8 - 68.6\,^{\circ}$C
$T_{Abs,V,in}$	$-10.5 - 28.2\,^{\circ}$C
Absorber Concentration	
$x_{Abs,in}$	$15.2 - 41.8\%$
$x_{Abs,out}$	$20.7 - 44.2\%$
$x_{Abs,V,in}$	$80.7 - 99.9\%$
Absorber Pressure	
$P_{Abs,ave}$	$169 - 520$ kPa
Non-Dimensional Parameters	
Re_l	$26 - 157$
Pr_l	$2.2 - 10.4$
Sc_l	$45.4 - 588.1$
Pr_v	$0.5 - 0.93$
Ra_v	$14800 - 202534$
Gr_v	$4223 - 59893$
Sc_v	$0.5 - 0.53$
Ja_v	$9.8 \times 10^{-3} - 3.87 \times 10^{-2}$

CHAPTER 7 CONCLUSIONS AND RECOMMENDATIONS

7.1 Conclusions

A detailed investigation of ammonia-water absorption heat and mass transfer in a horizontal-tube falling-film absorber was conducted. A large test facility was designed and constructed with numerous design features and control and plumbing options to enable absorption experiments over a large range of flow rates (0.019 - 0.034 kg/s), concentrations (5 - 40%) and pressures (150 - 500 kPa). Measured quantities such as temperatures, pressures and flow rates at numerous locations around the test loop were analyzed to obtain absorber heat duties, overall and solution heat transfer coefficients and mass transfer coefficients for the various test conditions both at the component and the local level.

At the component level, for the range of experiments conducted, the absorber heat duty varied from 3.11 to 10.2 kW, the overall heat transfer coefficient varied from 753 to 1853 W/m^2-K, the solution heat transfer coefficient varied from 923 to 2857 W/m^2-K, and the mass transfer coefficient varied from 0.0026 to 0.25 m/s and the liquid mass transfer coefficient varied from 5.51×10^{-6} to 3.31×10^{-5} m/s, depending on the test condition. Care was also taken throughout the study to not only establish the desired conditions, but also to maintain the solution-side thermal resistance as the governing resistance so that absorption heat and mass transfer phenomena could be measured accurately. A detailed component level analysis of these experiments was presented by Lee (2007). In addition, local measurements allowed quantification of the variation of

266

heat and mass transfer rates along the solution flow path within the absorber. To aid the local analysis, videos of the solution flowing over the horizontal tube bank while absorbing refrigerant vapor were recorded. For the range of the experiments conducted, the droplet mode was found to be the dominant flow mode between successive tube rows. The effects of several parameters such as solution flow rate, concentration, and pressure on droplet spacing and size, film thickness, residence time and Reynolds number were investigated. The primary droplet diameter was found to vary in a narrow range (between 5.86 to 6.58 mm) because both the surface tension and the density varied in similar manner with the changes in operating conditions in the present study. The droplet formation time varied between 0.22 and 0.51 s. The droplet spacing was found to increase with an increase in the solution flow rate and to decrease with an increase in both the solution concentration and absorber pressure. Both the film thickness and the residence time in the falling-film were found to increase with increasing solution concentration and decreasing pressure. In addition, it was also found that the observed values of the primary droplet diameter and the droplet spacing were in reasonable agreement with the values predicted from the literature; however, the droplet formation time and the residence time in the falling-film were shorter than the predictions. The differences are most likely due to a multi-column geometry, influences of the neighboring droplet sites, and the momentum carried forward by the solution from above. The solution Reynolds number was found to have the largest effect on the solution heat transfer coefficient.

To study the progression of absorption rates in the absorber, the absorber assembly was divided into six distinct segments. Segment-wise heat duty, vapor mass

absorbed, and heat and mass transfer coefficients were then calculated. Using the insights gained from the videos, absorption in the three segments involving heat exchange with the coolant was further sub-divided into two phases: falling-film and droplet. It was found that most of the vapor is absorbed in the lower segments (which include 5 out of the 6 tube rows of the array), although the amount of the vapor absorbed per tube decreased in the lower segments due to the decreasing driving potential. The amount of vapor absorbed in the droplet mode was estimated using an analogy between heat and mass transfer for vapor flowing around a spherical droplet. It was found that the liquid-phase resistance to mass transfer in the droplets was negligible for most data points. These estimates showed that absorption in the droplet mode is less than 6% of the total absorption for most of the data points. The segmental film heat transfer coefficient varied from 78 to 6116 W/m^2-K. Similarly, the segmental vapor mass transfer coefficient varied from -0.42 to 2.8 m/s, and the local liquid mass transfer coefficients varied from -3.59×10^{-5} (indicating local desorption in some cases) to 8.96×10^{-5} m/s.. The negative mass transfer coefficient implies local desorption in some instances (which could also be represented with a positive mass transfer coefficient and a negative absorption rate).

The absorber heat duty and the solution heat transfer coefficient were found to increase with increasing solution flow rate. In general, the solution heat transfer coefficient was found to decrease with increasing pressure and dilute solution concentration at a given solution flow rate. The mass transfer coefficient showed little effect of the solution flow rate; instead, it was found to be primarily determined by the operating conditions (that affect both the solution and the vapor properties). Heat and mass transfer correlations were developed from the data obtained in this study in terms of

the relevant dimensionless parameters. The segmental film heat transfer coefficient was found to be affected primarily by the solution Re and Pr. In addition, a pressure correction term was found to improve the predictive capability of the correlation for the segmental heat transfer coefficient.

$$Nu_{l,segment} = 7.589 \times 10^{-3} \times Re_{seg,l}^{1.04} \times Pr_{seg,l}^{0.45} \times \left(\frac{P_{abs}}{345\,kPa} \right)^{-0.145} \tag{7.1}$$

The segmental liquid-phase mass transfer coefficient was found to be affected primarily by the solution Re and Sc. In addition, a pressure correction term was found to improve the predictive capability of the correlation for the segmental liquid-phase mass transfer coefficient.

$$Sh_{seg,l} = 1.298 \times 10^{-4} \times \left(Re_l \right)^{0.57} \times \left(Sc_l \right)^{1.32} \times \left(\frac{P_{abs}}{345\,kPa} \right)^{0.644} \tag{7.2}$$

Due to the coupled nature of heat and mass transfer processes in ammonia-water absorption, the vapor-phase mass transfer was analyzed on the basis of the heat and mass transfer analogy. Vapor-phase heat transfer was considered to be a natural convection process, because it was deemed that the vapor is relatively quiescent in the large absorption chamber with no obvious forced-flow related parameters. Thus, the heat and mass transfer processes are idealized to be governed primarily by temperature and concentration differences, respectively, between the liquid and vapor phases. Because of this idealization, segmental differences in vapor conditions are not appreciable. As a first approximation, the overall vapor-phase mass transfer correlation of Lee (2007) may be used to predict transfer coefficients at the local level.

In summary, systematic experiments were conducted over a wide range of air-conditioning and heat pumping operating conditions in this study to understand heat and mass transfer in falling-film ammonia-water absorbers. The primary contribution of this work is the measurement and modeling of local absorption heat and mass transfer phenomena using heat and mass transfer measurements and simultaneous high-speed video recording while operating in a complete absorption chiller. In addition, these measurements and models cover a wide range of operating conditions representative of all postulated absorption system operating modes such as refrigeration, air-conditioning, warm-ambient heat pumping, and cold-ambient heat pumping. This is unlike all other studies in the literature, which either measure system-level performance, or component-level performance in stand-alone test rigs that most often do not provide solution and vapor conditions representative of actual operating heat pumps. These results can therefore be used to design absorbers at realistic operating conditions, and also provide insights for the design and operation of other components in an absorption system.

7.2 Recommendations

The present study yielded an understanding of heat and mass transfer in falling-film ammonia-water absorbers over a wide range of air-conditioning and heat pumping operating conditions. It is known, and was further demonstrated here that absorption is a complex, coupled heat and mass transfer phenomenon governed by liquid and vapor phase saturation conditions, operating pressures and component geometry. The various driving potentials and local gradients inherent in these phases can be quite different at conditions close to saturation and those that involve subcooling of the incoming liquid solution. The inlet subcooling characteristic of the dilute solution entering an absorber

270

that is part of an operational heat pump system introduces considerable confounding influences that make it challenging to isolate the contribution, to absorption, of the corresponding equilibrium conditions, and those due to the subcooling. Many studies in the literature have circumvented this issue by conducting studies on individual absorber components, in which a single-pressure test facility is used to supply dilute solution and vapor at near-saturation conditions that can be readily obtained because of the relative independence from conditions at the heat source (evaporator) and heat sink (condenser.) In such cases, the inlet subcooling absorption portion is fairly minimal and does not significantly affect the overall process. In addition, definition of the driving temperature difference is fairly straightforward in such cases, with most investigators choosing the saturation temperature of the liquid phase to establish quantities such as the log-mean-temperature difference between the solution and the coolant. When testing in an overall heat pump facility necessarily introduces large degrees of subcooling, however, the saturation temperature does not appear to be the appropriate basis temperature, and it is better to use the bulk fluid temperature as being more representative of the liquid phase, as was done in the present study. It may be best, however, to first opt for the much better process control offered by the single-pressure test facility and understand absorption in great detail and with much better accuracies at saturated conditions, even if they are not most representative of an actual operating absorption system. Once absorption heat and mass transfer are understood at these saturated conditions, additional tests at subcooled conditions, either in a single-pressure facility, or in a complete system such as the one developed in this study, would yield additional insights about the influence of subcooled inlet conditions.

Attempts were made to record process parameters as accurately as possible both at the overall and the local levels. However, the complete absorption system used in this study also introduced additional uncertainties in establishing the dilute solution concentration and flow rate entering the absorber, and in the other important flow rates and concentrations, i.e., of the concentrated solution and the ammonia vapor. This is because mass, species and energy balances must be satisfied iteratively and simultaneously in all the major components (desorber, separator, rectifier, condenser, expansion device, refrigerant pre-cooler, evaporator, and absorber, and their respective coupling loops) to be able to obtain the conditions at the absorber. In particular, for example, the reflux liquid stream exiting the rectifier can alter the dilute solution conditions to varying degrees; but the typically very low flow rates of the reflux stream make it very difficult to measure accurately. Thus, the choice of testing using the complete absorption system introduces three major confounding influences: a) the absorption process itself results from a combination of actual subcooled inlet conditions and the corresponding equilibrium conditions, with the individual contributions difficult to isolate, b) the definition of driving temperature differences becomes a significant issue unlike the situation where the liquid phase enters at near-saturated conditions, c) overall component mass, species and energy balances are affected to a considerable degree by the accuracy with which every other component in the system can be analyzed, whereas in a single-pressure facility, these balances must be accurately established only for the test component, i.e., the absorber. Based on the experience gained from this study, some areas for future investigation are identified and discussed here.

7.2.1 Local Level Measurements

During the absorption experiments, row-wise solution temperature was measured by thermocouples attached on the tube surface. Due to the dynamic behavior of the solution flow, it is almost impossible to ascertain that the thermocouples will always contact the solution. It is quite possible that the thermocouples alternatively measure solution temperature and vapor temperature, introducing considerable intermittency in the measured temperatures. It was therefore necessary to rely on a temperature profile to obtain the segmental solution temperatures, which inherently introduces additional uncertainties. Although it is very difficult to move thermocouples during experiments to bring them into contact with the solution, an alternative can be the use of multiple thermocouples on each tube row, which would provide a more representative estimate of the solution temperature.

7.2.2 Coolant-side Temperature Difference

The primary objective of this study was to investigate absorption phenomena at specific operating conditions. For many test conditions, combinations of the absorber pressure and the dilute solution concentration required either very large or very small coolant flow rates. The issue of smaller coolant flow rates was partially overcome by the use of an electric heater in the absorber coolant loop. However, some of the cases with larger coolant flow rates resulted in small overall coolant side temperature differences (ΔT_C). A smaller overall ΔT_C results in an even smaller segmental ΔT_C. Therefore, the uncertainties associated with temperature measurements on the coolant side can also be large. To gain further insight into local absorption rates, experiments may be conducted at other operating conditions where a reasonable coolant ΔT_C can be maintained.

7.2.3 Absorber Configurations

The absorber fabricated in this study consisted of a rectangular assembly of 24 tubes placed in a cylindrical shell with a variety of flanges and penetrations for inlets, outlets, instrumentation, illumination and visualization. Because the vapor density of ammonia is much larger than that of water vapor in Lithium Bromide-Water systems, vapor-phase pressure drop is not a critical issue in determining saturation conditions in ammonia-water absorbers, and such large vapor spaces are not necessary in ammonia-water absorption systems. Similarly, the horizontal tube bank, falling-film geometry for the liquid solution phase is not essential, because pressure drop incurred in the liquid phase is not a critical penalty in ammonia-water systems, unlike LiBr-H_2O systems, which almost necessarily must have negligible pressure drops in the absorbers. Therefore, other configurations with smaller vapor spaces and greater forced-convective transport in both phases should be studied in future investigations on ammonia-water absorption. Examples include plate heat exchangers (Christensen *et al.* 1998), shell-and-tube heat exchangers (Meacham and Garimella 2002b), and innovative enhanced geometries for bubble-type absorbers (Merrill *et al.* 1994) that capitalize on the properties of the ammonia-water fluid pair.

Along the lines of the above discussion, ammonia-water absorbers are amenable to miniaturization, which has been shown to yield significant reductions in component size by Meacham and Garimella (2002a; 2004). Thus, absorption in miniaturized geometries should be investigated in further detail, which will benefit small capacity and portable heat pump applications, and also small-scale absorption systems driven by solar energy and waste heat, issues that are gaining prominence in today's energy landscape.

Also, the present study was conducted only on tubes of a specific diameter (9.5 mm) with a specific transverse (30.6 mm) and longitudinal (20.1 mm) pitch. This study should be extended to tubes of different diameters and pitches to increase the range of applicability of the results.

7.2.4 Numerical Analysis

The primary nature of the present study is experimental. Numerical analyses that solve the governing equations for mass, momentum, and energy may be carried out and compared with the results of the present study. However, the ammonia-water mixture has a volatile absorbent; therefore, the refrigerant vapor always contain small amounts of water, resulting in a different concentration of the condensing flux from the vapor concentration both at the interface and in the bulk. This makes numerical analysis extremely difficult; as a result of this, there are only a few studies (Gommed *et al.* 2001; Kim 1998; Lee *et al.* 2005; Wassenaar and Segal 1999) that have attempted to analyze ammonia-water absorption numerically as opposed to water-Lithium bromide absorption.

7.2.5 Flow Visualization

For the range of experiments conducted ($Re_l = 4 \cdot \Gamma_l / \mu_l$ < 100), the droplet mode was observed to be the dominant flow mode for a majority of the test conditions. Detailed quantitative analysis of the film and drop evolution with time could provide additional quantitative information on the interface area and liquid volume in different phases of the absorption process. Additional experiments at higher flow rates may be conducted to study the column (jet) and falling-film modes. At the fundamental level, the findings of the present study, and the underlying modeling of the flow phenomena would

275

be further aided by detailed investigations on a single tube to understand the evolution of the falling film, the formation of droplets, etc., and the resulting species concentration profiles in ammonia-water absorbers. These studies should be conducted using computational techniques as well as localized measurements of solution temperatures at different transverse and circumferential locations within the liquid film and along the tube length. Such studies, combined with the component and row-level measurements achieved in this study, would assist in strengthening the hydrodynamic bases used for the correlations developed in the present study.

Finally, similar studies on other fluid pairs would assist in the understanding of coupled heat and mass transfer processes in space-conditioning, chemical processing, waste heat recovery, and other diverse applications.

APPENDIX A AMMONIA-WATER MIXTURE PROPERTIES

This appendix discusses the calculation procedures to obtain the thermodynamic and transport properties of ammonia-water mixtures.

A.1 Thermodynamic Properties

The thermodynamic properties of ammonia-water mixture in the liquid and vapor phases are obtained from *Engineering Equation Solver* (EES) V7.697-3D software (Klein 2006). EES can provide the thermodynamic properties of ammonia-water mixture in subcooled, saturated and superheated states. The procedures used to calculate these properties are based on the correlations provided by Ibrahim and Klein (1993). First, they use separate equations of state (in the form of Gibbs free energy) for pure ammonia and pure water to calculate the properties of individual component in each phase. For the vapor phase, they assume the ammonia-water vapor mixture to behave as an ideal gas to obtain the mixture properties. For the liquid phase, they use the Gibbs excess energy to account for the departure from ideal solution behavior. The Gibbs free energy can be obtained using the following equation,

$$G = h_o - T \cdot s_o + \int_{T_o}^{T} C_P dT + \int_{P_o}^{P} v dP - T \int_{T_o}^{T} \frac{C_P}{T} dT \qquad (A.1)$$

This equation uses empirical correlations for specific volume (v) and specific heat capacity (C_P) as a function of T and P for the liquid and vapor phases. For the liquid phase,

$$v_l = a_1 + a_2 P + a_3 T + a_4 T^2 \tag{A.2}$$

$$C_{P,l} = b_1 + b_2 T + b_3 T^2 \tag{A.3}$$

And, for the vapor phase,

$$v_V = RT/P + c_1 + c_2/T^3 + c_3 T^{11} + c_4 P^2/T^{11} \tag{A.4}$$

$$C_{P,V} = d_1 + d_2 T + d_3 T^2 \tag{A.5}$$

All the coefficients in the above equation are determined empirically and can be found in Ziegler and Trepp (1984). The Gibbs free energy is also presented in terms of reduced parameters. The reduced parameters are defined with respect to a reference state as follows:

$$T_r = T/T_B \tag{A.6}$$

$$P_r = P/P_B \tag{A.7}$$

$$G_r = G/(RT_B) \tag{A.8}$$

$$h_r = h/(RT_B) \tag{A.9}$$

$$s_r = s/R \tag{A.10}$$

$$v_r = vP_B/(RT_B) \tag{A.11}$$

Ibrahim and Klein (1993) use the reference state at T_B = 100 K and P_B = 10 bar where R = 8.314 kJ/kmol-K. The molar specific enthalpy, volume and entropy can be obtained from the Gibbs free energy as follows:

$$h = -RT_B T_r^2 \left[\frac{\partial}{\partial T_r}(G_r/T_r) \right]_{P_r} \tag{A.12}$$

$$s = -R \left[\frac{\partial G_r}{\partial T_r} \right]_{P_r} \tag{A.13}$$

$$v = -\frac{RT_B}{P_B} \left[\frac{\partial G_r}{\partial P_r} \right]_{T_r} \tag{A.14}$$

Once these properties are known for individual species, mixture rules are applied to obtain the properties of the vapor and liquid mixtures. Since the vapor is assumed to be an ideal gas, a simple mass fraction weighted average is sufficient to obtain the vapor mixture properties. For example,

$$h_{V,mix} = x_{V,NH_3} \cdot h_{V,NH_3} + \left(1 - x_{V,NH_3}\right) \cdot h_{V,H_2O} \tag{A.15}$$

$$v_{V,mix} = x_{V,NH_3} \cdot v_{V,NH_3} + \left(1 - x_{V,NH_3}\right) \cdot v_{V,H_2O} \tag{A.16}$$

However, for the liquid phase, the excess Gibbs energy (G_{excess}) should be known to account for the deviation from ideal solution behavior. Ibrahim and Klein (1993) use the equation presented by Ziegler and Trepp (1984) to obtain G_{excess} but recalculated the coefficients by including additional experimental data of Gillespie *et al.* (1987). The excess Gibbs energy is given as:

$$G_{l,excess} = \left\{ F_1 + F_2 \cdot \left(2x_l - 1\right) + F_3 \cdot \left(2x_l - 1\right)^2 \right\} \times \left(1 - x_l\right) \tag{A.17}$$

where

$$F_1 = E_1 + E_2 \cdot P_r + \left(E_3 + E_4 \cdot P_r\right) T_r + E_5 / T_r + E_6 / T_r^2 \tag{A.18}$$

$$F_2 = E_7 + E_8 \cdot P_r + \left(E_9 \cdot E_{10} \cdot P_r\right) T_r + E_{11} / T_r + E_{12} / T_r^2 \tag{A.19}$$

$$F_3 = E_{13} + E_{14} \cdot P_r + E_{15} / T_r + E_{16} / T_r^2 \tag{A.20}$$

279

The excess specific enthalpy, entropy and volume are obtained using equations (A.12), (A.13) and (A.14) with G substituted by G_{excess}. Using a mass fraction weighted average, mixture specific enthalpy and volume can be obtained as:

$$h_{l,mix} = x_{l,NH_3} \cdot h_{l,NH_3} + \left(1 - x_{l,NH_3}\right) \cdot h_{l,H_2O} + h_{excess} \qquad (A.21)$$

$$v_{l,mix} = x_{l,NH_3} \cdot v_{l,NH_3} + \left(1 - x_{l,NH_3}\right) \cdot v_{l,H_2O} + v_{excess} \qquad (A.22)$$

These correlations cover vapor-liquid equilibrium pressures of 20 to 11000 kPa (0.2 to 110 bar) and temperatures of -43°C to 327°C (230 to 600 K). All the experimental conditions of the present study fall under these ranges.

A.1.1 EES Library Function

A procedure called NH3H2O using the above-mentioned equations is used to return the properties of ammonia-water mixture in sub-cooled, saturated and super-heated states. The call statement for this procedure in an EES program is as follows (this information is taken from EES help):

CALL NH3H2O(Code,In1,In2,In3: T, P, x, h, s, u, v, q)

The 4 parameters to the left of the colon are inputs to the procedure and the eight values to the right are outputs whose values are set by the NH3H2O procedure. The NH3H2O routine operates in SI units with T in K, P in bar, x as ammonia mass fraction, h in kJ/kg, s in kJ/kg-K, u in kJ/kg, v in m³/kg, and q is the mixture quality. For saturated states, 0 <=q <= 1. Subcooled states are indicated with q = -0.01 and superheated states have q = 1.01. The code is combination of 3 digits corresponding to 3 of the 8 parameters to the right of the colon. Digits 1 to 8 refer to the parameter in the sequence listed above, e. g.,

1 corresponds to T, 2 corresponds to P, and so on. It is necessary to know at least three parameters in order to compute the others. For example, if the temperature, pressure and concentration are known; the enthalpy, entropy, specific volume, etc. can be computed. If one of the inputs is unknown but one of the outputs is known, then EES can calculate the remaining parameters iteratively.

A.2 Transport Properties

The main transport properties of interest in heat and mass transfer calculations are the viscosity, thermal conductivity, surface tension and diffusion coefficient of the liquid and vapor phases. In the present study, the liquid-phase transport properties (viscosity, conductivity and surface tension) are obtained using curve-fits to the data provided by Herold *et al.* (1996), while the vapor-phase transport properties are obtained using the Chapman-Enskog Kinetic Theory of Gases outlined in Mills (1995).

A.2.1 Liquid Phase

Herold *et al.* (1996) provide the liquid-phase viscosity, thermal conductivity and surface tension data for ammonia-water mixtures in graphical format. Empirical correlations as a function of the solution temperature and concentration are developed using these data (Meacham 2002).

A.2.1.1 Liquid-Phase Viscosity

The liquid-phase viscosity of the ammonia-water solution in centiPoise (cP) is obtained using following equations (here, T should be in ^{o}F):

For T < 145°F (63°C),

$$\mu_{cP} = 2.5210 + 1.0675 \cdot x_{l,ave} + 2.2685 \times 10^{-03} \cdot T - 0.0322 \cdot (1 - x_{l,ave}) \cdot T - 5.2229 \cdot x_{l,ave}^2$$
$$+ 112.90 \times 10^{-06} \cdot (1 - x_{l,ave})^2 \cdot T^2 - 0.8639 \cdot x_{l,ave}^3 + 2.4387 \cdot x_{l,ave}^4$$

$$(A.23)$$

For T > 145°F (63°C) and T < 195°F (91°C),

$$\mu_{cP} = 1.0816 - 0.2202 \cdot x_{l,ave} - 2.1732 \times 10^{-03} \cdot T - 1.9322 \times 10^{-03} \cdot (1 - x_{l,ave}) \cdot T - 0.3905 \cdot x_{l,ave}^2$$
$$(A.24)$$

For T > 195°F (91°C),

$$\mu_{cP} = 0.5279 + 0.1654 \cdot x_{l,ave} - 1.8905 \times 10^{-03} \cdot T - 734.47 \times 10^{-06} \cdot (1 - x_{l,ave}) \cdot T \quad (A.25)$$

The viscosity obtained in centiPoise is converted in kg/m-s as follows:

$$\mu_l = \mu_{cP} \cdot 0.001 (kg/m - s) \qquad (A.26)$$

A.2.1.2 Liquid-Phase Thermal Conductivity

The liquid-phase thermal conductivity of ammonia-water solution is calculated using following equation (here, T should be in °C):

$$k_l = 0.5727 + 1.7021 \times 10^{-03} \cdot T_l - 0.0541 \cdot x_l - 5.8359 \times 10^{-06} \cdot T_l^2 + 8.4900 \times 10^{-09} \cdot x_l^2$$
$$- 3.3410 \times 10^{-03} \cdot T_l \cdot x_l \ (W/m\text{-}K)$$

$$(A.27)$$

A.2.1.3 Liquid-Phase Surface Tension

The liquid-phase surface tension (in kg/s^2) of ammonia-water solution is calculated using following equation (here, T should be in °F):

$$\sigma_l = [(1.1211 \times 10^{-06} \cdot T^3 - 1.1955 \times 10^{-03} \cdot T^2 + 0.2970413 \cdot T - 6.2041 \times 10^{01} \cdot x_l^3$$
$$+ 103.3571 \cdot x_l^2 - 4.8571 \times 10^{01} \cdot x_l + 39.92207 + 1.9450 \times 10^{-04} \cdot x_l^2 \cdot T^2 \qquad (A.28)$$
$$+ 0.1851776 \cdot x_l^2 \cdot T + 1.40568 \times 10^{-03} \cdot x_l \cdot T^2 - 7.0072 \times 10^{-01} \cdot x_l \cdot T)] \times 0.001$$

A.2.1.4 Liquid-Phase Diffusivity

Ammonia-water binary diffusion coefficient in the liquid-phase is obtained using the following equation suggested by Frank *et al.* (1996).

$$D_{aw,l} = (1.65 + 2.47 \cdot x_l) \times 10^{-6} \times e^{\left(\frac{-16600}{R \cdot (T_l + 273.15)}\right)} \, (m^2/s) \qquad (A.29)$$

In this equation, R is the universal gas constant. The solution temperature should be in °C. This equation provides the best estimate for ammonia-water liquid-phase binary diffusion coefficients for ammonia concentrations of up to 31%. In the absence of other correlations, this equation was used for test cases at 40% dilute solution concentration also.

A.2.2 Vapor Phase

Transport properties of the ammonia-water vapor mixture are calculated using the Chapman-Enskog kinetic theory (Mills 1995) for pure substances and the mixture rules of Wilke (1950).

A.2.2.1 Vapor-Phase Viscosity of Individual Components

The viscosities of ammonia and water are obtained using a Lennard-Jones potential model, which represents the potential energy of interaction between a pair of molecules during collision. Although the Lennard-Jones potential model is valid only for non-polar molecules, in the absence of other reliable approaches, it is deemed to be adequate for ammonia and water molecules, which have appreciable dipole moments.

$$\mu_v = 2.67 \times 10^{-6} \cdot \frac{\sqrt{M_v \cdot T_{v,bulk}}}{\sigma_v^2 \cdot \Omega_{\mu,v}} \qquad (A.30)$$

where, σ_v is the collision diameter at zero potential energy in angstroms,

$T_{v,bulk}$ is the bulk temperature in K of each component in the vapor phase,

M_v is molecular mass of each component,

$\Omega_{\mu,v}$ is the collision integral as a function of temperature and maximum energy attraction,

ε_v is the maximum energy of attraction between a pair of molecules tabulated for chemical species.

A.2.2.2 Vapor-Phase Conductivity of Individual Components

To calculate the thermal conductivities of ammonia and water, the relationship between thermal conductivity and the viscosity for monatomic gases is used and the modified Eucken correction is applied to account for the rotational and vibrational modes caused by nonlinearity of polyatomic ammonia and water vapor.

$$k_{v,translational} = \frac{5}{2} C_{v,v} \cdot \mu_v \tag{A.31}$$

$$k_v = k_{v,translational} + 1.32 \cdot \left(C_{p,v} - \frac{5}{2} \frac{R}{M_v} \right) \cdot \mu_v \tag{A.32}$$

where, $C_{v,v} = \frac{3}{2} \frac{R}{M_v}$, $C_{p,v} = (5 + N_r) \cdot \left(\frac{1}{2} \frac{R}{M_v} \right)$, and N_r is the rotational degrees of freedom of each molecule. Both the ammonia and the water molecules have three rotational degrees of freedom.

A.2.2.3 Vapor-Phase Mixture Properties

Once the viscosities and thermal conductivities of pure ammonia and water are obtained, ammonia-water mixture viscosity and thermal conductivity are estimated using mixture rules (Wilke 1950).

$$\mu_{12,v} = \sum_{i=1}^{2} \frac{x_{i,v} \cdot \mu_{i,v}}{\sum_{j=1}^{n} x_{j,v} \cdot \Phi_{ij,v}} \tag{A.33}$$

$$k_{12,v} = \sum_{i=1}^{2} \frac{x_{i,v} \cdot k_{i,v}}{\sum_{j=1}^{2} x_{j,v} \cdot \Phi_{ij,v}} \tag{A.34}$$

$$\Phi_{12,v} = \frac{\left[1 + \left(\mu_{1,v} \middle/ \mu_{2,v} \right)^{\!\!1/2} \cdot \left(M_{2,v} \middle/ M_{1,v} \right)^{\!\!1/4} \right]^{2}}{\sqrt{8} \cdot \left[1 + \left(M_{1,v} \middle/ M_{2,v} \right) \right]^{1/2}} \tag{A.35}$$

The binary vapor-phase diffusion coefficient is obtained from the following formula.

$$D_{12,v} = 1.86 \times 10^{-7} \cdot \frac{\sqrt{T_{v,bulk}^{3} \cdot \left(\dfrac{1}{M_{1,v}} + \dfrac{1}{M_{2,v}} \right)}}{\sigma_{12,v}^{2} \cdot \Omega_{D,v} \cdot P_{v,bulk}} \tag{A.36}$$

where, $P_{v,bulk}$ is the bulk vapor pressure in atmospheres,

$\Omega_{D,v}$ is the collision integral for diffusion and is different from $\Omega_{\mu,v}$

$$\sigma_{12,v} = \frac{1}{2} \cdot \left(\sigma_{w,v} + \sigma_{a,v} \right)$$

$$\varepsilon_{12,v} = \sqrt{\varepsilon_{w,v} \cdot \varepsilon_{a,v}}$$

In all these equations, 1 and 2 refer to ammonia and water vapor, respectively. The specific heat of the ammonia-water mixture is obtained from the enthalpy change for a

temperature change of 1^oC at the temperature of the vapor of interest at the given pressure and concentration.

APPENDIX B UNCERTAINTY CALCULATIONS

An uncertainty propagation analysis was conducted on the data obtained in this study. The main parameters of interest are the various solution stream concentrations, the absorber heat duties, and the coolant, the overall and the film heat transfer coefficients, the mass transfer coefficient in the absorber, and the reflux flow rate, which affects the dilute solution concentration and flow rate. The calculation of heat duties, heat and mass transfer coefficients, and the reflux flow rate is affected both directly by errors in the measurements of temperature, pressure and flow rate, and indirectly due to errors in the estimation of various concentrations based on the measured temperatures and pressures at various state points in the system. The effect of the following measurement uncertainties is accounted for in the uncertainty calculations for the parameters of interest:

- *Pressures and Temperatures at*: Desorber outlet, rectifier inlet and outlet, reflux outlet, separator liquid outlet, absorber solution inlet and outlet, and absorber vapor inlet
- *Flow rate of*: Dilute and concentrated solution, and refrigerant flow rates
- *Coolant Side*: Inlet and outlet temperatures, and coolant flow rate
- *Geometry*: Tube ID, OD, and length

B.1 Uncertainties in Measurements

The absolute pressures in the system were measured using pressure transducers manufactured by Rosemount, the temperatures were measured using T-type thermocouples and RTDs, the solution flow rates were measured using Coriolis mass

flow meters by Micromotion, and the coolant flow rates were measured using various magnetic, positive displacement and Coriolis type flow meters. Instrument uncertainties for the pressure transducers and flow meters are shown in Tables B.1 and B.2, respectively. The absolute uncertainty in temperature measurement is taken as $\pm 0.5^{\circ}C$, while the uncertainty in geometrical parameters of the absorber tube array such as tube diameter and length is taken as ± 0.0025 mm (± 0.0000025 m).

B.2 Sample Uncertainties

In the computation of the propagation of errors, the uncertainties in the dependent (or calculated parameters) are calculated as described below. Consider a calculated parameter, x, which is affected by uncertainties in measurements of several other parameters (a, b, c, d, e... etc).

Table B.1 Uncertainties of the Pressure Transducers (from Rosemount Inc.)

Location	Model	Calibrated Span (psi)	Accuracy (of Cal Span)	Total Uncertainty (psi)
$P_{Abs,in}$	2088	800	$\pm 0.25\%$	± 2
$P_{Abs,out}$	3051 TA4	4000	$\pm 0.075\%$	± 3
$P_{Abs,V,in}$	3051 TA5	10000	$\pm 0.075\%$	± 7.5
$P_{Des,in}$	2088	800	$\pm 0.25\%$	± 2
$P_{Des,out}$	2088	800	$\pm 0.25\%$	± 2
$P_{Sep,out}$	2088	800	$\pm 0.25\%$	± 2
$P_{Reflux,out}$	3051 TA5	10000	$\pm 0.075\%$	± 7.5
$P_{Con,in}$	2088	800	$\pm 0.25\%$	± 2
$P_{Con,out}$	3051 TA5	10000	$\pm 0.075\%$	± 7.5
$P_{Evap,in}$	3051 TA5	10000	$\pm 0.075\%$	± 7.5
$P_{Evap,out}$	3051 TA4	4000	$\pm 0.075\%$	± 3
$DP_{Abs,C}$	3051 CD	2000	$\pm 0.075\%$	± 1.5

Table B.2 Uncertainties of the Solution and Coolant Flow Meters

Locations	Model	Calibrated Span	Accuracy	Total Uncertainty
Dilute Solution	CMF025 Elite (Micromotion)	0-80 lb$_m$/min 0-10 GPM	±0.1% (Flow) ±0.5 kg/m^3 (Density)	Relative
Concentrated Solution	CMF025 Elite (Micromotion)	0-80 lb$_m$/min 0-10 GPM	±0.1% (Flow) ±0.5 kg/m^3 (Density)	Relative
Refrigerant	C25 (Micromotion)	0-3 lb$_m$/min	±0.1%	Relative
Absorber Coolant	8711 (Rosemount)	0-20 GPM	±0.5%	Relative
Condenser Coolant	CMF100 Elite (Micromotion)	0-1000 lb$_m$/min	±0.1% (Flow) ±0.5 kg/m^3 (Density)	Relative
Evaporator Coolant	JVM-60KL (AW Company)	2 – 20 GPM	±0.5% @ ν = 3 × 10^{-5} m^2/s	Relative

$$x = f(a,b,c,d,e,....) \tag{B.1}$$

The total uncertainty in the calculation of x is given as:

$$U_x^2 = \left(\frac{\partial x}{\partial a}U_a\right)^2 + \left(\frac{\partial x}{\partial b}U_b\right)^2 + \left(\frac{\partial x}{\partial c}U_c\right)^2 + \left(\frac{\partial x}{\partial d}U_d\right)^2 + \left(\frac{\partial x}{\partial e}U_e\right)^2 + .. \tag{B.2}$$

where, U_a, U_b etc. are uncertainties in the measurements of a, b, and so on.

In determining uncertainties in the present study, the effects of 25 measured inputs were accounted for. Table B.3 lists these parameters with their nominal measured values and uncertainties in measurement for the representative data point at an absorber pressure of 345 kPa, dilute solution concentration of 25% and concentrated solution flow rate of 0.026 kg/s.

Table B.3 List of Parameters included in Uncertainty Analysis for Absorber (345 kPa, 25%, 0.026 kg/s)

Measured Parameter	Measured Value ± Uncertainty
Flow Rates	
$\dot{m}_{Abs,C}$ (gpm)	4.804 ± 0.02402
$\dot{m}_{Ref,Measured}$ (lb$_m$/min)	0.374 ± 0.0003738
$\dot{m}_{Dilute}$ (lb$_m$/min)	3.01 ± 0.00301
$\dot{m}_{Concentrated}$ (lb$_m$/min)	3.506 ± 0.00351
Absolute Pressures (Psi)	
$P_{Abs,in}$ (Absorber Inlet)	51.02 ± 2
$P_{Abs,out}$ (Absorber Outlet)	50.85 ± 3
$P_{Abs,V,in}$ (Absorber Vapor In)	52.62 ± 7.5
$P_{Con,in}$ (Condenser Inlet)	163.5 ± 2
$P_{Des,out}$ (Desorber Outlet)	161 ± 2
P_{Rec} (Rectifier)	162.6 ± 7.5
$P_{Sep,out}$ (Separator Outlet)	161.7 ± 2
Absorber Coolant Temperatures (°C)	
$T_{Abs,C,in}$ (Coolant In)	12.47 ± 0.5
$T_{Abs,C,out}$ (Coolant Outlet)	18.75 ± 0.5
Working Fluid Temperatures (°C)	
$T_{Abs,Dil,in}$ (Absorber Inlet)	70.42 ± 0.5
$T_{Abs,Conc,out}$ (Absorber Outlet)	30.99 ± 0.5
$T_{Abs,V,in}$ (Absorber Vapor In)	-0.25 ± 0.5
$T_{Des,out}$ (Desorber Outlet)	132.1 ± 0.5
$T_{Rec,in}$ (Rectifier Vapor In)	119..6 ± 0.5
$T_{Rec,out}$ (Rectifier Vapor Out)	80.99 ± 0.5
$T_{Reflux,out}$ (Reflux Outlet)	51.4 ± 0.5
$T_{Sep,out}$ (Separator Sol Out)	119 ± 0.5

Table B-3 Continued...

Measured Parameter	Measured Value ± Uncertainty
$T_{Sep,V,out}$ (Separator Vapor Out)	122.4 ± 0.5
Geometrical Parameters (m)	
$Tube_{ID}$	0.008103 ± 0.0000025
$Tube_{Length}$	0.2921 ± 0.0000025
$Tube_{OD}$	0.009525 ± 0.0000025

Using the uncertainty values from Tables B.1 and B.2 for the various measurements, the overall uncertainties in the various solution stream concentrations, the absorber heat duties, and the coolant, overall and film heat transfer coefficients, the overall mass transfer coefficient, and the reflux flow rate are computed using an error propagation method (Taylor and Kuyatt 1993) as implemented in *Engineering Equation Solver* (EES) V7.697-3D software (Klein 2006). Table B.4 shows sample uncertainties for some of the parameters of interest at the absorber. In this table, partial derivatives and percent contributions to the total uncertainty for the respective calculated parameter as reported by EES are shown. Uncertainties in the coolant temperature measurement (±0.5°C) are the largest contributor (~80%) followed by the vapor pressure measurement (~13%) to the overall uncertainty in the film heat transfer coefficient.

Table B.4 Sample Uncertainties in the Main Parameters of Interest

Partial Derivative	% Uncertainty (of Total)
$x_{des,out} = 0.2386 \pm 0.003083 \ (\pm 1.29\%)$	
$\partial x_{des,out} / \partial P_{Des,out} = 0.001144$	55.11%
$\partial x_{des,out} / \partial T_{Des,out} = -0.004132$	44.89%
$x_{abs,in} = 0.2671 \pm 0.003426 \ (\pm 1.28\%)$	
$\partial x_{abs,in} / \partial \dot{m}_{Ref,measured} = 0.07611$	0.01%
$\partial x_{abs,in} / \partial \dot{m}_{Dilute} = -0.009452$	0.01%
$\partial x_{abs,in} / \partial \dot{m}_{Concentrated} \sim 0$	0.00%
$\partial x_{abs,in} / \partial P_{Con,in} = 0.000043$	0.06%
$\partial x_{abs,in} / \partial P_{Des,out} = 0.000653$	14.53%
$\partial x_{abs,in} / \partial P_{Rec} = 0.000388$	72.25%
$\partial x_{abs,in} / \partial T_{Rec,out} = -0.000271$	0.16%
$\partial x_{abs,in} / \partial T_{Reflux} = 0.001682$	6.02%
$\partial x_{abs,in} / \partial T_{Sep,out} = -1.138 \times 10^{-17}$	0.00%
$\partial x_{abs,in} / \partial T_{Sep,V,out} = -0.001808$	6.96%
$x_{abs,out} = 0.3336 \pm 0.002975 \ (\pm 0.9\%)$	
$\partial x_{abs,out} / \partial \dot{m}_{Ref,measured} = 0.3443$	0.19%
$\partial x_{abs,out} / \partial \dot{m}_{Dilute} = 0.06807$	0.47%
$\partial x_{abs,out} / \partial \dot{m}_{Concentrated} = -0.09515$	1.26%
$\partial x_{abs,out} / \partial P_{Con,in} = 0.000059$	0.16%

Table B-4 Continued...

Partial Derivative	% Uncertainty (of Total)
$\partial x_{abs,out} / \partial P_{Des,out} = 0.000561$	14.21%
$\partial x_{abs,out} / \partial P_{Rec} = 0.000333$	70.63%
$\partial x_{abs,out} / \partial T_{Rec,out} = -0.000369$	0.39%
$\partial x_{abs,out} / \partial T_{Reflux} = 0.001444$	5.89%
$\partial x_{Dilute} / \partial T_{Sep,out} = -1.138 \times 10^{-17}$	0.00%
$\partial x_{abs,out} / \partial T_{Sep,V,out} = -0.001552$	6.81%
$x_V = 0.9781 \pm 0.000764 \ (\pm 0.08\%)$	
$\partial x_V / \partial P_{Con,in} = 0.000206$	28.99%
$\partial x_{Concentrated} / \partial T_{Rec,out} = -0.001288$	71.01%
$h_{abs,in} = 128.9 \pm 2.701 \ \text{kJ/kg} \ (\pm 2.09\%)$	
$\partial h_{abs,in} / \partial \dot{m}_{Ref,measured} = -35.9$	0.00%
$\partial h_{abs,in} / \partial \dot{m}_{Dilute} = 4.459$	0.00%
$\partial h_{abs,in} / \partial P_{abs,in} = 0.005016$	0.00%
$\partial h_{abs,in} / \partial P_{Con,in} = -0.02039$	0.02%
$\partial h_{abs,in} / \partial P_{Des,out} = -0.308$	5.20%
$\partial h_{abs,in} / \partial P_{Rec} = -0.1832$	25.86%
$\partial h_{abs,in} / \partial T_{Abs,in} = 4.329$	64.21%
$\partial h_{abs,in} / \partial T_{Rec,out} = 0.1276$	0.06%
$\partial h_{abs,in} / \partial T_{Reflux} = 0.7933$	2.16%
$\partial h_{abs,in} / \partial T_{Sep,V,out} = 0.8527$	2.49%

Table B-4 Continued...

Partial Derivative	% Uncertainty (of Total)
$h_{abs,out}$ = -68.93 ± 2.444 kJ/kg (±3.49%)	
$\partial h_{abs,out}/\partial \dot{m}_{Ref,measured} = -130.3$	0.04%
$\partial h_{abs,out}/\partial \dot{m}_{Dilute} = -25.76$	0.10%
$\partial h_{abs,out}/\partial \dot{m}_{Concentrated} = 36.01$	0.27%
$\partial h_{abs,out}/\partial P_{abs,out} = 0.006326$	0.01%
$\partial h_{abs,out}/\partial P_{Con,in} = -0.02235$	0.03%
$\partial h_{abs,out}/\partial P_{Des,out} = -0.2122$	3.02%
$\partial h_{abs,out}/\partial P_{Rec} = -0.1262$	14.99%
$\partial h_{abs,out}/\partial T_{Abs,out} = 4.338$	78.77%
$\partial h_{abs,out}/\partial T_{Rec,out} = 0.1399$	0.08%
$\partial h_{abs,out}/\partial T_{Reflux} = 0.5465$	1.25%
$\partial h_{abs,out}/\partial T_{Sep,V,out} = 0.5874$	1.44%
h_V = 1086 ± 122.8 kJ/kg (±11.29%)	
$\partial h_V/\partial P_{Abs,V,in} = -16.19$	97.83%
$\partial h_V/\partial P_{Con,in} = 1.773$	0.08%
$\partial h_V/\partial T_{Abs,V,in} = 33.65$	1.88%
$\partial h_V/\partial T_{Rec,out} = -11.1$	0.20%
Q_{abs} = 7.854 ± 0.3552 kJ/kg (±4.5%)	
$\partial Q_{abs}/\partial \dot{m}_{Ref,measured} = 10.84$	0.01%
$\partial Q_{abs}/\partial \dot{m}_{Dilute} = 1.759$	0.02%

Table B-4 Continued...

Partial Derivative	% Uncertainty (of Total)
$\partial Q_{abs}/\partial \dot{m}_{\text{Concentrated}} = -0.4279$	0.00%
$\partial Q_{abs}/\partial P_{Abs,in} = 0.000114$	0.00%
$\partial Q_{abs}/\partial P_{Abs,out} = -0.000167$	0.00%
$\partial Q_{abs}/\partial P_{Abs,V,in} = -0.04575$	93.30%
$\partial Q_{abs}/\partial P_{Con,in} = 0.00514$	0.08%
$\partial Q_{abs}/\partial P_{Des,out} = -0.001385$	0.01%
$\partial Q_{abs}/\partial P_{\text{Rec}} = 0.0008236$	0.03%
$\partial Q_{abs}/\partial T_{Abs,in} = 0.09851$	1.92%
$\partial Q_{abs}/\partial T_{Abs,out} = -0.115$	2.62%
$\partial Q_{abs}/\partial T_{Abs,V,in} = 0.0951$	1.79%
$\partial Q_{abs}/\partial T_{\text{Rec},out} = -0.03217$	0.21%
$\partial Q_{abs}/\partial T_{\text{Reflux}} = 0.003568$	0.00%
$\partial Q_{abs}/\partial T_{\text{Sep,out}} = 0.003835$	0.00%
$\alpha_{\text{Film,abs}} = 1632 \pm 130.9 \text{ kJ/kg } (\pm 8.0\%)$	
$\partial \alpha_{\text{Film,abs}}/\partial \dot{m}_{Abs,C} = 159$	0.09%
$\partial \alpha_{\text{Film,abs}}/\partial \dot{m}_{\text{Ref,measured}} = 1496$	0.00%
$\partial \alpha_{\text{Film,abs}}/\partial \dot{m}_{\text{Dilute}} = -58.74$	0.00%
$\partial \alpha_{\text{Film,abs}}/\partial \dot{m}_{\text{Concentrated}} = 242.6$	0.00%
$\partial \alpha_{\text{Film,abs}}/\partial P_{Abs,in} = 0.01574$	0.00%
$\partial \alpha_{\text{Film,abs}}/\partial P_{Abs,out} = -0.02312$	0.00%

Table B-4 Continued...

Partial Derivative	% Uncertainty (of Total)
$\partial\alpha_{\text{Film,abs}}\big/\partial P_{Abs,V,in} = -6.31$	13.06%
$\partial\alpha_{\text{Film,abs}}\big/\partial P_{Con,in} = 0.709$	0.01%
$\partial\alpha_{\text{Film,abs}}\big/\partial P_{Des,out} = -0.1911$	0.00%
$\partial\alpha_{\text{Film,abs}}\big/\partial P_{\text{Re}c} = -0.1136$	0.00%
$\partial\alpha_{\text{Film,abs}}\big/\partial T_{Abs,C,in} = -127.3$	23.62%
$\partial\alpha_{\text{Film,abs}}\big/\partial T_{Abs,C,out} = 196.7$	56.39%
$\partial\alpha_{\text{Film,abs}}\big/\partial T_{Abs,in} = 13.59$	0.27%
$\partial\alpha_{\text{Film,abs}}\big/\partial T_{Abs,out} = -65.57$	6.27%
$\partial\alpha_{\text{Film,abs}}\big/\partial T_{Abs,V,in} = 13.12$	0.25%
$\partial\alpha_{\text{Film,abs}}\big/\partial T_{\text{Re}c,out} = -4.438$	0.03%
$\partial\alpha_{\text{Film,abs}}\big/\partial T_{\text{Reflux}} = 0.4921$	0.00%
$\partial\alpha_{\text{Film,abs}}\big/\partial T_{\text{Sep,V,out}} = 0.5289$	0.00%
$\partial\alpha_{\text{Film,abs}}\big/\partial Tube_{\text{ID}} = -65719$	0.00%
$\partial\alpha_{\text{Film,abs}}\big/\partial Tube_{\text{OD}} = -80387$	0.00%
$\partial\alpha_{\text{Film,abs}}\big/\partial Tube_{\text{LengthID}} = -7465$	0.00%
$\beta v = 0.0304 \pm 0.0018 \ (\pm 6\%)$	
$\partial\beta_V\big/\partial\dot{m}_{\text{Ref,measured}} = 0.08141$	0.03%
$\partial\beta_V\big/\partial P_{Abs,in} = 0.000388$	17.47%
$\partial\beta_V\big/\partial P_{Abs,out} = 0.000388$	39.32%
$\partial\beta_V\big/\partial T_{Abs,in} = -0.00165$	19.73%

Table B-4 Continued...

Partial Derivative	% Uncertainty (of Total)
$\partial \beta_V / \partial T_{Abs,out} = -0.00165$	19.73%
$\partial \beta_V / \partial T_{min} = 0.000716$	3.72%

B.3 Range of Uncertainties

Table B.5 summarizes the observed uncertainties in several parameters obtained in the present study. As shown in this table, only two data points show uncertainties > 20% in the film heat transfer coefficient. There are 5 data points showing uncertainties > 25% for the reflux; this is to be expected because of the relatively low flow rates of the reflux, and also the large sensitivity of the vapor phase properties to the vapor concentration in the vicinity of the rectifier. The highest uncertainties in the reflux calculation are for the data at 345 kPa (50 psi) and 40% desorber outlet concentration – this is because at such high solution concentrations, the reflux flow rate is very small. In this table, it is also seen that uncertainties in determining the various enthalpies at the absorber are sometimes as high as 50%, however there are only 5 data points where uncertainties of this magnitude were observed. In the case of vapor enthalpy, the largest uncertainties (greater than 15%) were observed for the test cases at an absorber pressure of 345 kPa and dilute solution concentration of 5%, where the vapor enthalpies were found to be the lowest (less than 500 kJ/kg).

Table B.5 Observed Uncertainties in the Present Experimental Data

Parameter	Range	Uncertainty Range (Absolute)	Uncertainty Range (%)	Average Uncertainty (%)
$X_{des,out}$	0.091 – 0.408	0.0028 – 0.0046	0.85 – 3.48	1.86
$X_{Abs,in}$	0.152 – 0.418	0.0025 – 0.0185	0.92 – 9.52	2.88
$X_{Abs,out}$	0.207 – 0.442	0.0022 – 0.0159	0.76 – 6.13	1.97
X_V	0.807 – 0.999	0.0001 – 0.0047	0.01 – 0.57	0.20
$h_{Abs,in}$	-70.2 – 343.3	2.41 -49.59	0.8 – 28	6.31
$h_{Abs,out}$	-166.1 – 152.7	2.27 – 8.605	1.42 – 27.54	5.37
h_V	336 – 1327	5.75 – 184	0.45 – 54	8.96
Q_{Abs} (kW)	3.26 – 10.75	0.06 – 1.54	1.31 – 20.51	6.18
$Q_{Abs,C}$ (kW)	2.96 – 9.79	0.17 – 1.63	3.32 – 30.27	13.31
$Q_{Abs,ave}$ (kW)	3.11 – 10.20	0.10 – 0.99	1.84 – 15.89	7.84
α_C (W/m^2-K)	2634 – 11408	14.99 – 114.3	0.42 – 1.46	0.63
U_{Abs} (W/m^2-K)	753.2 - 1853	24.11 - 170.1	2.43-15.63	7.95
$\alpha_{Film,Abs}$ (W/m^2-K)	922.8 - 2857	67.86 – 430.50	4.171-20.04	11.21
β_V (m/s)	0.002588-0.2541	0.0001 - 0.0171	4.63 – 14.2	7.91
β_l (m/s)	$5.51 \times 10^{-6} - 3.31 \times 10^{-5}$	$7.34 \times 10^{-7} - 4.97 \times 10^{-8}$	0.468–2.92	1.06
Reflux (kg/s)	$1.9 \times 10^{-5} -$ 0.00811	1.8×10^{-6} - 0.0012	4.35 – 107.94	16.99

In the present study, the solution and vapor properties were estimated using correlations from the literature that are functions of temperature, pressure and concentration. Therefore, uncertainties are also calculated in these properties. Table B.6 shows the range of uncertainties in solution and vapor properties as well as solution Re and Pr for the range of experiments conducted. These are the uncertainties estimated from an error propagation approach on the measurement uncertainties. In addition, for the vapor-phase transport properties, the deviations between the values estimated in this study and those reported in the literature for pure components were also calculated, and are reported below as additional vapor-phase uncertainties. Table B.6 also shows these additional uncertainties.

Table B.6 Uncertainties in the Solution and Vapor Properties in the Present Study

Parameter		Range	Uncertainty Range(Absolute)	Uncertainty Range (%)	Average Uncertainty (%)
$C_{p,l}$ (kJ/kg-K)		4.22 – 4.42	8.69×10^{-5}– 0.08167	0.02 – 1.89	0.25
k_l (W/m-K)		0.55 – 0.62	$5.0 \times 10^{-4} - 3.78 \times 10^{-3}$	0.09 – 0.63	0.24
μ_l (kg/m-s)		$3.21 \times 10^{-4} - 1.04 \times 10^{-3}$	$2.28 \times 10^{-6} - 2.12 \times 10^{-5}$	0.35 – 2.15	0.81
ρ_l (kg/m³)		841 – 908	0.94 – 5.69	0.11 – 0.65	0.25
$D_{aw,l}$ (m²/s)		$3.29 \times 10^{-9} - 8.23 \times 10^{-9}$	$2.83 \times 10^{-11} - 9.05 \times 10^{-11}$	0.62 – 2.04	0.98
Re_l		29 – 170	0.21 – 1.27	0.36 – 2.20	0.81
Pr_l		2.23 – 8.23	0.016– 0.14	0.34– 1.8	0.86
$C_{p,v}$ (kJ/kg-K)	Measurement	2.06 – 2.39	0.001 – 1.15	0.06 – 54	7.8
	Deviation from Literature	2.20 – 2.66	0.244 – 0.703	11.1 – 26.5	15.5
k_v (W/m-K)	Measurement	0.026 – 0.029	$4.87 \times 10^{-5} - 4.9 \times 10^{-5}$	0.16 – 0.19	0.18
	Deviation from Literature	0.0237 – 0.0325	0.00324 – 0.00446	9.97 – 17.7	14.6
μ_v (kg/m-s)	Measurement	$9.27 \times 10^{-6} - 1.07 \times 10^{-5}$	$1.75 \times 10^{-8} - 1.79 \times 10^{-8}$	0.16 – 0.19	0.17
	Deviation from Literature	$9.41 \times 10^{-6} - 1.25 \times 10^{-5}$	$2.5 \times 10^{-7} - 5.79 \times 10^{-7}$	1.99 – 6.15	3.77
ρ_V (kg/m³)		1.277 – 8.805	0.39 – 4.84	11.59 – 54.9	25.6
$D_{aw,v}$ (m²/s)		$4.9 \times 10^{-6} - 1.53 \times 10^{-5}$	$4.79 \times 10^{-7} - 4.5 \times 10^{-6}$	9.78 – 29.85	16.95

B.3.1 Validity of the Kinetic Theory for Vapor Property Evaluation

In the absence of any literature on ammonia-water vapor-phase mixture properties, transport properties of the ammonia-water vapor mixture were obtained using the Chapman-Enskog kinetic theory (Mills 1995) for pure substances and mixture rules of Wilke (1950). It should be noted that ideal gas properties of pure ammonia and pure water vapor predicted using the kinetic theory were used instead of values available in the literature for the pure components to ensure consistency with the mixture rules. To estimate potential errors introduced by the use of this approach, in this section, the specific heat, thermal conductivity, and viscosity of ammonia obtained from the Lennard-Jones potential model are compared with real gas properties available in the internal library in EES (Klein 2006), which uses correlations developed by Tillner-Roth *et al.* (1993) for the ammonia vapor specific heat, Tufeu *et al.* (1984) for the ammonia vapor conductivity, and Fenghour *et al.* (1995) for the ammonia vapor viscosity.

Figures B.1 – B.3 show comparisons of the ammonia vapor properties of specific heat, thermal conductivity, and viscosity for temperatures between 10°C and 90°C and the three pressures of interest in this study, i.e., 150, 345 and 500 kPa. The properties obtained from the kinetic theory are independent of pressure. This is because the kinetic theory is developed for an ideal gas; therefore, vapor properties are only dependent on temperature.

Figure B.1 shows a comparison of ammonia vapor specific heats obtained from the kinetic theory and those obtained from Tillner-Roth *et al.* (1993). The specific heat of ammonia obtained from the kinetic theory is lower than that obtained from Tillner-Roth *et al.* (1993). The specific heat decreases as pressure decreases, with a decreasing

influence of pressure at the higher temperatures. The deviations ranged between 11.1%

and 26.5% with an average deviation of 15.5%.
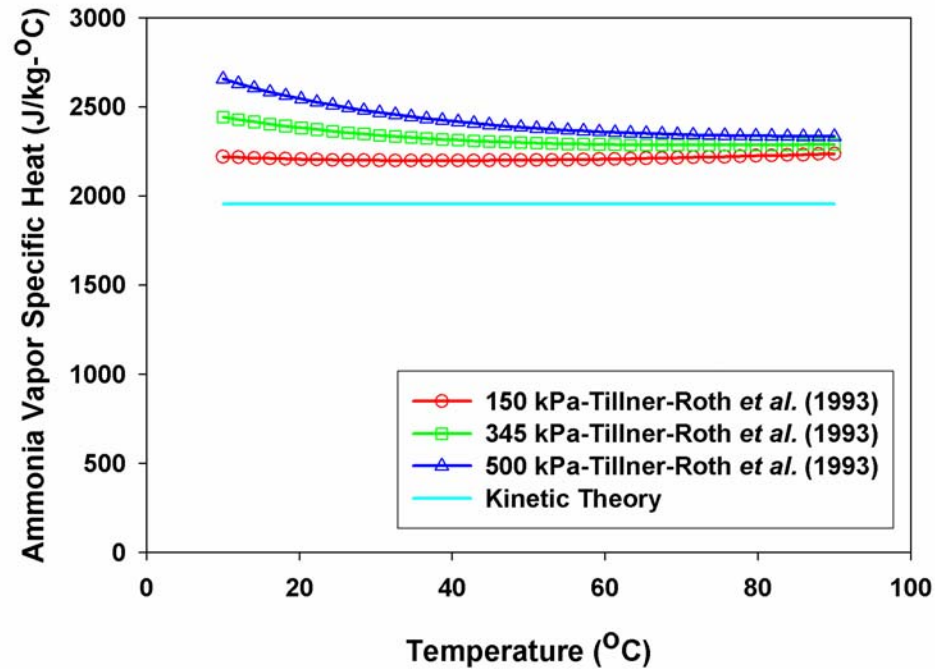
Figure B.1 Ammonia Vapor Specific Heat

Figure B.2 shows a comparison of ammonia vapor thermal conductivities

obtained from the kinetic theory and those obtained from Tufeu *et al.* (1984). The

thermal conductivity of ammonia obtained from the kinetic theory is higher than that

obtained from Tufeu *et al.* (1984). The conductivity increases as vapor temperature

increases, while there is no significant effect of pressure. The deviations ranged between

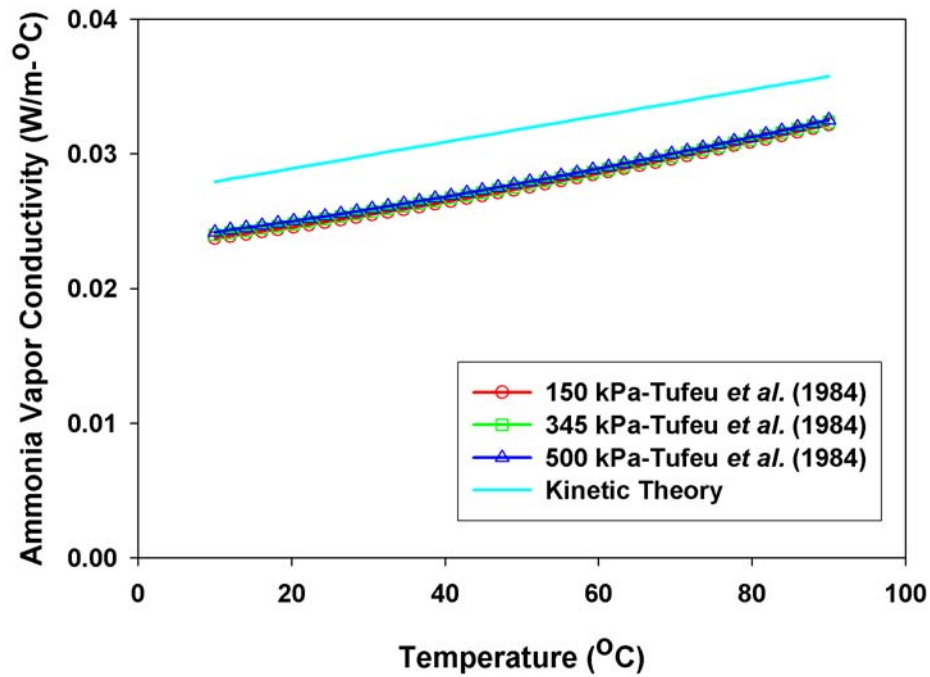10% and 17.7% with an average deviation of 14.6%.

Figure B.2 Ammonia Vapor Thermal Conductivity

Figure B.3 shows a comparison of ammonia vapor viscosities obtained from the kinetic theory and those from Fenghour *et al.* (1995). The viscosity of ammonia obtained from the kinetic theory is higher than that obtained from Fenghour *et al.* (1995). The viscosity increases as the vapor temperature increases, while there is no significant effect of pressure. The deviations ranged between 2% and 6.2% with an average of 3.8%.

Table B.6 shows these deviations from the values in the literature as additional uncertainties in these vapor-phase properties, over and above those corresponding to measurement uncertainties.

Table B.7 shows the range of uncertainties in non-dimensional vapor parameters. Uncertainties in non-dimensional vapor-phase parameters such as Gr_v, Ra_v, Re_v, Pr_v, and Sc_v are calculated based on the maximum property deviations between the literature and

the kinetic theory. It should be noted that these additional uncertainties will also adversely affect the predictive capabilities of the vapor-phase mass transfer correlation developed in this study.
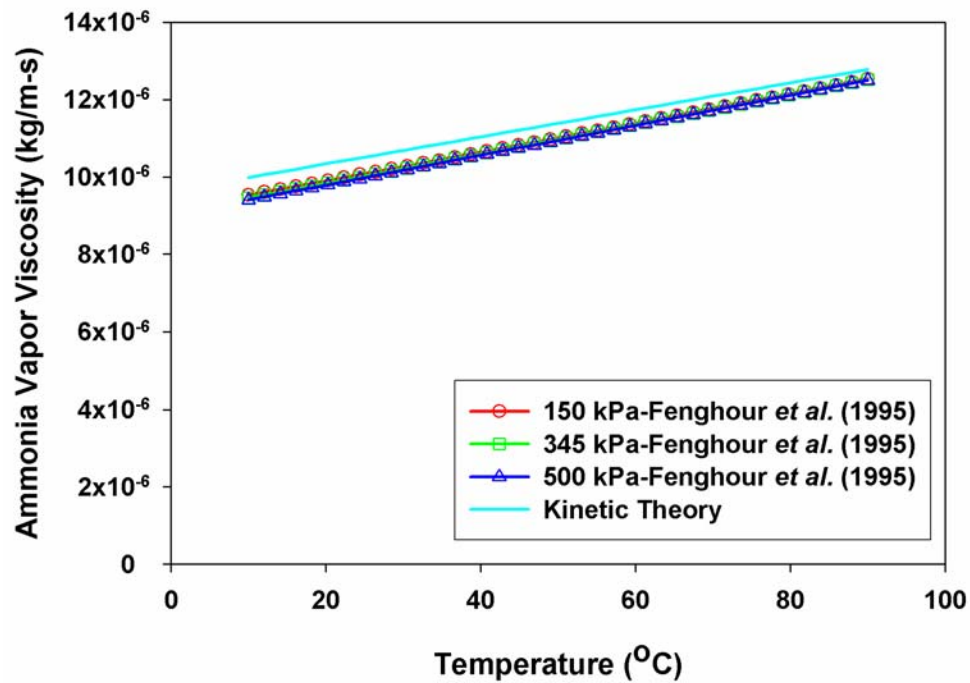

Figure B.3 Ammonia Vapor Viscosity

The uncertainties of Ra_v and Pr_v range from 16.1 to 19.9% with average uncertainties of 18.2% due to the component uncertainties in the thermal conductivity and specific heat. The uncertainties in Re_v and Sc_v range from 5.3 to 6.6% with average uncertainties of 6% due to the above mentioned deviations in the vapor viscosity. The

uncertainties in Gr_v range from 10.6 to 13.4% with average uncertainties of 12.2% due to the deviations in the vapor viscosity.

Table B.7 Uncertainties in Vapor Non-Dimensional Parameters

Parameter	Range	Uncertainty Range(Absolute)	Uncertainty Range (%)	Average Uncertainty (%)
Gr_v	4222 – 59879	52.87 – 722.6	10.6 – 13.4	12.2
Ra_v	3471 – 48824	657.4 - 9144	16.1 – 19.9	18.2
Re_v	30.37 – 134.1	1.94 – 7.819	5.3 – 6.6	6.0
Pr_v	0.671 – 0.898	0.1309 – 0.1687	16.1 – 19.9	18.2
Sc_v	0.504 – 0.527	0.02788 – 0.03356	5.3 – 6.6	6.0

APPENDIX C SOLUTION TEMPERATURE PROFILE

This appendix discusses the procedure to obtain the solution temperature profile in the absorber from the measured temperatures.

C.1 Temperature Measurement

Figure C.1 shows the arrangement of the absorber segments and temperature measurement locations. In this figure, the solution temperatures are measured at locations denoted by x = 0, 1, 2, 3, 4, 5, 6, 7 and 8. Location 0 refers to the solution inlet, location 1 is the drip tray, locations 2 – 7 refer to the solution temperature measurement locations on the tubes, and, finally, location 8 refers to the solution pool. The coolant temperature measurement locations are also shown in this figure.

C.2 Temperature Profile

The solution temperature is known at 9 locations identified by x = 0 to 8. A profile for temperature can be developed as a function of x. In the present study, a 3rd order polynomial was fitted to the measured temperatures. The functional form is as follows:

$$T = a_o + a_1 \cdot x + a_2 \cdot x^2 + a_3 \cdot x^3 \tag{C.1}$$

The coefficients a_0, a_1, a_2 and a_3 are determined from regression analysis. If a solution temperature is observed to be very close (within 5°C) to the coolant temperatures; that temperature is not used to generate the temperature profile because that will make the regression analysis skewed towards lower temperatures.
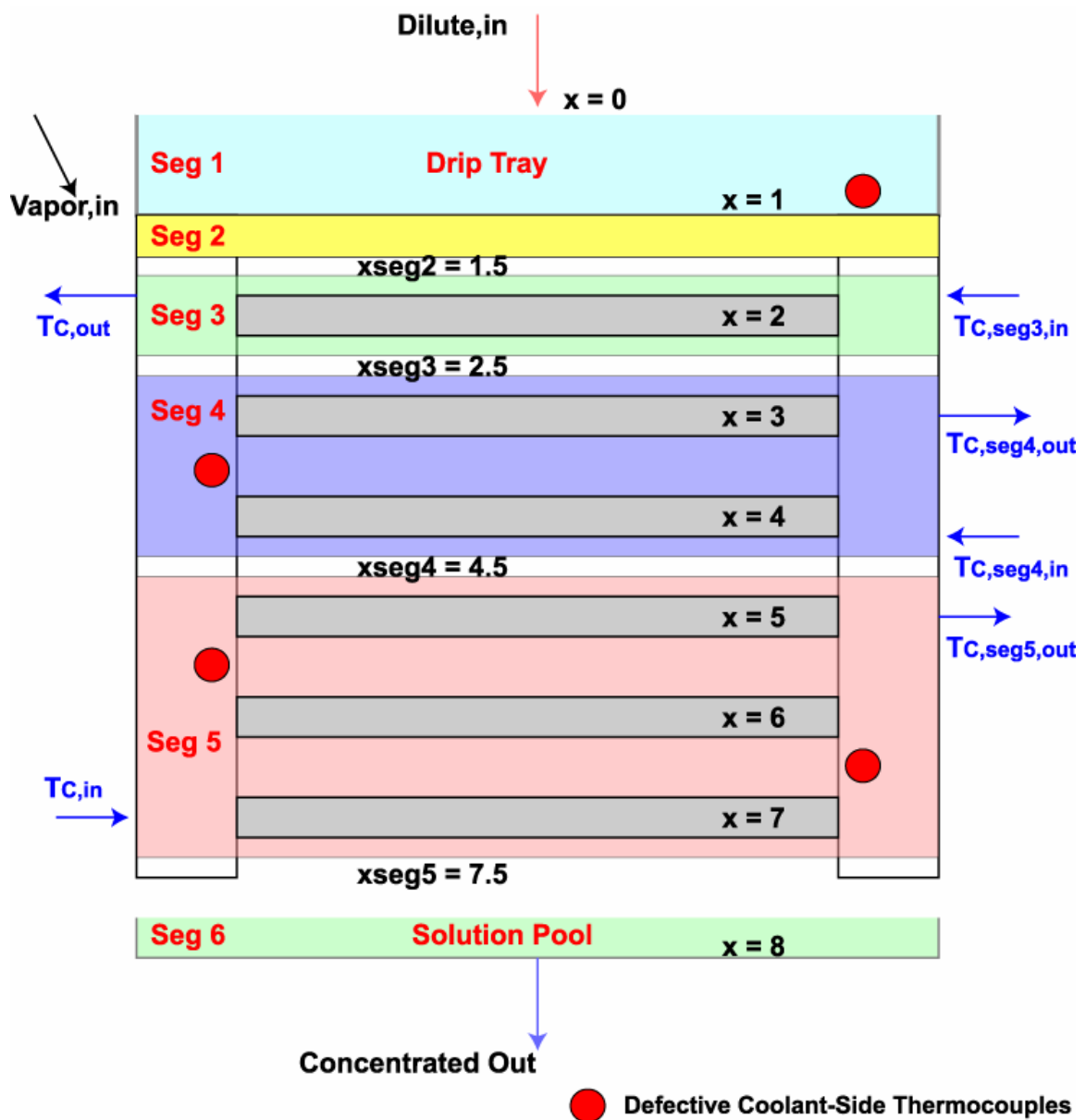
Figure C.1 Segmental Temperature Measurement

The drip tray temperature was found to be significantly lower (usually, close to the coolant outlet temperature) for all the data points; therefore, this temperature was not used in the generation of temperature profile. It was found that for a majority of the test conditions, the other temperatures, not used for the generation of the temperature profile, came from one of the 4th, 5th or the 6th tube solution temperatures (lower tubes of the tube array). It should be noted that progressively reduced wetting was observed in the experiments; therefore, the probability of a thermocouple not contacting the solution is higher at the lower tubes. A total of 51 solution temperatures out of 288 (excluding the drip tray temperature) were not used in obtaining a solution profile for various test conditions. With the temperature profile known, the solution temperature can be obtained anywhere in the absorber along the solution flow path.

C.3 Obtaining Solution Temperature

As can be seen in Figure C.1, segment 1, between $x = 0$ and $x = 1$, consists of the drip tray. Segment 2 is, however, defined by $x = 1$ and $x_{seg} = 1.5$. For the segments involving coolant, the inlet and outlet for a segment are taken between two tubes, e.g., segment 3 starts at $x_{seg} = 1.5$ and ends at $x_{seg} = 2.5$. Similarly, segment 4 is defined between $x_{seg} = 2.5$ and $x_{seg} = 4.5$, and segment 5 is defined by $x_{seg} = 4.5$ and $x_{seg} = 7.5$. It should be noted that the non-uniform allocation of number of tubes to segments (1 tube in segment 3, 2 in segment 4, and 3 in segment 5) is to account for the fact that some of the coolant thermocouples in the header malfunctioned (marked by a circle in Figure C.1). Thus, the tube array was subdivided into 3 segments, i.e., the largest possible number of segments that still allowed computation of coolant-side duty. The solution pool segment is defined between $x_{seg} = 7.5$ and $x = 8$. To obtain the solution temperature at the outlet

of any segment, the appropriate x_{seg} or x value is substituted in the temperature profile. The outlet temperature of a particular segment is the same as the inlet temperature to the next segment. For example, to obtain the solution temperature at the outlet of segment 3 (or inlet of segment 4),

$$T_{seg3,out} = T_{seg4,in} = a_o + a_1 \cdot x_{seg3} + a_2 \cdot \left(x_{seg3}\right)^2 + a_3 \cdot \left(x_{seg3}\right)^3 \qquad \text{(C.2)}$$

Figure C.2 shows the temperature profile (measured and calculated) for a representative test condition at a dilute solution concentration of 25%, absorber pressure of 345 kPa, and solution flow rate of 0.019 kg/s. In this figure, the tube wall temperatures are also shown calculated using a thermal resistance network between the coolant bulk and the tube outer wall. It can be seen that a 3rd degree polynomial approximates the solution temperatures reasonably well within the absorber.
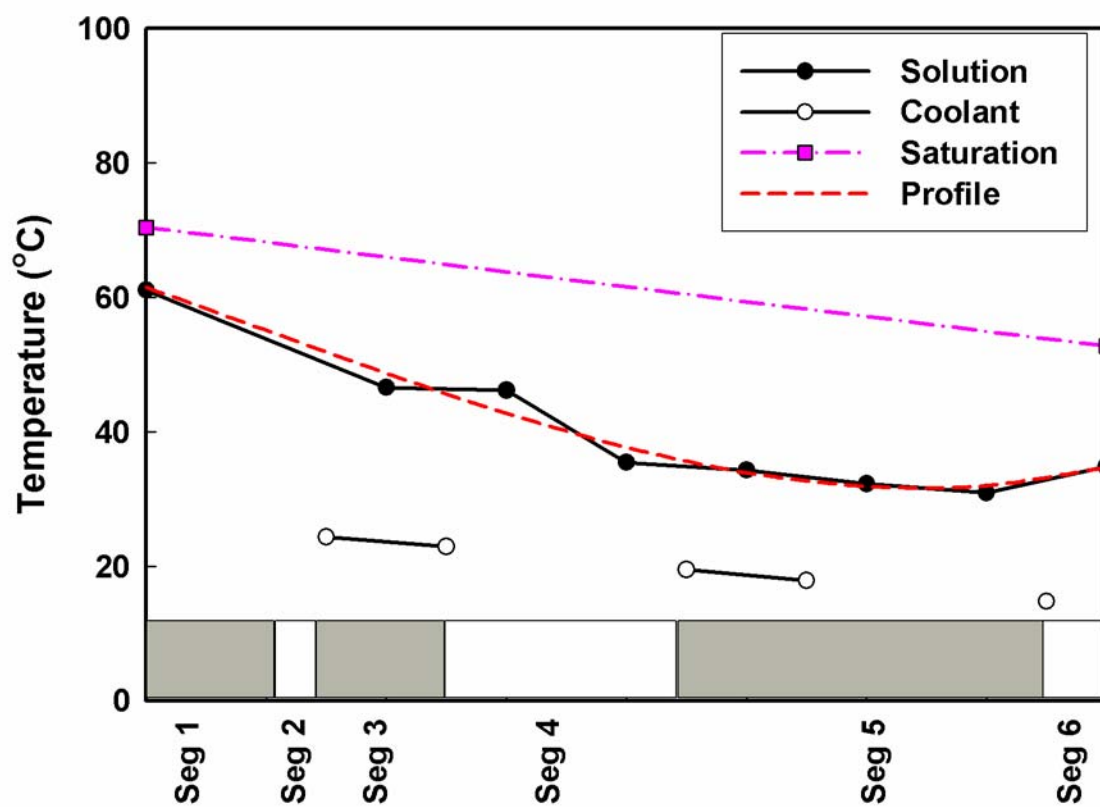
Figure C.2 Representative Temperature Profile (345 kPa, 25%, 0.019 kg/s)

APPENDIX D COOLANT HEADER DETAILS AND CONDUCTION HEAT TRANSFER CALCULATIONS

Heat transfer between the solution, vapor, and the coolant is affected by conduction between the drip tray and the tube array through the contact with the coolant headers. Also, the headers for each pass of the coolant are fabricated from steel plates, which provide another direct path for conduction heat transfer between the coolant passes. These alternative/additional heat transfer paths were accounted for in this study and the respective segmental heat duties appropriately adjusted to yield accurate transfer rates between the working fluid and the coolant. This appendix discusses geometrical details of the coolant headers and these conduction heat loss calculations.

Figure D.1 shows a schematic of the coolant headers and the drip tray. Both the left and right headers have 3 compartments each, i.e., segments 3, 4 and 5. Some of these dimensions ($h_{seg,3}$, $h_{seg,4}$ and $h_{seg,5}$) are different for the left and right headers, while the length (HL = 0.12 m) and width (HW = 25.4 mm) are the same for the two headers. The header wall thicknesses ($t_{seg,side2} = t_{seg,main} = 1.52$ mm) are also the same. A summary of all the dimensions is shown in Table D.1. The coolant nodes (shown as gray circles) are located at the center of the coolant passage. The wall nodes (shown as black circles) are located in the header walls. It should be noted that the coolant compartment is closed from all sides. Therefore, for each compartment, there are four side walls, a top (roof) and a bottom surface (floor) (Figure D.2).
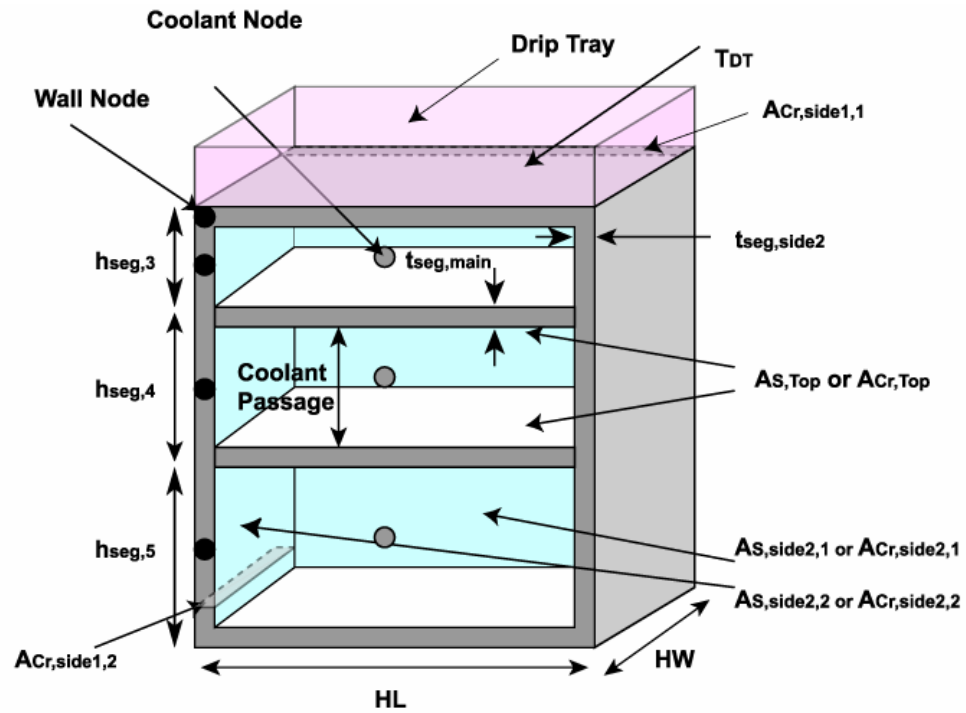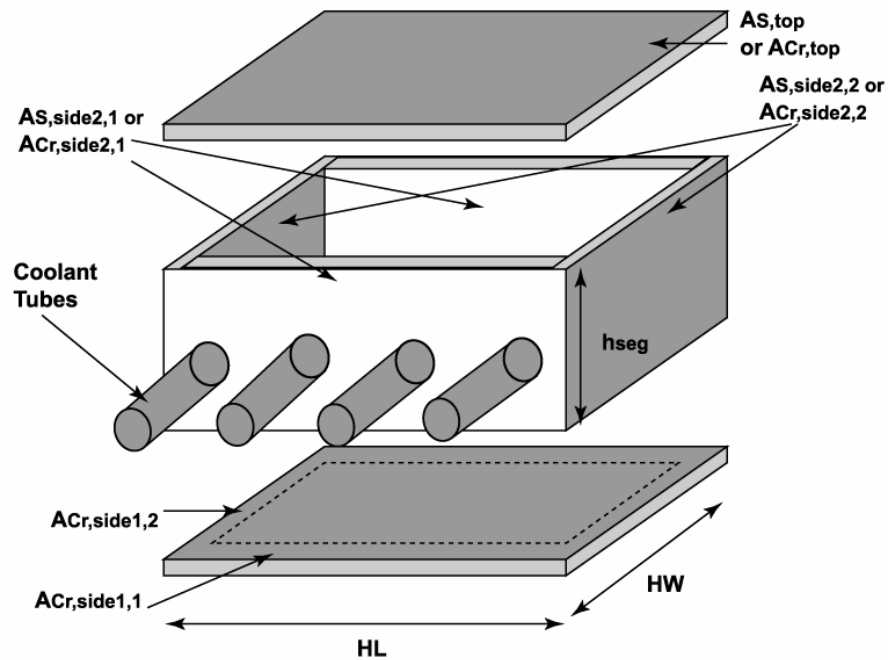
Figure D.1 Schematic of the Coolant Header

Figure D.2 A Header Compartment (Segment)

Table D.1 Summary of Header Segment (Compartment) Dimensions

	Left Header	Right Header
Header Length (HL) (m)	0.12	0.12
Header Width (HW) (mm)	25.4	25.4
Wall Thickness (t_{seg}) (mm)	1.52	1.52
$h_{seg,3}$ (mm)	24.1	44.2
$h_{seg,4}$ (mm)	38.6	38.6
$h_{seg,5}$ (mm)	63.0	44.2

The thermal conditions of the side walls are assumed to be identical; therefore, for calculation purposes, the only parameter of the interest is the total surface area of each coolant compartment. The surface heat transfer areas for convection can easily be visualized from Figure D.2 (i.e. $2 \times (HL + HW) \times h_{seg3}$ for the side walls and $HL \times HW$ for the top/bottom surfaces). However, there are two paths for conduction heat transfer in the side walls. One is along the height of the compartment and the other is across the side wall. These two paths are denoted as *side1* and *side2*, as shown in Figure D.3.

The following sections list the equations to obtain the cross-sectional and surface areas, and the thermal resistances of these segments that are in contact with the coolant. The values for the left and right headers are obtained by substituting the appropriate dimensions from Table D.1.
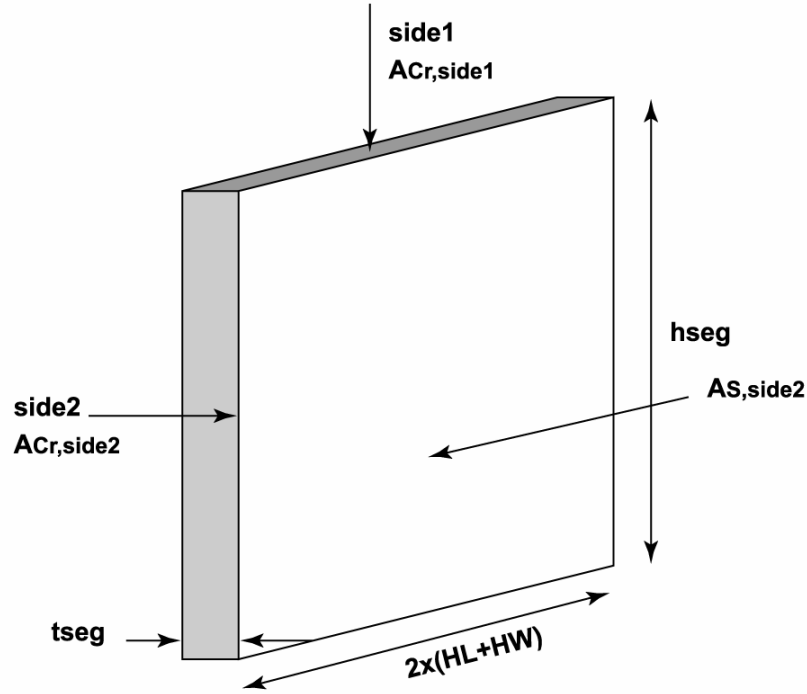
Figure D.3 Effective Side Wall

D.1 Segment 3

In segment 3, the possible heat transfer paths are conduction in the side walls and top wall, and convection at the top wall. Therefore, the cross-section areas for conduction in the side wall are (Figure D.3),

$$A_{Cr,side1,seg3} = \left(A_{Cr,side1,1} + A_{Cr,side1,2} \right)_{seg3} = 2 \times (HL + HW) \times t_{seg} \tag{D.1}$$

$$A_{Cr,side1,seg3} = 2 \times (0.12 + 0.0254) \times 0.00152 = 4.428 \times 10^{-4} \, m^2 \tag{D.2}$$

$$A_{Cr,side2,seg3} = \left(A_{Cr,side2,1} + A_{Cr,side2,2} \right)_{seg3} = 2 \times (HL + HW) \times h_{seg3} \tag{D.3}$$

$$A_{Cr,side2,seg3} == 2 \times (0.12 + 0.0254) \times 0.0241 = 7.012 \times 10^{-3} \, m^2 \tag{D.4}$$

The convection area of the side wall is the same as $A_{Cr,side2}$. Therefore,

$$A_{S,side2,seg3} = A_{Cr,side2,seg3} \tag{D.5}$$

$$A_{S,side2,seg3} = 7.012 \times 10^{-3} m^2 \tag{D.6}$$

Finally, both the convection and conduction areas of the top wall (and of the separating wall between the two segments) are (Figure D.2),

$$A_{S,top,seg3} = A_{Cr,top,seg3} = HL \times HW \tag{D.7}$$

$$A_{S,top,seg3} = 0.12 \times 0.254 = 3.045 \times 10^{-3} m^2 \tag{D.8}$$

The various thermal resistances for segment 3 can be obtained as follows:

$$R_{main,seg3} = \frac{t_{seg}}{k_{main,seg3} \times A_{Cr,top,seg3}} + \frac{1}{\alpha_C \times A_{S,top,seg3}} \tag{D.9}$$

$$R_{main,seg3} = \frac{0.00152}{15.06 \times 3.045 \times 10^{-3}} + \frac{1}{7653 \times 3.045 \times 10^{-3}} = 0.076 K/W \tag{D.10}$$

$$R_{side1,seg3} = \frac{\left(h_{l,seg3}\right)/2}{k_{side1,seg3} \times A_{Cr,side1,seg3}} \tag{D.11}$$

$$R_{side1,seg3} = \frac{(0.0241)/2}{15.06 \times 4.428 \times 10^{-4}} = 1.81 K/W \tag{D.12}$$

$$R_{side2,seg3} = \frac{\left(t_{seg}\right)/2}{k_{side2,seg3} \times A_{Cr,side2,seg3}} + \frac{1}{\alpha_C \times A_{S,side2,seg3}} \tag{D.13}$$

$$R_{side2,seg3} = \frac{(0.00152)/2}{15.06 \times 7.012 \times 10^{-03}} + \frac{1}{7653 \times 7.012 \times 10^{-03}} = 0.026 K/W \tag{D.14}$$

D.2 Segment 4

The possible heat transfer paths in segment 4 are the same as those for segment 3, except that both sides of the separating wall participate in convection. The cross-section

area for conduction along the side wall height is the same for all the segments; however, the area across the wall thickness varies depending upon the segment height. Therefore,

$$A_{Cr,side1,seg4} = \left(A_{Cr,side1,1} + A_{Cr,side1,2} \right)_{seg4} = A_{Cr,side1,seg3} \tag{D.15}$$

$$A_{Cr,side1,seg4} = 4.428 \times 10^{-4} m^2 \tag{D.16}$$

$$A_{Cr,side2,seg4} = \left(A_{Cr,side2,1} + A_{Cr,side2,2} \right)_{seg4} = 2 \times (HL + HW) \times h_{seg4} \tag{D.17}$$

$$A_{Cr,side2,seg4} = 2 \times (0.12 + 0.0254) \times 0.0386 = 0.0112 m^2 \tag{D.18}$$

The convection area of the side wall is the same as $A_{Cr,side2}$. Therefore,

$$A_{S,side2,seg4} = A_{Cr,side2,seg4} \tag{D.19}$$

$$A_{S,side2,seg4} = 0.0112 m^2 \tag{D.20}$$

Finally, the convection area of one side of the separating wall is,

$$A_{S,top,seg4} = HL \times HW \tag{D.21}$$

$$A_{S,top,seg4} = 0.12 \times 0.0254 = 3.045 \times 10^{-3} m^2 \tag{D.22}$$

The cross-sectional area of the separating wall for conduction is,

$$A_{Cr,top,seg4} = HL \times HW \tag{D.23}$$

$$A_{Cr,top,seg4} = 0.12 \times 0.0254 = 3.045 \times 10^{-3} m^2 \tag{D.24}$$

The various thermal resistances of segment 4 can be calculated as:

$$R_{main,seg4} = \frac{t_{seg}}{k_{main,seg4} \times A_{Cr,top,seg4}} + \frac{2}{\alpha_C \times A_{S,top,seg4}} \tag{D.25}$$

$$R_{main,seg4} = \frac{0.00152}{15.04 \times 3.045 \times 10^{-3}} + \frac{2}{7653 \times 3.045 \times 10^{-3}} = 0.12 K/W \tag{D.26}$$

Here, a factor of 2 is used in the convection term (second term on the right side of the above equation), since both sides of the separating wall participate in convection heat transfer.

$$R_{side1,seg4} = \frac{\left(h_{seg3} + h_{seg4}\right)/2}{k_{side1,seg4} \times A_{Cr,side1,seg4}} \tag{D.27}$$

$$R_{side1,seg4} = \frac{\left(0.0241 + 0.0386\right)/2}{15.04 \times 4.428 \times 10^{-4}} = 4.82K/W \tag{D.28}$$

$$R_{side2,seg4} = \frac{\left(t_{seg}\right)/2}{k_{side2,seg4} \times A_{Cr,side2,seg4}} + \frac{1}{\alpha_C \times A_{S,side2,seg4}} \tag{D.29}$$

$$R_{side2,seg4} = \frac{\left(0.00152\right)/2}{15.04 \times 0.0112} + \frac{1}{7653 \times 0.0112} = 0.016K/W \tag{D.30}$$

D.3 Segment 5

The various cross-sectional and surface areas for segment 5 are as follows:

$$A_{Cr,side1,seg5} = \left(A_{Cr,side1,1} + A_{Cr,side1,2}\right)_{seg5} = A_{Cr,side1,seg3} \tag{D.31}$$

$$A_{Cr,side1,seg5} = 4.428 \times 10^{-4} m^2 \tag{D.32}$$

$$A_{Cr,side2,seg5} = \left(A_{Cr,side2,1} + A_{Cr,side2,2}\right)_{seg5} = 2 \times (HL + HW) \times h_{seg5} \tag{D.33}$$

$$A_{Cr,side2,seg5} = 2 \times (0.12 + 0.0254) \times 0.063 = 0.0183 m^2 \tag{D.34}$$

$$A_{S,side2,seg5} = A_{Cr,side2,seg5} \tag{D.35}$$

$$A_{S,side2,seg5} = 0.0183 m^2 \tag{D.36}$$

$$A_{S,top,seg5} = HL \times HW \tag{D.37}$$

$$A_{S,top,seg5} = 0.12 \times 0.0254 = 3.045 \times 10^{-3} \, m^2 \tag{D.38}$$

$$A_{Cr,top,seg5} = HL \times HW \tag{D.39}$$

$$A_{Cr,top,seg5} = 0.12 \times 0.0254 = 3.045 \times 10^{-3} \, m^2 \tag{D.40}$$

The thermal resistances for segment 5 can be calculated as follows:

$$R_{main,seg5} = \frac{t_{seg}}{k_{main,seg5} \times A_{Cr,top,seg5}} + \frac{2}{\alpha_C \times A_{S,top,seg5}} \tag{D.41}$$

$$R_{main,seg5} = \frac{0.00152}{14.61 \times 3.045 \times 10^{-4}} + \frac{2}{7653 \times 3.045 \times 10^{-4}} = 0.12 K/W \tag{D.42}$$

$$R_{side1,seg5} = \frac{\left(h_{seg4} + h_{seg5}\right)/2}{k_{side1,seg5} \times A_{Cr,side1,seg5}} \tag{D.43}$$

$$R_{side1,seg5} = \frac{\left(0.0386 + 0.063\right)/2}{14.61 \times 4.428 \times 10^{-4}} = 7.85 K/W \tag{D.44}$$

$$R_{side2,seg5} = \frac{\left(t_{seg}\right)/2}{k_{side2,seg5} \times A_{Cr,side2,seg5}} + \frac{1}{\alpha_C \times A_{S,side2,seg5}} \tag{D.45}$$

$$R_{side2,seg5} = \frac{\left(0.00152\right)/2}{14.61 \times 0.0183} + \frac{1}{7653 \times 0.0183} = 0.01 K/W \tag{D.46}$$

D.4 Conduction Heat Transfer Calculations

A thermal resistance network for the coolant header is shown in Figure D.4. The various resistances and surface areas were calculated as discussed in the previous section. Once the thermal resistances are calculated, the heat flow equations in terms of the temperature differences and resistances between nodes can be formulated. Representative equations are shown here for segment 4.
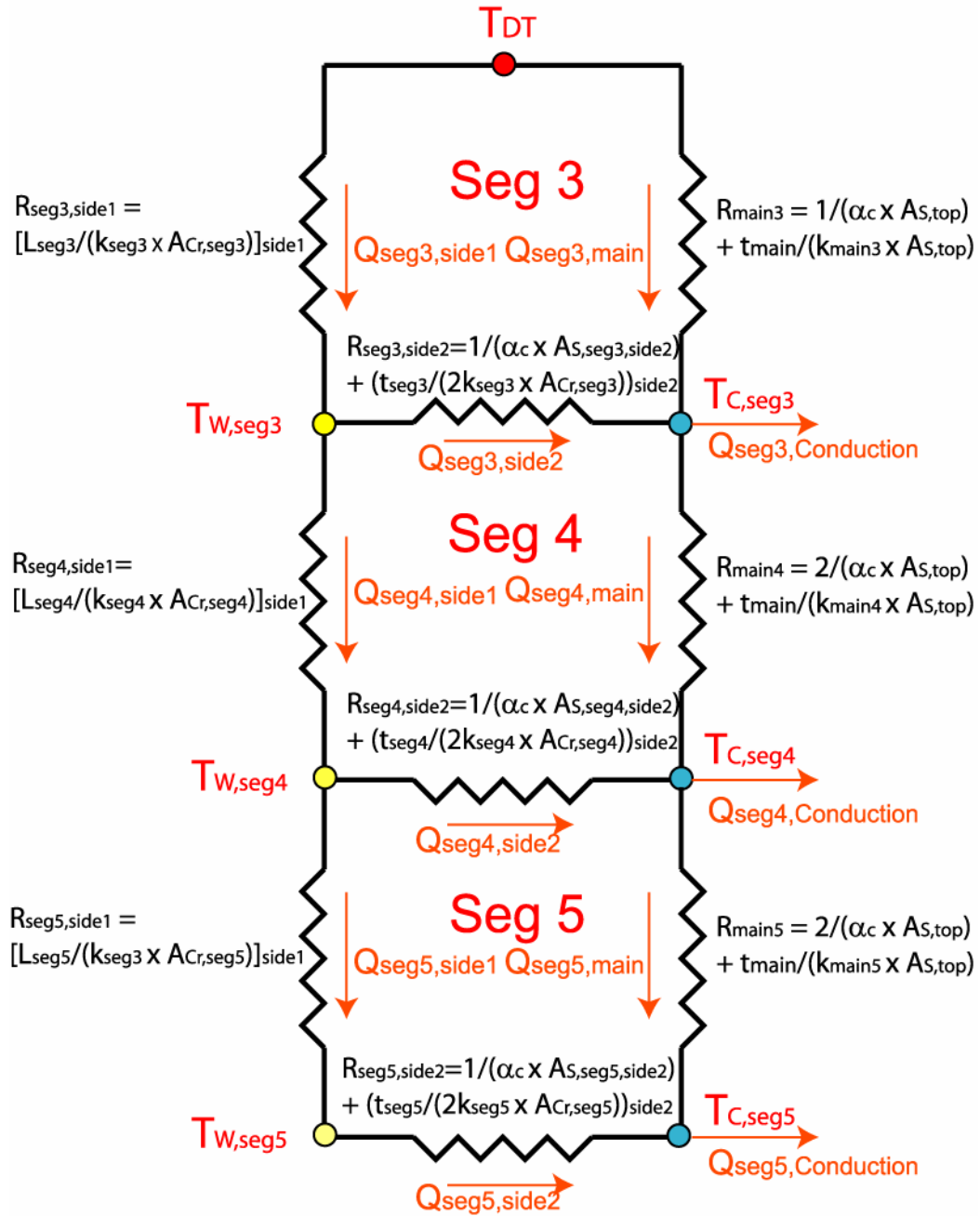
318

Figure D.4 Thermal Resistance Network (One Header Only)

The functional form remains similar for the other segments, except for the temperature differences and the thermal resistances.

$$Q_{side1,seg4} = \frac{T_{W,seg3} - T_{W,seg4}}{R_{side1,seg4}} \tag{D.47}$$

$$Q_{side1,seg4} = \frac{19.22 - 16.14}{4.82} = 0.64\,W \tag{D.48}$$

$$Q_{side2,seg4} = \frac{T_{W,seg4} - T_{C,seg4}}{R_{side2,seg4}} \tag{D.49}$$

$$Q_{side2,seg4} = \frac{16.14 - 16.137}{0.016} = 0.17\,W \tag{D.50}$$

$$Q_{main,seg4} = \frac{T_{C,seg3} - T_{C,seg4}}{R_{main,seg4}} \tag{D.51}$$

$$Q_{main,seg4} = \frac{18.75 - 16.13}{0.12} = 21.81\,W \tag{D.52}$$

Once the heat flow equations for each node are defined, the heat balance equations are formulated for all the nodes. Using these heat balance equations, the temperatures at the header walls can be obtained. The heat balance equations at the *wall nodes* are as follows:

$$Q_{side1,seg3} = Q_{side2,seg3} + Q_{side1,seg4} \tag{D.53}$$

$$Q_{side1,seg4} = Q_{side2,seg4} + Q_{side1,seg5} \tag{D.54}$$

$$Q_{side1,seg5} = Q_{side2,seg5} \tag{D.55}$$

Similarly for the *coolant nodes*, the heat balance equations are:

$$Q_{seg\,3,conduction} = Q_{main,seg\,3} + Q_{side\,2,seg\,3} - Q_{main,seg\,4} \qquad (D.56)$$

$$Q_{seg\,4,conduction} = Q_{main,seg\,4} + Q_{side\,2,seg\,4} - Q_{main,seg\,5} \qquad (D.57)$$

$$Q_{seg\,5,conduction} = Q_{main,seg\,5} + Q_{side\,2,seg\,5} \qquad (D.58)$$

The above heat balance equations are solved iteratively to yield the respective conduction heat duties in the headers and from the drip tray. It was observed for the majority of the test conditions that the coolant heat-transfer coefficient is very large (e.g., 7653 W/m^2-K for the representative case, 25%, 345 kPa and 0.026 kg/s); therefore, the dominating resistance lies in the header walls. For the representative case, the following conduction heat duties were obtained for the left header.

$$Q_{seg\,3,conduction,left} = 453.6 + 18.19 - 21.81 = 450W \qquad (D.59)$$

$$Q_{seg\,4,conduction,left} = 21.81 + 0.17 - 30.52 = -8.54W \qquad (D.60)$$

$$Q_{seg\,5,conduction,left} = 30.52 + 0.47 = 31W \qquad (D.61)$$

Similar calculations were performed for the right header also. The total absorption heat duties in the various segments for the representative case were obtained as follows:

$$Q_{seg\,3,conduction} = Q_{seg\,3,conduction,left} + Q_{seg\,3,conduction,right} \qquad (D.62)$$

$$Q_{seg\,3,conduction} = 450 + 463.2 = 0.91kW \qquad (D.63)$$

$$Q_{seg\,4,conduction} = Q_{seg\,4,conduction,left} + Q_{seg\,4,conduction,right} \qquad (D.64)$$

$$Q_{seg\,4,conduction} = -8.54 - 1.14 = -0.01kW \qquad (D.65)$$

$$Q_{seg\,5,conduction} = Q_{seg\,5,conduction,left} + Q_{seg\,5,conduction,right} \qquad (D.66)$$

$$Q_{seg\,5,conduction} = 30.99 + 21.12 = 0.052\,kW \qquad (D.67)$$

Finally, the total conduction heat duty for the entire tube array was obtained as follows:

$$Q_{conduction} = Q_{seg\,3,conduction} + Q_{seg\,4,conduction} + Q_{seg\,5,conduction} \qquad \text{(D.68)}$$

$$Q_{conduction} = 0.913 - 0.01 + 0.052 = 0.96\,kW \qquad \text{(D.69)}$$

For this case, the coolant-side absorber heat duty was 7.954 kW. Therefore, the total contribution of the conduction heat duty is about 12%.

APPENDIX E HEAT LOSS TO AMBIENT

This appendix discusses the procedures to estimate the heat loss to the ambient from the absorber shell. The calculations are also illustrated with representative values for the test case at an absorber pressure of 345 kPa, dilute solution concentration of 25%, and solution flow rate of 0.026 kg/s. Heat is lost to the ambient both via natural convection and radiation. The absorber shell is assumed to be at an average of the solution inlet and outlet temperatures. The shell is insulated with ½" thick fiber glass insulation. Figure E.1 shows a schematic used for the heat loss calculations.
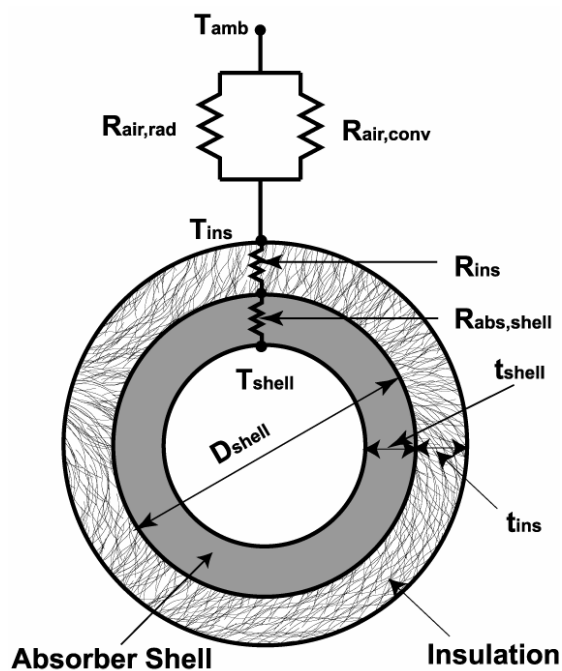

Figure E.1 Thermal Resistance Network for Heat Loss Calculations

To calculate the natural convection heat transfer coefficient, the Grashof (Gr) number is calculated first. This is followed by the calculation of the Nusselt number (Nu_{air}) using an empirical correlation (Incropera and DeWitt 2002). To include the effect of the side flanges, a characteristic length is defined.

$$L_{char} = L_{shell} + D_{shell} / 4 \tag{E.1}$$

$$L_{char} = 0.489 + 0.254 / 4 = 0.55\, m \tag{E.2}$$

$$R_{abs,shell} = \frac{\ln\left(\dfrac{D_{shell}}{D_{shell} - 2 \times t_{shell}}\right)}{2 \times \pi \times k_{shell} \times L_{char}} \tag{E.3}$$

$$R_{abs,shell} = \frac{\ln\left(\dfrac{0.254}{0.254 - 2 \times 0.0127}\right)}{2 \times \pi \times 15.31 \times 0.55} = 1.98 \times 10^{-3}\, K / W \tag{E.4}$$

$$R_{ins} = \frac{\ln\left(\dfrac{D_{shell} + 2 \times t_{ins}}{D_{shell}}\right)}{2 \times \pi \times k_{ins} \times L_{ins}} \tag{E.5}$$

$$R_{ins} = \frac{\ln\left(\dfrac{0.254 + 2 \times 0.0127}{0.254}\right)}{2 \times \pi \times 0.043 \times 0.55} = 0.639\, K / W \tag{E.6}$$

To calculate the Grashof and Nusselt numbers for the air, the properties are calculated at an average of the insulation surface and the ambient temperatures.

$$T_{ave,air} = \frac{T_{ins} + T_{amb}}{2} \tag{E.7}$$

$$T_{ave,air} = \frac{30.16 + 23}{2} = 26.58^o C \tag{E.8}$$

324

$$Gr_{air} = \frac{g \times (T_{ins} - T_{amb}) \times (D_{shell} + 2 \times t_{ins})^3}{v^2 \times (T_{ave,air} + 273.15)} \tag{E.9}$$

$$Gr_{air} = \frac{9.81 \times (30.16 - 23) \times (0.254 + 2 \times 0.0127)^3}{(1.6 \times 10^{-5})^2 \times (26.67 + 273.15)} = 2.056 \times 10^7 \tag{E.10}$$

$$Ra_{air} = Gr_{air} \cdot Pr_{air} \tag{E.11}$$

$$Ra_{air} = 2.056 \times 10^7 \times 0.723 = 1.496 \times 10^7 \tag{E.12}$$

The air-side Nusselt number is obtained using a correlation for natural convection heat flow from a horizontal cylinder (Incropera and DeWitt 2002).

$$Nu_{air} = \left[0.6 + \frac{0.387 \times Ra_{air}^{1/6}}{\left(1 + [0.559/Pr_{air}]^{9/16}\right)^{9/27}} \right]^2 \tag{E.13}$$

$$Nu_{air} = \left[0.6 + \frac{0.387 \times (1.496 \times 10^7)^{1/6}}{\left(1 + [0.559/0.723]^{9/16}\right)^{9/27}} \right]^2 = 31.96 \tag{E.14}$$

Therefore, the natural convection heat transfer coefficient is,

$$\alpha_{air,conv} = (Nu_{air} \cdot k_{air}) / (D_{shell} + 2 \times t_{ins}) \tag{E.15}$$

$$\alpha_{air,conv} = (31.96 \times 0.0256) / (0.254 + 2 \times 0.0127) = 2.931 \ W/m^2 - K \tag{E.16}$$

The natural convection thermal resistance is then calculated as follows:

$$R_{air,conv} = \frac{1}{\alpha_{air,conv} \times \left(\pi \times (D_{shell} + 2 \times t_{ins}) \times L_{shell} + 2 \times \pi \times (D_{shell} + 2 \times t_{ins})^2 / 4 \right)} \tag{E.17}$$

$$R_{air,conv} = \cfrac{1}{2.931 \times \left(\pi \times (0.254 + 2 \times 0.127) \times 0.489 + 2 \times \pi \times (0.254 + 2 \times 0.127)^2 / 4 \right)} \quad \text{(E.18)}$$
$$= 0.6182 \, K / W$$

Here it is assumed that the same heat transfer coefficient applies for vertical, horizontal, and cylindrical shell walls. The radiation thermal resistance is calculated as follows:

$$\alpha_{air,rad} = 5.67 \times 10^{-8} \cdot \varepsilon \cdot \left((T_{air} + 273.15) + (T_{ins} + 273.15) \right) \cdot \left((T_{air} + 273.15)^2 + (T_{ins} + 273.15)^2 \right)$$

$$\text{(E.19)}$$

$$\alpha_{air,rad} = 5.67 \times 10^{-8} \times 0.85 \times \left((23 + 273.15) + (30.16 + 273.15) \right) \times$$
$$\left((23 + 273.15)^2 + (30.16 + 273.15)^2 \right) = 5.192 \, W / m^2 - K \quad \text{(E.20)}$$

$$R_{air,rad} = \cfrac{1}{\alpha_{air,rad} \times \left(\pi \times (D_{shell} + 2 \times t_{ins}) \times L_{shell} + 2 \times \pi \times (D_{shell} + 2 \times t_{ins})^2 / 4 \right)} \quad \text{(E.21)}$$

$$R_{air,rad} = \cfrac{1}{5.192 \times \left(\pi \times (0.254 + 2 \times 0.127) \times 0.489 + 2 \times \pi \times (0.254 + 2 \times 0.127)^2 / 4 \right)} \quad \text{(E.22)}$$
$$= 0.349 \, K / W$$

The heat loss to the ambient is now calculated as follows:

$$Q_{loss} = \cfrac{(T_{shell} - T_{amb})}{R_{abs,shell} + R_{ins} + \left(\cfrac{R_{air,conv} \times R_{air,rad}}{R_{air,conv} + R_{air,rad}} \right)} \quad \text{(E.23)}$$

Here T_{shell} is the average of the absorber inlet and outlet temperatures,

$$T_{shell} = \frac{T_{abs,in} + T_{pool}}{2} \quad \text{(E.24)}$$

$$T_{shell} = \frac{70.42 + 30.99}{2} = 50.71^o C \quad \text{(E.25)}$$

Therefore, the heat loss to the ambient is,

$$Q_{loss} = \frac{\left(50.71 - 23\right)}{1.983 \times 10^{-3} + 0.639 + 0.223} = 32.08 \ W \qquad (E.26)$$

The heat loss can also be calculated from the surface of the insulation to the ambient. This equation is used to calculate the insulation surface temperature iteratively.

$$Q_{loss} = \frac{\left(T_{ins} - T_{amb}\right)}{\left(\dfrac{R_{air,conv} \times R_{air,rad}}{R_{air,conv} + R_{air,rad}}\right)} \qquad (E.27)$$

The resulting insulation surface temperature is 30.16 ºC.

REFERENCES

Altwicker, E. R. and Lindhjem, C. E. (1988), "Absorption of Gases into Drops," *AIChE Journal* Vol. 34(2) pp. 329-332.

Angelo, J. B., Lightfoot, E. N. and Howard, D. W. (1966), "Generalization of the Penetration Theory for Surface Stretch: Application to Forming and Oscillating Drops," *AIChE Journal* Vol. 12(4) pp. 751-760.

Armbruster, R. and Mitrovic, J. (1998), "Evaporative Cooling of a Falling Water Film on Horizontal Tubes," *Experimental Thermal and Fluid Science* Vol. 18(3) pp. 183-194.

Asano, K. (2006). *Mass Transfer: From Fundamentals to Modern Industrial Applications*. Wiley-VCH. Weinheim, Germany

Bird, R. B., Stewart, W. E. and Lightfoot, E. N. (2002). *Transport Phenomena*. 2nd Ed. J. Wiley. New York

Bogart, M. J. P. (1982), "Pitfalls in Ammonia Absorption Refrigeration," *International Journal of Refrigeration* Vol. 4 pp. 203-208.

Carey, V. P. (1992). *Liquid-Vapor Phase-Change Phenomena: An Introduction to the Thermophysics of Vaporization and Condensation Processes in Heat Transfer Equipment*. Hemispehere Publishing Corporation. Washington, D.C.

Chen, W. and Christensen, R. N. (2000), "Inlet Subcooling Effect on Heat and Mass Transfer Characteristics in a Laminar Film Flow," *International Journal of Heat and Mass Transfer* Vol. 43(2) pp. 167-177.

Christensen, R. N., Garimella, S., Kang, Y. T. and Garrabrant, M. A. (1998). *Perforated-Fin Heat and Mass Transfer Device*. USA.

Churchill, S. W. (1977a), "Comprehensive Correlating Equations for Heat, Mass and Momentum Transfer in Fully Developed Flow in Smooth Tubes," *Industrial & Engineering Chemistry, Fundamentals* Vol. 16(1) pp. 109-116.

Churchill, S. W. (1977b), "Friction-Factor Equation Spans All Fluid-Flow Regimes," *Chemical Engineering* Vol. 84(24) pp. 91-92.

Churchill, S. W. and Bernstein, M. (1977), "A Correlating Equation for Forced Convection from Gases and Liquids to a Circular Cylinder in Crossflow,"

Transactions of the ASME. Series C, Journal of Heat Transfer Vol. 99(2) pp. 300-306.

Clift, R., Grace, J. R. and Weber, M. E. (1978). *Bubbles, Drops, and Particles*. Academic Press, New York

Colburn, A. P. and Drew, T. B. (1937), "Condensation of Mixed Vapors," *American Institute of Chemical Engineers -- Transactions* Vol. 33 pp. 197-212.

Coulson, J. M. and Skinner, S. J. (1952), "The Mechanism of Liquid-Liquid Extraction across Stationary and Moving Interfaces : Part I. Mass Transfer into Single Dispersed Drops," *Chemical Engineering Science* Vol. 1(5) pp. 197-211.

Danckwerts, P. V. (1951), "Significance of Liquid-Film Coefficients in Gas Absorption," *Industrial & Engineering Chemistry* Vol. 43(6) pp. 1460 - 1467.

Dorokhov, A. R. and Bochagov, V. N. (1983), "Heat Transfer to a Film Falling over Horizontal Cylinders," *Heat Transfer - Soviet Research* Vol. 15(2) pp. 96-101.

Erickson, D. C., Gomezplata, A. and Papar, R. A. (1998), "Use of the Colburn-Drew Equations to Model Mass Transfer," *International Communications in Heat and Mass Transfer* Vol. 25(1) pp. 93-98.

Fenghour, A., William, A. W., Vesovic, V., Watson, J. T. R., Millat, J. and Vogel, E. (1995), "The Viscosity of Ammonia," *Journal of Physical and Chemical Reference Data* Vol. 24(5) pp. 1649-1667.

Fernandez-Seara, J., Sieres, J., Rodriguez, C. and Vazquez, M. (2005), "Ammonia-Water Absorption in Vertical Tubular Absorbers," *International Journal of Thermal Sciences* Vol. 44(3) pp. 277-288.

Frank, M. J. W., Kuipers, J. A. M. and van Swaaij, W. P. M. (1996), "Diffusion Coefficients and Viscosities of CO2+H2O, CO2+CH3OH, NH3+H2O, and NH3+CH3OH Liquid Mixtures," *Journal of Chemical and Engineering Data* Vol. 41(2) pp. 297-302.

Garimella, S. (1999), "Miniaturized Heat and Mass Transfer Technology for Absorption Heat Pumps," *Proceedings of the International Sorption Heat Pump Conference*, Munich, Germany, pp. 661-670.

Garimella, S. (2000), "Microchannel Components for Absorption Space-Conditioning Systems," *ASHRAE Transactions* Vol. 106(1) pp. 453-462.

Garimella, S. (2004). *Method and Means for Miniaturization of Binary-Fluid Heat and Mass Exchangers*. USA.

Garner, F. H. and Lane, J. J. (1959), "Mass Transfer to Drops of Liquid Suspended in a Gas Stream. II: Experimental Work and Results," *Trans. Inst. Chem. Engr.* Vol. 37 pp. 162 -

Garrabrant, M. A. and Christensen, R. N. (1997), "Modeling and Experimental Verification of a Perforated Plate-Fin Absorber for Aqua-Ammonia Absorption Systems," *Proceedings of the 1997 ASME International Mechanical Engineering Congress and Exposition, Nov 16-21 1997*, Dallas, TX, USA, ASME, Fairfield, NJ, USA, pp. 337-347.

Gillespie, P. C., Wilding, W. V. and Wilson, G. M. (1987), "Vapor-Liquid Equilibrium Measurements on the Ammonia-Water System from 313 K to 589 K," *AIChE Symposium Series* Vol. 83(256) pp. 97-127.

Goel, N. and Goswami, D. Y. (2005a), "Analysis of a Counter-Current Vapor Flow Absorber," *International Journal of Heat and Mass Transfer* Vol. 48(7) pp. 1283-1292.

Goel, N. and Goswami, D. Y. (2005b), "A Compact Falling Film Absorber," *Journal of Heat Transfer* Vol. 127(9) pp. 957-965.

Gommed, K., Grossman, G. and Koenig, M. S. (1999), "Numerical Model of Ammonia-Water Absorption inside a Vertical Tube," *Proceedings of the International Sorption Heat Pump Conference*, Munich, Germany, March 1999, pp. 275-281.

Gommed, K., Grossman, G. and Koenig, M. S. (2001), "Numerical Study of Absorption in a Laminar Film of Ammonia-Water," *ASHRAE Transactions* Vol. 107(Part 1) pp. 453 - 462.

Groothuis, H. and Kramers, H. (1955), "Gas Absorption by Single Drops During Formation," *Chemical Engineering Science* Vol. 4(1) pp. 17-25.

Hadamard, J. (1911), *Comptes Rendus* Vol. 152 pp. 1735 -

Handlos, A. E. and Baron, T. (1957), "Mass and Heat Transfer from Drops in Liquid-Liquid Extraction," *AIChE Journal* Vol. 3(1) pp. 127-136.

Haselden, G. G. and Malaty, S. A. (1959), "Heat and Mass Transfer Accompanying the Absorption of Ammonia in Water," *Institution of Chemical Engineers -- Transactions* Vol. 37(3) pp. 137-146.

Heertjes, P. M. and de Nie, L. H. (1966), "The Mechanism of Mass Transfer During Formation, Release and Coalescence of Drops. Part I—Mass Transfer to Drops Formed at a Moderate Speed," *Chemical Engineering Science* Vol. 21(9) pp. 755-768.

Heertjes, P. M., Holve, W. A. and Talsma, H. (1954), "Mass Transfer between Isobutanol and Water in a Spray-Column," *Chemical Engineering Science* Vol. 3(3) pp. 122-142.

Herold, K. E., Radermacher, R. and Klein, S. A. (1996). *Absorption Chillers and Heat Pumps*. CRC Press, Inc., Boca Raton, Florida

Higbie, R. (1935), "The Rate of Absorption of a Pure Gas into a Still Liquid During Short Periods of Exposure," *Transactions of the AICHE* Vol. 35 pp. 365 - 389.

Hoffmann, L. and Ziegler, F. (1996), "Experimental Investigation of Heat and Mass Transfer with Aqueous Ammonia," *International Ab-Sorption Heat Pump Conference*, Montreal, Quebec, Canada, pp. 383-392.

Honda, H., Nozu, S. and Takeda, Y. (1987), "Flow Characteristics of Condensate on a Vertical Column of Horizontal Low Finned Tubes," *Proceedings of the 1987 ASME-JSME Thermal Engineering Joint Conference*, Honolulu, HI, USA, pp. 517-524.

Honda, H., Uchima, B., Nozu, S., Nakata, H. and Torigoe, E. (1991), "Film Condensation of R-113 on in-Line Bundles of Horizontal Finned Tubes," *Journal of Heat Transfer, Transactions of ASME* Vol. 113(2) pp. 479-486.

Hu, X. and Jacobi, A. M. (1996a), "The Intertube Falling Film: Part 1 - Flow Characteristics, Mode Transitions, and Hysteresis " *Journal of Heat Transfer, Transactions of ASME* Vol. 118(3) pp. 616 - 625.

Hu, X. and Jacobi, A. M. (1996b), "The Intertube Falling Film: Part 2 - Mode Effects on Sensible Heat Transfer to a Falling Liquid Film," *Journal of Heat Transfer: Transactions of the ASME* Vol. 118 pp. 626-633.

Ibrahim, O. M. and Klein, S. A. (1993), "Thermodynamic Properties of Ammonia-Water Mixtures," *ASHRAE Transactions* Vol. 99(1) pp. 1495-1502.

Incropera, F. P. and DeWitt, D. P. (2002). *Fundamentals of Heat and Mass Transfer*. 5th Ed. John Wiley & Sons. New York

Inoue, N., Yabuuchi, H., Goto, M. and Koyama, S. (2004), "Heat and Mass Transfer of Ammonia Gas Absorption into Falling Liquid Film on a Horizontal Tube," *Transactions of the JSRAE* Vol. 21(4) pp. 299-308.

Jeong, S. and Garimella, S. (2002), "Falling-Film and Droplet Mode Heat and Mass Transfer in a Horizontal Tube LiBr/Water Absorber," *International Journal of Heat and Mass Transfer* Vol. 45(7) pp. 1445-1458.

Jeong, S. and Garimella, S. (2005), "Optimal Design of Compact Horizontal Tube LiBr/Water Absorbers," *HVAC and R Research* Vol. 11(1) pp. 27-44.

Jeong, S., Koo, K.-K. and Lee, S. K. (1998), "Heat Transfer Performance of a Coiled Tube Absorber with Working Fluid of Ammonia/Water," *Proceedings of the 1998 ASHRAE Winter Meeting. Part 2 (of 2)*, San Francisco, CA, USA, ASHRAE, Atlanta, GA, USA, pp. 1577-1583.

Kang, Y. T., Akisawa, A. and Kashiwagi, T. (1999), "Experimental Correlation of Combined Heat and Mass Transfer for NH3-H2O Falling Film Absorption," *International Journal of Refrigeration* Vol. 22(4) pp. 250-262.

Kang, Y. T., Akisawa, A. and Kashiwagi, T. (2000), "Analytical Investigation of Two Different Absorption Modes: Falling Film and Bubble Types," *International Journal of Refrigeration* Vol. 23(6) pp. 430-443.

Kang, Y. T., Chen, W. and Christensen, R. N. (1997), "Generalized Component Design Model by Combined Heat and Mass Transfer Analysis in NH_3/H_2O Absorption Heat Pump Systems," *Proceedings of the 1997 ASHRAE Winter Meeting, Jan 26-29 1997*, Philadelphia, PA, USA, ASHRAE, Atlanta, GA, USA, pp. 444-453.

Kang, Y. T. and Christensen, R. N. (1994), "Development of a Counter-Current Model for a Vertical Fluted Tube GAX Absorber," *Proceedings of the International Absorption Heat Pump Conference, Jan 19-21 1994*, New Orleans, LA, USA, ASME, New York, NY, USA, pp. 7-16.

Kang, Y. T. and Christensen, R. N. (1995), "Combined Heat and Mass Transfer Analysis for Absorption in a Fluted Tube with a Porous Medium in Confined Cross Flow," *Proceedings of the 1995 ASME/JSME Thermal Engineering Joint Conference. Part 1 (of 4), Mar 19-24 1995*, Maui, HI, USA, ASME, New York, NY, USA, pp. 251-260.

Killion, J. D. and Garimella, S. (2001), "A Critical Review of Models of Coupled Heat and Mass Transfer in Falling-Film Absorption," *International Journal of Refrigeration* Vol. 24(8) pp. 755-797.

Killion, J. D. and Garimella, S. (2003), "Gravity-Driven Flow of Liquid Films and Droplets in Horizontal Tube Banks," *International Journal of Refrigeration* Vol. 26(5) pp. 516-526.

Killion, J. D. and Garimella, S. (2004a), "Pendant Droplet Motion for Absorption on Horizontal Tube Banks," *International Journal of Heat and Mass Transfer* Vol. 47(19-20) pp. 4403-4414.

Killion, J. D. and Garimella, S. (2004b), "Simulation of Pendant Droplets and Falling Films in Horizontal Tube Absorbers," *Journal of Heat Transfer* Vol. 126(6) pp. 1003-1013.

Kim, B. (1998), "Heat and Mass Transfer in a Falling Film Absorber of Ammonia-Water Absorption Systems," *Heat Transfer Engineering* Vol. 19(3) pp. 53-63.

Kirby, M. J. and Perez-Blanco, H. (1994), "A Design Model for Horizontal Tube Water/Lithium Bromide Absorbers," *Proceedings of the 1994 International Mechanical Engineering Congress and Exposition*, Chicago, IL, USA, pp. 1-10.

Klein, S. A. (2006). *Engineering Equation Solver*, Middleton, WI.

Kronig, R. and Brink, J. C. (1950), "On Theory of Extraction from Falling Droplets," *Applied Scientific Research* Vol. A2(2) pp. 142-154.

Kurem, E. and Horuz, I. (2001), "A Comparison between Ammonia-Water and Water-Lithium Bromide Solutions in Absorption Heat Transformers," *International Communications in Heat and Mass Transfer* Vol. 28(3) pp. 427 - 438.

Kwon, K. and Jeong, S. (2004), "Effect of Vapor Flow on the Falling-Film Heat and Mass Transfer of the Ammonia/Water Absorber," *International Journal of Refrigeration* Vol. 27(8) pp. 955-964.

Kyung, I., Herold, K. E. and Kang, Y. T. (2007), "Model for Absorption of Water Vapor into Aqueous LiBr Flowing over a Horizontal Smooth Tube," *International Journal of Refrigeration* Vol. 30(4) pp. 591-600.

Lee, C. H., Kang, Y. T., Kang, H. U. and Kim, S. H. (2005), "Numerical and Experimental Study of Falling Film in Ammonia Absorption Refrigeration Systems," *Journal of Chemical Engineering of Japan* Vol. 38(7) pp. 520-527.

Lee, K. B., Chun, B. H., Lee, J. C., Lee, C. H. and Kim, S. H. (2002), "Experimental Analysis of Bubble Mode in a Plate-Type Absorber," *Chemical Engineering Science* Vol. 57 pp. 1923 - 1929.

Lee, S. (2007). Development of Techniques for in-Situ Measurement of Heat and Mass Transfer in Ammonia-Water Absorption Systems. PhD Dissertation, Georgia Institute of Technology. Atlanta.

Lewis, W. K. and Whitman, W. G. (1924), "Principles of Gas Absorption," *Industrial and Engineering Chemistry* Vol. 16(12) pp. 1215-1220.

Licht, J., W. and Pansing, W. F. (1953), "Solute Transfer from Single Drops in Liquid-Liquid Extraction," *Industrial & Engineering Chemistry* Vol. 45(9) pp. 1885-1896.

Meacham, J. M. (2002). An Integrated Experimental and Analytical Study of Ammonia-Water Absorption in Microchannel Geometries. MS Thesis, Iowa State University. Ames.

Meacham, J. M. and Garimella, S. (2002a), "Experimental Demonstration of a Prototype Microchannel Absorber for Space-Conditioning Systems," *International Sorption Heat Pump Conference*, Shanghai, China, pp. 270-276.

Meacham, J. M. and Garimella, S. (2002b), "Miniaturized Shell-and-Tube Heat and Mass Exchangers for Absorption Heat Pumps," *12th International Heat Transfer Conference*, Grenoble, France

Meacham, J. M. and Garimella, S. (2003), "Modeling of Local Measured Heat and Mass Transfer Variations in a Microchannel Ammonia-Water Absorber," *ASHRAE Transactions* Vol. 109(1) pp. 412-422.

Meacham, J. M. and Garimella, S. (2004), "Ammonia-Water Absorption Heat and Mass Transfer in Microchannel Absorbers with Visual Confirmation," *2004 Winter Meeting - Technical and Symposium Papers, American Society of Heating, Refrigerating and Air-Conditioning Engineers, Jan 24-28 2004*, Anaheim, CA, United States, Amer. Soc. Heating, Ref. Air-Conditoning Eng. Inc., Atlanta, GA 30329, United States, pp. 513-520.

Merrill, T. L., Setoguchi, T. and Perez-Blanco, H. (1994), "Compact Bubble Absorber Design and Analysis," *Proceedings of the International Absorption Heat Pump Conference*, New Orleans, LA, USA, pp. 217-223.

Merrill, T. L., Setoguchi, T. and Perez-Blanco, H. (1995), "Passive Heat Transfer Enhancement Techniques Applied to Compact Bubble Absorber Design," *Journal of Enhanced Heat Transfer.* Vol. 2(3) pp. 199-208.

Mills, A. F. (1995). *Heat and Mass Transfer*. Concord, MA Richard D. Irwin, Inc.

Mitrovic, J. (1986), "Influence of Tube Spacing and Flow Rate on Heat Transfer from a Horizontal Tube to a Falling Liquid Film," *Proceedings of the 8th International Heat Transfer Conference*, San Francisco, CA, USA, Hemisphere Publ Corp, Washington, DC, USA, pp. 1949-1956.

Mitrovic, J. (2005), "Flow Structures of a Liquid Film Falling on Horizontal Tubes," *Chemical Engineering and Technology* Vol. 28(6) pp. 684-694.

Nernst, W. (1904), "Theorie Der Reaktiongeschwindigkeit in Heterogenen Systemen," *Zeitschrift für Physikalische Chemie* Vol. 47 pp. 52-55.

Nosoko, T., Miyara, A. and Nagata, T. (2002), "Characteristics of Falling Film Flow on Completely Wetted Horizontal Tubes and the Associated Gas Absorption," *International Journal of Heat and Mass Transfer* Vol. 45(13) pp. 2729-2738.

Olander, D. R. (1966), "The Handlos-Baron Drop Extraction Model," *AIChE Journal* Vol. 12(5) pp. 1018-1019.

Onda, K., Takeuchi, H. and Okumoto, Y. (1968), "Mass Transfer Coefficients between Gas and Liquid Phases in Packed Columns," *Journal of Chemical Engineering of Japan* Vol. 1(1) pp. 56-62.

Palmer, S. C. and Christensen, R. N. (1996), "Experimental Investigation and Model Verification for a GAX Absorber," *International ab-sorption heat pump conference*, Montreal, pp. 367-374.

Panchal, C. B., Kuru, W. C., Chen, F. C., Domingo, N. and HuangFu, E. P. (1997), "Experimental and Analytical Study of Condensation of Ammonia-Water Mixtures," *AIChE Symposium Series*, p. 239.

Patnaik, V. and Perez-Blanco, H. (1996a), "Roll Waves in Falling Films: An Approximate Treatment of the Velocity Field," *International Journal of Heat and Fluid Flow* Vol. 17(1) pp. 63-70.

Patnaik, V. and Perez-Blanco, H. (1996b), "Study of Absorption Enhancement by Wavy Film Flows," *International Journal of Heat and Fluid Flow* Vol. 17(1) pp. 71-77.

Perez-Blanco, H. (1988), "A Model of an Ammonia-Water Falling Film Absorber," *ASHRAE Transactions* Vol. 94(1) pp. 467-483.

Pigford, R. L. (1941). Counter Diffusion in a Wetted Wall Column. PhD Dissertation, University of Illinois. Urbana.

Potnis, S. V., Gomezplata, A., Papar, R. A., Anand, G. and Erickson, D. C. (1997), "GAX Component Simulation and Validation," *ASHRAE Transactions* Vol. 103(1) pp. 454-459.

Price, B. C. and Bell., K. J. (1973), "Design of Binary Vapor Condensers Using the Colburn-Drew Equations," *Alche Symposium*, pp. 163-171.

Roques, J. F., Dupont, V. and Thome, J. R. (2002), "Falling Film Transitions on Plain and Enhanced Tubes," *Journal of Heat Transfer* Vol. 124(3) pp. 491-499.

Roques, J. F. and Thome, J. R. (2003), "Falling Film Transitions between Droplet, Column, and Sheet Flow Modes on a Vertical Array of Horizontal 19 FPI and 40 FPI Low-Finned Tubes," *Heat Transfer Engineering* Vol. 24(6) pp. 40-45.

Rose, P. M. and Kintner, R. C. (1966), "Mass Transfer from Large Oscillating Drops," *AIChE Journal* Vol. 12(3) pp. 530-534.

Ruckenstein, E. (1967), "Mass Transfer between a Single Drop and a Continuous Phase," *International Journal of Heat and Mass Transfer* Vol. 10(12) pp. 1785-1792.

Ruckenstein, E. and Berkente, C. (1968), "Mass Transfer to Falling Liquid Films at Low Reynolds Numbers," *International Journal of Heat and Mass Transfer* Vol. 11 pp. 743 - 753.

Ruhemann, M. (1947), "A Study of the Transfer of Heat and Matter in an Ammonia Absorber," *Transactions of the Institute of Chemical Engineering* pp. 158-162.

Ryan, W. A. (1994), "Water Absorption in an Adiabatic Spray of Aqueous Lithium Bromide Solution," *Proceedings of the International Absorption Heat Pump Conference*, New Orleans, LA, USA, Jan 19-21 1994, ASME, New York, NY, USA

Seader, J. D. and Henley, E. J. (1998). *Separation Process Principles*. John Wiley & Sons, Inc., New York, NY

Sherwood, T. K., Pigford, R. L. and Wilke, C. R. (1975). *Mass Transfer*. McGraw-Hill. New York

Shih, S.-M., Huo, Y.-L. and Hsu, C.-T. a. (1995), "Liquid-Phase Physical Mass Transfer Coefficient for Drops: Comparison of Models and Measurement Results," *Journal of the Chinese Institute of Chemical Engineers* Vol. 26(2) pp. 95-102.

Skelland, A. H. P. and Minhas, S. S. (1971), "Dispersed Phase Mass Transfer During Drop Formation and Coalescence in Liquid-Liquid Extraction," *AIChE Journal* Vol. 17(6) pp. 1316-1324.

Takuma, M., Yamada, A. and Matsuo, T. (1993). Condensation Heat Transfer Characteristics of Ammonia-Water Vapor Mixture on Tube Bundles. *Condensation and Condenser Design: Proceedings of the Engineering Foundation Conference on Condensation and Condenser Design, St. Augustine, Florida, March 7-12, 1993*, ASME pp. 207-217.

Taylor, B. N. and Kuyatt, C. E. (1993). Guidelines for Evaluating and Expressing the Uncertainty of NIST Measurement Results. National Institute of Standards and Technology. Washington, DC, USA, NIST/TN 1297, 15 p.

The Mathworks Inc. (2002). *Matlab 6.5.0.180913a Release 13*. Natick, MA.

Tillner Roth, R., Harms-Watzenberg, F. and Baehr, H. D. (1993), "Eine Neue Fundamentalgleichung Für Ammoniak," *DKV-Tagungsbericht* Vol. 20 pp. 167-181.

Tufeu, R., Ivanov, D. Y., Garrabos, Y. and Le Neindre, B. (1984), "Thermal Conductivity of Ammonia in a Large Temperature and Pressure Range Including the Critical Region," *Berichte der Bunsengesellschaft fuer Physikalische Chemie* Vol. 88(4) pp. 422-427.

Wassenaar, R. H. and Segal, G. (1999), "Numerical Results of Falling Film Absorption with Water/Ammonia," *International Journal of Thermal Sciences* Vol. 38(11) pp. 960-964.

Whitman, W. G. (1923), "Two-Film Theory of Gas Absorption," *Chemical and Metallurgical Engineering* Vol. 29 pp. 146-148.

Wilke, C. R. (1950), "A Viscosity Equation for Gas Mixtures," *Journal of Chemical Physics* Vol. 18 pp. 517-519.

Wilke, W. (1962), "Waermeuebergang an Rieselfilme (Heat Transfer to Falling Liquid Films)," *VDI -- Forschungsheft*(490) p. 36.

Yung, D., Lorenz, J. J. and Ganic, E. N. (1980), "Vapor/Liquid Interaction and Entrainment in Falling Film Evaporators," *Journal of Heat Transfer, Transactions ASME* Vol. 102(1) pp. 20-25.

Ziegler, B. and Trepp, C. (1984), "Equations of State for Ammonia-Water Mixtures," *International Journal of Refrigeration* Vol. 7(2) pp. 101-106.